

Adam Mickiewicz University in Poznań
NanoBioMedical Centre / Faculty of Physics

**Photoluminescent and electrochemical
(bio)sensors based on porous silicon and zinc
oxide for continuous mycotoxins and glucose
detection**

by

VALERII MYNDRUL

Supervisor: Prof. UAM dr hab. Igor Iatsunskyi

Auxiliary supervisor: Dr. Mikhael Bechelany

This dissertation is submitted for the degree of

DOCTOR OF PHILOSOPHY

In Physics



ADAM MICKIEWICZ
UNIVERSITY
POZNAŃ

Poznań 2022

Acknowledgments

First of all, I want to express my deepest gratitude to my supervisor Prof. UAM dr hab. *Igor Iatsunskyi* for his support, guidance through all these years, the opportunity to work independently, valuable advice and discussions. I very much appreciate your patience, engorgement and enthusiasm, they helped me to tackle all the problems that I faced while doing and writing my dissertation.

I would like to express my gratitude to all members of NanoBioMedical Centre, for the support, valuable comments and questions during my seminars. Particularly, I am thankful to Prof. UAM dr hab. *Emerson Coy* for the XDR and TEM analysis, dr *Nataliya Babayevska* for her contribution to the samples synthesis, and *Mykola Pavlenko* for his assistance during (bio)sensing measurements.

I would like to thank all the coauthors of my publications, and international collaboration from different countries. I have a special debt of gratitude to dr *Roman Viter* who hosted me during my first secondment (in Riga, University of Latvia), and who inspired me to work on (bio)sensors. I also want to express my grateful acknowledgment to Prof. habil. dr. *Arūnas Ramanavičius* for his valuable advice and support, to dr. *Mikhael Bechelany* for his co-supervision and contribution to the samples synthesis and analysis.

I owe thanks to a very special person, my wife *Julia* who supported me through all my frustrations, stresses, absences, and sorrows. Thank you for your continued love, support and understanding while working on my dissertation, this made it possible to completed the mission.

I am sending special thanks to all people who supported me all these years, to my family, and to my friends. Dear *Mother!* Words are not enough to express my gratitude to you for all the support and love you have given me!

I am immensely grateful to my grandparents *Liudmyla and Oleksandr*. I know you would be proud of me; I will never forget what you had done for me!

Jestem niezmiernie wdzięczny *Państwu i Narodowi Polskiemu* za to wspaniałe i wszechstronne wsparcie dla mojego kraju w tym niezwykle trudnym czasie. Nisko się kłaniam!

I also thank the Polish National Science Center for its financial support through the research projects within OPUS programs (project no. 2017/27/B/ST8/01506). I acknowledge the financial support from the projects “Srodowiskowe interdyscyplinarne studia doktoranckie w zakresie nanotechnologii” no. POWR.03.02.00-00-I032/16, and H2020-MSCA-RISE-2017, “Novel 1D photonic metal oxide nanostructures for early stage cancer detection” (project no. 778157). I am very grateful to the Foundation for Polish Science for the START 2021 scholarship for young scientists (START 57.2021).

Abstract

Amid the ongoing global health crisis that requires timely and precise detection/screening of dangerous, harmful, and deadly microorganisms or their metabolites, (bio)sensors have become irreplaceable tools that enable out-of-lab large-scale everyday testing. They are usually applicable in many areas including the marine sector, air pollution monitoring, and the agriculture/food industry. In food production, (bio)sensors are used to detect and eliminate the negative effects of foodborne pathogens, namely bacteria, viruses, fungi, and their toxic metabolites (mycotoxins). Among all mycotoxins, Ochratoxins (OTs) and Aflatoxins (AFs) are the most dangerous to consume, as they suppress the immune system, cause cancer, and damage the liver and kidneys. For example, Ochratoxin A (OTA) is proven to be cancerogenic and neurotoxic, while Aflatoxin B₁ (AFB₁) is well known for its genotoxicity, immunotoxicity, embryotoxicity, and carcinogenicity. Therefore, it is essential to manage the exposure of OTA and AFB₁ via measures aimed to detect and decontaminate infected food or feed, especially in the face of global warming that promotes fungi growth in food commodities. Currently, despite strict control of mycotoxin levels in many countries all over the world, especially in Europe, there are a large number of reports on mycotoxin-contaminated food/feed delivered to consumers. This indicates that traditional methods for mycotoxins detection (e.g. ELISA, chromatography) no longer allow timely testing of the growing number of contaminated samples. To address these limitations, new strategies need to be developed and implemented as soon as possible to enable rapid, low-cost detection outside the laboratory.

The series of publications [**Publications I-III**] that represent substantive chapters of present Ph.D. thesis are devoted to the rapid, label-free, real-time detection of OTA and AFB₁ using porous silicon (PSi), PSi/Au and ZnO-based photoluminescent (PL) transducers. The starting point of the researcher was to fabricate transducers that possess a high surface to volume ratio and eminent PL in visible range utilized as the response of the immunosensor. In the case of Si, a high surface to volume ratio has been achieved by introducing pores into the Si structure using a metal assisted chemical method (MACE), while the intense PL appears as the result of the so-called quantum confinement effect in Si crystallites. The APTES-modified PSi PL-based transducer then was used to detect different concentrations of OTA in real-time mode. The results showed that the proposed method can detect OTA

concentrations as low as 4.4 pg/ml, which is significantly below the levels tolerated by the European Commission.

Taking into account that PSi PL-based transducers possess zero-point response drift due to the passivation of the PSi surface in liquid media, the essential issue appeared to minimize that unnecessary response instability. To address this disadvantage, PSi transducers were modified (chemically and electrochemically) with gold nanoparticles, whose formation is able to reduce charge transfer, and as a consequence minimize zero-point response drift and detection time. Once fabricated, PSi/Au transducers were functionalized with NHS/EDC, allowing the bioreceptors to be directly attached onto the Au nanoparticles. The real-time detection showed a very low limit of detection (LOD) to AFB₁ in the range of 2.1-2.7 pg/ml, indicating that even minimal exposure to hazardous AFB₁ could be eliminated.

The high surface to volume ratio of ZnO PL-based transducers was achieved by combining with 1D interconnected polymer nanofibers (polyacrylonitrile (PAN) nanofibers), where nanofibers form an enclosed core part while the ZnO serves as a shell. The thickness of the shell part varied from 5 to 50 nm, and for the AFB₁ real-time label-free detection was used transducer with a 20 nm ZnO shell because of the best ZnO crystallinity and PL intensity. The lowest AFB₁ concentration that can be detected using this PL-based method was about 39 pg/ml, thus providing highly-precise control of the food/feed contamination.

It is also worth emphasizing the importance of (bio)sensors in medicine, where they are used to monitor metabolism, disease development, hormonal profile, etc. Continued efforts are now being made to safely and continuously detect the analytes of interest in non-invasive body fluids such as saliva, tears, and sweat. These efforts are driven by the need of minimizing everyday invasive sampling such as finger-pricking for blood sugar measurements. In this dissertation, a successful attempt was made to produce and test a flexible, stretchable, skin-attachable enzymatic sensor for real-time sweat glucose monitoring on ZnO TPs/MXene electrode. ZnO TPs were used as the transducer, while MXene decorative elements were utilized to improve the catalytic activity of the ZnO TPs towards glucose oxidation [**Publication IV**]. The study shows that ZnO TPs/MXene electrodes are able to detect glucose concentrations down to 17 μ M in experimental samples (PBS and

artificial sweat). Moreover, the on-body tests showed that there was a direct correlation between sweat glucose measured by our electrochemical sensor and blood glucose, measured by a conventional commercially-available glucometer. Interestingly, the ZnO TPs/MXene sensor allowed us to track sweat glucose dynamics under sweets consumption and exercising, emphasizing the applicability of this method.

This dissertation consists of 8 main chapters and also includes a list of publications constituting the dissertation, co-author statements, and my declaration. The substantive chapters are preceded by a short introduction (**Chapter 1**) to (bio)sensing and immunosensing. **Chapters 2-3** are dedicated to the materials that have been used within the series of (bio)sensing experiments as transducers. There are also described fundamental aspects of the materials, their fabrication processes, and their application in (bio)sensing. **Chapter 4** describes the analytes that were detected during the experiments and the importance of their detection. **Chapters 5-8** represent the core of my dissertation, the content of these chapters has already been published in peer-review articles. The appendices representing my other publication and conference presentations are added at the end of the dissertation.

Streszczenie

W obliczu trwającego globalnego kryzysu zdrowotnego, który wymaga szybkiego i precyzyjnego wykrywania niebezpiecznych, szkodliwych i potencjalnie śmiertelnych mikroorganizmów lub ich metabolitów, (bio)czujniki stały się niezastąpionymi narzędziami, które umożliwiają codzienne testy na dużą skalę poza laboratorium. Są one stosowane w wielu obszarach, takich jak sektor morski, monitorowanie zanieczyszczenia powietrza, czy rolnictwo. W sektorze spożywczym (bio)czujniki wykorzystywane są do wykrywania patogenów żywności, tj. bakterii, wirusów, grzybów i ich toksycznych metabolitów (mikotoksyn), w celu wyeliminowania ich negatywnego wpływu na ludzi i zwierzęta. Spośród wszystkich mikotoksyn, Ochrotoksyny (OT) i Aflatoksyny (AF) są najbardziej niebezpieczne w przypadku spożycia, ponieważ hamują prawidłowe działanie układu odpornościowego, mogą powodować raka, uszkodzenia wątroby i nerek. Ochrotoksyna A (OTA) jest substancją rakotwórczą i neurotoksyczną, gdyż z kolei Aflatoksyna B₁ (AFB₁) może mieć działanie genotoksyczne, immunotoksyczne, embriotoksyczne i rakotwórczego. W związku z tym niezwykle ważne jest kontrolowanie produktów żywnościowych pod kątem obecności OTA i AFB₁ oraz odkażanie skażonej żywności i paszy, zwłaszcza w obliczu globalnego ocieplenia, które sprzyja rozwojowi grzybów w żywności. Obecnie, pomimo ścisłej kontroli poziomu mikotoksyn w artykułach spożywczych, w wielu krajach na całym świecie, zwłaszcza w Europie, pojawia się wiele doniesień o dostawach zanieczyszczonej żywności lub pasz do konsumentów. Oznacza to, że tradycyjne metody wykrywania mikotoksyn (np. ELISA, chromatografia) nie pozwalają już na skuteczne badanie rosnącej liczby skażonych próbek. Aby przewyciężyć te ograniczenia, należy jak najszybciej opracować i wdrożyć nowe strategie, umożliwiające szybkie i tanie wykrywanie mikotoksyn poza laboratorium.

Cykl publikacji [**Publikacje I-III**] reprezentujący merytoryczne rozdziały niniejszej rozprawy doktorskiej poświęcony jest szybkiemu, bezznacznikowemu wykrywaniu OTA i AFB₁ w czasie rzeczywistym za pomocą fotoluminescencyjnych (PL) (bio)czujników opartych na P-Si (krzemie porowatym), P-Si/Au i ZnO. Punktem wyjścia badań było wytworzenie (bio)czujników o wysokim stosunku powierzchni do objętości oraz intensywnej widzianej PL. W przypadku Si, wysoki stosunek powierzchni do objętości osiągnięto poprzez wprowadzenie porów do struktury Si metodą chemicznego trawienia wspomaganego metalem (CWWM), podczas gdy

intensywna PL pojawia się w wyniku tzw. efektu uwięzienia kwantowego w krystalitach Si. Po zmodyfikowaniu APTESem, P*Si* (bio)czujnik oparty na zjawisku PL został zastosowany do wykrywania różnych stężeń OTA w czasie rzeczywistym. Wyniki eksperymentów wykazały, że proponowana metoda umożliwia wykrycie obecności OTA przy bardzo niskiej wartości stężenia (jak 4.4 pg/ml), czyli znacznie poniżej poziomów dopuszczalnych przez Komisję Europejską.

Biorąc pod uwagę, że (bio)czujniki oparte na PL P*Si* mają zerowy dryft sygnału z powodu utleniania powierzchni P*Si* w ciekłych mediach, zasadniczym problemem okazało się zminimalizowanie tej niekorzystnej niestabilności sygnału. Aby przezwyciężyć tę wadę, (bio)czujniki P*Si* zostały zmodyfikowane (chemicznie i elektrochemicznie) nanocząstkami złota, mającymi zdolność redukcji przenoszenia ładunku, co w konsekwencji pozwoliło na zminimalizowanie zerowy dryft sygnału i skrócić czas detekcji. W kolejnym etapie (bio)czujniki P*Si*/Au funkcjonalizowano za pomocą NHS/EDC, umożliwiając bezpośrednie przyłączenie bioreceptorów do nanocząstek Au. Pomiar w czasie rzeczywistym wykazały bardzo niską granicę wykrywalności (GW) dla AFB₁ w zakresie 2.1-2.7 pg/ml, co pozwolić może na wyeliminowanie nawet minimalnej ekspozycji na tę niebezpieczną substancję.

Wysoki stosunek powierzchni do objętości (bio)czujników opartych na ZnO osiągnięto dzięki połączeniu z jednowymiarowymi, wzajemnie połączonymi nanowłóknami polimerowymi (nanowłókna poliakrylonitrylowe (PAN)), gdzie nanowłókna tworzyły rdzeń, a ZnO stanowił zewnętrzną powłokę. Grubość powłoki wahała się od 5 do 50 nm, natomiast do bezznacznikowego wykrywania AFB₁ czasie rzeczywistym zastosowano (bio)sensor o grubości powłoki ZnO wynoszącej 20 nm ze względu na najlepszą krystaliczność ZnO i intensywną PL. Najniższe stężenie AFB₁, które można wykryć za pomocą metody opartej na PL ZnO, wynosiło około 39 pg/ml, zapewniając w ten sposób wysoce precyzyjną kontrolę zanieczyszczenia żywności/paszy.

Warto również podkreślić ważną rolę, jaką (bio)czujniki odgrywają w medycynie, gdzie wykorzystywane są do monitorowania metabolizmu, rozwoju choroby, profilu hormonalnego, itp. Obecnie podejmowane są nieustanne wysiłki, aby bezpiecznie i w sposób ciągły wykrywać anality będące przedmiotem zainteresowania w nieinwazyjnych płynach ustrojowych, takich jak ślina, łzy i pot. Wysiłki te wynikają z chęci ograniczenia potrzeby codziennego pobierania próbek w sposób inwazyjny,

taki jak nakłuwanie opuszków palców w celu pomiaru poziomu cukru we krwi. W niniejszej rozprawie podjęto udaną próbę wyprodukowania i przetestowania elastycznego, rozciągliwego, mocowanego do skóry czujnika enzymatycznego do monitorowania stężenia glukozy w pocie w czasie rzeczywistym. Jako czujnik zastosowane zostały tetrapody ZnO (ZnO TPs), natomiast nanopłatki MXene wybrane zostały jako dekoracyjne elementy poprawiające aktywność katalityczną ZnO TPs w stosunku do glukozy. **[Publikacja IV]**. Badania pokazały, że elektrody ZnO TP/MXene są w stanie wykryć stężenia glukozy do 17 μM w próbkach eksperymentalnych (PBS i sztuczny pot). Co więcej, testy na ciele wykazały, że istnieje bezpośrednia korelacja między poziomem glukozy w pocie mierzonym przez nasz czujnik elektrochemiczny a poziomem glukozy we krwi mierzonym konwencjonalnym, komercyjnie dostępnym glukometrem. Co ciekawe, czujnik ZnO TPs/MXene pozwolił śledzenie zmian stężenia glukozy w pocie podczas spożywania słodczy i wykonywania ćwiczeń, co dodatkowo podkreśla praktyczność tej metody.

Niniejsza dysertacja podzielona została na 8 głównych rozdziałów, zawiera również spis publikacji wchodzących w skład pracy, wypowiedzi współautorów oraz moją deklarację. Na wstępie przedstawione zostały rozdziały wprowadzające do merytorycznej części niniejszej rozprawy. W **Rozdziale 1** opisane zostały główne aspekty (bio)czujników, ich typy, struktura, zasady działania. **Rozdziały 2-3** poświęcone są materiałom, które zostały użyte w serii eksperymentów jako (bio)czujniki. Opisano również podstawowe aspekty materiałów, procesy ich wytwarzania oraz zastosowanie w (bio)czujnikach. W **Rozdziale 4** opisane zostały analizy, które były wykrywane podczas eksperymentów, jak również zaznaczona została istotność ich wykrywania. **Rozdziały 5-8** stanowią rdzeń mojej dysertacji, treść tych rozdziałów została opublikowana w artykułach recenzowanych. Załączniki zawierające pozostałe publikacje oraz doniesienia konferencyjne umieszczone zostały na końcu rozprawy doktorskiej.

List of publications constituting the dissertation

[I]. V. Myndrul, R. Viter, M. Savchuk, N. Shpyrka, D. Erts, D. Jevdokimovs, V. Silamiķelis, V. Smyntyna, A. Ramanavicius, I. Iatsunskyi, *Porous silicon based photoluminescence immunosensor for rapid and highly-sensitive detection of Ochratoxin A*, **Biosensors and Bioelectronics**. 102 (2018) 661–667. doi:10.1016/j.bios.2017.11.048;

IF₂₀₂₁ = 12.545

Ministerial Points₂₀₂₁ = 200 points

[II]. V. Myndrul, R. Viter, M. Savchuk, M. Koval, N. Starodub, V. Silamiķelis, V. Smyntyna, A. Ramanavicius, I. Iatsunskyi, *Gold coated porous silicon nanocomposite as a substrate for photoluminescence-based immunosensor suitable for the determination of Aflatoxin B1*, **Talanta**. 175 (2017) 297–304. doi:10.1016/j.talanta.2017.07.054;

IF₂₀₂₁ = 6.556

Ministerial Points₂₀₂₁ = 100 points

[III]. V. Myndrul, E. Coy, M. Bechelany, I. Iatsunskyi, *Photoluminescence label-free immunosensor for the detection of Aflatoxin B1 using polyacrylonitrile/zinc oxide nanofibers*, **Materials Science and Engineering C**. 118 (2021) 111401. doi:10.1016/j.msec.2020.111401;

IF₂₀₂₀ = 7.328

Ministerial Points₂₀₂₁ = 140 points

[IV]. V. Myndrul, E. Coy, N. Babayevska, V. Zahorodna, V. Balitskyi, I. Baginskiy, O. Gogotsi, M. Bechelany, M.T. Giardi, I. Iatsunskyi, *MXene nanoflakes decorating ZnO tetrapods for enhanced performance of skin-attachable stretchable enzymatic electrochemical glucose sensor*, **Biosensors and Bioelectronics**. 207 (2022) 114141. <https://doi.org/10.1016/j.bios.2022.114141>.

IF₂₀₂₁ = 12.545

Ministerial Points₂₀₂₁ = 200 points

Content

Acknowledgments	I
Abstract	II
Streszczenie	V
List of publications constituting the dissertation	VIII
Content	IX
List of abbreviations.....	1
Motivation and outline.....	6
1. (Bio)sensors and immunosensors	9
1.1. Electrochemical immunosensors.....	12
1.2. Electrical immunosensors	13
1.3. Piezoelectric and acoustic immunosensors.....	13
1.4. Thermometric immunosensors.....	15
1.5. Optical immunosensors	15
1.5.1. SPR-based immunosensors	16
1.5.2. LSPR-based immunosensors	17
1.5.3. SERS-based immunosensors	18
1.5.4. Immunosensors based on reflectance and interference	20
1.5.5. Immunosensors based on chemiluminescence and electrochemiluminescence.....	22
1.5.6. Fluorescence-based immunosensors	23
1.5.7. Immunosensors based on photoluminescent substrates.....	25
1.6. Enzymatic electrochemical sensors	27
2. Fundamental aspects of porous silicon, fabrication methods, photoluminescence, and label-free (bio)sensing performance	29
2.1. Fundamental aspects of porous silicon.....	29
2.2. Metal-assisted chemical etching.....	30
2.3. Photoluminescence of PSi.....	32
2.4. PSi photoluminescence as a tool for (bio)sensing applications	34
2.5. Combination of PSi with noble metal nanoparticles	35
3. Fundamental aspects of zinc oxide, its electrochemical and photoluminescent properties, label-free (bio)sensing applications based on zinc oxide substrates....	38
3.1. Fundamental aspects of zinc oxide. ZnO tetrapods and their electrochemical properties	38

3.2. The role of 2D conductive materials in improving the electrochemical characteristics of ZnO	40
3.3. Photoluminescence of ZnO	41
3.4. Electrospinning and ALD for the fabrication of 1D ZnO interconnected nanofibers.....	43
3.5. ZnO photoluminescence as a tool for (bio)sensing applications	45
4. Analytes to be detected in this dissertation	47
4.1. Mycotoxins and importance of their detection	47
4.2. Diabetes and importance of glucose detection in human	49
Overview of the publications constituting the dissertation.....	51
5. Porous silicon based photoluminescence immunosensor for rapid and highly-sensitive detection of Ochratoxin A	55
5.1. Introduction.....	55
5.2. Materials and Methods	57
5.2.1. Chemical and Reagents	57
5.2.2. The preparation and characterization of PSi.....	57
5.2.3. The biofunctionalization of the PSi surface.....	57
5.2.4. The evaluation of photoluminescence signal of immunosensor.....	58
5.3. Results and Discussion.....	59
5.3.1. Structural properties of PSi.....	59
5.3.2. The evaluation of PSi photoluminescence during OTA determination ...	61
5.3.3. Analysis of adsorption isotherms	62
5.4. Conclusions	66
6. Gold coated porous silicon nanocomposite as a substrate for photoluminescence-based immunosensor suitable for the determination of Aflatoxin B1	67
6.1. Introduction.....	67
6.2. Experimental Section.....	69
6.2.1. Materials	69
6.2.2. Fabrication of PSi samples.....	69
6.2.3. Fabrication of PSi/Au nanocomposites.....	69
6.2.4. Characterization of PSi and PSi/Au nanocomposites	70
6.2.5. Formation of self-assembled monolayers on PSi/Au structures and immobilization antibody against of Aflatoxin B1	71
6.2.6. Immunosensor testing.....	72
6.3. Results and Discussion	72

6.3.1. Structural properties of PSi and PSi/Au	72
6.3.2. Optical properties of Si, PSi and PSi/Au structures.....	76
6.3.3. Determination of analytical characteristics of biosensors	78
6.4. Conclusion.....	83
7. Photoluminescence label-free immunosensor for the detection of Aflatoxin B1 using 1D ZnO/polyacrylonitrile nanofibers	84
7.1. Introduction.....	84
7.2. Experimental section.....	87
7.2.1. Materials	87
7.2.2. PAN fiber fabrication	87
7.2.3. ALD of ZnO.....	88
7.2.4. Characterization techniques	88
7.2.5. The evaluation of PL signal of immunosensor	89
7.3. Results and discussion	90
7.3.1. Structural and optical properties	90
7.3.2. Biofunctionalization of PAN/ZnO	93
7.3.3. Aflatoxin B1 PL detection.....	95
7.3.4. The mechanism of PL biosensing	97
7.3.5. Kinetic and thermodynamic aspects.....	101
7.3.6. Microscopy visualization.....	104
7.4. Conclusions	105
8. MXene nanoflakes decorating ZnO tetrapods for enhanced performance of skin- attachable stretchable enzymatic electrochemical glucose sensor.....	107
8.1. Introduction.....	107
8.2. Experimental section	110
8.2.1. Materials.....	110
8.2.2. Instruments.....	110
8.2.3. Preparation of ZnO TPs	111
8.2.4. Preparation of MXene.....	111
8.2.5. Fabrication of skin-attachable, stretchable electrodes	111
8.2.6. Preparation of ZnO/MXene based electrodes.....	111
8.2.7. Electrochemical glucose detection in PBS and artificial sweat	113
8.2.8. On-body sweat analysis	113
8.2.9. Electrode stretching tests	114
8.3. Results and discussion	114

8.3.1. Material selection	114
8.3.2. Characterization of ZnO TPs/MXene nanocomposite	114
8.3.3. Electrochemical properties of the fabricated electrodes.....	119
8.3.4. CV-based sensor performance.....	121
8.3.5. Chronoamperometry-based sensor performance in PBS (pH = 7.4).....	123
8.3.6. Chronoamperometry-based sensor performance in artificial sweat (pH = 6.5).....	125
8.3.7. Sensors performance under different applied strains.....	127
8.3.8. Qualitative glucose monitoring using stretchable ZnO TPs/MXene/GOx electrode	128
8.4. Conclusions	129
Supporting information	130
References	133
List of other publications	XIII
List of conference presentations	XIV
Contribution statements	XV
Copyright and Permissions	XXXIV

List of abbreviations

1D – one dimensional

2D – two dimensional

3D – three dimensional

11-MUA – 11-Mercaptoundecanoic acid

A

AA – ascorbic acid

AFs – Aflatoxins

AFB1 – Aflatoxin B1

anti-OTA – antibodies against OTA

anti-AFB1 – antibodies against AFB1

APTES – 3-Triethoxysilylpropylamine

B

BET – Brunauer-Emmett-Teller

BSA – bovine serum albumin

C

CCD – A charge-coupled device

CE – chemical enhancement

CL – chemiluminescence

CNTs – carbon nanotubes

CPR – C-reactive protein

CV – cyclic voltammetry

D

DEZ – Diethyl zinc

DI-water – Deionized water

DLE – deep-level emission band

DMF – dimethylformamide

DNA – Deoxyribonucleic acid

E

EC – European Commission

Ec – conduction band

EDC – N-(3-Dimethylaminopropyl)-N'-ethylcarbodiimide hydrochloride

EDX analyzer – dispersive energy X-ray analyzer

EF – enhancement factor

E_F – Fermi level

EGFET – electrolyte-gated field-effect transistor

EGOFET – electrolyte-gated organic field-effect transistor

ELC – electrochemiluminescence

ELISA – enzyme-linked immunosorbent assay

EM – electromagnetic enhancement

E μ PAD – electrochemical microfluidic paper-based analytical device

EtOH – ethanol

E_v – valence band

EWA – evanescent wave all-fiber

F

FAD – flavin adenine dinucleotide

FET – field-effect transistor

FIA – flow-injection analyzer

FL – fluorescence

FRET – Förster resonance energy transfer

FTIR – Fourier-transform infrared spectroscopy

FWHM – full width at half maximum

G

GA – glutaraldehyde

GIXRD – grazing incidence X-ray diffraction

GO_x – glucose oxidase

H

HA – hyaluronic acid

HCC – Hepatocellular carcinoma

HF – hydrofluoric acid

HPR – horseradish peroxidase

L

LDR – linear detection range

LEDs – light-emitted diodes

LOD – limit of detection

LSPR – localized surface plasmon resonance

LSV – linear sweep voltammetry

M

MACE – metal assisted chemical etching

MIP – membrane interface probe

MTL – maximum tolerated levels

MZI – Mach-Zender interferometer

N

NBE – near-band edge excitonic

NBs – nanobeams

nc – nanocrystallites

nc-Si – silicon nanocrystallites

NHS – N-Hydroxysuccinimide

NPs – nanoparticles

NRs – nanorods

NSs – nanospheres

O

OTs – Ochratoxins

OTA – Ochratoxin A

ORR – oxygen reduction reaction

P

P₃HT – poly(3-hexylthiophene-2,5-diyl)

PAN – polyacrylonitrile

PBS – phosphate-buffered saline

pBTTT – Poly[2,5-bis(3-dodecylthiophen-2-yl)thieno[3,2-b]thiophene]

PET – polyethylene

PL – photoluminescence

PLA – polylactic acid

PSi – porous silicon

Q

QCM – quartz crystal microbalance

R

rGO – reduced graphene oxide

RiFS – reflectometric interference spectroscopy

ROS – reactive oxygen species

RT – room temperature

S

SAED – selected area electron diffraction

SAW – surface acoustic wave

SCR – space charge region

SEM – scanning electron spectroscopy

SERS – surface enhanced Raman scattering

SI – Supporting information

SiNWs – silicon nanowires

SP – surface plasmon

SPR – surface plasmon resonance

T

TELISA – thermometric enzyme-linked immunosorbent assay

TEM – transmission electron microscopy

TPE-Z – quaternized tetraphenylethene salt

U

UA – uric acid

UV – ultraviolet

UV-VIS – ultraviolet-visible

V

VOC – volatile organic compounds

v-Au NWs – vertically aligned Enokitake-like gold nanowires

W

WHO – World Health Organization

X

XPS – X-ray photoelectron spectroscopy

XRD – X-ray diffraction

Y

YI – Young interferometer

Z

ZnO – zinc oxide

ZnO TPs – zinc oxide tetrapods

Motivation and outline

The primary intention of this thesis is to fabricate and apply well-known semiconductors and their composites in the design of optical and electrochemical (bio)sensors suitable for continuous detection of hazardous species as well as healthcare applications. In this regard, the development and application of (bio)sensors are of paramount importance in this dissertation and represent its substantive part. Since the main component of each (bio)sensor is a transducer that converts the event of the (bio)receptor-analyte interaction into a signal, it is extremely important to have a nanostructured and biocompatible transducer that is non-toxic and has high surface to volume ratio. From this point of view, silicon (Si) or its nanoscale derivation – porous silicon (PSi) and zinc oxide (ZnO) are the most acceptable, as they meet the above-mentioned requirements. Besides, owing to the relatively low cost and availability of PSi and ZnO, their production can be easily scaled up to industrial scale, which would meet the high demand for currently growing point-of-care testing.

Among all types of (bio)sensors (e.g. electrical, piezoelectric, acoustic), only optical ones provide non-destructive, contactless detection of analytes, simultaneously ensuring high sensitivity, low limit of detection (LOD), and accuracy. The design of optical (bio)sensors strongly depends on the phenomenon that is supposed to be used as a response. For example, the simplest architecture is in the case of reflectance-based biosensors, while it is much more complex for biosensors based on fluorescence (FL) or surface plasmons resonance (SPR), where apart from the transducer and light source, auxiliary components (e.g. prism, analyte with fluorescent labels) are needed. Owing to their eminent light-emitting characteristics, nanoscaled Si and ZnO are ideal for use as labels in FL-based (bio)sensors, however, these type (bio)sensors are much more expensive as labeled analytes cost more than unlabeled ones. To compare, 1 ml solution of labeled Aflatoxin B1 (AFB1) at a concentration of 0.5 $\mu\text{g}/\text{ml}$ costs ~11,000 zloty (~2350 Euro), while 2 ml of 2 $\mu\text{g}/\text{mL}$ of label-free AFB1 solution costs about 1300 zloty (~280 Euro). On the other hand, labeling of analytes can be carried out in the laboratory, but it is usually labor intensive and takes hours or even days to obtain a solution of high purity. Thus, there is a legitimate question of how to minimize costs by avoiding expensive labeled analytes and using superior light-emitting characteristics of nanoscaled Si and ZnO.

Given the variety of shapes of nanosized Si (PSi) and ZnO, it is possible to fabricate light-emitting substrates that serve as transducers while their light emission (usually referred to as photoluminescence (PL)) can be used as the response upon the (bio)receptor-analyte interaction. The design of this type of (bio)sensor is simplified to the construction of a reflectance-based one, which means lower cost and easier maintenance. It is worth mentioning that PL itself is highly sensitive to any disturbances occurred at the (bio)sensor interface; therefore, even one event of (bio)receptor-analyte interaction can be recognized. In particular, this work focuses on PL-based detection of foodborne pathogens AFB₁ and Ochratoxin A (OTA), in order to demonstrate the effectiveness of PSi-, and ZnO-based (bio)sensors for precise, contactless detection of hazardous species in real-time mode.

Another aim of this thesis is to demonstrate the ability of ZnO-based electrodes for electrochemical point-of-care continuous glucose detection in non-invasive body fluid (e.g. sweat). Similar to PL-based (bio)sensors, considerable care must be taken to produce an electrode with a high surface to volume ratio, long term stability, reproducibility and selectivity, which will provide low LOD and high selectivity. The high surface to volume ratio of nanoscaled ZnO is easily achieved due to its variety of shapes and sizes (e.g. rods, tetrapods), while detection parameters can be improved by combining ZnO with 2D conductive nanomaterials (e.g. MXene), which contributes to its catalytic activity towards glucose oxidation. These composite transducers are able to provide extremely low LOD for glucose detection suitable for contentious glucose detection in non-invasive body fluids where glucose concentration is negligible (tens or hundreds of μM). Moreover, it is also advantageous to incorporate highly sensitive transducers into flexible, stretchable electrodes to allow real-time on-body glucose detection in human sweat. This can give insight into the dynamics of glucose levels during food intake or exercise, given that there is an approximate correlation between sweat and blood glucose levels.

Thus, the motivation for this thesis is to demonstrate the applicability of nanoscaled Si and ZnO in PL-based and electrochemical (bio)sensor performances for highly sensitive and selective detection of foodborne pathogens and non-invasive point-of-care testing. Considerable attention has been given to the development of simple (bio)sensors that do not use labeled analytes and complex constructions that increase the cost of detection.

The remainder of this dissertation is structured as follows:

Chapter 1 represents a short overview of (bio)sensors and immunosensors, their types, and their underlying mechanisms.

Chapter 2 continues literature review by introducing PSi substrate including, fabrication and modification processes, physicochemical and photoluminescence properties, and its utilization in different (bio)sensing application.

Chapter 3 shows up the fundamental aspects of ZnO, its physicochemical properties, and photoluminescence. Furthermore, the experimental method for the fabrication of the two different ZnO-based composite used in this work are addressed.

Chapter 4 emphasize the importance of OTA and AFB₁ detection, as well as the importance of point-of-care glucose monitoring.

Chapter 5 displays the fabrication of PSi and application for PL-based detection of OTA in real-time mode. There are also paragraph describing structural and optical properties of the fabricated PSi PL-based transducer.

Chapter 6 points up how the decoration of the PSi transducer with gold will affect the overall detection process, and how this decoration would change the thermodynamic and (bio)sensing characteristics upon AFB₁ detection.

Chapter 7 demonstrates a successful attempt to fabricate ZnO nanofibers and apply them in a PL-based (bio)sensor for real-time detection of hazardous AFB₁.

Chapter 8 covers the application of the ZnO/MXene composite for electrochemical glucose detection, including attempts to monitor body sweat glucose levels. In addition, the details of the ZnO/MXene composites manufacturing process are discussed.

1. (Bio)sensors and immunosensors

Biosensors are devices designed for precise, fast, quantitative, and selective analysis of the analyte (target of interest) content in various media, such as liquid [1], gas [2], or even solid [3]. They usually equipped with two main components: *bioreceptors* (*biorecognition elements*), transducer, and may include some auxiliary components such as an amplifier, detector, processor, display, etc. (Fig. 1.1) [4]. *Biorecognition elements* are biomolecules capable of recognizing the analyte content in a medium of interest. A key element of the entire device is a transducer that can transform the event of the bioreceptor-analyte interaction into a biosensor signal change. Depending on the type of transducer, biosensors can be divided into five groups: electrochemical, optical, electrical, pyroelectric, piezoelectric and acoustic [5].

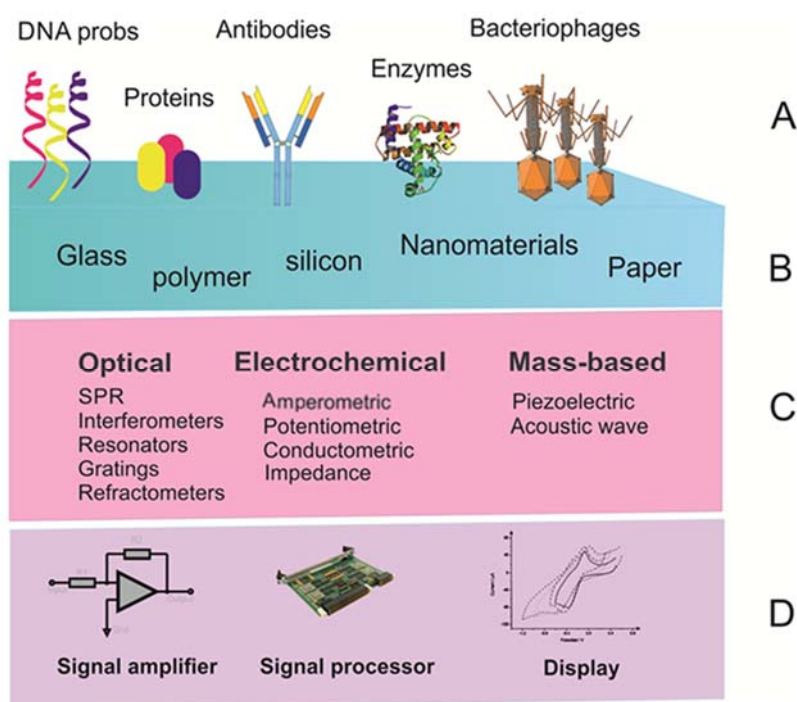


Figure 1.1. Biosensor typical configuration: (a) bioreceptors (b) transducers (c) types of converted signals and (d) electronic part. Reprinted from Ref. [4].

Over the past several decades, biosensors have gained an advantage over other detection methods and unhesitatingly displacing traditional analytical methods (e.g. ELISA, chromatography) from everyday use. The main superiorities of biosensors over the well-known analytical methods are low cost, time-saving, and availability not only for industry but also for households [6]. Moreover, biosensors usually do not require specially trained stuffs and are not labor-intensive when compared to

chromatography, which considered as one of the most popular traditional detection method [7]. Due to their portability, biosensors are essential for express tests in urgent situations, for example, to control the blood glucose levels in diabetic patients [8]. Besides, biosensors play an important role in the primary out-of-lab diagnosis of diseases [9], in the food/beverage industry to control contamination [10], in ecology to determine environmental pollutants, such as air or water pollutants [11]. One can say that biosensors have become indispensable tools for diagnostics and detection in everyday life, and, most likely, their positions their positions will only strengthen.

Since molecular recognition and interaction determine the correct biosensing, special care must be taken when choosing a biorecognition molecule whose affinity and specificity will lead to the formation of a stable complex with analytes. Biorecognition molecules, i.e., antigen/antibody, enzyme, nuclear acid, hormone receptor, live cell, nanobodies, and tissues can specifically interact with other biological species via catalysis and affinity binding [12]. Among others, the specific antigen-antibody interaction is considered one of the most preferred in biosensing because of the high affinity between antigen and antibody provides stable immunocomplex formation [13]. Moreover, the extraction of antigens and antibodies from the medium of interest is much easier than, for example, the extraction of DNA, nuclear acid or nanobodies, etc. Biosensors that utilize antigens or antibodies as biorecognition elements are usually called *immunosensors* [14].

The detection of target analytes with an immunosensor means the detection of antigens or antibodies in a complex background medium (e.g. sweat, tears, serum). Currently, two general approaches have been developed for the detection of antigens/antibodies, the first is so-called label-free format, which implies formation of direct antigen-antibody assay (Fig. 1.2a), and indirect (competitive or binding inhibition) assays which are more preferable for the small biomolecules (Fig. 1.2b,c) [15]. The label-free direct assay requires the target biomolecules to be large enough to generate a measurable signal change, while in indirect assays, a weighting agent can be added in order to achieve a measurable response of the immunosensor [15].

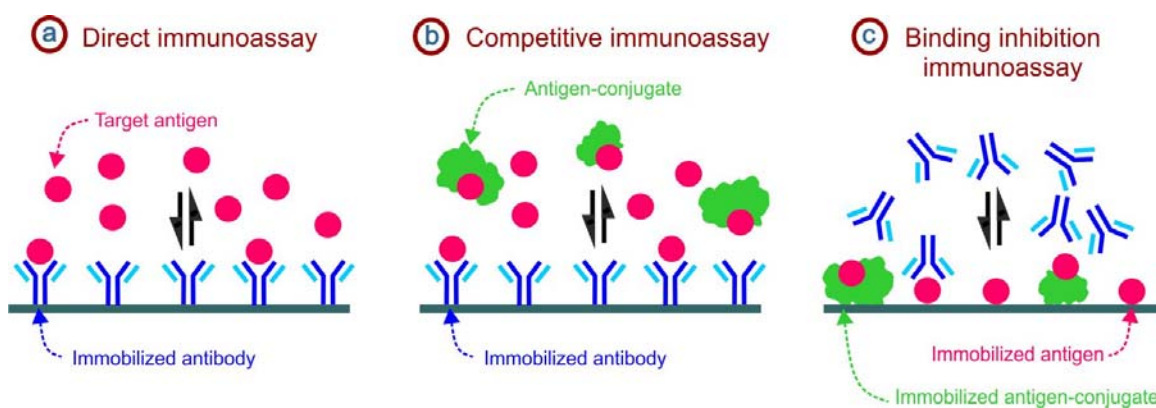


Figure 1.2. Schematic presentation of assay formats generally used for small-molecule detection. (a) in a direct assay, target analyte binds to the recognition element, e.g., the antibody which is immobilized on the sensor surface; (b) in a competitive assay, the analyte competes with its conjugate for the binding to the immobilized recognition element; (c) in a binding inhibition assay, similarly the analyte and analyte-conjugate compete for the binding, but the analyte-conjugate is the one immobilized on the sensor surface either directly via a linker or as a protein-conjugate. Adopted from Ref. [15].

The second approach (which utilizes labeled antibodies/antigens) is much more suitable for extremely low analyte concentrations that cannot cause a measurable signal change [16]. In such case, label-free immunosensors cannot be used since they will not have sufficient sensitivity, and therefore the detection results will be questionable. The labeled immunoassays can be performed in three main formats: competitive, sandwich and indirect immunoassays [17]. The competitive format means that the targets to be measured and labeled targets mixed in the medium of interest will compete with each other for binding to the limited number of antibody-binding sites (Fig.1.3a) [16]. Finally, by determining the intensity of the labeled targets bound to the antibody-binding sites, the concentration of the "true" targets can be quantified. In sandwich format, antigens are literally sandwiched between two antibodies (immobilized on the surface of an immunosensor and labeled); therefore, it is critical for antigens to have at least two epitopes (Fig. 1.3b) [18]. The concentration of antigens in this case is proportional to the signal generated by the labeled antibodies. The indirect format usually requires labeled secondary antibodies as the signal source, which means that primary antibodies are not directly measured or labeled. Labeled secondary antibodies can recognize primary antibodies or antigens and serve as signal amplifiers (Fig. 1.3c) [19].

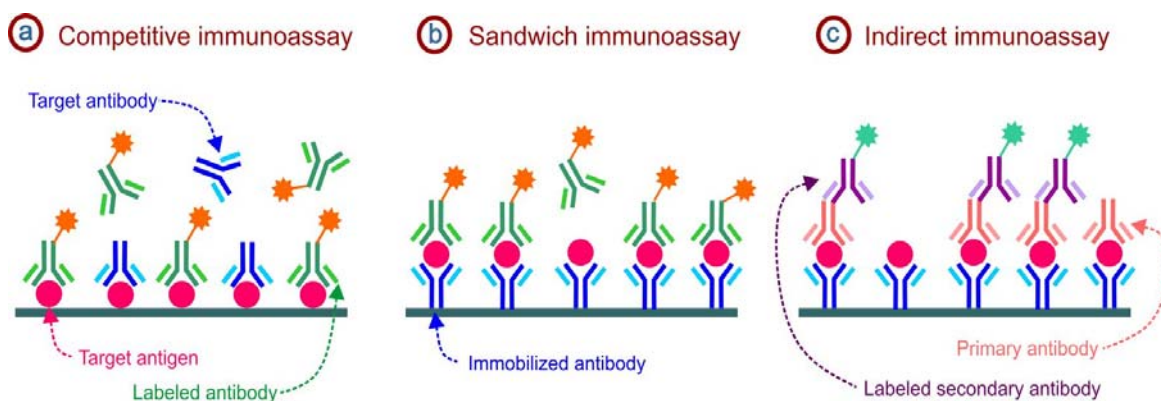


Figure 1.3. Labeled immunoassay formats. (a) Competitive immunoassay; (b) sandwich immunoassay; (c) indirect assay.

Immunosensors are a large branch of the entire biosensor family, which also can be divided into five general groups depending on the nature and physicochemical properties of the transducers. Thereby, immunosensors can be electrochemical, electrical, piezoelectric and acoustic, pyroelectric, and optical [20].

1.1. Electrochemical immunosensors

Electrochemical immunosensors are devices used to detect a binding event between antigens and antibodies by converting it into a measurable electrical signal. The key element of the entire sensing system is a conductive (working) electrode, which can be made of metal, semiconductor, polymer, or a compound thereof [21]. This electrode is sensitive to a change in the electrolyte potential caused by the movement (diffusion) of negative and/or positive ions during the formation of the immunocomplex. In electrochemical immunosensing, target antigens or antibodies are supposed to be extracted from the test sample, while highly-purified bioreceptors are usually commercially available. Currently, a large number of electrochemical immunosensors (potentiometric, amperometric, impedimetric, capacimetric, etc.) have been proposed and various formats of immunoassay have been adapted for electrochemical detection of different antigens or antibodies [20]. Electrochemical immunosensing in general can be carried out in three-electrode electrochemical cell connected to the potentiostat that maintains the constant potential of the working electrode with respect to the reference electrode by adjusting the current at an auxiliary electrode. The output signal of the three-electrode electrochemical cell can be further amplified, processed with a potentiostat and displayed by portable devices (laptop, smartphone, etc.) [22].

1.2. Electrical immunosensors

Electrical detection mainly uses an electrolyte-gated field-effect transistor (EGFET) as the sensing part capable of recognizing an antibody-antigen binding event. A transistor is a three-terminal device in which the current flows through the channel confined between the source (S) and the drain (D) electrodes. The third electrode (so-called gate electrode) serves as a controller of the channel conductivity [23]. Unlike a conventional field-effect transistor (FET), in which the gate electrode coupled to the source and drain electrodes via an insulator, in the EGFET, the gate electrode is distant and coupled to the channel through the electrolyte [24]. The channel, which serves as a key sensitive element, can be made from both inorganic (silicon nanowires (SiNWs), carbon nanotubes (CNTs)), and organic semiconductors (polymers: P3HT, pBTTT, α -sexithiophene, and pentacene, etc.) [25]. The transistors based on organic semiconductors are called electrolyte-gated organic field-effect transistors (EGOFET), they are much preferred for electronic devices in terms of flexibility and printability [24]. From the standpoint of a general mechanism, EGFET and EGOFET are sensitive to changes in threshold voltage (V_{th}), drain current and carrier density in the conductive channel upon the antibody-antigen binding events. Considering low voltage operation (i.e. <0.4 V), EGOFET is a good candidate for detecting analytes in various body fluids (saliva, blood, serum, mucus, sweat, etc. in-vivo and in-vitro) without noticeable interference [26]. To meet the requirements of favorable immunosensing, the electronic transducer should possess: i) continuous and ordered molecular packing in the conductive channel to ensure high carriers mobility and ii) a diminished molecular barrier between the channel and the target biomolecules in medium of interest [27].

1.3. Piezoelectric and acoustic immunosensors

Piezoelectricity (piezoelectric effect) is the unique ability of certain solid materials to generate electricity when mechanically squeezed, leading to the linear electromechanical interaction of mechanical and electrical states inside crystals without a center of symmetry. Materials that can generate an electrical output signal when mechanically compressed are called piezoelectrics. Two types of piezoelectric effects are currently described; the first, the so-called direct piezoelectric effect, occurs when a mechanically compressed material produces an electrical output that is directly proportional to the magnitude of strain. The second type is the inverse piezoelectric effect that can occur when the piezoelectric material is subjected to

stress caused by the electric field [28]. Piezoelectrics can be naturally occurring crystals (berlinite, quartz, cane sugar, rochelle, topaz, tourmaline) and natural non-crystalline materials such as tendon, silk, dentin, etc. In addition, several synthetic piezoelectrics have been proposed, including crystalline gallium orthophosphate and langasite, ceramics such as barium titanate and potassium niobate, and polymers (polyvinylidene fluoride, polyvinyl chloride, etc.) [28].

In immunosensing, both types of piezoelectric effects have been utilized, and each of them has shown stable, reproducible, and accurate results of detection. The inverse piezoelectric immunosensor typically made up of quartz crystal microbalance (QCM) configuration equipped by quartz transducer with pre-immobilized bioreceptors and two electrodes attached to its surface. When an electric field is created between two electrodes, it generates an acoustic shear wave that penetrates the crystal perpendicular to its surface, and thus, a certain resonant frequency is established within the crystal due to the propagation of the acoustic wave. The resonance frequency is determined by the interelectrode gap, the thickness of quartz and an acoustic wave velocity in quartz crystal. From the viewpoint of immunosensing, the formation of an immunocomplex over the pre-immobilized crystal will cause an increase in the total mass, and, therefore, the resonant frequency will decrease. In turn, the total concentration of target biomolecules can be correlated with the change in the resonance frequency of the crystal and calculated using the frequency difference before and after the formation of immunocomplexes [29].

The direct piezoelectric effect, as above-mentioned, occurs when the piezoelectric material undergoes mechanical stress, thereby generating output electricity. Mechanical stress can be addressed directly to the transducer by means of conventional compression, however, for more accurate detection, it is essential to avoid direct mechanical squeeze of the transducer. To meet this requirement, the surface acoustic wave-based (SAW) piezoelectrics are usually employed. The immunosensing based on the direct piezoelectric effect, generally utilizes thin wave-guide layers (micron or sub-micron) made of silicon dioxide, zinc oxide, polymers, etc. [30]. A typical SAW-based immunosensor consists of metal contact electrodes attached to a wave-guide coated with a piezoelectric transducer to produce mechanical acoustic wave [31]. When the SAW-based immunosensor in run, a specific acoustic resonance is established inside the piezoelectric, and the specific

acoustic energy is concentrated in the immediate vicinity of the piezoelectric surface, which makes it very sensitive to surface adsorption [29]. While the formation of immunocomplexes on the surface will increase the total mass, the acoustic wave that travels along that surface will experience a frequency change on its way. The obtained difference in initial and final frequency will be proportional to the change in target analyte concentration.

1.4. Thermometric immunosensors

From the point of view of immunosensing, thermometric detection is unattractive due to poor release/absorption of heat during the formation of the immunocomplex and as consequence, the weak influence of this reaction on the heat-sensitive transducer. Most thermometric immunosensors/biosensors exploit thermistors - resistors whose resistivity is dependent on the ambient temperature. Thus, it is crucial to have bioreceptors and targets whose interaction induces temperature evolution proportional to the molar enthalpy change [32]. Since the specific antibody-antigen interaction is not accompanied by a sufficient change in temperature, the thermometric enzyme-linked immunosorbent assay (TELISA) is commonly utilized for temperature-based detection [29]. In TELISA, antibodies/antigens are usually conjugated to enzymes that can produce heat as a result of a catalytic reaction [33]. The amount of the formed enzyme-conjugated immunocomplexes in thermometric immunosensing is proportional to the enthalpy change (recorded as peak height) and is related to the analyte content in the medium of interest [34]. Thermometric immunosensing based on TELISA can be carried out in an enzymatically immobilized column placed in a microcalorimeter acting as a flow-injection analyzer (FIA) [32].

1.5. Optical immunosensors

Optical immunosensing is one of the most attractive detection technique due to its simplicity, availability, and versatility. Depending on the need of experiment, optical immunosensors can be based on surface plasmon resonance (SPR), surface enhance Raman scattering (SERS), reflectance, transmittance/absorbance, fluorescence, photoluminescence, chemiluminescence, interference, light polarization or rotation, etc. [20]. Moreover, optical immunosensing can be performed in two formats: direct and indirect optical detection. Direct optical detection (label-free) means the signal will be collected directly from the transducer, especially for the

detection based on SPR, reflectance, interference, transmittance/absorbance, or photoluminescence. While the indirect one implies the signal that collected from the analyte with optical labels (immunosensors based on fluorescence, SERS, photoluminescence quantum dots [35]. It can be noted, that the main principle behind each optical detection method is the change of light parameters when the antibody-antigen complexes are formed over the optical transducer.

Optical immunosensors take advantage of the above-described immunosensors as they typically provide rapid, low-cost and real-time detection of target analytes in medium of interest. Furthermore, they can be easily miniaturized facilitating development of lab-on-chip devices. The novel strategy is also to integrate optical transducers into microfluidic systems to minimize the amount of biological material required for testing [36].

1.5.1. SPR-based immunosensors

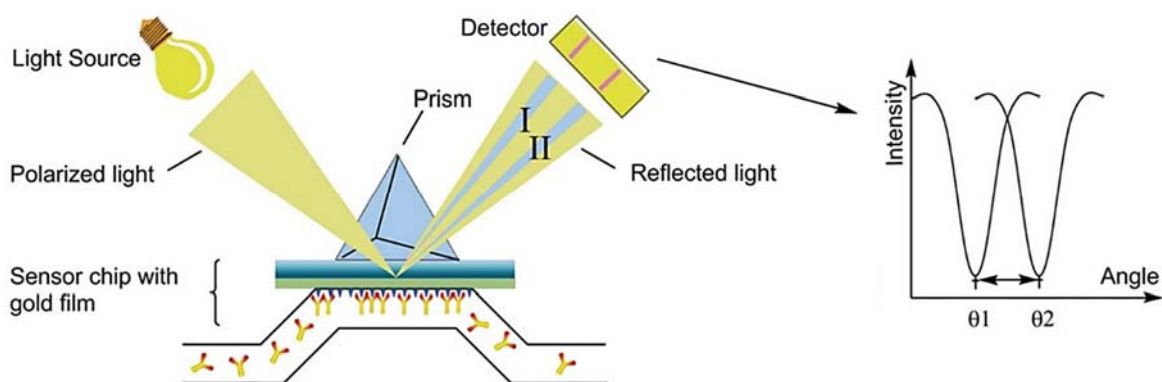


Figure 1.4. Scheme of biosensor based on SPR. The SPR angle shifts from θ_1 to θ_2 when analytes bind to bioreceptors. Reprinted and adapted from Ref. [37].

SPR is the phenomenon in which the surface-confined electrons interact with incident light resulting in *polaritons* (coupled collective oscillations of surface plasmons and the incident electromagnetic field) [38]. SPR generally occurs in metals and highly-ligand semiconductors with quasi-free electrons in the conductive band. Since the intensity of the electromagnetic field in metal/semiconductor and a dielectric medium decrease exponentially toward the surface normal, this indicates longitudinal propagation of the field and charge distribution along the metal/semiconductor surface. Consequently, surface plasmons propagate along the interface, and their electromagnetic field, localized in

the interface plane, is very sensitive to various changes in metals or semiconductors (e.g. roughness) and dielectrics (refractive index).

SPR cannot be excited by simple plane electromagnetic wave incidence because the dispersion of plasmons is lower than the dispersion of photons in the entire energy range. Moreover, the momentum of surface plasmons is always higher at the same frequency as the plane wave incidence, regardless of incidence angle. To overcome this problem, some extra momentum (sufficient to excite the SPR) can be provided by light passing through a medium with a high refractive index (prism, etc.). There are two approaches to excite SPR in thin metal films by means of a prism. The first one (so-called Otto-configuration) implies the prism location from the side of dielectric (air, liquid) [39]. While in the second approach (Kretschmann configuration), the prism is placed beneath the metal film thin enough to be penetrated by light [40]. The Kretschmann configuration is much more preferable for immunosensing due to the lack of direct contact between prism and analyte. As known, the surface plasmons propagating along a flat metal-dielectric interface can be scattered and reflected by biomolecules (e.g. antibodies, antigens). Therefore, the formation of immunocomplexes on the metal surface (usually gold or silver) will also scatter surface plasmons, and consequently, the spectral position of the SPR will be shifted (Fig. 1.4) [40]. This detection technique can provide information about the kinetic of analyte adsorption as well as the correlation between the SPR angular shift and analyte concentration.

1.5.2. LSPR-based immunosensors

When it comes to surface plasmons, it is necessary to distinguish between two types of their resonance with the incident light. The above-mentioned SPR is the first type, in which excited plasmons propagate along the metal/dielectric interface, while the second type – LSPR (localized surface plasmon resonance) occurs in nanoparticles where propagation of plasmons is impossible due to the strong confinement. Thus, when nanoparticles (usually a colloidal solution of nanoparticles) are illuminated by incident light, LSPR arises from collective and coherent oscillations of localized electrons and an electromagnetic wave (light). This collective oscillation, in term of optics, promotes enhanced absorption and scattering of light within the ultraviolet-visible (UV-VIS) region [41].

In general, the LSPR occurs in nanoparticles of noble metals (e.g. silver, gold, platinum) whose chemical stability and biocompatibility are also attractive for biosensing with reliable results. Although silver nanoparticles have a much sharper and more intense LSPR peak, gold nanoparticles are much preferred in biosensors because of their higher chemical stability in aqueous solutions. The red color of the gold colloidal solution is the typical manifestation of LSPR, which is intensively exploiting for the aggregation-based immunosensors [42]. The mechanism behind this type of immunosensing is the drastic change in the color of nanoparticles when they aggregate into bigger clusters. In the case of gold nanoparticles, a decrease in the distance between two nanoparticles will result in an LSPR redshift due to the near-field electromagnetic coupling. Therefore, if antigen-conjugated nanoparticles and antibody-conjugated nanoparticles are mixed, the specific antigen-antibody will promote aggregation of the nanoparticles, which will lead to a resonance shift and color change [43,44].

On the other hand, LSPR is strongly dependent on the shape, size, composition of nanoparticles, as well as the refractive index of the medium surrounding them. Therefore, it is reasonable to exploit this property in immunosensing based on local refractive index change upon binding of antigens to the antibody-conjugated nanoparticles. The change in the local refractive index, in turn, will cause a redshift of the LSPR, which will be directly proportional to the number of immunocomplexes formed over the nanoparticles [43].

1.5.3. SERS-based immunosensors

Raman spectroscopy provides important information about the “fingerprint” vibrational modes of a material, which are determined by its molecular structure and localization. To date, the number of applications exploiting the spontaneous Raman effect is restricted due to the weak measurable signal caused by small vibrational Raman scattering cross-sections ($10^{-30} \text{ cm}^2 \text{ sr}^{-1}$). The detection limits corresponding to those cross-sectional orders cannot be lower than millimolar, which excludes the detection of single molecules [45]. Therefore, the straightforward utilization of Raman spectroscopy for biosensing is quite questionable and. To overcome this limitation, the SERS was found as a powerful technique being able to recognize even single target molecules. As it comes from its name, the technique based on the enhancement of inelastic light scattering from the micro-objects located in the immediate vicinity of the nanostructured surface [46].

The exact mechanism of SERS is currently unknown, but there are two hypotheses describing its possible origin. The first one is the long-distance electromagnetic enhancement (EM), and the second – the short-distance chemical enhancement (CE) [47]. The EM implies the excitation of the surface plasmons [48], while CE proposes the formation of charge-transfer complexes that able to transfer electrons from/to the metal during the formation of metal-molecule bonds [49]. It is important to emphasize that these hypotheses are not mutually exclusive, and even vice versa, it was agreed that each of them contributes to the overall enhancement factor (EF) [50].

There are ways to enhance Raman scattering using a single nanoparticle of noble metals (Au, Ag, Pt, etc.), but more complex structures are preferable because they can provide large enhancement around $EF \approx 10^5$ - 10^{14} , for example, when the analyte molecule is placed at the gap (so-called hotspot) between two nanoparticles [50]. This gap has to be small enough (below 1 nm) to alter their properties, which, in turn, can change the photophysical and/or photochemical properties of the adsorbed molecule, and affect the SERS intensity [51]. Moreover, the deposition of noble metal nanoparticles on the spatio-temporal geometries and materials with the variation of refractive index can bring an additional 20-folder enhancement of SERS in comparison with the nanoparticle deposited on flat substrates [52].

When it comes to SERS-based immunosensors, they have been found attractive due to the above-mentioned high EF, ability to detect multiple targets [53], and high signal stability that facilitate repetitive detection with diminished errors. The typical SERS-based immunosensing requires the inclusion of two important details in the contracture: the antigen/antibody complexes and the SERS substrate. Bioreceptors can be directly attached to the SERS substrate to capture affinitive targets. Thus, SERS substrate bears two simultaneous functions: the site of the antibody-antigen binding event and provision of the SERS signal to be measured for quantitative analysis of the analyte content. Depending on the different types of immunoassays, SERS-based immunosensors can be competitive or noncompetitive, and labeled or label-free, which satisfies many applications [54]. Moreover, SERS-based detection can be performed using different types of the substrates: Au, Ag, and Pt (nanoparticles, nanospheres nanorods nanowires, nanostars), nonmetallic substrate (glass slides, quartz slides, multiwall plates, etc.), nonmagnetic substrate (silica spheres, polystyrene spheres, metal nanoparticles, and photonic crystal

beads), magnetic substrate (Fe_3O_4 and Fe_2O_3 nanospheres, etc.) [55]. SERS also looks attractive for incorporation into microfluidic (lab-on-chip) devices, such as microfluidic channels for real-time detection [56], for microfluidic droplet technique [57], for optical fibers immunoassays [58], for paper-based platforms [59], etc.

1.5.4. Immunosensors based on reflectance and interference

Reflection is the ability of a material to reflect incident light on its surface or in volume (for light-scattering materials). Since reflectance is highly dependent on surface roughness, and even local disturbances can significantly affect reflectance, it has proven to be an attractive tool for detecting antigen-antibody binding events. The simplest reflectometric immunosensors usually employ flat-surface transducers with pre-immobilized bioreceptors that are capable of recognizing affinitive targets. When the polarized light is reflected from the transducer surface, the minimum in reflectance intensity will be observed at the so-called pseudo-Brewster angle (θ_B) [60]. Thus, if one fix the angle of incidence at the pseudo-Brewster angle, the reflection intensity will increase due to the adsorption of antigens and antibodies or due to the formation of immunocomplexes on the transducer surface. This approach can provide kinetic aspects of molecular adsorption and interaction in real-time mode. Furthermore, the analyte concentration can be determined by analyzing the initial and final intensities of reflectance.

On the other hand, reflectance plays an important role in reflectometric interference spectroscopy (RIfS), in which an incident light beam interferes with beams reflected from the top and bottom surfaces of a thin film or porous (rough) layer [61]. Such porous layers can be created on the basis of well-known semiconductor substrates (Si, Al_2O_3 , etc.) by chemical or electrochemical etching. Practically, interference pattern appears from Fabry-Perot interference of light reflected from the gas/liquid-porous layer and porous layer-substrate interfaces. The wavelength of interference peak maximum can be described by Fabry-Perot equation:

$$m\lambda = 2nL, \quad (1.1)$$

where λ is the wavelength of interference maximum for spectral fringe of order m , n - refractive index of the porous layer, and L is the geometric thickness of the porous layer. The adhesion of antigens and antibodies to the porous layer causes a change

in the refractive index (n), and, therefore, the interference pattern undergoes a change. In this case, the thickness of the porous structure rather remains unchanged since biological species diffuse into the pores, in contrast to the RI_fS method based on a thin film, where the geometric change in the film thickness is essential [62]. However, the basic RI_fS method possesses zero-point drift that results from changes in temperature, matrix composition, or nonspecific binding to the transducer. Therefore, it is rational to use a double-beam interferometer (e.g. Mach–Zender-type) in which one optical beam serves as a reference. This approach provides important information about the zero-point drift by recording signals from two spatially different areas of the transducer [63].

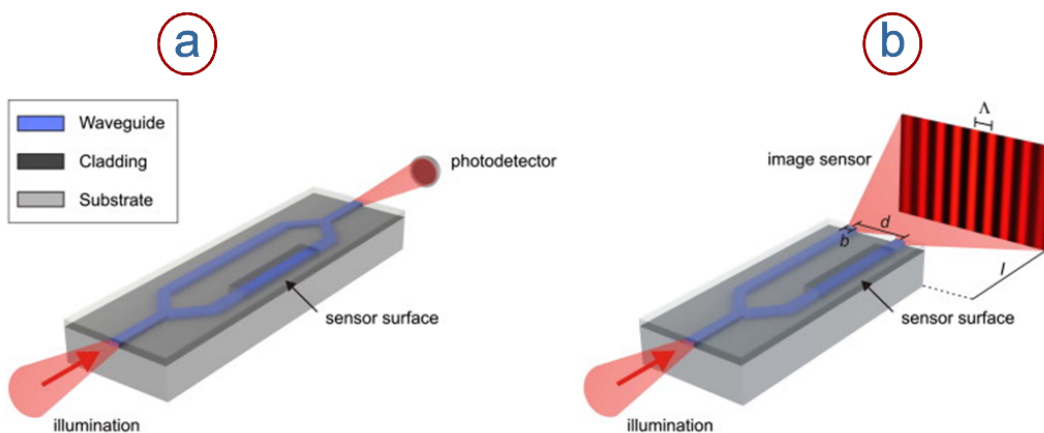


Figure 1.5. Typical (a) Mach–Zender and (b) Young interferometer configurations. Reprinted from Ref. [37].

When it comes to the classic Mach–Zender interferometer (MZI), it is based on the waveguiding method in which the change in the refractive index of the immunosensor arm against the reference arm is monitored. Typical MZI configuration (Fig. 1.5a) includes a monochromatic light source (laser) connected to the single-mode waveguide with its following splitting into two arms: immunosensor and reference. If any changes occur in the immunosensor arm (e.g. antigen-antibody binding), this leads to the beam phase-shift, while the beam passing through the reference arm remains unchanged. The interference arises when these arms merge and beams passed through the immunosensor and reference arms can now interfere. Finally, the relationship between the initial and final interferences can provide information about analyte concentration or mass density adhered to the immunosensor [64]. The sensitivity of MZI-based

immunosensor can be tuned by the change of sensing window length, however, the detection of small analyte concentrations is still a challenge [65].

Another option to construct the interference-based immunosensor is to utilize a Young interferometer (YI). A typical YI-based immunosensor (Fig. 1.5b) consists of a monochromatic light source whose beam is directed into a waveguide, followed by splitting into two arms, as it is for MZI-based immunosensor. In contrast to MZI, the immunosensor and reference arms are not finally recombined to get the interference, in this case interference pattern appears due to the beams interaction in free-space (far-field). The change in the interference patterns can then be analyzed by means of a CCD camera and correlated to the analyte concentration [66]. Hartman and Michelson interferometric immunosensors are also regarded as good candidates for cost-effective and label-free analyte detection [67,68].

1.5.5. Immunosensors based on chemiluminescence and electrochemiluminescence

Chemiluminescence (CL) is the unique property of certain materials (luminophores) to emit light when interacting with compounds that could facilitate their oxidation. Typically, luminophore undergoes oxidation when interacting with hydrogen peroxidase or enzymes, thus becoming a product in an excited state, while its relaxation to a lower energy state is accompanied by the emission of light [69]. CL immunosensors represent classic labeled approach for analyte detection, using different types of immunoassays and substrates. CL substrates such as luminol, isoluminol, or enzymes (e.g. horseradish peroxidase (HPR) and alkaline phosphatase) are used to label antibodies or antigens to generate a measurable optical response that correlates to the analyte concentration [70]. Furthermore, some CL substrates (e.g. acridinium ester and acridinium sulfonamide ester) can be directly attached to antigens or antibodies, while indirect (via metal nanoparticles) labeling provides even a 100% improvement in the CL signal [71]. Such a CL improvement appears due to the fact that metal nanoparticles (e.g. Au⁺³) act as efficient catalysts for luminophore oxidation [72]. On the other hand, some semiconductor nanoparticles, such as Si nanospheres, can replace metal nanoparticles in CL performances, ensuring a significant signal enhancement due to the increased number of attached CL substrates that correspond to one antigen-antibody complex in a 10:1 ratio. This suggests that one event of immunocomplex

formation will be accompanied by the simultaneous oxidation of 10 CL substrates attached to the Si nanosphere, and therefore the response of immunosensor proportionally amplifies [73]. Another way to amplify the CL signal is to use HPR-encapsulated liposomes that are lysed when treated with a surfactant [74]. Lysis releases HPR from within the liposomes into a buffered solution where ones react with H_2O_2 to produce light during the oxidation process. The optimal concentration of HPR within the liposomes is the key factor for the low detection limit and sensitivity enhancement in CL detection. The CL signal of the immunosensor can be recorded with a fluorescence spectrophotometer in real-time mode, which gives important information about the kinetic aspects of antigen-antibody interaction.

In parallel with the conventional CL-based immunosensor, the electrochemiluminescent (ECL) immunosensor has gained immense popularity in the scientific community due to the reduced signal-to-noise ratio caused by the strong amplifying effect of luminophore light emission [75]. The general mechanism of the ECL immunosensor is very similar to that of CL; however, the major difference lies in the fact that the co-reactant of the ECL process must be oxidized at the electrode prior the interaction with the CL substrate/label. Thus, when the co-reactant gets oxidized on the electrode it usually migrates within the working volume (e.g. chamber) of the immunosensor to reach labeled analyte. As in the case of the CL immunosensor, the interaction between the CL substrate and the oxidized co-reactant transforms the former into an excited state, while its relaxation to the ground state gives light emission in the visible range [76]. As for the CL-based detection, the ELC approach provides important information about the kinetic processes of antibody-antigen binding events.

1.5.6. Fluorescence-based immunosensors

Many molecules do not require auxiliary chemical reactions (as it for the CL- or ECL-detection) in order to get excited to emit light. Part of these molecules can be turned to the excited state by absorbing the incident light, while their relaxation to the ground state occurs with the emission of the light. If this radiative (light-emitting) process lasts between 10^{-9} - 10^{-6} seconds, then it calls fluorescence (FL) [77]. Since the FL was found easily to launch in certain molecules or nanoparticles, it has gained significant popularity within the scientific community, especially in biomedicine, biosensing or immunosensing, biochemistry, etc. In immunosensing, FL tags are

used to label antigens or antibodies in order to perform qualitative and quantitative detection. Typically, fluorescent labeling is carried out by simply binding fluorescent dyes to surface functional groups of biomolecules so that they can be visualized using fluorescence imaging or spectroscopy [78]. Nowadays, the FL is considered to be the most sensitive detection method, and to date, the detection limit achieved by FL-based devices has reached the picomolar (pM) order for the antigens screening [79]. Moreover, different types of assays have been also adjusted for FL-based immunosensing, among others: competitive assay [80], sandwich assay [81], indirect assay [82].

The second possibility to design the FL-based immunosensor is to use Förster resonance energy transfer (FRET) between two light-sensitive molecules at the Försters distance (from 1 to 10 nm) [83]. The immunosensors based on the FRET phenomenon permit the determination of the approach between antigens and antibodies at distances (several nanometers) sufficient for the occurrence of molecular interactions. The classic mechanism behind this type of immunosensing involves a donor FL-tag in an excited electronic state, which capable of transferring its excitation energy to the closely located acceptor FL-tag. This energy transfer occurs in non-radiative mode via long-range dipole-dipole interaction, thus acceptor FL-tag gets excited [84]. The acceptor FL-tag must have an excitation band that spectrally overlaps with the emission spectrum of the donor FL-tag, but must not overlap with the donor's excitation band [85]. Thus, if the donor-labeled antibody and the antigen labeled with the acceptor are in close proximity, the donor absorbs the excitation light (λ_0), nonradiatively transfers energy to the acceptor, which gets excited and emits a photon (λ_2). The emitted fluorescent photon, in turn, confirms the binding interaction between antigen-antibody and the correct operation of the immunosensor. When labeled antigens and antibodies are separated by distances greater than the Försters distance for the defined FL-tags, then the donor-tag will absorb incident light (λ_0) and emit a fluorescent photon (λ_1), while the emission (λ_2) from the acceptor tag will be absent or negligible, which indicates weak or no binding affinity between antigens and antibodies [86]. For the FRET-based detection, a confocal microscope is commonly used as a fluorescence signal analyzer and for fluorescence imaging technique [87].

1.5.7. Immunosensors based on photoluminescent substrates

Immunosensors based on photoluminescent substrates have a completely different mechanism of action and, in contrast to CL, ECL, and FL immunosensors, they exclude the use of any labels which indicate the presence/absence of the analyte. In this case, bioreceptors are supposed to be attached to the surface of the PL transducer for the following selective interaction with the analyte molecules, as it is for SPR-, interference-based transducers. The detection technique is entirely based on the phenomena that occur on the surface or in the bulk of the photoluminescent transducer during the binding of bioreceptors and analytes. The possible mechanisms that can contribute to the change in photoluminescence during the antigen-antibody interaction are mainly based on the passivation of the transducer's surface states, the charge transfer rate, and the electrostatic interaction of bio-objects and the solid transducer [88].

For PL-based immunosensors that are performed without a surface functionalization procedure (direct deposition of bioreceptors on an untreated surface), the most possible interaction mechanisms between the sensor surface and bioreceptors (antibodies or antigens of interest) can be explained by electrostatic and van der Waals forces [89]. These types of interactions occur due to the presence of differently charged protein (in this particular case, antibodies or antigens) domains (δ^+ and δ^-), which can be attracted by the oppositely charged surface of the transducer [89]. During detection, when the analyte molecules approach the transducer with bioreceptors, a selective interaction occurs between the analyte and bioreceptors, which affects the PL intensity and the peak location. The difference in the PL intensity, as well as the shift in the PL peak position before and after the formation of immunocomplexes, can be used (as a response) for the qualitative or quantitative detection of analytes [89]. Thus, for an immunosensor with the directly immobilized bioreceptors, the mechanism based on the electrostatic interaction “transducer-bioreceptor-analyte” is more plausible.

On the other hand, the change in PL signal (both, intensity or peak position) may be induced by the charge transfer between the transducer and redox bioreceptors/analytes, or between the transducer and non-redox bioreceptors/analytes with conjugated redox enzymes (e.g. HPR) [90]. In immunosensing, most receptors and analytes are not redox and therefore require conjugation with redox enzymes in order to launch direct charge transfer to induce

the change (intensity or peak position) in PL. For example, analytes conjugated with redox enzymes can supply extra electrons that affect the rate of exciton-phonon interaction and near band edge excitonic transitions, which contribute to the UV emission of the semiconductive transducers [90]. In this case, a decrease in PL may also occur as a result of the transducer reaction with quenchers (analyte (bio)molecules), which may introduce non-radiative surface defects [88].

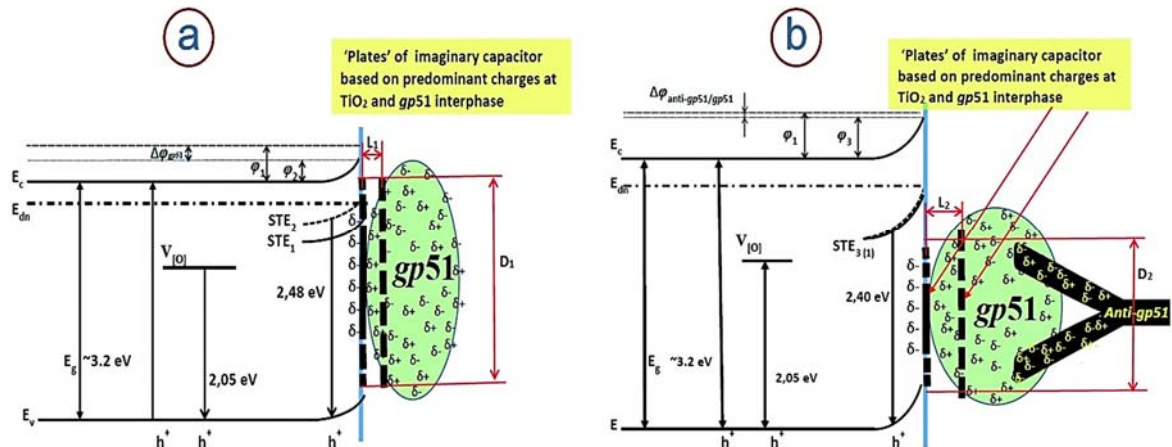


Figure 1.6. Energetic levels and the model based on 'imaginary flat capacitor': L_1 and L_2 are the distances between 'plates' area of imaginary capacitor, D_1 and D_2 – plate sizes of imaginary capacitor; φ_1 and φ_2 – potential barrier value for surface of the transducer (TiO_2 in this case) interphase with air (air// TiO_2 /glass). $\Delta\varphi_{gp51}$ and $\Delta\varphi_{gp51}$ represents deviations of potential barriers before and after analyte attachment. Reprinted and adopted from Ref. [91].

Another hypothesis describing the PL-based immunosensor mechanism is based on the 'imaginary flat capacitor' model, which can explain the change in the PL signal when the transducer interacts with non-redox biomolecules. [91]. In this case, the 'imaginary capacitor' consists of a negatively charged plate on the semiconductor surface and an 'imaginary positively charged plate' formed inside a bioreceptor molecule (e.g. antigen *gp51*) in close proximity to the semiconductor (e.g. TiO_2) interface. Figure. 1.6a is a schematic view of an 'imaginary flat capacitor' after antigen immobilization for selective binding to affinity antibodies. The adsorption of antigens is possible due to the electrostatic interaction between the partially uncompensated antigen charges and the negatively charged surface of the semiconductor, especially at extremely small (Debye screening length) distances between them. This type of electrostatic interaction affects the band gap parameters (e.g. potential barrier φ) of the semiconductor, and as a consequence, the rates of radiative and non-radiative recombinations will be changed. Moreover, a stronger interaction between the bioreceptor and the semiconductor will lead to a higher

deformation of the bioreceptor from its spherical shape to an ellipsoidal one, thereby increasing the size of the capacitor plates and strongly changing the band gap parameters (Fig. 1.6a) [91].

The opposite situation occurs during the formation of the immunocomplexes on the surface of the transducer. The interaction of affinitive antigens and antibodies leads to the backward deformation of the antigens due to the redistribution and partial compensation of charges. Antigens become more spherical and the size of the 'imaginary capacitor plate' decreases, as shown in Figure 1.6b. This reduction in the size of the plate leads to a decrease in the capacity of this imaginary capacitor, and therefore, the electrostatic interaction between the transducer and antigens becomes reduced. In this case, reverse changes occur in the band gap of semiconductors, and the rates of radiative and non-radiative recombination also changes. It should be noted that the capacitance of an imaginary capacitor has a direct effect on the PL intensity or peak position, and a larger amount of charges in the immediate vicinity of its surface (Debye screening length) causes a stronger PL change, making this effect suitable for immunosensors performance.

1.6. Enzymatic electrochemical sensors

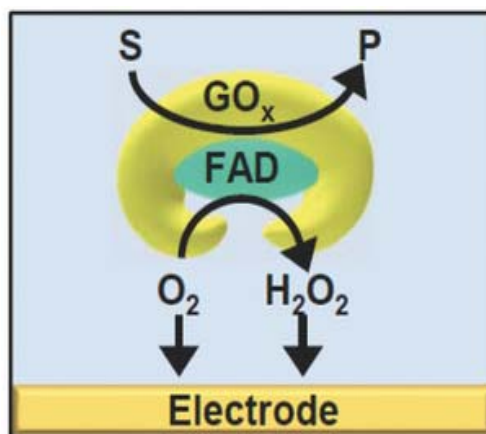


Figure 1.7. Schematic illustration of the mechanism underlies electrochemical enzymatic glucose sensor (*S* and *P* mean substrate and product respectively, *FAD* (flavin adenine dinucleotide) is a redox-active coenzyme). Reprinted and adopted from Ref. [92].

Enzymatic electrochemical sensors are a wide class of sensors that able to detect events of enzyme-substrate interaction (interaction between immobilized enzyme and analyte of interest) on its surface. These interactions usually occur with the generation of sub-products or with the consumption of the surrounding species and

may influence both anodic and cathodic currents. For example, the specific interaction of glucose oxidase (GOx) with glucose results in the formation of hydrogen peroxide (H_2O_2), while the oxidation of H_2O_2 at the electrode can change the anode current which serves as the sensor's response. On the other side, this interaction utilizes surrounding free oxygen, as it required for H_2O_2 to be produced [1]. Taking into account that the cathode current of the electrode is mainly determined by the oxygen reduction reaction (ORR), it can be concluded that the more oxygen enzymatic reactions consume, the less oxygen will be reduced at the working electrode [93]. Thereby, this principle can also underlie enzymatic electrochemical glucose sensors (Fig. 1.7).

The above-described principles and mechanisms are fundamental in first-generation glucose sensors that allow determining the amount of glucose consumed. The main advantage of such sensors is that they do not require additional mediators (electron shuttles) that transfer electrons from GOx to the electrode. In first generation glucose sensors, a high positive potential (above 1 V) should not be applied as it can promote side reactions including oxidation of ascorbic acid, urea, uric acid, and lactic acid, which degrades analyte selectivity [92].

2. Fundamental aspects of porous silicon, fabrication methods, photoluminescence, and label-free (bio)sensing performance

2.1. Fundamental aspects of porous silicon

It is difficult to imagine current progress in science and technology without silicone as it plays not just an important role, but a key role in the construction of a huge number of electronic and optoelectronic devices. Silicon is the most widely used semiconductor in the solar cell industry, and today about 90% of solar cell modules are made of silicon, ensuring high efficiency, low cost, and long lifetime [94]. Moreover, in accordance with modern trends in science and technology which tend to minimize the dimension and the weight of the devices and tools, there have been many successful approaches to creating nanoscale silicon for use in portable electronics and optoelectronics. The very first form of nanoscale silicon produced was PSi, but it did not represent any value to scientists for several decades after it was discovered, even though it possessed several unique properties, such as controllable pore diameter and density, the thickness of the porous layer, complex refractive index, bioactivity, non-toxicity, superhydrophobic. Depending on the pore diameter (d), PSi can be classified as microporous ($d < 2$ nm), mesoporous (2 nm $< d < 50$ nm), and macroporous ($d > 50$ nm).

The history of PSi began with its accidental discovery by Arthur Uhlir Jr. and Ingeborg Uhlir in the process of polishing and shaping the silicon surface in 1956 [95]. However, it only became popular in the 90s of the 20th century when Leigh Canham reported visible light emission due to quantum size effects in PSi [96]. Since then, the number of reports on the fabrication and application of PSi has grown rapidly, and even today the number of publications on PSi is on an upward trend. A tremendous number of works have been devoted to the fabrication of PSi using various chemical, electrochemical approaches, combined with the different lithography techniques to create a pattern on the silicon surface. Electrochemical anodization and stain-etching are two well-known and common methods for PSi fabrication, however there are also another ways for introducing pores in silicon wafers [97]. The electrochemical anodization of silicon wafer for the porous layer formation can be carried out in the anodization cell made of HF-resistant Teflon equipped with a counter electrode and a power supply. Hydrofluoric acid (HF) is the

most common electrolyte for the anodization process of the highly doped ($p^{+,++}$, $n^{+,++}$) silicon wafers, while for the lightly doped wafers, additional assistance of the light is required for the anodization process to be launched. The electron-holes are generated in the illuminated area, and due to the applied potential, the hole merges into the silicon valence band, promoting the silicone dissolution process. Using this method, three different types of morphology can be obtained: microporous, mesoporous, and macroporous silicon [97].

Stain etching or so-called spontaneous electroless etching is another popular method for the PSi fabrication, which utilizes “porous-silicon forming” oxidants such as NO_3^- , VO_2^+ , Fe^{3+} , etc. [98]. In this case, the etching process occurs without the deposition of metal films or nanoparticles on silicon surface, and the holes are injected directly from the oxidant solution. It is also important to distinguish between stain etching and conventional chemical etching as there are different mechanisms behind them. The mechanism of the stain etching is based on the free charge transfer, while the chemical etching is initiated by the action of hydroxyl groups and used to produce flat, hydrogen-terminated Si surfaces [99]. Moreover, it can be found that stain etching sometimes may be called metal-assisted etching because it utilizes metal ions of the oxidant for the etching process, but this nomenclature can be confused with a catalytic etching process in which the etching process is preceded by the metal nanoparticles deposition on the Si surface [97]. The latter catalytic etching is commonly referred to as metal-assisted chemical etching (MACE).

2.2. Metal-assisted chemical etching

Metal-assisted chemical etching is a promising method for the production of PSi samples with the required parameters, such as pore depth and diameter. Due to its simplicity and low cost, MACE can be an alternative to other expensive methods (e.g. deep reactive ion etching) for PSi fabrication with an even better surface to volume ratio of the porous layer [100]. The method involves metal nanoparticles to catalyze the local oxidation of silicon substrate that facilitates enhanced etching process in presence of oxidizing agents (e.g. H_2O_2) [101]. The general etching process takes place on Si beneath the metal nanoparticles that move to the bulk of Si substrate during the etching process, forming pores. There are two options for MACE implementation, the first one is the so-called 1-step MACE involves two

simultaneous processes: the metal nanoparticle deposition and the etching of the Si substrate. In this case, metal ions are dissolved in HF, and when the redox potentials of ions are more positive than the valence band of Si, the galvanic reaction will turn them into metal nanoparticles, which oxidize Si and enhance the etching process [101]. Despite its simplicity, the 1-step MACE method has several drawbacks including the limited control over the pore parameters and homogeneity of the porous layer.

To overcome the limitations that arise during the 1-step MACE process, the deposition of metal nanoparticles on the Si surface can be performed prior to etching using metallization aqueous solutions (e.g. AgNO_3 aqueous solutions for Ag nanoparticles formation) [102]. The homogeneity of the metal nanoparticles on the Si surface can be tuned by the deposition time, while the depth of the pores is controlled by the etching time of Si in HF. This method is based on two separated processes, and therefore it was denoted as the 2-step MACE process (Fig. 2.1.)

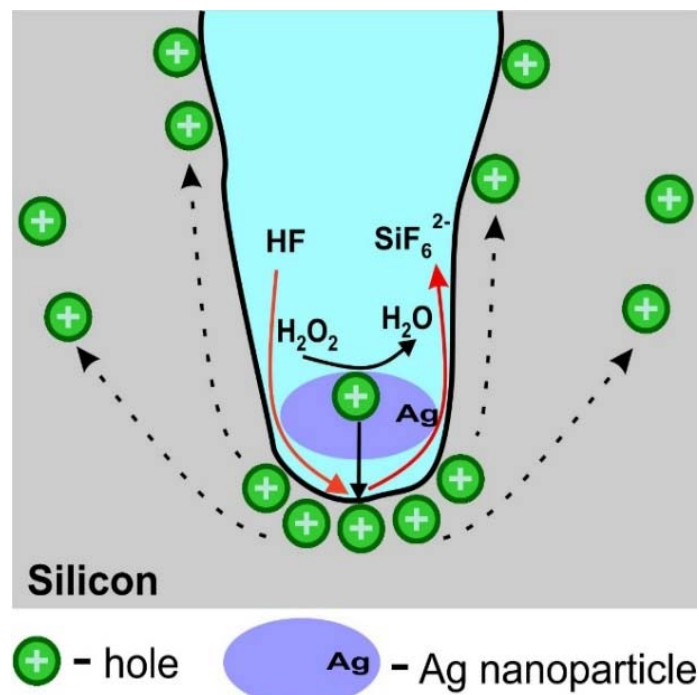
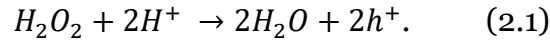


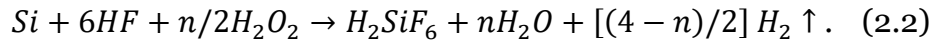
Figure 2.1. Sketch of the MACE process, where H_2O_2 is reduced to H_2O at the noble metal particles and the holes are injected into Si that leads to the dissolution of Si as SiF_6^{2-} species.

Analogically to the electrochemical formation of the porous layer in Si, where two electrodes (anode (Si) and cathode made of metal) are required. In MACE, Si substrate plays the role of the anode, while the deposited metal nanoparticles represent local cathodes. During the redox reaction of metal nanoparticles and an

oxidizing agent (e.g. H_2O_2), the H_2O_2 become reduced, forming electrical holes, and the reaction at the cathode is as follows [104]:



Once generated, holes are injected into the valence band of Si beneath the nanoparticles, inducing dissolution of Si and its transformation into SiF_6^{2-} . It was also found, that depending on the concentration of H_2O_2 , etching occurs according to the 2-hole or 4-hole process, leading to the direct dissolution of Si in a divalent or tetravalent state, respectively [104]. Considering that both processes are highly probable, the overall etching reaction, which includes the divalent and tetravalent dissolution of Si, can be as follows [103]:



The morphology of the PSi layer depends on a large number of different parameters, including the initial parameters of the metal nanoparticles (e.g. the type of metal used and its electrochemical properties), the initial parameters of the Si substrate (e.g. crystallographic orientation, type of conductivity, resistance), and also depends on the etching conditions, such as etching time and temperature, etchant concentration and composition. In this dissertation all PSi and PSi/Au samples were fabricated according to the MACE method.

2.3. Photoluminescence of PSi

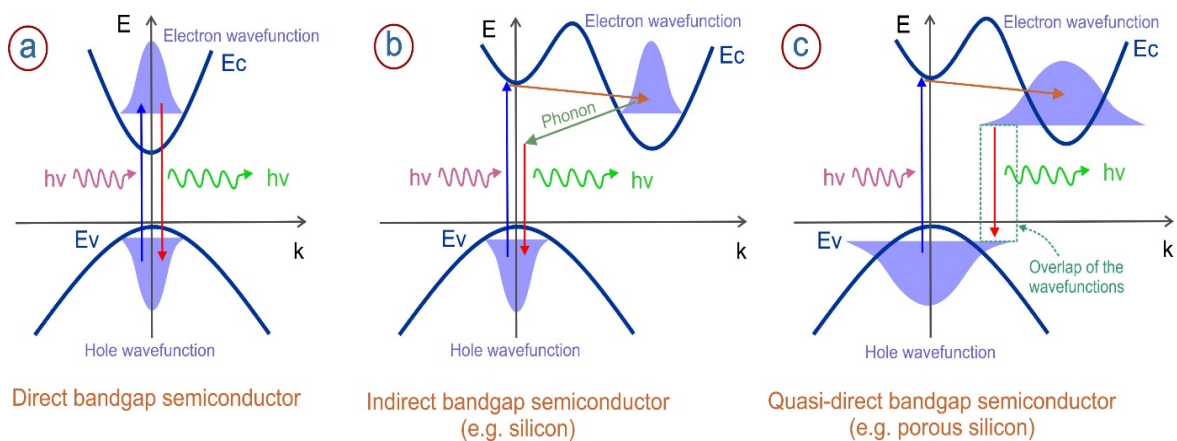


Figure 2.2. Schematic representation of the direct bandgap (a), indirect bandgap (b), and quasi-direct bandgap semiconductors (c). Adopted from Ref. [105], [106].

Photoluminescence is a phenomenon based on two successive processes: the adsorption of an incident photon (or electromagnetic wave) followed by the

transition of an electron to a higher electronic state and the return of an electron to a lower electronic state, which is accompanied by light emission. The energy of the incident photon must be high enough for the electron to overcome the bandgap and to reach the conduction band (E_c). Photoluminescence emission is highly dependent on the type of the semiconductor bandgap. There are three of them, direct and indirect bandgap - these are classical types (Fig. 2.2a,b), inherent in most of the known bulk semiconductors (e.g. CdSe and Si, respectively) [106], and the third is a quasi-direct bandgap (Fig. 2.2c), which arises as a result of the quantum confinement effect in nanosized semiconductors (e.g. PSi) [105].

Bulk silicon is the semiconductor with the indirect bandgap and due to this fact, it is barely possible to excite the photoluminescence since the bottom of the conduction band (E_c) is shifted towards the top of the valence band (E_v) and the direct transitions of the electrons are forbidden (Fig. 2.2b). There is also a possibility for the indirect transitions of the electron with the participation of phonons, however, but the probability of such a transition is too negligible and can hardly compete with the probability of a direct transition in a direct-gap semiconductor. Owing to the indirect bandgap and, as a consequence, low quantum efficiency, bulk Si remains unsuitable for the light-emitting application (e.g. light-emitted diodes (LEDs)).

Nevertheless, Si is not as useless as it might seem, and it still has a chance to be used as a light emitter, most likely not in its natural form, but in the form of nanosized derivations. For example, the nanosized layer of PSi consists of a broad range of nanocrystallites that play an essential role in the photoluminescence process due to the quantum confinement effect [107]. The bandgap of PSi differs from the bandgap of bulk Si since electrons and holes are spatially separated within the nanocrystallites, breaking the rule of the wavefunction conversation (k -conversation). In this case, the reduction of the material from bulk to nanosize causes increased spreading of the holes and electrons wavefunctions in momentum space in such a way that these wavefunctions overlap, providing the possibility of quasi-direct radiative transitions (Fig. 2.2c) [108]. The energy and the wavelength of the emitted photon are highly dependent on the Si nanocrystallites size (vary from 1 to 5 nm) and as a consequence the value of the bandgap [109]. It is suggested, that the smaller the Si nanocrystallites, the longer the wavelength they emit, and contrary [110]. Moreover, the emission associated with oxide-related defects on pure

silica core can also contribute to the overall PL band of PSi substrate [111]. The typical PSi PL band may lay in the range of 400-900 nm [109].

2.4. PSi photoluminescence as a tool for (bio)sensing applications

Taking into account that PL of PSi, similarly to PL of other semiconductors, can be affected by various physic-chemical processes (e.g. event of antibody-antigen interaction) that occur at the semiconductor's interface, this phenomenon was found attractive to be used in different sensing and biosensing applications. Currently, PL-based PSi transducers were examined for the detection of different gases and vapors including CO₂ [112], singlet oxygen [113], molecular oxygen [114], Ethanol, Trichloroethylene, n-Hexane [115], etc. In most cases, gases/vaporous quench the PL signal because their adsorbed molecules can introduce new non-radiative recombination centers (traps) on the PSi surface [112,114,115]. Moreover, PSi PL-based biosensor has proven to be effective in detecting glucose, and most interestingly, both PL quenching and enhancement effects are inherent in glucose detection depending on the concentration of the glucose in the analyte solution [116]. It was found, the PL intensity quenches while low glucose concentrations (10^{-5} - 10^{-2} mM) are detected, and the main mechanism that describes such behavior of PL is based on the interaction of the H₂O₂ (product of glucose decomposition) and PSi surface [116]. This process occurs with the consumption of electrons from the PSi conduction band and incorporation of holes in the valence band, thus the rate of their radiative recombination is decreased. The opposite situation occurs when the concentration of glucose is beyond 0.1 mM, the PL is enhancing instead of quenching. The possible reason for such a PL behavior is that, at high glucose concentration, the Si-H bonds on the PSi surface are replaced with different functional groups (e.g. C-C, C=C, C-OH, C=C), which favorably affect radiative recombination rate and as a consequence, the PL intensity increases [116].

Photoluminescence of Si NW (PSi-like structure) has also been used in immunosensing applications, such as detection of the C-reactive protein (CPR) with a concentration as low as 1.6 fM [117]. The interaction of the CPR with the PSi-like surface and its accumulation led to the PL intensity quenching that is associated with the introduction of non-radiative sites in the PSi-like surface. The comparison of PL lifetimes before and after exposure to the CPR molecules indicates post-exposure PL lifetime reduction caused by the decrease in the total number of the

emitting centers within the P*Si*-likes structure [117]. Additionally, PL-based detection exhibited high selectivity and sensitivity, that makes it attractive for different noninvasive analysis, such as analysis of biofluids content [117].

Figure 2.3 summarizes the general factors that can cause PL quenching when P*Si* interacts with the (bio)molecules to be detected. There are several photochemical and photophysical mechanisms that may be involved in P*Si* PL quenching process: (i) charge/energy transfer between P*Si* and analyte, (ii) surface state recombination (in analyte), (iii) bulk trapping, (in P*Si* matrix) (iv) nonradiative recombination (in P*Si* matrix) [118].

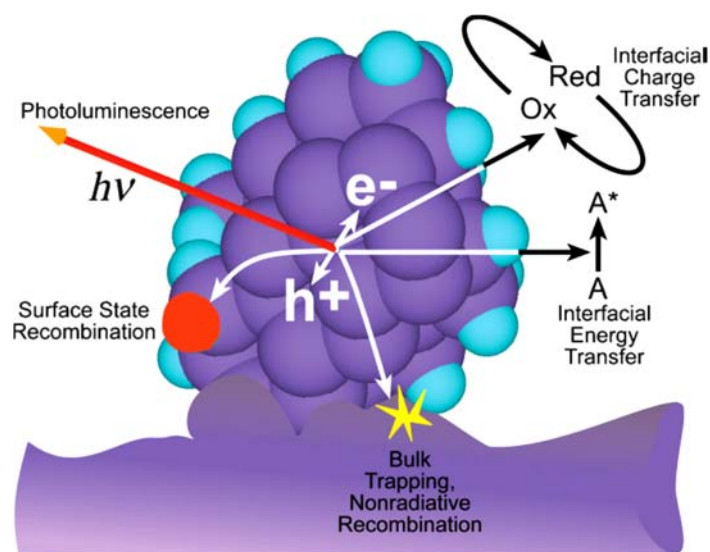


Figure 2.3. Schematic diagram depicting possible pathways of the P*Si* PL quenching. Reprinted from Ref. [118].

In this dissertation, all PL-based immunosensing experiments on P*Si* substrates were carried out in real-time mode with the sequential addition of the analyte to the cell/chamber designed for immunosensing applications.

2.5. Combination of P*Si* with noble metal nanoparticles

With modern advances in science and technology, the trend of producing hybrid or composite materials consisting of two or more components is becoming more and more evident. This tendency is driven by the desire to improve some chemical, physical, electrical properties of the material and enhance its efficiency in different applications including sensing and biosensing. For instance, the usage of pure P*Si* in optical SERS and (L)SPRS-based detection techniques is rather to be useless because it does not contribute significantly to optical signal transduction [119,120].

In this case, PSi can only serve as a matrix for other SERS/(L)SPR active materials, such as nanoparticles of metals (especially noble metals). Moreover, PSi proved to be a suitable material for the direct reduction of metal nanoparticles on its surface [121]. Interestingly, a comparison of the PSi matrix loaded with Au nanoparticles (PSi/Au) and the Si/Au composite showed an enhanced influence of the PSi matrix on the total SERS signal with an improved (about 176%) EF value [122].

If considering SERS and (L)SPRS-based detection, the PSi performs a secondary function, while most of the effects are associated with processes in noble metal nanoparticles. However, there are several detection methods (e.g. reflectance and voltammetry) in which PSi plays a crucial role in signal transduction process. For example, Au nanoparticles (~15 nm) decorating the PSi surface can increase the detection efficiency due to the enhanced mirror effect of the metalized surface [119]. On the other hand, 4 nm Au nanoparticles can settle to the inner parts of the pores, enhancing the efficiency of photonic/plasmonic-based optical detection performance [119]. Moreover, in H₂O₂ voltammetry-based detection, Au nanoparticles decorating PSi can efficiently adsorb hydroxide ions (OH⁻) inducing synergetic coupling effect between Au nanoparticles and PSi, and as consequence, accelerating the catalytic process towards H₂O₂ reduction [123].

Since the PL property of PSi is regarded as a powerful tool for (bio)sensing applications, it is also important to understand the behavior of PSi PL when it is coupled with noble metal nanoparticles, such as Au nanoparticles. The deposition of Au nanoparticles can induce both enhancing and quenching processes of PSi PL, and there are different mechanisms behind these processes [124–126]. The PL enhancement is usually attributed to the surface plasmon (SP) coupling effect, however, this statement is true only when PSi PL and Au adsorption bands overlap and the concentration of Au nanoparticles is high enough to change the overall PL spectrum [124,127]. There are also several factors that could contribute to the SP enhanced PL: (i) porosity of PSi player (or Si nanostructures), (ii) surface chemical modification [125], (iii) size/shape and distribution of Au nanoparticles [127].

The PL quenching can be promoted by the passivation of the PSi surface in the process of Au deposition (in oxygen contacting solution at a high temperature) and the formation of SiO_x insulating layer between PSi and Au [126]. In this case, the influence of plasmonic effects becomes smaller, while the influence of surface

chemistry become more pronounced [125]. It is assumed that SiO_x in some cases can slow down/block electron transfer between PSi and Au (Fig. 2.4), preventing subsequent PL quenching in oxygen-containing solutions [126]. This effect could be applied in PSi PL-based biosensing to eliminate signal zero-point drift. Moreover, immobilization of bioreceptors can be carried out directly on noble metal nanoparticles rather than on the passivated PSi surface [128].

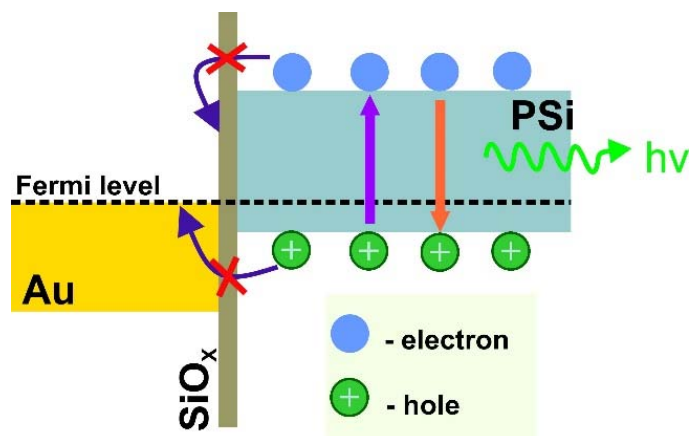


Figure 2.4. Schematic diagram illustrating charge transfer between Au nanoparticles and PSi. The Fermi level of Au nanoparticles is close to the Fermi level of PSi. Adopted from Ref. [126].

3. Fundamental aspects of zinc oxide, its electrochemical and photoluminescent properties, label-free (bio)sensing applications based on zinc oxide substrates

3.1. Fundamental aspects of zinc oxide. ZnO tetrapods and their electrochemical properties

Zinc oxide (ZnO) is well-known direct bandgap ($\sim 3.37\text{eV}$) semiconductor with n-type conductivity, high exciton energy (60 meV) and superior optoelectronic properties. ZnO belongs to the II–IV semiconductor groups, and has mixed covalent and ionic bonding [129]. It usually crystallizes in the hexagonal wurtzite structure with no inversion symmetry, which results in piezo- and pyroelectricity. Owing to its biocompatibility, low toxicity, stability in aqueous solutions, and high surface to volume ratio, ZnO is widely used as a transducer in different detection techniques, such as piezo- and pyroelectric, optical, etc. [88,130]. Moreover, the high isoelectric point (IEP ~ 9.5) of ZnO enables direct immobilization of reduced IEP proteins and enzymes, such as glucose oxidase (IEP ~ 4.2 at physiological pH of 7.4), and therefore it has been regarded as one of the most suitable and efficient in electrochemical (bio)sensing applications [131].

There is a wide availability of different ZnO morphologies including one-dimensional (1D), two-dimensional (2D), and three-dimensional (3D) structures. From the viewpoint of (bio)sensing application, 3D structures (or interconnected 1D structures) look the most promising as they have enhanced surface to volume ratio, and as result, they can provide more active sites, which will increase the number of the binding event between bioreceptors and analytes (Fig. 3.1a). Among all 3D and interconnected 1D shapes, ZnO tetrapods (ZnO TPs) possess the best mechanical stability and lower resistivity due to the direct and stable pathway for electron transfer (Fig. 3.1b) [132]. It has been found that both the high porosity of the interconnected ZnO TPs matrix and the large active area provide a low electrochemical peak separation and, as a result, a minimization of the background current, which is beneficial for the electrochemical (bio)sensing applications [130]. It is known, that all ZnO nanostructures have the same crystal structure, and their resistivity depends on the number of the barriers at the particle-particle junctions. The greater number of barriers on the electron percolation path through the ZnO matrix will lead to a greater potential drop and vice versa. Due to their geometry,

the radially-spread and elongated legs of ZnO TPs may form percolation paths with fewer barriers, while ZnO morphologies with the lower surface to volume ratio (interconnector nanoparticles (NPs) or nanorods(NRs)) will provide more barriers, degrading electronic conductivity and increasing overall resistance (Fig. 3.1c) [130]. In this regard, ZnO TPs are considered as the most suitable for electrochemical (bio)sensing applications, as they provide better conductivity, increased electron transfer rate, and enhance catalytic activity toward analyte oxidation (e.g. glucose oxidation).

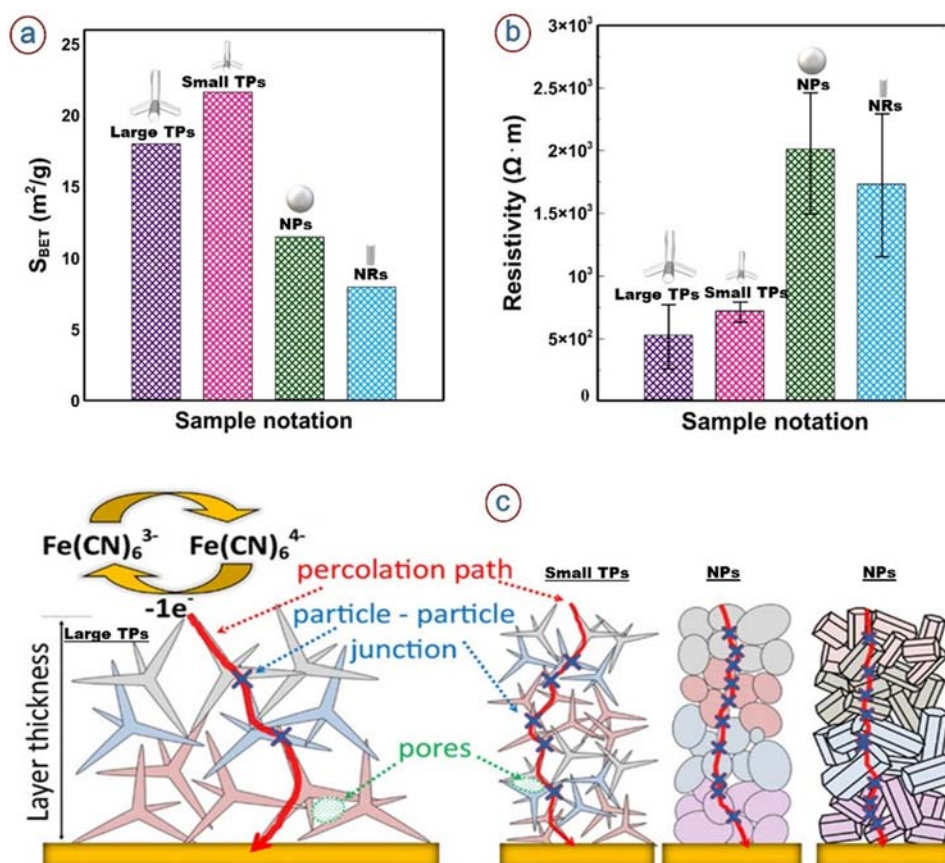


Figure 3.1. Brunauer–Emmett–Teller (BET) surface area calculated from N_2 adsorption/desorption measurements (a). Resistivity measurement for different ZnO shapes (b). Electron transport through the different interconnected ZnO nanostructures (percolation path ways are red arrows; blue crosses represent particle–particle junctions) (c). Reprinted and adopted with the permission from Ref. [130].

ZnO TPs can be fabricated in accordance with several different methods including hydrothermal deposition, chemical vapor deposition, vapor phase growth, flame transport synthesis, catalyst-free oxidative-metal-vapor-transport method, etc. [132]. Among these and many other methods, the catalyst-free oxidative-metal-vapor-transport is the simplest and cheapest one, as it requires only a few steps to

be performed [133]. On the first step Zn (99,9%) powder is loaded in a furnace at a high temperature ($> 600\text{ }^{\circ}\text{C}$) and in an air atmosphere. While other steps, including the evaporation of Zn metal, oxidation, nucleation and growth, take place directly in the furnace [134]. Once nucleated, ZnO TPs grow rapidly in the high-temperature region and reach more than 100 nm in diameter and more than 2 μm in length. It is important to note that the catalyst-free oxidative-metal-vapor-transport method provides a high yield of ZnO TP and no tetrapods' agglomeration, which is essential for large-scale production [134].

In this dissertation, all ZnO TPs samples were fabricated by an environmentally-friendly, high-yield catalyst-free oxidative-metal-vapor-transport method.

3.2. The role of 2D conductive materials in improving the electrochemical characteristics of ZnO

There is a huge amount of research devoted to electrochemical biosensors based on ZnO, and the prospects in this area are rather bleak since all issues have already been discussed, therefore, further efforts should be made to improve electrochemical performance by combining ZnO with other materials. There are several examples of how a modified ZnO nanocomposite demonstrates improved electrochemical performance by increasing charge transfer between redox-reaction products and modifiers. It can be modified, among others, by metal nanoparticles [135], other semiconductors [136], 2D conductive materials such as graphene oxide [137], MoS₂ [138], MXene [139], etc. Gold nanoparticles, for instance, could facilitate electron transfer between ZnO transducer the products of a glucose oxidation reaction, thus improving the electrochemical glucose detection performance [140]. The same effect appears, when ZnO is decorated with some 2D conductive materials, that also contribute to the overall charge transfer process. For example, reduced graphene oxide (rGO) introduced into the substrate of ZnO nanorods facilitates the percolation of electrons through ZnO to the electrode [137]. Both, modified by Au and rGO, ZnO nanocomposites exhibited enhanced catalytic activity toward glucose oxidation when compared with pure ZnO transducers [141].

Among all 2D conductive materials, MXenes (transition metal carbide, nitride, or carbonitride) have recently received particular attention in electrochemistry because they not only facilitate the electron transfer, as graphene-based materials do, but also represent accessible hydrophilic surfaces in contrast to the hydrophobic

nature of graphene-based and many other 2D materials [142]. Moreover, large active surface area, biocompatibility, metal-like conductivity, long-term stability, and tunable terminal functional groups (OH, O, and F) make them important elements that improve various electrochemical (bio)sensing applications. For example, the combination of MXene with ZnO resulted in a higher catalytic activity towards the glucose oxidation and improved electrochemical glucose detection [139]. Interestingly, in most cases, ZnO is used as a decorative element, and MXene is the substrate to be decorated [139,143–145], however the role of MXene as a decorative element still needs to be studied.

In this dissertation, ZnO TPs fabricated by the catalyst-free oxidative-metal-vapor-transport method were decorated by MXene nanosheets, in order to enhance catalytic activity towards glucose oxidation and increase the efficiency of electrochemical glucose detection on ZnO TPs/MXene (Fig. 3.2) modified substrates.

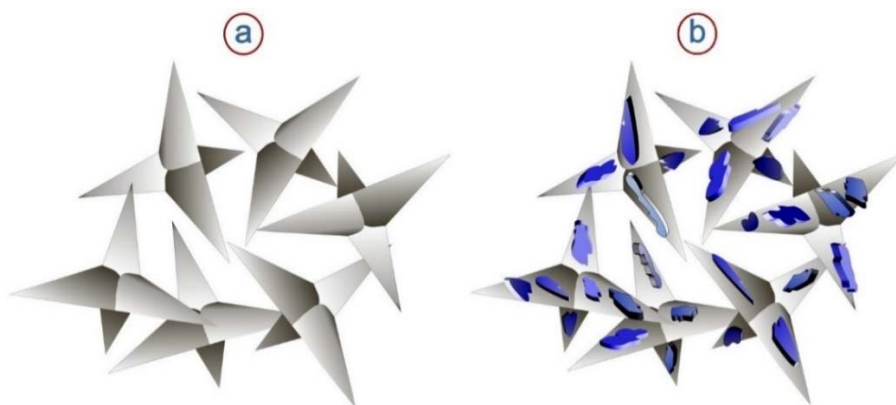


Figure 3.2. (a) Pure ZnO TPs, (b) ZnO TPs decorated by MXene nanosheets (ZnO TPs/MXene).

3.3. Photoluminescence of ZnO

ZnO as a direct band-gap semiconductor that possess eminent PL consisting of two independent bands: near-band edge excitonic (NBE), and deep-level emission band (DLE) [146]. There are different mechanisms behind these bands, the NBE band is due to the exciton recombination, while the DLE band is related to the defects' emission. To date, the exact mechanism of the DLE band have not been finally determined; however it is usually associated with both types of transitions: recombination of electrons from the E_c with holes in deep-level traps and recombination of holes from the E_v with electrons trapped inside the band-gap [147]. These traps are typically electronic defects in ZnO, which can be represented

by oxygen vacancies, oxygen interstitials, antisite oxygen, zinc vacancies, zinc interstitials, and surface states [148]. Highly crystallized and purified ZnO exhibits strong UV emission promoted by band-band recombination, while with the increasing of the defect concentration in ZnO band-gap, the visible PL becomes more pronounced, and under certain conditions it can become dominant (Fig. 3.3) [146].

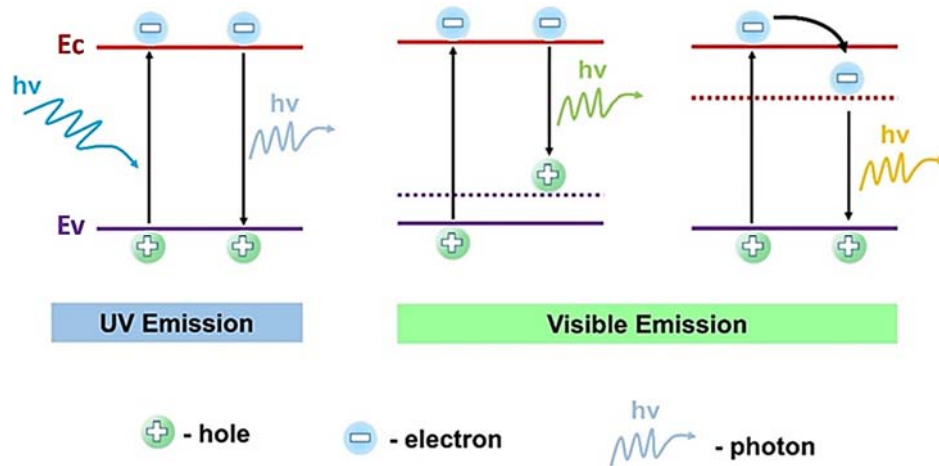


Figure 3.3. The main mechanisms of UV and visible PL in ZnO structures. Adopted from Ref. [146].

The best example of highly crystalline and pure ZnO is a thin layer synthesized by the atomic layer deposition process (ALD) on a flat substrate (e.g. Si) [149–151]. These flat thin layers are usually characterized by intense luminescence in the UV range and little emission in the visible range (when ALD is performed at $\sim 100^\circ\text{C}$), however, some redistribution between the UV and visible PL can occur when ALD is performed at the temperatures elevating 100°C [149]. The main reason behind this effect is the high-temperature-induced introduction of different types of the defects into ZnO structure such as various oxygen vacancy defects that contribute to visible PL band [149].

In parallel with the deposition of the ZnO films (thin layers) on flat surfaces, the ALD method could be used to cover substrates with enhanced surface to volume ratio and porosity such as 1D interconnected polymer nanofibers, the use of which is can improve different (bio)sensing applications, as they could provide more active sites than flat substrates [152]. The main feature of such structures is a strong visible PL caused by increased rate of deep level emission, while the UV emission becomes diminished, since the rate of exciton recombination become reduced [152]. There

are several probable reasons why this effect might occur: an increase in the concentration of defects inside the ZnO layer [153], on the other hand, the redistribution of NBE and DLE emission could be affected by the stresses created by the flexible polymer nanofibers after the ALD process [154]. For example, ZnO/PAN (ZnO/polyacrylonitrile) nanofibers prepared by the combination of the ALD and electrospinning techniques usually possess intense visible PL and homogeneous ZnO coverage, which is essential for the reproducibility of PL-based transducers [153]. It also turned out that PAN nanofibers fabricated by electrospinning are one of the most suitable substrates for ZnO ALD synthesis since they could provide uniform distribution of ZnO [155] in comparison with other polymers for which the ALD of ZnO occurs abnormally and high inhomogeneity takes place [156].

3.4. Electrospinning and ALD for the fabrication of 1D ZnO interconnected nanofibers

Interconnected 1D nanofibers are unique class of materials with high surface to volume ratio and porosity, which make them popular in different types of applications, among others air or liquids filtration, wound healing, and (bio)sensing [157]. Nanofibers can be fabricated in accordance to different protocols, including drawing [158], template synthesis [159], phase separation [160] and electrospinning [161]. The last one is considered to be the most advanced as it can provide smooth nanofibers with desired parameters from different types of polymers [162].

Electrospinning usually utilizes high potential to drive nanofibers out of a charged polymer solution through a metal needle. The electrospinning device consist of four main parts: a glassy syringe with the charged polymer solution, metallic needle, power supply, and collector (may has different shapes) [163]. The process usually starts when a strong electromagnetic field is created between the collector and the needle and charges begin to move into the polymer solution and induce instabilities [164]. These instabilities are due to the repulsive interaction between surface charges that tend to form the Taylor cone on the needle's tip from which a few nanometers-polymer jet is propelled [157]. When ejected, the jet is drawn out in a straight line, and then experiences unstable whipping movements caused by internal and external charge forces. During these movements solvent evaporates from the jet due to the convection and only elongated and solidified nanofibers

remain. The collection of nanofibers typically occurs on a grounded metal collector. Figure 3.4 illustrates the scheme of the entire electrospinning process [165].

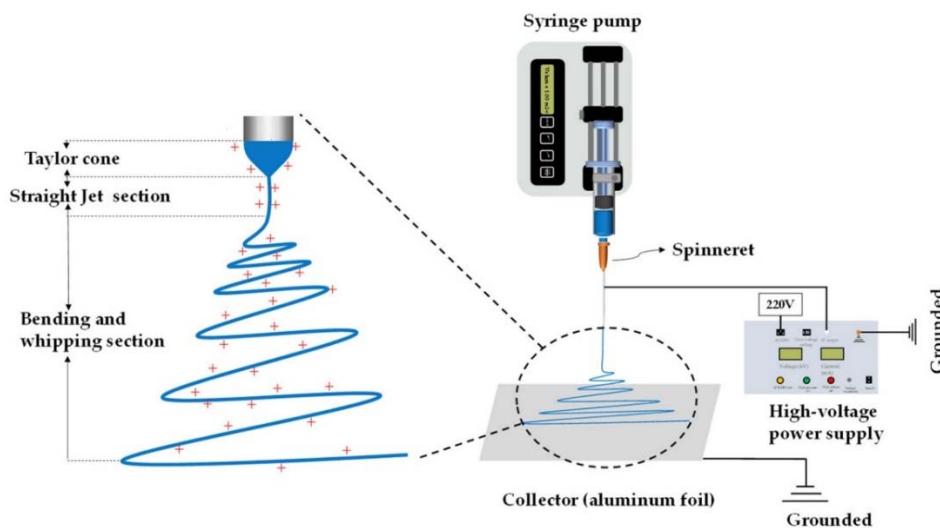


Figure 3.4. Schematic illustration of the electrospinning process. Reprinted from Ref. [165].

Once produced, 1D interconnected polymer nanofibers can be coated with thin layers of various metals or semiconductors to produce materials with desired shapes, properties, and characteristics [166]. The deposition of these films (layers) must be carried out at temperatures low enough so that the polymer remains unmelted. In this regard, ALD is considered the most convenient method, as it can be carried out at low temperatures down to 40 °C [167].

Atomic layer deposition is a gas phase thin film deposition technique that includes four sequential steps as shown in Figure 3.5 [168]. The general idea of ALD is the explosion of the substrate to an alternating sequence of vapor phase reactants. Owing to the self-saturating behavior of surface reactions, the thickness of the layer is controlled at the atomic level. The steps of ALD technique are as following [169]:

1. Introduction of the precursor into the reactor chamber and its interaction with available functional groups on the OH-terminated surface.
2. Purging or pumping away unreacted precursor using inert gases such as N₂ or Ar.
3. Introduction of the second precursor (co-reactant) and its self-terminating reaction with the molecules of the first precursor adsorbed on the surface of the substrate.
4. Purging or pumping away unreacted co-reactant and by-products molecules.

In this way, one layer (monolayer) of certain materials can be deposited on different substrates, both flat and rough. Repeating this cycle results in a multilayer film of the desired material [170].

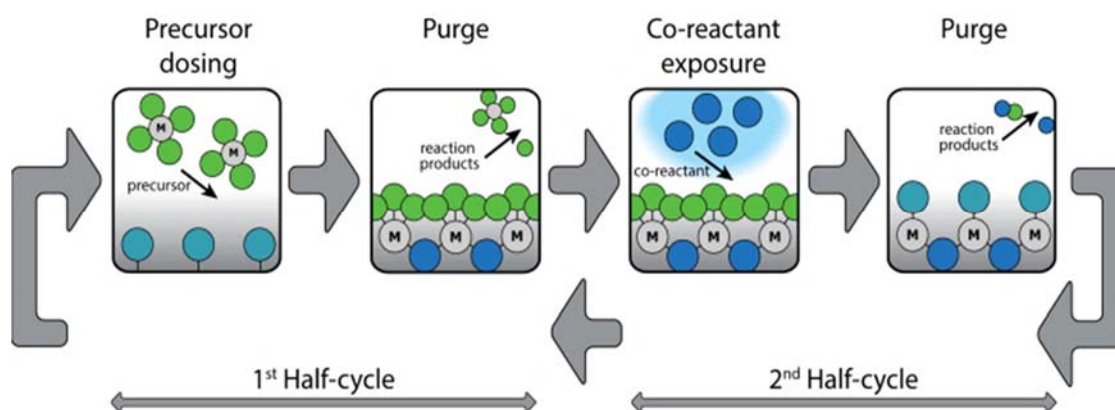


Figure 3.5. Schematic representation of the ALD process, consisting of two half-cycles. Each half-cycle includes the sequential introduction of a precursor or co-reagent with the following purging or pumping processes. "M" indicates metal atoms that may interact with oxygen or nitrogen (blue spheres) on the substrate's surface forming metal oxides or metal nitrides. By-products (green spheres) of the reactions are purged or pumped after each half-period. Reprinted from Ref. [170].

In this dissertation, 1D PAN/ZnO nanofibers were fabricated by the combination of electrospinning and ALD techniques for the synthesis of PAN nanofibers and ZnO deposition, respectively.

3.5. ZnO photoluminescence as a tool for (bio)sensing applications

PL of ZnO such as a PL of PSi has been regarded as the advanced tool for detecting various analytes of interest in different media (gases or liquids). The state of the ZnO band-gap can undergo slight modification while the ZnO surface is being occupied by the (bio)molecules (non-redox) that change the local electromagnetic field [88]. This principle underlies the general idea of PL-based (bio)sensing applications since the PL is extremely dependent on the changes occurring in the ZnO band-gap. For example, covalently immobilized ZnO can experience surface band-bending variation when immunocomplexes are being formed on its surface, hence disturbing the electromagnetic field at the intimate vicinity of the ZnO surface [171]. Depending on the electromagnetic properties of the formed immunocomplexes, bend-bending would promote either the expansion of depletion region (the region with lack of excitons) or constriction of depletion region which is favorable for the PL. The expansion of the depletion region within the bulk of ZnO will reduce the PL-active region, hence the intensity of PL (no matter NBE or DLE) will decrease [172]. In

contrast, the constriction of the depletion region expands the PL-active region in the bulk of ZnO, and PL becomes more intensive. Figure 3.6 represents the mechanism of PL-based detection using ZnO transducer where surface functionalization and analyte detection lead to the upwards bend-bending, expansion of the depletion region, and a decrease in PL intensity [173]. The expansion and contraction of the depletion region are mainly determined by the pH of the medium in which the detection takes place, and also depends on the transducer isoelectric point (IEP), as well as on the dipole moment of protein since the charges can be separated within the molecule (for example, inside the bioreceptors and analytes that settled down on the transducer surface).

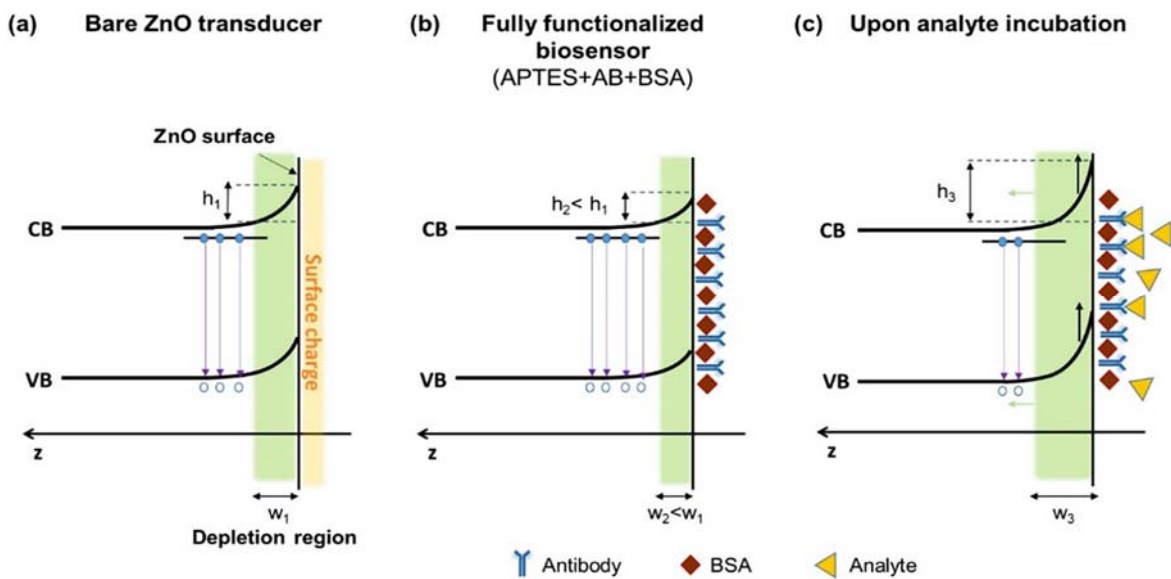


Figure 3.6. Schematic illustration of the band-bending phenomena occurring near the surface of ZnO upon surface functionalization and analyte incubation: bare ZnO transducer (a), after APTES treatment and incubation of bioreceptors (b), and biosensor performance/addition of the analyte (c). CB and VB stand for conduction and valence bands, respectively. h corresponds to the height of the potential barrier, while W denotes the width of the depletion region. The full circles illustrate electrons while the open circles denote holes and the straight arrow represent radiative recombination. Reprinted and adopted from Ref. [173].

4. Analytes to be detected in this dissertation

4.1. Mycotoxins and importance of their detection

Mycotoxins are secondary metabolites produced by *Aspergillus*, *Fusarium*, *Alternaria*, and *Penicillium* fungi during their life cycle. About 400 types of mycotoxins have been described so far, but only a small number of them pose a danger for humans/animals, including Aflatoxins (AFs) and Ochratoxins (OTs) [174]. Mycotoxins could be found in high amounts of different goods such as animal feeds, cereal crops, cacao seeds, wine, leguminous plants, eggs, and milk products, etc. [174]. Two variants of food/feed contamination are possible: pre-harvest contamination occurring in regions with high temperature and humidity, and post-harvest contamination occurring when agricultural products are stored in improper conditions. Pre-harvest contamination is usually associated with several physical factors: (i) the spread of fungal spores by insects, (ii) frequent watering or rainfall, and (iii) plant diversity. During storage, food/feed can be contaminated if the humidity exceeds 7-8% [175]. Besides, the spread of mycotoxigenic fungi can be facilitated by chemical factors, such as the use of fungicides and/or fertilizers, and biological factors, such as interactions between colonizing toxigenic fungal species and agricultural products

Despite strict control of the spread of mycotoxins, especially in Europe, these pathogens continue to wreak havoc on agriculture and the economy year after year [176]. The average annual loss from mycotoxins is about 25% of the world's cereals, and in the future, these losses will only increase due to Global Climate Change, such as Global Warming and the Greenhouse Effect. To reduce damages caused by mycotoxins, the following recommendations should be considered [174]:

- 1.** Prevention of fungi growth through the early harvesting of groundnuts and proper drying of crops and other foods/feeds. This can slow down growth of mycotoxigenic fungi up to 60%.

- 2.** Decontamination using physical approaches such as sorting, washing and peeling of the crops, etc. Mycotoxigenic fungi can also be neutralized by chemical treatment of agricultural products with fungicides. Moreover, the spread of toxigenic fungal species can be slowed down biologically, by introduction of atoxigenic fungi, which can compete with toxigenic fungi in the environment.

3. Detection and control of mycotoxins with the following withdrawal and isolation of the contaminated food/feed. The impact of this approach is very high as it can minimize amount of food/feed that could be delivered to the consumers.

- **Aflatoxins and importance of their detection**

Aflatoxigenic fungi (*A. flavus* and *A. parasiticus*) are the most prevalent throughout the world, especially in tropical areas with high temperatures and humidity. They usually colonize soils that are used for growing crops, grazing, etc. [176]. Aflatoxigenic species can also colonize improperly stored food/feed and a higher Aflatoxin production rate was observed at 27 °C and 0.90 α_w [177]. There are several types of AFs, such as B1, B2, G1, G2, M1 and M2, but the most dangerous in widespread is AFB1. It commonly contaminates corn, wheat, rice, sorghum, peanuts, tree nuts and figs worldwide and can be mutagenic and carcinogenic to consumers [176]. The uptake of the AFB1 products can cause liver precancerous lesions, cirrhosis, Kwashiorkor and Reye's syndrome in humans and animals, while the chronic AFB1 exposure can become a reason of Hepatocellular carcinoma (HCC) [178].

To avoid or minimize the harmful effects of AFs on humans and animals, it is necessary timely and precise control of the content of AFs (especially for AFB1) in food/feed. In this regard, the development of novel, out-of-lab, simple detection methods that are accessible to both large and small food/feed companies is a priority. This dissertation proposes new approaches for PL-based detection of AFB1 on PSi/Au and PAN/ZnO substrates in real-time mode.

- **Ochratoxins and importance of their detection**

OTs is another class of dangerous toxic secondary fungal metabolite that widely contaminate various kinds of food stuffs and feeds. They usually occur in places colonized by different *Aspergillus* and *Penicillium* species, including *A. ochraceus*, *P. verrucosum*, *A. carbonarius* and *P. viridicatum* [179]. The most dangerous among OTs is the OTA which production rate is optimal at 30 °C and 0.99 α_w [176]. OTA mainly contaminates cereal grains (barley, wheat, oats, corn, and beans), peanuts, dried fruits, grape, cheese, etc. Moreover, due to the long life cycle, OTA accumulates in foods/feeds, making them more and more dangerous to consume. The main target of OTA is the kidney where it induces nephrotoxicity in animals and

human nephropathy. It can also cause hepatotoxicity, teratogenicity, carcinogenicity and general immunosuppressive effects in humans/animals [180].

The importance of OTs detection (especially OTA) is determined by the severe consequences of their consumption. Identically to the need of AFs detection, the OTs must be detected timely and precisely in order to minimize their negative effect on humans/animals. Therefore, the development of simple, inexpensive and accurate detection methods can improve the quality of foods/feeds supplied to stores and markets. In this dissertation, a PL-based method on a PSi substrate was used to detect harmful OTA in real-time mode.

4.2. Diabetes and importance of glucose detection in human

According to the World Health Organization (WHO), *diabetes is a chronic disease that occurs either when the pancreas does not produce enough insulin or when the body cannot effectively use the insulin it produces*. This disorder usually results in hyperglycemia (high blood glucose), which causes serious damage to many of the body's systems, especially the nerves and blood vessels. Depending on the causes of diabetes, they are classified as follows (according to WHO):

- 1.** Type 1 diabetes. This type is characterized by limited insulin production and requires regular control of glucose levels in order to minimize undesirable consequences. The main symptoms include thirst, constant hunger, weight loss, loss of sight, excessive excretion of urine.
- 2.** Type 2 diabetes. Type 2 diabetes occurs when the body becomes resistant to insulin. In this case, the cells cannot effectively use insulin. The symptoms are similar to type 1 diabetes, but are less obvious, and the disease may go unnoticed for a long time after its onset.
- 3.** Gestational diabetes. This type of diabetes occurs only in pregnant women, indicating that the woman and her child might have type 2 diabetes in the future. Gestational diabetes is usually diagnosed accidentally, and less often because of symptoms.

Diabetes has many serious consequences, including blindness, kidney failure, heart attacks, stroke, and leg inflammation or amputation, so it is important to check and monitor blood glucose daily.

There is a well-known method how to control blood glucose levels based on the utilization of commercially available electronic glucometers. However, these devices require pricking of the fingers in order to collect material for detection. The finger-pricking is not something that people wish to do on a day-to-day basis as it brings inconvenience and pain. Besides, owing to their design, conventional glucometers do not provide the option of contentious real-time glucose monitoring. In this regard, the tendency of fabrication of novel glucometers that can measure glucose levels in different body fluids has become more pronounced [93]. For example, there is a possibility to detect glucose levels in human sweat, which may correlate with blood glucose levels, thereby avoiding finger-pricking and ensuring continuous glucose monitoring. It was currently shown that the approximated levels of the sweat glucose are in the range of 35-280 μM , with respect to blood glucose levels in the range of 4.5-13.2 mM [181,182]. Therefore, the limits of detection of the proposed and designed sweat glucose sensors must be small enough to detect lower than 35 μM of glucose in human sweat. In this dissertation, the electrochemical sweat glucose sensor based on ZnO TPs/MXene composite has been proposed. During sensor development, the main efforts were directed towards continuous glucose monitoring and ensuring a low LOD.

Overview of the publications constituting the dissertation

The previous chapters of this dissertation represent the introduction to the optical and electrochemical bio(sensing) application on PSi- and ZnO-based substrates for the continuous detection of mycotoxins and time-resolved sweat glucose monitoring. Fabrication methods and physicochemical properties of the materials have been described in the “Introduction” chapter. Particular attention has also been paid to the elucidation of general mechanisms that can be involved in mycotoxin and glucose detection processes, highlighting the relationship of [Publications I-IV] to each other. The following paragraphs provide a summary of [Publications I-IV] that make up this dissertation.

Publication I:

The review on the high number of papers dedicated to the application of PSi in (bio)sensing has showed the limited number of detection techniques that utilize photoluminescence of PSi, especially for the real-time detection of the analytes. To make up for this omission, PSi samples were fabricated by metal-assisted chemical etching (described in paragraph 2.2), immobilized with antibodies against cancerogenic and mutagenic OTA, and tested as the PL-based immunosensor for OTA. The detection process consisted in successive addition of various OTA concentrations to the detection cell, where the immobilized PSi sample was placed. The specific interaction between antibodies (anti-OTA) and antigens (OTA) on the PSi substrate led to a change in the PL intensity, that hereinafter served as the basis for the entire detection process. In that particular case, the change of OTA concentration in the *detection cell* has always led to a decrease in PL intensity with the highest intensity change of about 30% at 100 ng/ml of OTA in the cell. The calculation of some thermodynamic parameters has shown the significant interaction between OTA and anti-OTA (since the power coefficient $n = 0.4$ is less than 1), whilst the Gibbs free energy ($\Delta G = -53.1$ kJ/mol) points to a strength of interaction between the surface and the target biomolecules. The advantages of this detection method also include a wide sensitivity range to OTA (0.01–5 ng/ml) and LOD as low as 4.4 pg/ml, which makes this approach applicable for detecting even the smallest OTA contamination.

To conclude I:

- The PL of PSi seems to be an attractive tool for the real-time detection of the analytes (e.g. OTA) because its intensity changes as the analyte is added.

- The immobilized PSi substrate provides strong interaction between the bioreceptors (anti-OTA) and analytes (OTA) adsorbed on its surface.
- The extremely low LOD and wide sensitivity range are in the line with those achieved by complex, labor-intensive, and expensive ELISA and chromatography techniques.

Publication II:

The biggest challenge in the PL-based PSi biosensing is getting rid of the PL quenching effect upon PSi surface passivation in liquid media. The partial stabilization of PSi PL can be achieved due to the decoration of PSi substrate with noble metal nanoparticles (e.g. Au nanoparticles), whose nucleation and growth process leads to the formation of a thin SiO_x layer, which can slow down the charge transfer between PSi and liquid media. Moreover, the Au-decorated PSi substrate provides another possibility for the functionalization of bioreceptors directly on Au nanoparticles and their conglomerates rather than on passivated PSi. The deposition of Au nanoparticles on the surface of PSi was carried out by chemical and electrochemical methods, then samples with the best structural properties were selected for the detection of the carcinogenic and immunosuppressive mycotoxin AFB₁. The detection technique was the same as in **[I Publication]**, in short, PSi/Au was placed in a biosensor cell and treated with various AFB₁ concentrations. The specific interaction between anti-AFB₁ and AFB₁ has resulted in a decrease of PSi/Au PL, which was in the line with OTA detection on PSi substrate in **[I Publication]**. The calculated thermodynamic parameters (power coefficients $n_{\text{Chem.}} = 0.25$ and $n_{\text{EL.}} = 0.47$ as well as Gibbs free energies $\Delta G_{\text{Chem.}} = -54.6$ kJ/mol and $\Delta G_{\text{EL.}} = -51.5$ kJ/mol) indicate the thermodynamically favorable process of AFB₁ and anti-AFB₁ binding. In addition, the LODs of AFB₁ on PSi/Au_(Chem.) and PSi/Au_(EL.) were estimated as 2.7 ± 0.11 pg/ml and 2.1 ± 0.11 pg/ml, respectively. Such low values of LODs enable the detection of even the smallest AFB₁ inclusions, which are below the levels tolerated by the European Commission (EC) regulations.

To conclude II:

- Au nanoparticles can be deposited onto PSi substrates chemically and electrochemically; their deposition led to the reduction of the detection time of AFB₁ on PSi/Au_(Chem.) and PSi/Au_(EL.) samples in comparison to bare PSi (Supporting information **[II Publication]**).

- Calculated thermodynamic parameters indicate the favorability of AFB₁ and anti-AFB₁ (immobilized on PSi/Au substrates) binding process.
- The estimated values of LODs for AFB₁ on PSi/Au_(Chem.) and PSi/Au_(EL.) permit detection of AFB₁ contamination at levels below those allowed by the EC.

Publication III:

ZnO is another semiconductor whose nanosizing results in eminence PL in ultraviolet and visible ranges suitable for (bio)sensing applications. Another advantage of ZnO is that it can be shaped in many different ways, including interconnected 1D nanofibers with an enhanced surface to volume ratio, which positively affects the sensitivity to target analytes. In this publication, an attempt was made to fabricate 1D PAN/ZnO nanofibers as PL-based platforms for AFB₁ detection in real-time mode. Nanofibers were fabricated in two-step fabrication process included electrospinning of PAN nanofibers and the ZnO ALD process. As a result, samples with different thicknesses of ZnO layers were fabricated and characterized, and then samples with the most intense PL were selected for the following AFB₁ detection, meaning the same detection approach as in previous studies [**I, II Publications**]. Similar to the PSi/Au nanocomposites [**II Publication**], the specific interaction between anti-AFB₁ and AFB₁ had resulted in PL intensity change; this time, however, an increase in the PL intensity was observed. Taking into account the behavior of the PL intensity, a model describing the mechanism of AFB₁ detection was developed. This mechanism was based on the Donnan model, in which the Donnan potential created by ions and proteins changes the ZnO surface potential and, as a consequence, the PL intensity. The favorability of Anti-AFB₁&AFB₁ complex formation on PAN/ZnO surface was confirmed by calculated thermodynamic parameters ($\Delta G = -44.6$ kJ/mol, $n = 0.95 < 1$). The calculated value of the LOD (39 pg/ml) was higher than those for PSi/Au_(Chem.) and PSi/Au_(EL.) from [**II Publication**], but yet, it was significantly lower than this tolerated by the EC regulations.

To conclude III:

- 1D interconnected PAN/ZnO nanofiber with a high surface to volume ratio and intense PL can be produced in a two-step fabrication process involving electrospinning and ALD.

- The change in ZnO PL upon real-time AFB₁ detection can be described based on the Donnan model in which the main role plays Donnan potential (created by ions and proteins), ZnO surface potential, and its relation with PL.
- Calculated Gibbs free energy and power coefficient indicate the favorability of AFB₁ and anti-AFB₁ (immobilized on PAN/ZnO nanofibers) binding process.
- The lowest concentration of AFB₁ that can be detected using PAN/ZnO nanofibers is 39 pg/ml, which is well below the level tolerated by the EC.

Publication IV:

Shape diversity of ZnO makes him attractive not only for PL-based biosensor applications but also for other types of detection techniques, such as electrochemical where well-selected ZnO morphology (with a minimized number of the barriers at the particle-particle junctions) is a crucial factor in efficient detection. In this case, ZnO TPs are the most suitable since they satisfy the above condition and, in addition, provide a high number of adsorption sites for the analytes. Besides, the efficiency of the detection on the ZnO TPs transducer can be improved by modifying it with different 2D conductive materials such as GOx or MXene. Considering the above, an attempt was made to fabricate ZnO TPs/MXene with the enhanced catalytic activity towards glucose oxidation and its consequent detection. The ZnO TPs/MXene electrode exhibited lower LOD of glucose detection in PBS/artificial sweat than bare ZnO TPs and MXene electrodes. Besides, the value of LOD (21 μ m) was small enough that the ZnO TPs/MXene electrode could be used as the transducer of a flexible, stretchable electrode for on-body glucose detection in sweat. The real-time glucose monitoring showed that electrodes based on ZnO TPs/MXene recognize fluctuations in glucose levels during the consumption of sweets and physical activity. Moreover, fabricated electrodes exhibited long-term stability and excellent stretchability (up to 30% without degrading response).

To conclude IV:

- Decorating ZnO TPs with MXene nanoflakes results in increased catalytic activity for glucose oxidation, while electrodes made of the above components have a lower LOD than pure ZnO TPs and MXene electrodes.
- The low LOD of ZnO TPs/MXene enables measuring sweat glucose content fluctuation in real-time mode. ZnO TPs/MXene incorporated in flexible stretchable electrode provides stable response up to 30% elongation.

Publication I

The content of this chapter has been already published in Biosensors and Bioelectronics Journal
Biosensors and Bioelectronics, Volume 102, 2018, Pages 661-667, ISSN 0956-5663,
<https://doi.org/10.1016/j.bios.2017.11.048>.

Authors: **Valerii Myndrul**, Roman Viter, Maryna Savchuk, Nelya Shpyrka, Donats Erts, Daniels Jevdokimovs, Viesturs Silamiķelis, Valentyn Smyntyna, Arunas Ramanavicius, Igor Iatsunskyi

5. Porous silicon based photoluminescence immunosensor for rapid and highly-sensitive detection of Ochratoxin A

5.1. Introduction

Mycotoxins are toxic secondary metabolites produced by some fungal species. Among all mycotoxins, OTA has received the most attention due to severe health effects of animals and human [183,184]. OTA is produced by *Aspergillus* and *Penicillium* fungi [185]. It has been classified as a possible carcinogen for humans [186]. OTA is a mycotoxin, which has been found in foods of plant origin, in human and animal tissues [187–191]. European Commission (1981/2006 regulation) has recently set maximum tolerated levels (MTL) [192] of OTA in cereals (5 µg/kg), cocoa (2 µg/kg), beer and grape juice (2 µg/kg) [193,194]. As OTA is present in a number of food products, a development of novel, sensitive and low cost methods for the OTA detection is demanded for control of food quality and protection of human health.

Typically, OTA detection has been performed by various types of chromatography methods [195–197], or ELISA method [198]. The LOD of the proposed methods is about 0.15 ng/ml. However, these mentioned methods have some disadvantages. The chromatography methods are time-consuming and expensive. They require experienced and well trained personnel. Despite, ELISA method is simple and reliable. However, the time consuming and the limited sensitivity of ELISA require new alternative technique for OTA detection such as immunosensors.

With intense development of nano- and bio-technologies, a number of immunosensors for OTA detection has been developed. Recent approaches of OTA detection by electrochemical (LOD ~4.57pM) [199], electrical (LOD ~0.07 ng/ml)

[190], and optical immunosensors (LOD \sim 0.01 nM) [200,201] have been reported. Aptamer-based biosensing strategy based on an evanescent wave all-fiber (EWA) platform have been developed with LOD values 0.4 nm/ml and 0.3 nM, respectively [202,203]. It was found that the sensitivity to OTA was enhanced through tailoring of bioselective layer, specific to OTA [204–206]. For instance, aptamer-based optical sensors showed the highest sensitivity towards OTA in the range of 0.1-10 ng/ml with LOD 0.2 ng/ml [204–206].

Optical immunosensors are the most perspective among the others [207]. Optical technique provides precise detection of optical signal change, induced by adsorption of biomolecules [208]. Optical immunosensors are portable, compact and compatible with computerized devices and are characterized by low LOD. Therefore, they are suitable for the development Lab-on-Chip-based bioanalytical systems [208]. Photoluminescence (PL) immunosensors, as a type of optical biosensors, are based on the variation of PL-emission intensity during the interaction of immobilized bio-receptors with target molecules [209–211].

In the recent works we have demonstrated the action of nanostructured PL immunosensors based on specific interaction between antigens and antibodies suitable for the determination of various food pathogens [210,212,213]. Such PL immunosensors demonstrated high sensitivity and selectivity towards: antibodies against bovine leukemia viruses [212], Salmonella [213], OTA [214] and AF [215].

Porous silicon (PSi) is a well-known template, which is suitable for the development of various biosensors [216–219]. Unique physicochemical properties of porous silicon, such as biocompatibility, high surface to volume ratio, tailored surface stoichiometry and simple surface functionalization procedure provide high response of PSi-based biosensors to target analytes. Biosensors based on PSi have been applied for the detection of bacteria [220], viruses [221] and toxins [222]. Stable photoluminescence signal of PSi in visible region is suitable for the development of PL-based biosensors [209,211,216]. PSi nanostructures can be fabricated by MACE [223].

In the present study, we report a low cost and sensitive OTA immunosensor based on PSi consequently functionalized with Protein-A, antibodies against OTA (anti-OTA) and then by bovine serum albumin (BSA) (BSA&anti-OTA/Protein-A/PSi). Structural and optical properties of the prepared PSi were characterized with

scanning electron microscopy (SEM), X-Ray diffraction analysis (XRD) and Raman spectroscopy. Due to high specificity of immobilized anti-OTA towards OTA molecules, the BSA&anti-OTA/Protein-A/PSi-based-based PL-immunosensor showed good sensitivity in a wide range of OTA concentrations 0.01-5 ng/ml with a detection limit of 4.4 pg/ml. According to our best knowledge, this was the first time of the application of BSA&anti-OTA/Protein-A/PSi-based PL-immunosensor for the determination of OTA.

5.2. Materials and Methods

5.2.1. Chemical and Reagents

Anti-OTA monoclonal antibodies, OTA, Protein A, BSA were purchased from Sigma Aldrich.

5.2.2. The preparation and characterization of PSi

The PSi samples were fabricated from (111) oriented and highly doped p-type Si (B-doped, $\rho = 0.005 \Omega \text{ cm}$) using MACE procedure according to our previous report [223]. Structural properties of PSi were characterized using grazing incidence X-ray diffraction (GIXRD) by BrukerD5000 from Bruker (Billerica, MA, USA), high resolution field emission scanning electron microscopy (SEM) by SU-70 from Hitachi (Hitachi, Japan) at accelerating voltage of 30 keV and Raman spectroscopy by Renishaw micro-Raman spectrometer equipped with a confocal microscope from Leica (Wetzlar, Germany) and laser ($\lambda_{\text{excitation}} = 514 \text{ nm}$) from Modu-Laser (Centerville, USA).

5.2.3. The biofunctionalization of the PSi surface

PSi samples were cleaned in Piranha solution ($\text{H}_2\text{SO}_4:\text{H}_2\text{O}_2 = 4:1$), then they were immersed into a 4% solution of APTES in toluene vapors for 1 h at 70° C. Then samples were removed from the solution and rinsed with toluene and dried at 70° C for 30 min. The APTES modified PSi samples were washed in PBS and allowed to react with 10% glutaraldehyde in PBS (pH 7.4) for 20 min at room temperature. This was followed by thoroughly rinsing the PSi with DI water to avoid non-specific adsorption of the Protein A. The glutaraldehyde-activated surface was then reacted with 5 $\mu\text{g/ml}$ of Protein A solution in PBS buffer at room temperature for 30 min to form a Protein A layer. Then 5 $\mu\text{g/ml}$ antibodies against Ochratoxin A (anti-OTA) were deposited on PSi samples for covalent capturing by previously immobilized

Protein A to provide for the sensing layer the selectivity against OTA (Fig. 5.1). Finally, 5 $\mu\text{g/ml}$ of BSA was added to block the remaining active sites capable for adsorption of proteins (Fig. 5.1). As result, BSA&anti-OTA/Protein-A/PSi-based structure was formed.

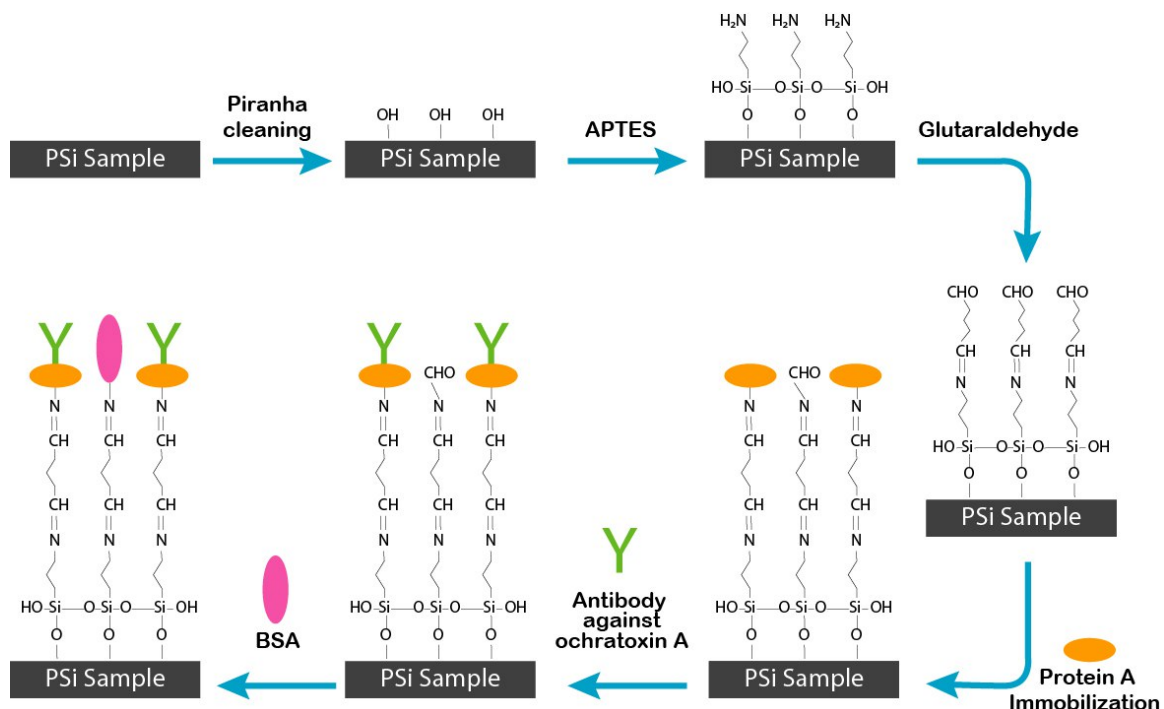


Figure 5.1. Functionalization of PSi sample surface by APTES and glutaraldehyde, which is followed by (i) immobilization of Protein A and antibody against OTA and (ii) blockage of surface by BSA.

5.2.4. The evaluation of photoluminescence signal of immunosensor

PL measurements were performed according to the experimental protocol, described in our previous researches [214,215]. The PL spectra were excited by UV laser from UltraLasers, Inc. (Toronto, Canada) at output power of 5 mW ($\lambda = 405$ nm). The PL spectra were collected by fiber optic spectrometer AvaSpec-ULS3648 from Avantes (Apeldoorn, Netherlands) in the range of 550-900 nm. The PL spectrum was recorded every 15 seconds within 30 minutes of the immunosensor interaction with OTA probes. The summarized experimental scheme of PL-immunosensor action is shown in Figure 5.2.

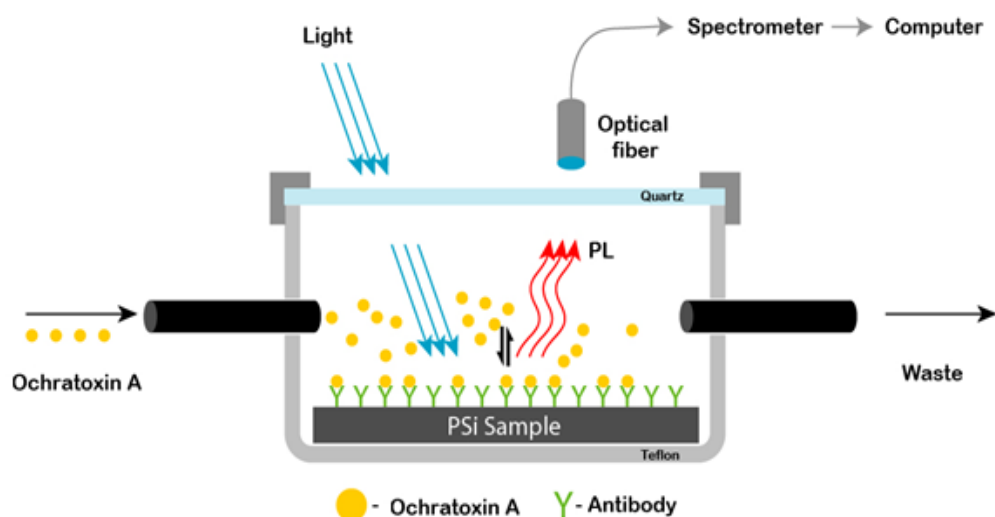


Figure 5.2. Experimental setup for OTA detection by PSi-based immunosensor using PL-spectroscopy.

5.3. Results and Discussion

5.3.1. Structural properties of PSi

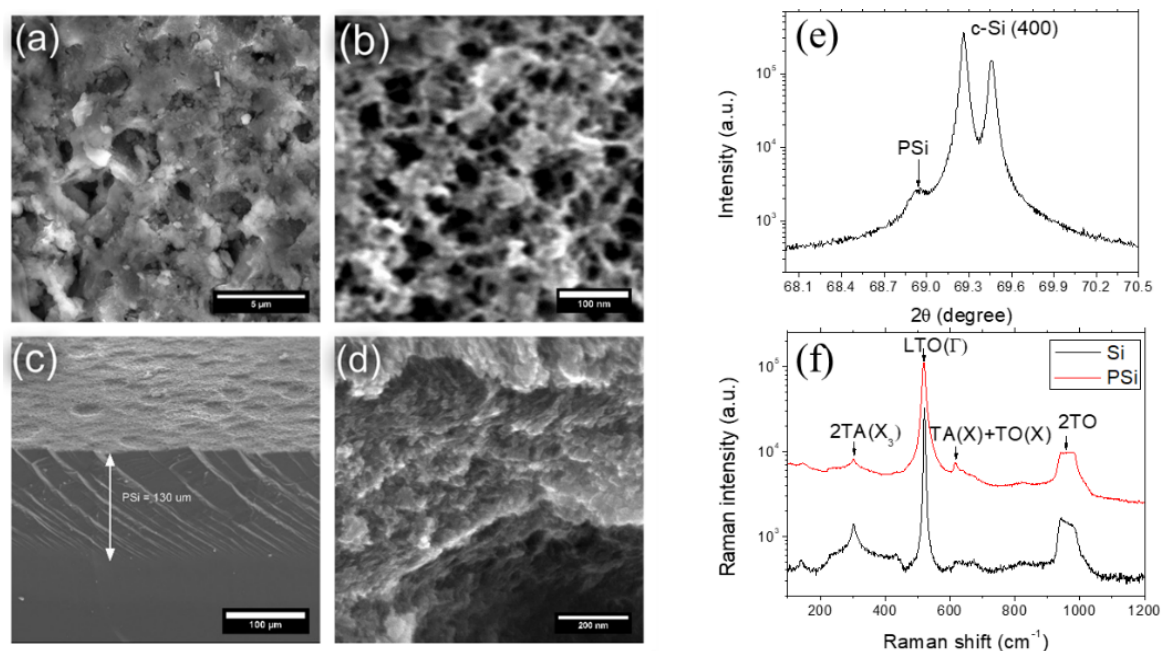


Figure 5.3. SEM images(a)-(d); XRD peak (e) and Raman spectra (f) of PSi (100) sample.

Figure 5.3a shows the plain-view SEM image of macroporous silicon (macro-PSi) obtained by MACE. High-resolution SEM showed that the surface of an individual macropore consists of a mesoporous silicon (meso-PSi) with an average pore size ranged from 10 until 50 nm (Fig. 5.3b). The average pore size is approximately 2-3 μm , and the thickness of the PSi layer is about 130 μm (Fig. 5.3c). As it is seen from Figure 5.3d, the obtained PSi samples had a rough morphology of the inner surface

of the macropore. The microstructure of the obtained PSi structures is affected by isotropic etching and high concentration of holes in silicon [224].

XRD spectrum of PSi is shown in Figure 5.3e. A strong peak at $2\theta = 69,3^\circ$ was assigned to the (400) plane of crystalline Si. A small peak at around $2\theta = 68,9^\circ$ indicates the presence of PSi layer. The peak position is shifted due to the crystal lattice expansion of PSi [225], which is related to interrelation between the deformation of PSi crystal lattice ($\Delta a/a$) and porosity of PSi [226]. We have calculated the deformation $\Delta a/a$ and this value was found as $14 \cdot 10^{-3}$, which corresponds to the porosity of 85 %. The mean size of Si nanocrystallites was determined from the full width at half maximum (FWHM) using Scherrer's equation [224]:

$$D = \frac{0.94\lambda}{FWHM \cdot \cos(\theta)}, \quad (5.1)$$

where D is the average size of nanocrystallites, λ – the X-ray wavelength (0.154184 nm). The average size of nc-Si was 32 ± 5 nm.

Raman spectra of PSi and Si wafer are presented in Figure 5.3f. The main Raman peak (LTO) of PSi was shifted to lower wavenumbers ($517 \pm 1 \text{ cm}^{-1}$) with consistent increase of its FWHM ($11 \pm 1 \text{ cm}^{-1}$) comparing to the Si wafer. The Raman shift and the broadening of the LTO peak could be attributed to phonon confinement in quasi-spherical Si nanocrystallites [227]. This can be used to estimate the average size of nc-Si [227]. Average value of crystalline size in PSi was calculated using the equation [227]:

$$I(\omega) \cong \int_{BZ} \frac{4\pi q^2 \exp(-\frac{q^2 L^2}{16\pi^2}) d^3 q}{(\omega - \omega(q))^2 - (\frac{\Gamma_0}{2})^2}, \quad (5.2)$$

where Γ_0 is the natural line width for Si wafer at room temperature, $\omega = \omega_0 - 120(\frac{q}{q_0})^2$, ω_0 is the position of the Si wafer Raman peak. The estimated values of crystalline size in PSi were about 3-4 nm. Properties of obtained structure will be evaluated in correlation with optical properties in the next section.

5.3.2. The evaluation of PSi photoluminescence during OTA determination

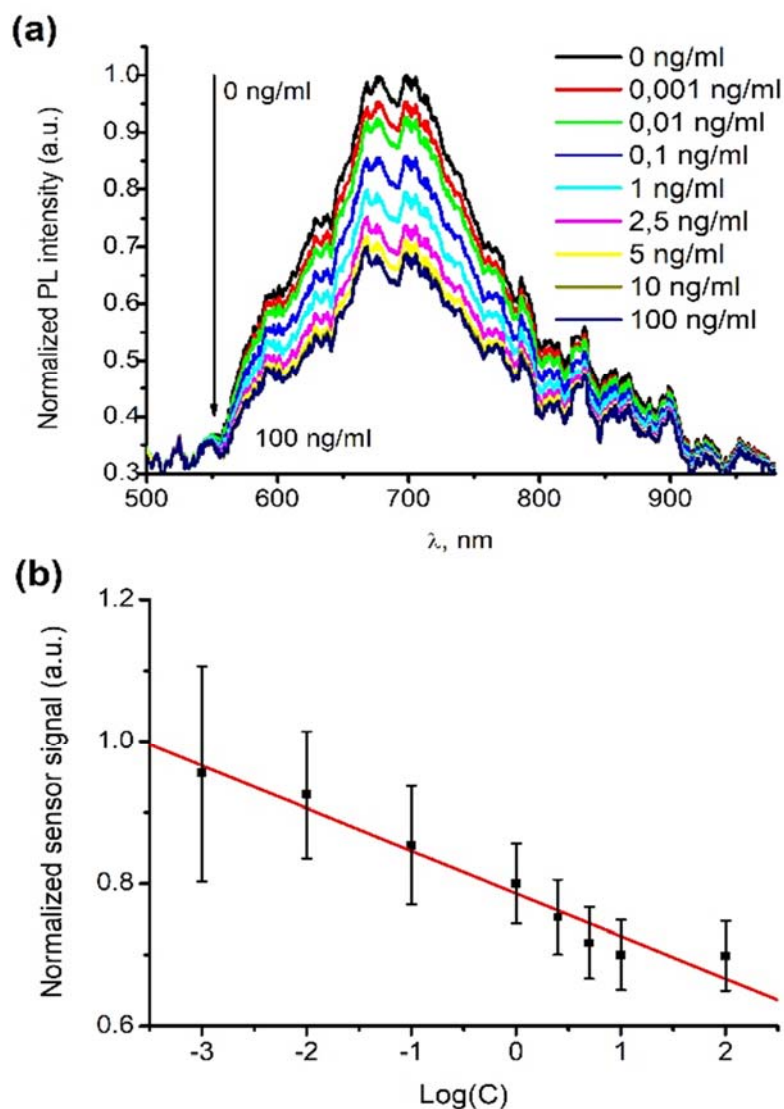


Figure 5.4. Photoluminescence spectra of BSA&anti-OTA/Protein-A/PSi-based immunosensor after incubation in different OTA concentrations (from top to bottom) containing samples after the reaching of steady state conditions (a); The dependence of immunosensor signal vs OTA concentration, measured at PL peak position ($\lambda = 675 \text{ nm}$) (b).

In order to simplify calculations, the PL signal before and after OTA injection was normalized towards PL spectrum of BSA&anti-OTA/Protein-A/PSi-based structure before OTA determination. Figure 5.4a shows the PL spectrum of PSi with two distinct PL bands, centered at about $675 \pm 5 \text{ nm}$ (1.84 eV) and $700 \pm 5 \text{ nm}$ (1.77 eV). The main mechanism of the red emission in PSi is explained by the quantum confinement of electrons from Si nanocrystallites [228]. We have calculated the

average size of nanocrystallites in the PSi samples using previously reported equation [215,229]:

$$E(eV) = E_g + \frac{h^2}{8d^2} \left[\frac{1}{m_e^*} + \frac{1}{m_h^*} \right], \quad (5.3)$$

where $E(eV) = 1.84/E(eV) = 1.77$ eV, $E_g = 1.12$ eV, h – Planck's constant, $m_e^* = 0.19m_0$; $m_p^* = 0.16m_0$ effective mass of electrons and holes in Si, $m_0 = 9.1 \times 10^{-31}$ kg. The calculated average size of nc-Si was about 2.7 ± 1 nm, which corresponds to the values obtained from Raman spectroscopy.

Figure 5.4a shows that the PL intensity of BSA&anti-OTA/Protein-A/PSi-based structure was quenched by OTA, which specifically bounded to the immobilized anti-OTA. The saturation of analytical signal occurs in OTA concentration range of 5-10 ng/ml (Fig. 5.4a). Figure 5.4b shows the PL intensity of BSA&anti-OTA/Protein-A/PSi-based structure at 675 nm, which is plotted in logarithmic scale of OTA concentration. The PL intensity of the immunosensor versus the OTA concentration can be interpolated by the following equation:

$$I_{675} = 0.77 - 0.06 \cdot \lg(C), \quad (5.4)$$

where C is OTA concentration.

The limit of detection (LOD) was determined using formula [215,230]:

$$LOD = 3.3 \cdot \sigma / b, \quad (5.5)$$

where σ is the standard deviation of negative control and b is the slope of the curve. The calculated value of LOD was approximately 4.4 pg/ml. This calculated value of LOD is almost the same as it was previously obtained for high-sensitive aptamer-based SPR-polarization platform [231].

5.3.3. Analysis of adsorption isotherms

Adsorption isotherms are providing some information on mechanisms of interaction between the immunosensor surface and target molecules [214]. Figure 5.5a shows a representative time-resolved changes of PL intensity of BSA&anti-OTA/Protein-A/PSi-based immunosensor *vs* several OTA concentrations. The sensor response S was calculated according to formula:

$$S(C) = 1 - I_{eq}(C), \quad (5.6)$$

where I_{eq} and C are the normalized PL signal value of BSA&anti-OTA/Protein-A/PSi-based structure in steady state conditions and OTA concentration, respectively.

The adsorption isotherm of OTA interaction with BSA&anti-OTA/Protein-A/PSi-based immunosensor is shown in Fig. 5.5b.

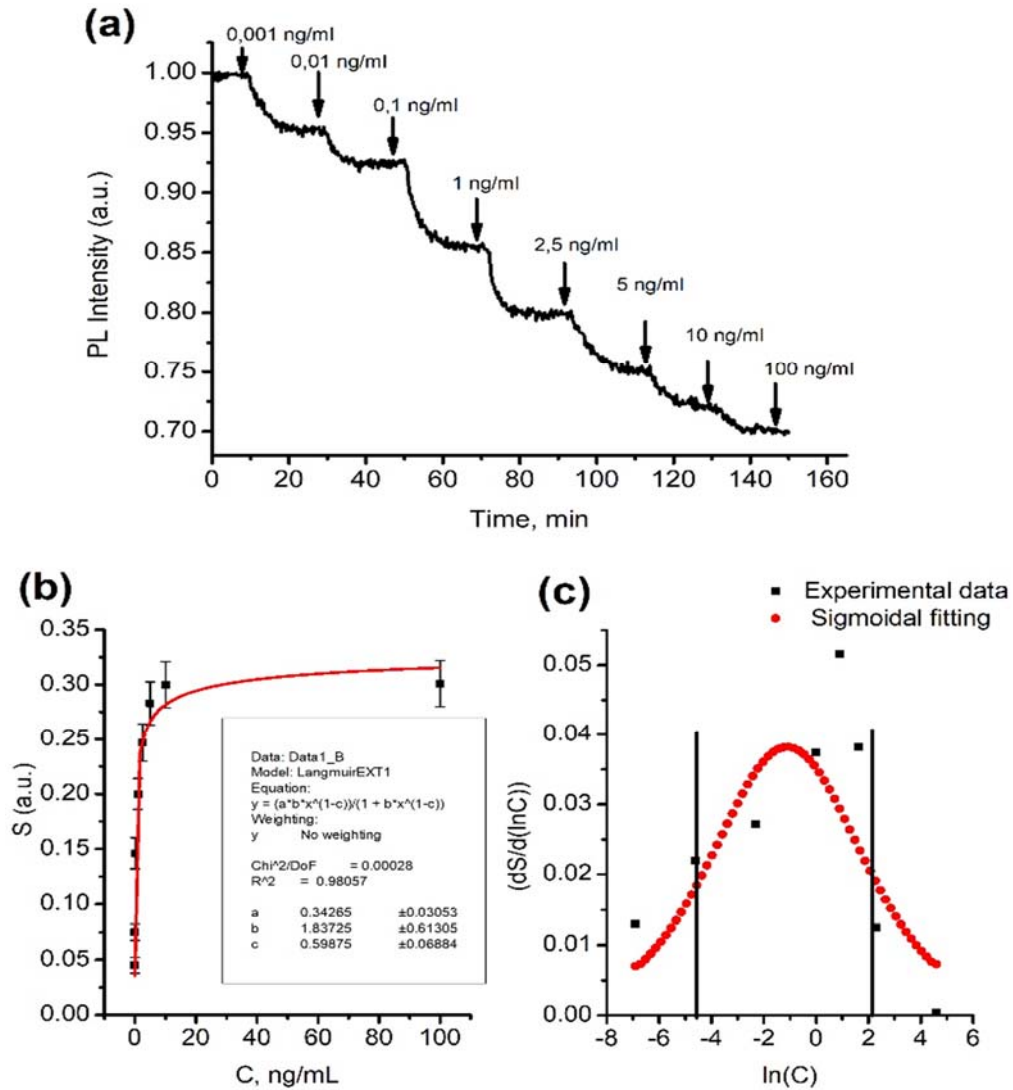


Figure 5.5. Dependence of PL peak maximum (at $\lambda = 675$ nm) vs OTA concentration (a); the isotherm of analyte (OTA) interaction with BSA&anti-OTA/Protein-A/PSi-based immunosensor (b); and calculated sensitivity of BSA&anti-OTA/Protein-A/PSi-based immunosensor towards OTA (c).

Calculations reveals that the interaction of the analyte (OTA) occurred according to the first order kinetics [232]:

$$\frac{dN}{dt} = k_a \cdot C \cdot (N_s - N) - k_d \cdot N \quad (5.7)$$

At steady state conditions when the $\frac{dN}{dt} = 0$, the isotherm of analyte (OTA) interaction was analyzed using Langmuir (5.8) and Langmuir-Freundlich (5.9) equations [214,215]:

$$\theta = \frac{B \cdot C}{K_D + C}, \quad (5.8)$$

$$\theta = \frac{B \cdot C^n}{K_D^n + C^n}, \quad (5.9)$$

where $\theta = \frac{N}{N_s}$ is surface coverage, $K_D = \frac{k_d}{k_a}$ is affinity constant and n is power coefficient.

Power coefficient 'n', which was calculated using equations 5.8 and 5.9, is lower than 1 ($n < 1$). Therefore, such value of power coefficient is pointing the significant interaction between OTA, which is present in solution, and anti-OTA, which is present on the interphase of BSA&anti-OTA/Protein-A/PSi-based immunosensor. The analysis of the adsorption isotherms showed better fitting using Langmuir-Freundlich equation (Fig. 5.5b). The obtained values of n and K_D are shown in the table 5.1. It points to the limitation of protein adsorption by high surface area of the BSA&anti-OTA/Protein-A/PSi-based immunosensor and additional diffusion process of the OTA molecules within the pores of modified PSi.

Table 5.1. Calculated parameters of OTA adsorption.

n	K_D, ng/ml	K_D, M	ΔG, kJ/mol
0.4 ± 0.02	0.22 ± 0.03	5.4·10 ⁻¹⁰ ± 0.3·10 ⁻¹¹	-53.1 ± 2.7

The interaction between OTA, which is present in the sample, and anti-OTA, which is present in BSA&anti-OTA/Protein-A/PSi-based immunosensor can be estimated by the calculation of Gibbs free energy (ΔG) according to equation:

$$\Delta G = -R \cdot T \cdot \ln(K_{D0}), \quad (5.10)$$

where T and R are absolute temperature and universal gas constant, respectively. The value of K_{D0} was calculated as:

$$K_{D0} = \frac{K_D}{C}, \quad (5.11)$$

where C is the OTA concentration, which in this calculation was equal to 1M.

Decrease of the Gibbs free energy point to a strength of interaction between the surface and the target biomolecule. It was reported, that ΔG value for OTA molecules varies in the range from -28 to -38 kJ/mol [197,198]. The present calculations points to even stronger interaction ($\Delta G = -53.1$ kJ/mol) between OTA and BSA&anti-OTA/Protein-A/PSi-based immunosensor surface. The obtained ΔG values correlate with the ones reported in [214,215]. We suppose that the increase of ΔG value might be related to better orientation of anti-OTA due to applied Protein A based layer, which was deposited on the PSi surface and is specifically binding antibodies *via* Fc-region, which is in the ‘tail’ of antibody. Therefore, in such way immobilized anti-OTA antibodies become uniformly and properly oriented on the surface of designed immunosensors [233].

Sensitivity of the immunosensors was calculated as a derivative of the sensor signal S to the natural logarithm of OTA concentration C (Fig. 5.5c) [214,215]. In addition, a differentiated data plot of fitted Sigmoid function was built for the comparison with experimental data. Analysis of the sensitivity showed, that BSA&anti-OTA/Protein-A/PSi-based immunosensor showed the sensitivity towards OTA in the range of 0.01-5 ng/ml (Fig. 5.5c). This shows sensitivity towards OTA, even better than the ELISA method, reported previously [214,234,235].

The PL quenching of BSA&anti-OTA/Protein-A/PSi-based immunosensor, was induced by OTA interaction with immobilized anti-OTA. The PL quenching mechanisms can rely on several factors: (i) energy transfer between PSi and BSA&anti-OTA/Protein-A/PSi-based structure, which is interacting with OTA, (ii) charge transfer, (iii) Fermi level shift during OTA interaction with Protein-A/anti-OTA&BSA-based structure, (iv) and change of dielectric constant of the surrounding media during increase of OTA concentrations [211,236–238]. However, we have no facilities to measure additional parameters of the immunosensor (e.g. conductivity, work function) simultaneously with PL measurements. But based on previously reported results and general knowledge about in this experiment used proteins we

can exclude energy and charge transfer between PSi and BSA&anti-OTA/Protein-A/PSi-based structure as a possible mechanisms of PL quenching [207,213,214]. We suppose that Fermi level shift during analyte adsorption and change of dielectric constant of the media, which is in close proximity to PL-sites of PSi, is the most plausible mechanisms of PL quenching in here reported system. Hence, the PL is quenched due to changes of local electric field near PSi surface through the interaction of OTA molecules with anti-OTA, which is present in the BSA&anti-OTA/Protein-A/PSi-based structure. Actually, understanding of the mechanisms of PL quenching still requires more experiments and analysis. It will be a topic for next research paper.

5.4. Conclusions

The investigation of optical properties of PSi showed that it is very promising material for the development of PL-based immunosensors. PL spectroscopy based immunosensor for the determination of OTA was developed using step-by-step modification of PSi surface with Protein A, anti-OTA and BSA (anti-OTA&BSA/Protein-A/PSi). Developed anti-OTA&BSA/Protein-A/PSi/ structure showed good sensitivity towards OTA. The anti-OTA&BSA/Protein-A/PSi-based immunosensor was integrated within portable fiber optics based measurement system. In this research reported design of immunosensor is suitable for direct and real time detection of toxins and other analytes. which could be used in the monitoring of food quality. It was shown that the decrease of the PL-intensity of anti-OTA&BSA/Protein-A/PSi-based structure is observed with the increase of OTA concentration in the samples used for investigations. Therefore, this decrease of PL was interpreted as analytical signal. The response time of the immunosensor to different OTA concentrations was in the range of 500-700 s. The developed immunosensor showed good sensitivity towards OTA in concentration range of 0.01-5 ng/ml with detection limit of 4.4 pg/ml. Langmuir-Freundlich isotherms were plotted for the interaction of OTA with anti-OTA&BSA/Protein-A/PSi-based structure, and some aspects of interaction mechanisms and PL quenching mechanisms are discussed. Further investigations will be focused on the evaluation of immunosensor performance and better understanding of interactions between analytes and biological recognition and signal transduction parts used in immunosensor design.

Publication II

The content of this chapter has been already published in Talanta Journal

Talanta, Volume 175, 2017, Pages 297-304, ISSN 0039-9140,

<https://doi.org/10.1016/j.talanta.2017.07.054>.

Authors: **Valerii Myndrul**, Roman Viter, Maryna Savchuk, Maryna Koval, Nikolay Starodub, Viesturs Silamiķelis, Valentyn Smyntyna, Arunas Ramanavicius, Igor Iatsunskyi

6. Gold coated porous silicon nanocomposite as a substrate for photoluminescence-based immunosensor suitable for the determination of Aflatoxin B₁

6.1. Introduction

Contamination of food by mycotoxins is one of the most actual problems because the toxins are harmful to human and animal health. Aflatoxins (AFs), which belongs to a group of mycotoxins, are often contaminating some food products such as cassava, corn, cotton seed, millet, peanuts, rice, sorghum, sunflower seeds, tree nuts, etc. [239]. AFB₁ is one of the most dangerous forms of aflatoxins with significant toxic effects (e.g. teratogenicity, and carcinogenicity) [240], and it has residual risk in the initiation of human cancer (HCC) [241]. Traditional methods for the determination of AFB₁ are based on chromatography [195–197], and ELISA-Kits [198]. These methods are highly precise but long lasting and expensive. Therefore, less sophisticated and cheaper methods for the determination of toxin concentrations are required.

Some biosensors have been developed for the determination of AFB₁. For instance, nanomolar concentrations of AFB₁ have been precisely detected by electrochemical [199], FET [242], and optical transducers based biosensors [201,205]. Among a number of biosensors, the optical ones have some advantages such as portability, low dimensions and high sensitivity towards selected analytes [150,207]. Sensitivity of optical biosensors can be improved by increased both optical signal detection area and signal-to-noise ratio. Therefore, the development of novel nanomaterials with high surface area and well established optical signal (e.g. absorption, reflectance, photoluminescence, etc.) might improve the performance of optical biosensors.

Among optical biosensing techniques, the most advanced are FL, SERS, and SPR. However, these techniques are quite expensive and time consuming. In addition to mentioned techniques, photoluminescence can be also used as analytical signal in optical biosensors. Photoluminescence-based biosensors have higher sensitivity, they also are portable and less expensive than the other types of optical biosensors and traditional techniques, which are used for the determination of AFB₁.

Among many different nanomaterials, PSi is known as one of the most efficient material for the design of optical biosensors [216–219]. PSi is biocompatible, it has high surface to volume ratio, high reactivity of the surface, and good integration ability with a standard silicon semiconductor technology. PSi structural properties can be easily tuned according technical requirements and well adopted in design of optical biosensors. The main challenge for PSi-based biosensors is to prevent a degradation of surface due to oxidation in oxygen containing environment (e.g. air) and contamination by impurities [243]. The deposition of noble metal layers over PSi and formation of PSi/(noble metal) structure can partially prevent PSi from oxidation and contamination [223,243,244].

Recently, a number of papers have been published focusing on the applications of PSi/Au nanostructures in biomedicine [245,246], photovoltaics [247,248], biosensors [249–251], and Li-ion batteries [252]. It was shown, that surface plasmon resonance effects of layered PSi/Au structure are much higher comparing to that of unmodified PSi [125,253,254]. In addition, PSi/Au structures demonstrated improved electrical, optical and sensing properties. It was reported that PSi/Au structures showed high rate of transfer of photogenerated charge carriers in Si/Au interface, which was used for the enhancement of biosensor sensitivity [251]. Due to well-developed methodology of covalent binding of biomolecules on the Au surface, PSi/Au structures are even more attractive for the design of biosensors. Au nanoparticles and/or Au-based nanolayers can be deposited onto the Si surface by various methods: electrochemical deposition [248], chemical reduction based synthesis [245], deposition of gold nanoparticles from colloidal solution [255] etc.

In this work, we report the structural and optical properties of electrochemically and chemically formed PSi/Au_(EL) and PSi/Au_(Chem.) structures. In order to design structures selective to AFB₁ the surfaces of the PSi/Au_(EL) and PSi/Au_(Chem.) were

functionalized by protein A (Protein-A), which was modified with antibodies against AFB₁ (anti-AFB₁) in the next step. Then both types of PSi/Au_(EL.)/Protein-A/anti-AFB₁ and PSi/Au_(Chem.)/Protein-A/anti-AFB₁ structures were used in the design of PL-based immunosensors suitable for the determination of AFB₁ concentration. Sensitivity range and limit of detection (LOD) of both PSi/Au_(EL.)/Protein-A/anti-AFB₁ and PSi/Au_(Chem.)/Protein-A/anti-AFB₁ structures towards AFB₁ were calculated.

6.2. Experimental Section

6.2.1. Materials

The biological samples (antigens (Ag) and antibodies (Ab) of aflatoxin B₁, protein A, bovine serum albumin (BSA)) and reagents (3-Triethoxysilylpropylamine (APTES), 11-Mercaptoundecanoic acid (11-MUA), N-Hydroxysuccinimide (NHS), N-(3-Dimethylaminopropyl)-N'-ethylcarbodiimide hydrochloride (EDC)), Si wafers and chemical materials were purchased from Sigma Aldrich.

6.2.2. Fabrication of PSi samples

The PSi samples were fabricated from highly doped p-type Si wafers (B-doped, $\rho = 0.005 \Omega \text{ cm}$) with (111) orientation utilizing MACE [224]. The silver particles were deposited on pre-cleaned Si samples by immersion in 0.2 M HF and 10^{-3} M AgNO₃ aqueous solutions. The duration of incubation in this solution was 60 s. Then, the samples were etched in aqueous solutions containing HF (40%), H₂O₂ (30%), and ultrapure H₂O at a ratio of 20/80/80 H₂O₂/H₂O/HF for 60 min. After etching, the samples were incubated in HNO₃ solution to remove the silver particles for 10 min and then incubated in 5% HF solution to remove an SiO₂ layer from the Si wafer surface. During the final step, the samples were cleaned with deionized water and then dried in nitrogen flow. All mentioned procedures were performed at room temperature.

6.2.3. Fabrication of PSi/Au nanocomposites

PSi/Au nanocomposites were fabricated by chemical and electro-chemical deposition and two different structures PSi/Au_(Chem.) and PSi/Au_(EL.) were formed, respectively (Table 6.1).

Table 6.1. Parameters applied in formation of different structures.

Sample abbreviation	Method	Deposition parameters
PSi/Au _(Chem.0.5)	Chemical deposition	30 min deposition
PSi/Au _(Chem.20)		20 h deposition
PSi/Au _(Chem.48)		48 h deposition
PSi/Au _(El.20)	Electro-chemical deposition	20 mV vs Ag/AgCl _(3M KCl)
PSi/Au _(El.50)		50 mV vs Ag/AgCl _(3M KCl)

Chemical deposition method included following steps: (i) solution A, which consisted of 10 ml of H₂O and 0,25 ml of 1% HAuCl₄, was heated up to 60 °C, and solution B, which consisted of 2 ml of 1% aqueous solution of trisodium citrate, 8ml of H₂O, 15µl of Tannin, was also heated up to 60°C; then solutions A and B were mixed and heated up to 95 °C and after that PSi samples were incubated in this mixed solution for 0.5, 20, and 48 hours, and three different structures (PSi/Au_(Chem.0.5), (PSi/Au_(Chem.20), PSi/Au_(Chem.48)) were formed, respectively.

Electrochemical deposition of gold onto PSi samples was performed with a computerized potentiostat PGSTAT 30/Autolab from EcoChemie (Utrecht, The Netherlands) controlled by GPES 4.9 software in cyclic voltamperometry mode. The deposition was performed within 20 cycles with the potential -0.6 - 0 V vs Ag/AgCl_(3M KCl). The scanning rate was 20 mV/sec and 50 mV/sec for two groups of samples, referred as PSi/Au_(El.20) and PSi/Au_(El.50), respectively. The electrolyte solution was prepared by the same method as for the chemical deposition. The electrodeposition of Au onto the PSi was carried out with a three-electrode cell. Platinum and Ag/AgCl_(3M KCl) from Metrohm AG (Herisau, Switzerland) were used as the auxiliary and reference electrodes, respectively.

6.2.4. Characterization of PSi and PSi/Au nanocomposites

Fabricated PSi and PSi/Au structures were evaluated by a high resolution field emission scanning electron microscope (SEM) SU-70 (Hitachi, Japan) at accelerating voltage 30 keV. Structural properties of PSi and PSi/Au structures were characterized using Grazing Incidence X-ray Diffraction (GIXRD; BrukerD5000).

Photoluminescence (PL), reflectance and PL biosensing tests were measured using high-resolution fiber optic spectrometer AvaSpec-ULS3648 from Avantes (Apeldoorn, Netherlands). The excitation of the PL was performed by solid state laser (405 nm, 1000 Hz, 10 mW).

6.2.5. Formation of self-assembled monolayers on PSi/Au structures and immobilization antibody against of Aflatoxin B1

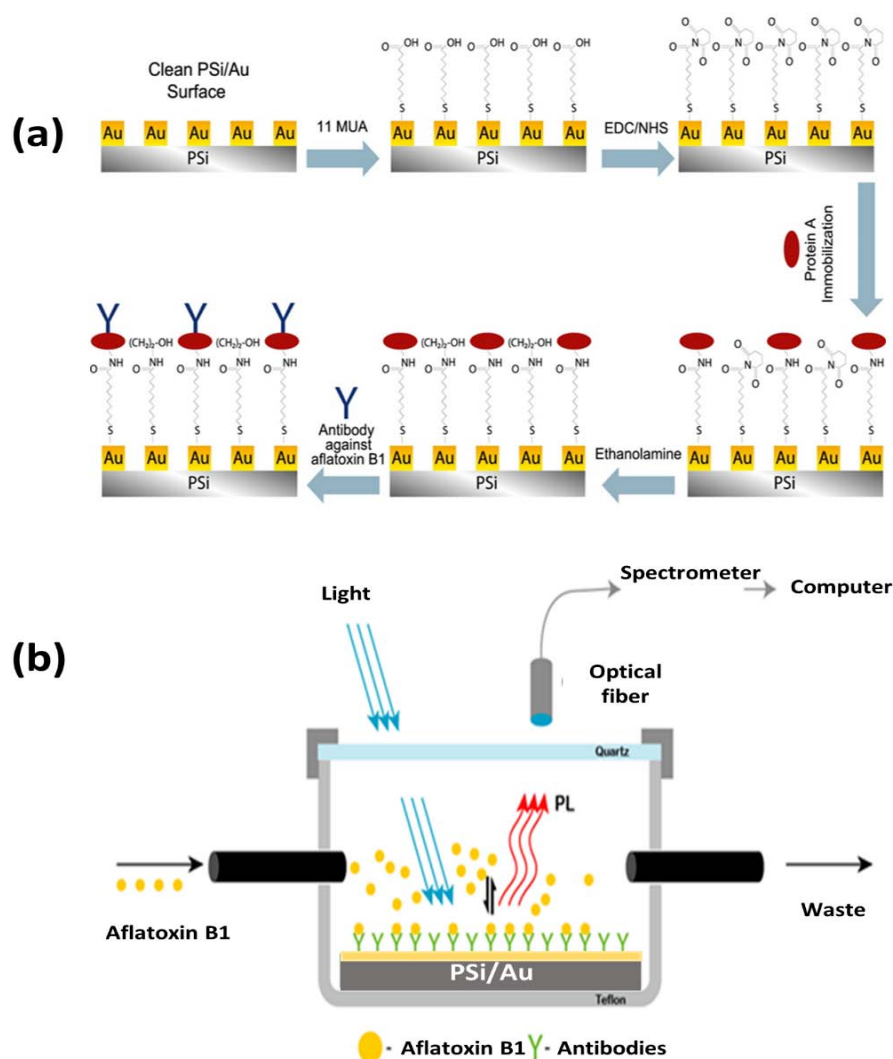


Figure 6.1. Sequence of procedures applied for the functionalization PSi/Au surface and immobilization of antibody against AFB1 (anti-AFB1) (a); The scheme of photoluminescence measurement based cell used for the evaluation of AFB1 and anti-AFB1 interaction kinetic (b).

Clean PSi/Au samples were incubated in 1 mM solution of 11-Mercaptoundecanoic acid (11 MUA) in ethanol at room temperature for 18 hours. Then carboxyl groups of 11-MUA were activated using a mixture containing 0.1 M of 1-Ethyl-3-(3-dimethylaminopropyl)carbodiimide (EDC) and 0.1 M of *N*-Hydroxysuccinimide (NHS) for 300 s. The activated PSi/Au was incubated in 10 mM sodium acetate

buffer, pH 4.5, containing 5 $\mu\text{g/ml}$ of protein A for 1000 s and in such way PSi/Au/protein-A structure was formed. The deactivation of not reacted activated carboxyl groups was performed by incubation in 1 M ethanolamine, pH 8.5, for 900 s. Then PSi/Au/protein-A samples were incubated in 6.7 $\mu\text{g/ml}$ water-based solution of anti-AFB1 to form complex of anti-AFB1 with protein A, formed structure is indicated as PSi/Au/protein-A/anti-AFB1. The principle scheme of these modifications is shown in the Fig. 6.1a.

6.2.6. Immunosensor testing

Analytical characteristics of biosensors based on PSi/Au_(EL.)/protein-A/anti-AFB1 and PSi/Au_(Chem.)/protein-A/anti-AFB1 structures were performed in a homemade experimental cell (Fig. 6.1b), which was made of Teflon. A cavity, which was dedicated for a sample, was isolated by optical quartz glass to provide an excitation by laser light and PL signal collection. The cell was equipped with inlet and outlet for biomolecules probes. Photoluminescence was excited with solid state laser ($\lambda = 405 \text{ nm}$) and collected by optical fiber spectrometer using multimode optical fibers equipped with semispherical lenses. Before measurement, 200 microliters of buffer solution were injected into the cell. The PL signal of the sample at fixed wavelength ($\lambda = 700 \text{ nm}$) was collected every 5 seconds. The sample was stored in buffer solution until the PL signal reached equilibrium. Then, 200 microliters of aliquots, which contained different concentrations of AFB1, were subsequently injected into the cell.

6.3. Results and Discussion

6.3.1. Structural properties of PSi and PSi/Au

PSi and PSi/Au structures were investigated by XRD and SEM technique. Figure 6.2 represents the XRD patterns of PSi, PSi/Au_(Chem.) and PSi/Au_(EL.) structures. Within a measured range of 2θ , a distinct peak at $2\theta=28,35^\circ$ corresponding to Si(111) structure is present in all patterns. In spectra of both (PSi/Au_(Chem.⁰⁻⁵) and PSi/Au_(Chem.²⁰)) structures no peaks that are characteristic for gold-based crystals were observed, due to amorphous nature of deposited Au layer. Differently from previous two structures in spectra of both (PSi/Au_(EL.⁵⁰) and PSi/Au_(Chem.⁴⁸)) structures four XRD peaks (at: $2\theta = 38,18^\circ$, $2\theta = 44,36^\circ$, $2\theta = 64,62^\circ$, $2\theta = 77,65^\circ$) were registered, these peaks are attributed to Au (111), Au (200), Au (220) and Au (311), respectively [254]. The fact that no peaks attributed to Au crystalline

structures were observed in XRD spectrum of the P*Si*/Au_(El.²⁰) sample leads to conclusion that the potential of 20 mV *vs* Ag/AgCl_(3 KCl) is not high enough to form Au layer with well-defined crystalline structures.

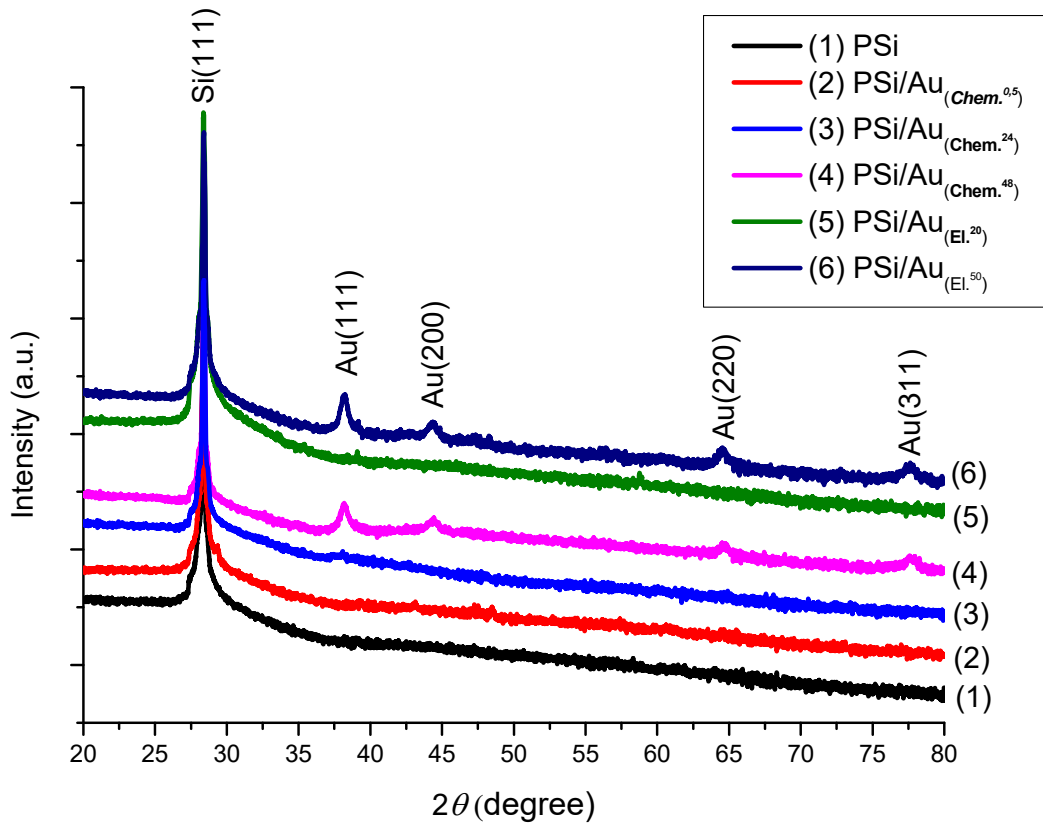


Figure 6.2. The XRD patterns of P*Si* and P*Si*/Au structures.

In P*Si*/Au_(El.⁵⁰) and P*Si*/Au_(Chem.⁴⁸) structures a mean size of Au nanocrystallites was determined from XRD data using Scherer's equation [256]:

$$D = \frac{0.94\lambda}{FWHM \cdot \cos(\theta)}, \quad (6.1)$$

where D is the average size of nanocrystallites, λ – the peak maximum of X-ray wavelength, $FWHM$ – the width at half maximum of the XRD peaks registered at θ degree.

Calculated average size values of Au nanocrystallites in the P*Si*/Au_(Chem.⁴⁸) and P*Si*/Au_(El.⁵⁰) structures were equal to 13.0 ± 2 nm and 13.7 ± 4 nm, respectively. The average size of Au nanocrystallites was almost the same in both fabricated structures.

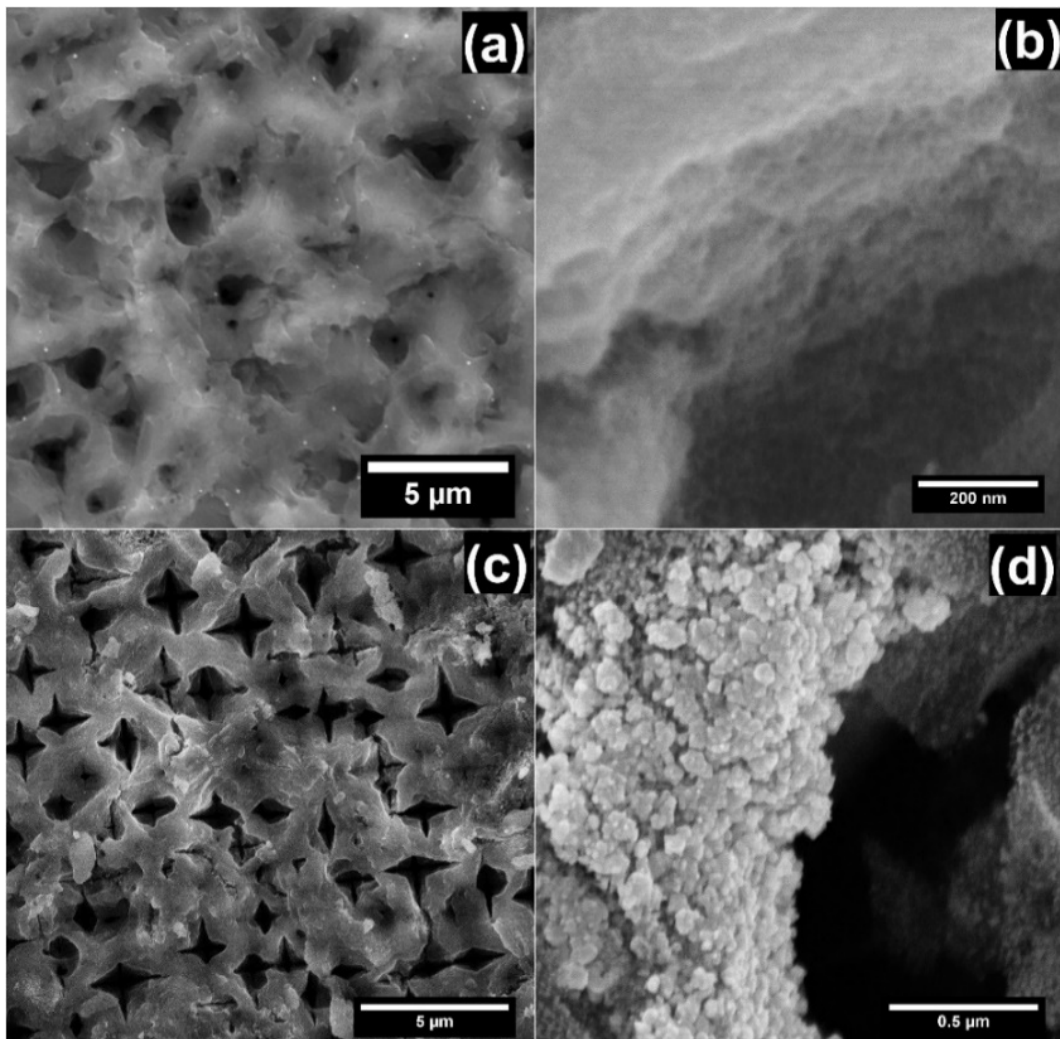


Figure 6.3. Top-view SEM images of PSi (111) structure (a,b); PSi/Au_(Chem.20) structure (c), PSi/Au_(Chem.48) structure (d).

Figure 6.3 represents the ‘top-view’ SEM images of the PSi/Au_(Chem.) and PSi/Au_(EL.) structures. Pores of 2 μm diameter are uniformly distributed on the PSi surface is observed (Figs. 6.3a and 6.3b). The ‘cross-sectional’ SEM view showed that the average thickness of the PSi layer was about 130 μm (Fig. 6.4a). Inner mesoporous structure of macropores with average pore diameter of 13-30 nm was revealed by high resolution SEM based visualization (Fig. 6.4b). Such mesoporous structure was formed due to competitive vertical and sidewall isotropic etching of the bulk Si substrate [223,224].

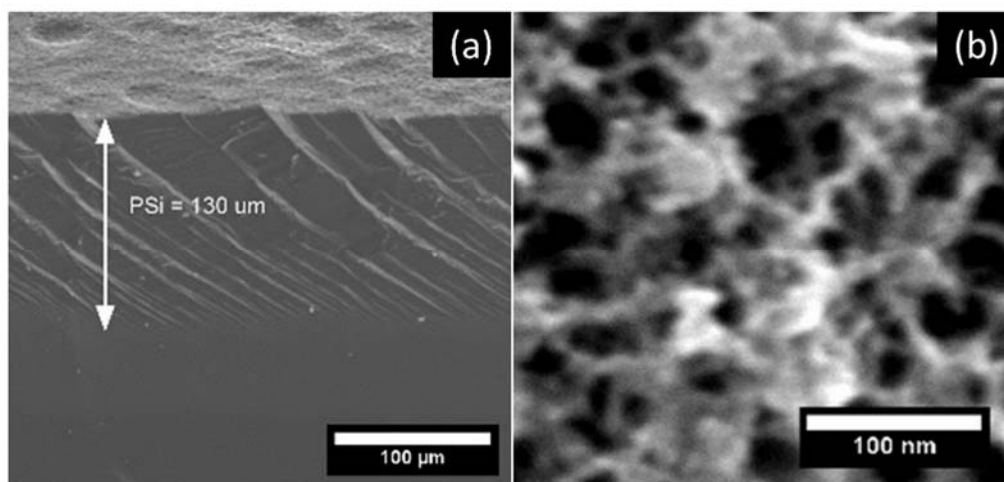


Figure 6.4. Cross-sectional SEM image of PSi layer (a) and SEM image of the inner structure of macropore (b).

SEM images of PSi/Au_(Chem.) structures are presented in Fig. 6.3c and 6.3d, which both reveals that the PSi substrates were well covered by gold layer that consisted of Au-based agglomerates of large surface with average size of 150 nm were uniformly distributed on the PSi surface (Figs. 6.3c and 6.3d). The SEM data are in good agreement with XRD data. In order to get crystalline Au-based structures on PSi longer duration of chemical deposition is required.

The formation of seed layer is a key factor of gold electrodeposition on PSi surface [257]. Gold nanoparticle formation using HAuCl₄, as an oxidation agent, and tannin as an reducing agent for chemical deposition process can be described by such chemical reaction [254]:

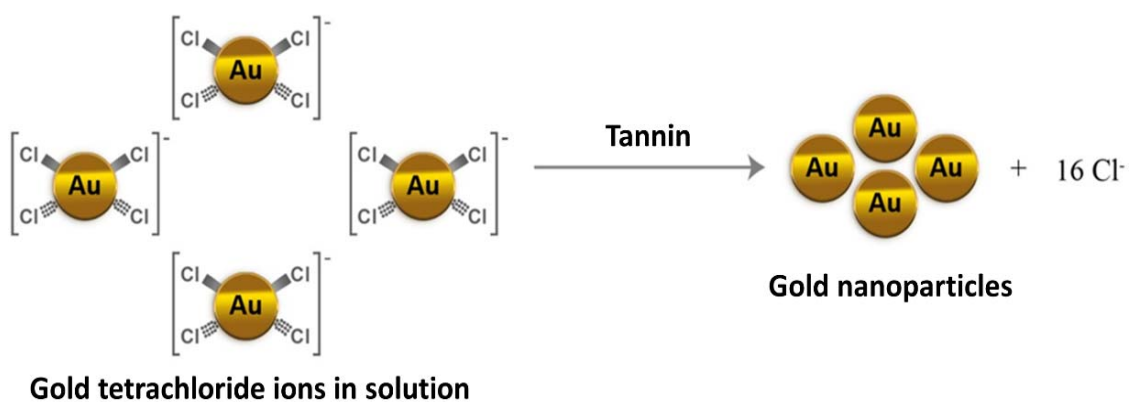
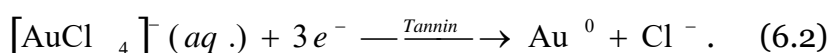


Figure 6.5. Complex ions AuCl₄⁻ reduction scheme.

Complex ion of $[\text{AuCl}_4]^-$ due to interaction with tannin is reduced to Au^0 during chemical deposition (Fig. 6.5). The initial phase of chemical deposition of Au layer is based on electrostatic interaction between $[\text{AuCl}_4]^-$ ions and PSi surface. If additional electrical field is applied during electrochemical deposition than the process of the gold nucleation/deposition is significantly facilitated by electrochemical reduction of $[\text{AuCl}_4]^-$.

6.3.2. Optical properties of Si, PSi and PSi/Au structures

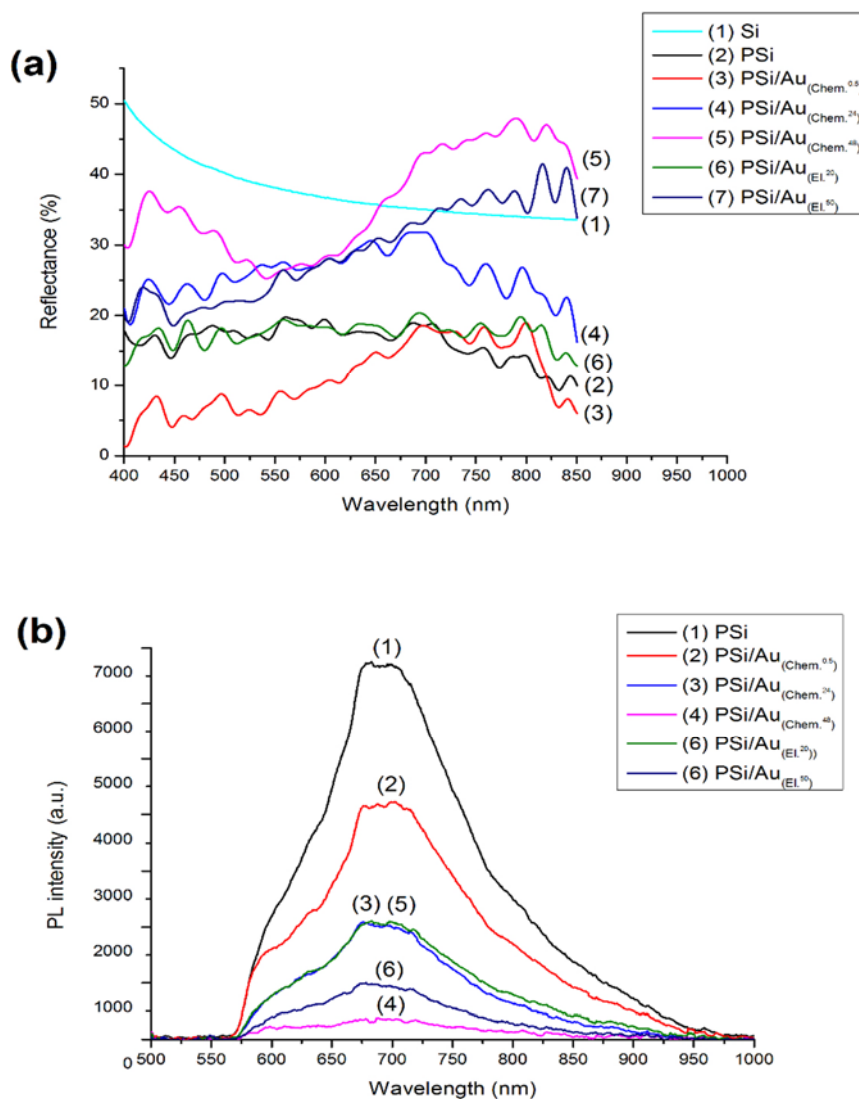


Figure 6.6. Reflectance spectra of Si, PSi and PSi/Au structures (a); The PL spectra of PSi and PSi/Au structures (b).

The main optical properties of Si, PSi and PSi/Au structures were studied by reflectance and photoluminescence (PL) spectroscopy. Figure 6.6a shows the absolute reflectance of fabricated PSi and PSi/Au structures in the wavelength range

of 400-850 nm. The optical reflectance of PSi decreases significantly comparing to polished Si surface. This result is consistent with that reported in previously published works [258,259]. The reflectance of PSi decreased by approximately 15% within the entire range of wavelengths due to the enhanced scattering and light absorption in the porous PSi. The total reflectance of the PSi/Au structures was lower or almost similar to that of PSi samples. While the reflectivity of PSi/Au structures increased especially in the range of 600-800 nm due to the gold layer formed on the PSi surface.

PL measurements were performed in order to assess the recombination ability of charge carriers at PSi/Au interface and to estimate the average size of Si nanocrystallites. In PSi/Au structure Au-based clusters are embedded within porous matrix of PSi therefore optical properties of PSi/Au are different from that of PSi due to additional scattering and/or SPR effect [248].

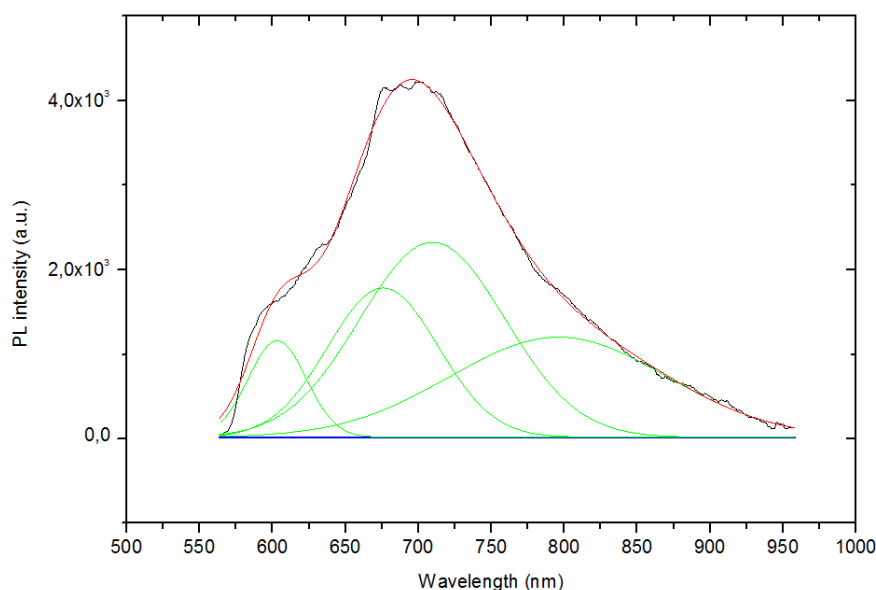


Figure 6.7. Deconvolution fitting of Au/PSi nanocomposite PL spectrum.

Figure 6.6b shows PL spectra of PSi and PSi/Au structures registered at room temperature. The PL emission band centered at 675 ± 5 nm (1.84 eV) was observed for PSi and PSi/Au nanostructures (Fig. 6.6b). It is clearly seen, that PL spectra had more than one emission line. The deconvolution of PL spectrum into single peaks by Gaussian fitting, which was performed using Origin 8.5 software, divided the PL spectrum into four distinct peaks at 600, 675, 710 and 790 nm (Fig. 6.7). Red emission of PSi is related to the quantum confinement of electrons within Si

nanocrystallites (nc) [260], therefore we suppose that a size distribution of Si nanocrystallites (nc-Si) in the PSi layer was significant. The average size of nc-Si was calculated by the following equation [229]:

$$E(\text{eV}) = E_g + \frac{h^2}{8d^2} \left[\frac{1}{m_e^*} + \frac{1}{m_h^*} \right], \quad (6.3)$$

where $E(\text{eV}) = 1.84 \text{ eV}$, $E_g = 1.12 \text{ eV}$, h - Planck's constant, $m_e^* = 0.19m_0$; $m_h^* = 0.16m_0$, $m_0 = 9.1 \times 10^{-31} \text{ kg}$. The calculated average diameter of nc-Si was in the range of 2,5 nm corresponding to the values obtained by other authors [229,260].

The main peak of PL in PSi/Au structures remains at the same position $675 \pm 5 \text{ nm}$ (Fig. 6.6b). This picture illustrates that the PL intensity of PSi/Au structures decreases gradually depending on the thickness of deposited Au layer. Such decrease of PL according to de la Mora et al. [125] is based on three main factors: porosity, chemical surface modification, and plasmonic effects. All these factors are increasing the efficiency of PL quenching in PSi/Au nanocomposites compared to that of PSi and pristine Si substrate. Moreover it is well known that the oxidation of PSi leads to an increase of intensity and a blue shift of the PL peak [261]. In the observed PL spectra of PSi and PSi/Au structures both the PL peak position and the shape of spectra are very similar. Therefore, the oxidation and chemical modification of the surface can be excluded from possible reasons, which are inducing changes in PL spectra. Thus, the most probably that in PSi/Au structures the PL quenching is mostly effected by surface plasmon resonance of Au nanolayer [28, 38]. The PL spectra of fabricated samples correlate with that reported in other researches where separated Au-nanoparticles were deposited on the PSi surface [262].

6.3.3. Determination of analytical characteristics of biosensors

During the evaluation of performance of biosensors based on PSi/Au(Chem.48)/protein-A/anti-AFB1 and PSi/Au(EL.50)/protein-A/anti-AFB1 structures the PL signal permanently decreased with an increase of the analyte concentration (Fig. 6.8a). If 100 ng/ml of AFB1 were present in the cell, then the PL intensity decreased almost twice. There is a relationship between the PL intensity (I) and the logarithm of AFB1 concentrations, which is expressed as a linear calibration curves (Fig. 6.8a): $I_{\text{PSi/Au(Chem.48)}} = 0.8 - 0.03 \lg(C)$, and $I_{\text{PSi/Au(EL.50)}} = 0.74$

$-0.08 \lg(C)$, respectively. The limit of detection (LOD) was determined using equation [230]:

$$LOD = 3.3\sigma/b, \quad (6.4)$$

where σ is the standard deviation in the presence of ‘negative control’ and b is the slope of the calibration curves (Fig.6.8a). The calculated values of LOD were about 2.7 ± 0.11 pg/ml and 2.1 ± 0.11 pg/ml for immunosensors based on PSi/Au_(Chem.48)/protein-A/anti-AFB1 and PSi/Au_(El.50)/protein-A/anti-AFB1 structures, respectively. These estimated values of LOD were much better than that for previously reported electrochemical biosensors based on DNA-apptamers [263].

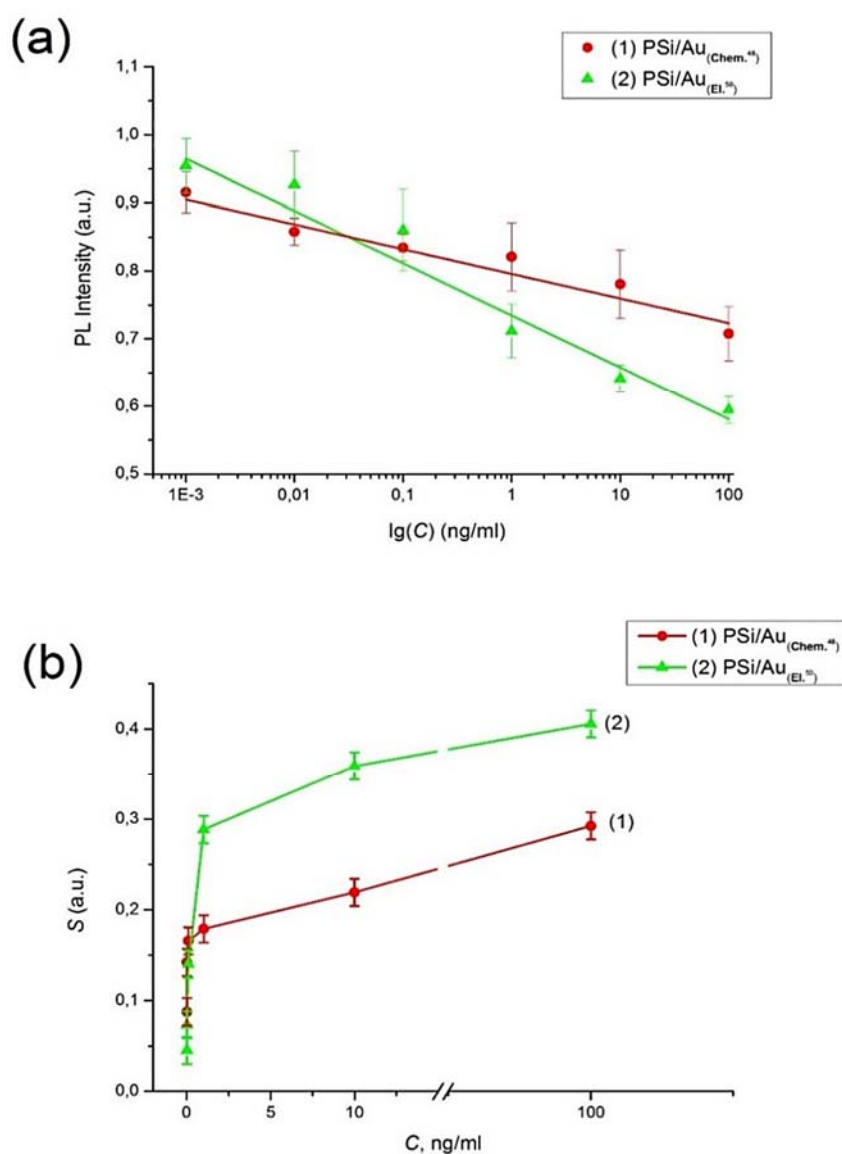


Figure 6.8. The dependence of PL intensity (a) and PL response of PSi/Au_(Chem.48) /protein-A/anti-AFB1 and PSi/Au_(El.50) /protein-A/anti-AFB1 structures on the logarithm of AFB1 concentration (b).

The immunosensor signal was normalized and the sensor response S was calculated according to this equation [210]:

$$S(C) = 1 - I_{eq}(C), \quad (6.5)$$

where I_{eq} is normalized signal value after the reaching of steady-state conditions at particular concentration (C) of AFB1.

The isotherms of interaction of AFB1 with PSi/Au_(Chem.48)/protein-A/anti-AFB1 and PSi/Au_(El.50)/protein-A/anti-AFB1 are plotted in the Figure 6.8b. The isotherm of PSi/Au_(El.50)/protein-A/anti-AFB1 sample has been saturated at high values of AFB1 concentrations. The isotherm of PSi/Au_(Chem.48)/protein-A/anti-AFB1 sample tended to increase in all range of the measured AFB1 concentrations. We suppose that the interaction of AFB1 occurred according to the first order kinetics, which is the most probable in the case when dissolved materials are adsorbing on the surface of interphase and/or interacting with specific molecules (in this particular case such molecules are anti-AFB1) immobilized on this surface [232,264]:

$$\frac{dN}{dt} = k_a \cdot c \cdot (N_s - N) - k_d \cdot N, \quad (6.6)$$

where N , k_a , k_d , N_s and C are a number of adsorbed molecules, association constant, dissociation constant, number of adsorption sites and concentration, respectively.

After some time, when steady-state conditions are achieved, then the equation becomes valid:

$$\frac{dN}{dt} = 0. \quad (6.7)$$

The adsorption isotherm was analyzed using Langmuir (eq. 6.8) and Langmuir-Freundlich (eq. 6.9) equations:

$$\theta = \frac{B \cdot C}{K_D + C}, \quad (6.8)$$

$$\theta = \frac{B \cdot C^n}{K_D^n + C^n}, \quad (6.9)$$

where $\theta = \frac{N}{N_s}$ is surface coverage, $K_D = \frac{k_d}{k_a}$ – affinity dissociation constant and n – power coefficient, pointing to interaction between AFB1 and surface ($n < 1$). The analysis of the adsorption isotherms (Fig. 6.9a,b) better fitted when Langmuir-Freundlich equation was applied for the evaluation of the data. The calculated values of n and K_D are shown in the Table 6.2. According to here presented calculations, the power coefficient n for the interaction of AFB1 with PSi/Au_(EL.50)/protein-A/anti-AFB1 structures was determined to be around 0.5. Such low power coefficient could be related to limited diffusion of AFB1 within advanced surface structures of PSi/Au surface. The power coefficient for the interaction of AFB1 with PSi/Au_(Chem.48)/protein-A/anti-AFB1 structure was equal 0.25. Such relatively low power coefficient most probably is related to more limited diffusion of AFB1 within advanced surface structures of PSi/Au_(Chem.48) surface.

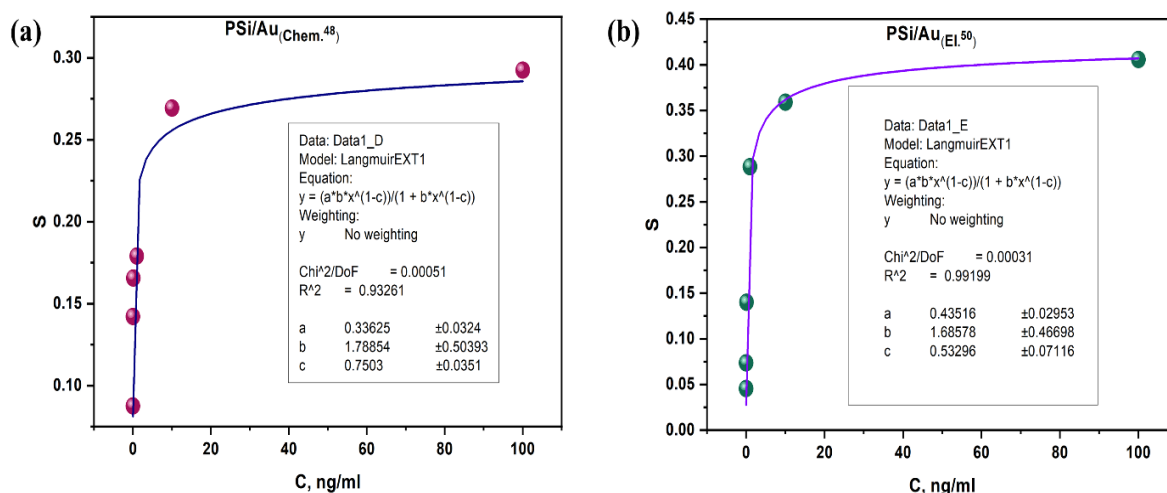


Figure 6.9. Fitting of the biosensor isotherms with Langmuir-Freundlich equation.

Table 6.2. Registered characteristics of interaction between AFB1 and different structures.

Sample abbreviation	n	K_D , M	ΔG , kJ/mol
PSi/Au _(Chem.48) /protein-A/anti-AFB1	0.25±0.04	3.1·10 ⁻¹⁰ ±0.22·10 ⁻¹⁰	-54.6±2.3
PSi/Au _(EL.50) /protein-A/anti-AFB1	0.47±0.07	1.1·10 ⁻¹⁰ ±0.15·10 ⁻¹⁰	-51.5±2.0

The interaction between AFB1 and anti-AFB1 and/or surface could be estimated by calculation of the Gibbs free energy (ΔG) using this equation [232,264]:

$$\Delta G = -R \cdot T \cdot \ln(K_{D0}), \quad (6.10)$$

where T and R are absolute temperature and universal gas constant, respectively. The value of K_{D0} was calculated as:

$$K_{D0} = \frac{K_D}{C}, \quad (6.11)$$

where C is an AFB1 concentration equal to 1M.

According to the data, reported in Table 1, the toxin molecules showed more efficient adsorption onto the surface of PSi/Au_(Chem.48)/protein-A/anti-AFB1 in comparison to PSi/Au_(El.50)/ protein-A/anti-AFB1 structures. The binding energy between AFB1 and to PSi/Au_(El.50)/ protein-A/anti-AFB1 surface was lower in comparison with that of between AFB1 and PSi/Au_(Chem.48)/protein-A/anti-AFB1.

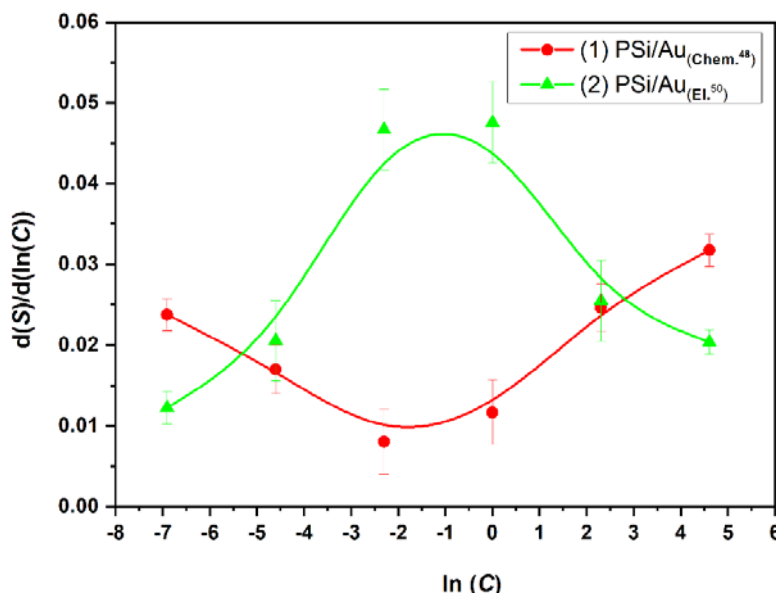


Figure 6.10. Sensitivity of PSi/Au_(Chem.48)/protein-A/anti-AFB1 and PSi/Au_(El.50)/protein-A/anti-AFB1 structures towards different concentrations of AFB1.

Sensitivity of the biosensors was calculated as derivative of sensor signal (S) versus natural logarithm of the toxin concentration (C). According to equation (6.9), a dimensionless value of sensitivity was obtained after differentiation. The obtained results are shown in the Figure 6.10. The sensitivity of PSi/Au_(El.50)-based samples showed maximum in the range of AFB1 concentrations 0.1-1 ng/ml. The sensitivity of PSi/Au_(Chem.48)-based samples showed minimum in the range of AFB1 concentrations 0.1-1 ng/ml and contentious increase at higher AFB1 concentrations. Analysis of the sensitivity was performed via estimation of full width of half maximum of the obtained curve. PSi/Au_(El.50)/protein-A/anti-AFB1 structures

showed the highest sensitivity to AFB1 in the range of 0.01-10 ng/ml. We have not performed testing of PSi/Au_(Chem.48)/protein-A/anti-AFB1 structures towards higher concentrations of AFB1. However, we can suppose that the lower sensitivity limit of PSi/Au_(Chem.48)/protein-A/anti-AFB1 structures starts in the range 1-5 ng/ml and the upper limit is over 100 ng/ml of AFB1 concentration. It is worth to mention that an average value of response time, which was calculated when 95% saturation of the analytical signal was observed, significantly decreased for PSi/Au_(Chem.48)/protein-A/anti-AFB1 (21 min) and PSi/Au_(El.50)/anti-AFB1 (18 min) structures. Thus, the deposition of Au layer within pores of PSi by electrochemical method resulted in the increase of sensitivity and the reduction of response time of PSi/Au_(El.50)/anti-AFB1 immunosensors to AFB1 molecules.

6.4. Conclusion

Novel PSi/Au structures were formed by chemical and electrochemical methods and they were applied in the design of PL-based immunosensors dedicated for the detection of AFB1. The morphology, chemical composition and optical properties of PSi and PSi/Au structures were evaluated. We observed clear decrease of the PL intensity PSi/Au/protein-A/anti-AFB1 structures with the increase of AFB1 concentration in samples. Such PL change has been used as analytical signal. Analytical characteristics of biosensors based on several different PSi/Au/protein-A/anti-AFB1 structures were evaluated and partially optimized. The calculated values of LOD were about 2.5 ± 0.5 pg/ml. Langmuir-Freundlich isotherms were plotted for the interaction of AFB1 with PSi/Au/protein-A/anti-AFB1 structures and some aspects of interaction mechanisms were determined. We have shown that formation of Au-based structures within pores of PSi by electrochemical method resulted in increase of sensitivity and decrease of response time of the immunosensors. Analytical performance of the Au/PSi immunosensor showed very good characteristic with maximal sensitivity range within 0.01-10 ng/ml. Comparing to the standard ELISA method, here proposed Au/PSi immunosensor has about 100 lower concentration range. PSi/Au/protein-A/anti-AFB1 structures show very promising properties suitable for PL-based immunosensors.

Publication III

The content of this chapter has been already published in Materials Science and Engineering: C Journal

Materials Science and Engineering: C, Volume 118, 2021, 111401, ISSN 0928-4931, doi.org/10.1016/j.msec.2020.111401.

Authors: **Valerii Myndrul**, Emerson Coy, Mikhael Bechelany, and Igor Iatsunskyi

7. Photoluminescence label-free immunosensor for the detection of Aflatoxin B1 using 1D ZnO/polyacrylonitrile nanofibers

7.1. Introduction

Mycotoxins are dangerous secondary metabolites produced by some organisms from the kingdom fungi. Generally, they can be released to the foodstuff during the fungi growth, especially in humid and warm conditions [265,266]. Moreover, they have been classified as possible carcinogens and immunosuppressive agents [267,268]. Therefore, precise control and detection of mycotoxins in human and animal rations can help to avoid their negative influence on the general health.

Despite the thorough monitoring of mycotoxin levels in food and beverages within the European Union, contaminated foodstuffs still have been delivered to the customers. Adegbeye et al. have reported on the current situation of foodstuff contamination by mycotoxins, and indeed it takes place worldwide, especially in the developing countries [269]. Furthermore, Global Climate Change could promote the spread of mycotoxins in Europe [269].

Among different mycotoxins, Aflatoxin B1 (AFB1) has been found to be one of the most food-contaminating toxins [270]. Being in the human liver, AFB1 stimulates cellular metabolism to generate high levels of reactive oxygen species (ROS) and free radicals. Such conditions lead to cell death, hepatotoxicity and initiate human hepatocellular carcinoma [271]. Based on the mentioned above, it is important to develop a high-sensitive and simple approach for AFB1 detection.

Traditional approaches for AFB₁ detection, such as chromatography methods, have a high sensitivity and specificity, but they require an expensive equipment and specially trained staff, which increase the costs of analysis [272,273]. Moreover, AFB₁ detection usually requires additional secondary labeled antibodies that makes this approach more complicated and expensive [265]. Due to the small size of AFB₁ molecules, it can be even undetectable by the Surface Plasmon Resonance based approach (SPR), which is considered to be the most sensitive label-free techniques. In order to solve this problem the “weighting agents” such as bovine serum albumin (BSA) has been used [274]. However, BSA weighting agents can adversely affect detection selectivity; therefore, the use of highly selective receptors (for example, nanobodies against AFB₁) is preferred over the AFB₁-BSA using [275]. Besides, a very limited number of studies represented a general mechanism for AFB₁ detection that may clarify the behavior and response during the AFB₁ binding. The well-studied mechanism of detection will clarify the nature of the “detection platform-AFB₁” interaction. Therefore, the major challenge is to develop a high-sensitive biosensing platform and/or a detection approach with a significantly reduced cost, when compared to traditional methods, and with a relative simplicity for application.

Among different types of biosensor transducers, the optical ones are small size, portable, and high precision devices. Currently, optical transducers have been successfully used in SPR, surface-enhanced Raman spectroscopy (SERS), reflectance, and photoluminescence (PL) biosensors [276]. Among optical transducers, PL - based biosensors are considered to be one of the most promising approaches, but stable, efficient and environment-friendly transducers are still required [277]. The change in the PL signal (e.g. relative PL intensity, the shape of PL curve) of semiconductors, as a function of the analyte concentration, can be used as an indicator for the detection of target molecules by the probe. The PL of semiconductors is very sensitive to small modifications of their surface (e.g. absorption of molecules on the surface) that enables to distinguish analyte concentration changes [278–284].

Nanostructured zinc oxide (ZnO) is the one of most attractive materials for PL biosensors due to high active surface area, strong room-temperature (RT) PL in the UV/VIS range [285], and high isoelectric point/IEP (pH = 9) suitable for the direct immobilization of low IEP acidic proteins or DNA via electrostatic interaction [286].

ZnO – based PL biosensors have been successfully applied for the detection of *Salmonella* [210], Ochratoxin A [281], and for the protein–protein biorecognition, etc. [283,285]. Recent discoveries show that the morphology and structural properties of ZnO are crucial for the efficient biosensor performance [287,288]. The comparison analysis of the ZnO surface topography (nanoparticles (NPs), nanorods (NRs), nanosheets (NSs) and nanobeams (NBs)) on the protein adsorption process showed that 1D ZnO nanostructures provided a higher number of surface adsorption sites [287,288]. Thus, to enhance the sensitivity of ZnO based biosensors, a high surface-to-volume ratio, such as the one present in a 1D structure, is needed.

Recently, it was proposed a novel approach to produce 1D ZnO nanostructures with a high surface architecture. This approach is based on the combination of two experimental techniques: electrospinning and atomic layer deposition (ALD) [154,155]. Electrospinning is a low-cost powerful technique, which can produce 1D organic or polymer nanofibers [289]. Electrospinning deposited 1D organic nanofibers, such as collagen, polyacrylonitrile (PAN), polylactic acid (PLA), gelatin, collagen, hyaluronic acid (HA) are widely used in tissue engineering and medicine as 3D scaffolds for cell growing [290]. At the same time, these nanofibers can be a template for PL biosensors via ALD coatings with a photonic material (e.g. ZnO based coatings). It is known that, ALD is one of the most versatile methods for fabrication of ZnO nanostructures [291]. It does not depend on the substrate geometry and can be applied for both planar samples, and porous media at relatively low temperatures [292,293]. This method provides a conformal coating of the substrate and allows the control of thickness and chemical composition of the deposited layers. In recent works, it was also demonstrated that 1D PAN/ZnO nanofibers produced by this approach can be used as an effective PL biosensor for volatile organic compounds (VOC) [154]. However, there are still several questions need to be solved: (i) what are the mechanisms for PL detection in ZnO; and (ii) is it possible to use this nanocomposite for mycotoxin (AFB₁) detection.

In the present study, we report on the development of 1D PAN/ZnO nanocomposites that can be applied for a low-cost, label-free and sensitive PL biosensor (immunosensor) towards AFB₁ as a model molecule. As a biorecognition layer, the antibody towards AFB₁ (anti-AFB₁) has been chosen. Structural and optical properties of the fabricated PAN/ZnO nanocomposites have been investigated by scanning electron spectroscopy (SEM), transmission electron microscopy (TEM), X-

Ray diffraction analysis (XRD), Fourier-transform infrared spectroscopy (FTIR) and confocal microscopy. The PL of PAN/ZnO nanocomposites functionalized with the anti-AFB₁, as well as the control samples (without anti-AFB₁), was measured for different concentrations of AFB₁. It was found that high surface to volume ratio of PAN/ZnO nanocomposites and high affinity of immobilized anti-AFB₁ to AFB₁ give the possibility of detecting AFB₁ in a wide sensitivity range 0.1-20 ng/ml and with detection limit (LOD) of 39 pg/ml. Furthermore, estimated values of power coefficient, and change of Gibbs free energy indicate strong electrostatic interaction between biosensor and the analyte (AFB₁). The general mechanism of the PL biosensor response change during the PAN/ZnO/APTES/GA/Anti-AFB₁&AFB₁ complex formation was proposed. Hereby, we propose a novel PL-based approach for AFB₁ detection on PAN/ZnO/APTES/GA/Anti-AFB₁ structure.

7.2. Experimental section

7.2.1. Materials

Polyacrylonitrile PAN (M_w = 150 000), and dimethylformamide (DMF) (ACS reagent, ≥99.8%) were purchased from Sigma Aldrich. Diethyl zinc (DEZ) (Zn(CH₂CH₃)₂, 95% purity, CAS: 557-20-0), was purchased from Sterm Chemical. Anti-AFB₁ monoclonal antibodies (1 mg/ml, mouse IgG1 isotype, N^o A9555), AFB₁ (2 μg/ml in acetonitrile, analytical standard, N^o34029), Protein A (N^o P3838), BSA, (purity ≥98.0%, N^o 05470), (3-Aminopropyl)triethoxysilane (APTES, purity ≥98%), and glutaraldehyde (GA, 50 wt. % in H₂O) were purchased from Sigma Aldrich. Phosphate-buffered saline (PBS, pH 7.4) was used as the diluent for AFB₁ dissolution. All biological components were diluted on the day of the experiment (without additional storage in dissolvent).

The quartz microfluidic cell (useable optic range: 170-2700 nm, v = 600 microliters, w = 8 mm, d = 2 mm, h = 40 mm) was purchased from Starna Cells. The diameter of the inlet and outlet tubes was 0.9 mm (inner diameter: 0.36 mm).

7.2.2. PAN fiber fabrication

Polyacrylonitrile (10 wt% PAN) was dissolved in DMF. The polymer solution was kept under stirring for 1 h with the following heating in an oil bath at 80 °C for 10 min. A home-made electrospinning machine with HPx 600 605 generator (physical instruments) and a KDS 100 syringe pump was used for the electrospinning

deposition process. The solution was electrospun under an applied voltage of 25 kV with a flow rate of 3 mlh⁻¹ using a 0.7 mm diameter syringe (connected to the positive output of the generator) in ambient air atmosphere. The collector, made of aluminum foil was fixed at the distance of 25 cm from the tip of the syringe and was connected to the negative output of the generator. The liquid was extruded from the spinneret to produce a pendant droplet that followed the Taylor cone formation due to the electrostatic repulsion among the surface charges upon electrification. The charged jet underwent stretching and thinning under the whipping instability and solidifies quickly into a fiber with tailored diameter.

7.2.3. ALD of ZnO

ZnO thin layers were deposited over the PAN nanofibers by a home-made ALD set-up at 100°C and sequential exposures to diethyl zinc (DEZ) and deionized water, separated by a purge with dry Argon (flow rate of 100 sccm). The deposition protocol included the following steps: i) 0.3 s pulse of DEZ, 30 s exposure and 50 s purge with dry Ar; ii) 2 s pulse of H₂O, 40 s of exposure, and 60 s purge with dry Ar. The growth rate was generally 2.1 Å/cycle for ZnO. The ZnO thickness growth per cycle was controlled by measuring the ZnO film's thickness on planar Si substrates placed in the reactor and proved by transmission electron microscopy on PAN nanofibers. After the ALD of ZnO over the PAN nanofibers were obtained, samples with different ZnO thicknesses were obtained: PAN/ZnO_{5nm}, PAN/ZnO_{10nm}, PAN/ZnO_{20nm}, PAN/ZnO_{50nm}.

7.2.4. Characterization techniques

Morphology of the PAN/ZnO nanocomposite surface was investigated by scanning electron microscopy (SEM) (JEOL, JSM7001F) with an energy dispersive X-ray (EDX) analyzer and transmission electron microscopy (TEM) (JEOL ARM 200F) high-resolution transmission electron microscope (200 kV) with an EDX analyzer. The structural state of PAN/ZnO was analyzed by means of X-ray diffraction (XRD) (PANalytical, X'pert³pro MRD diffractometer) working with a Cu lamp ($\lambda = 1.5418$ Å). The Fourier-transform infrared (FTIR) spectra were obtained with the Jasco FT/IR 4700 – Fourier Transform Infrared Spectrometer. Photoluminescence was generated by a He-Cd laser (325 nm) and the emission spectra were recorded in the range from 360 to 800 nm by Ocean Optics Spectrometer USB4000. Two-photon laser fluorescence confocal microscopy (Zeiss LSM 780, the Coherent Chameleon

laser with an excitation wavelength of 700 nm) was used to study the real-time PL during AFB1 adsorption.

7.2.5. The evaluation of PL signal of immunosensor

To prepare the biorecognition layer, the immobilization of antibodies toward AFB1 (anti-AFB1) was accomplished by the protocol described in the reference [278]. Briefly, the PAN/ZnO_{20nm} samples were functionalized by APTES, and then, after GA activation, anti-AFB1 were conjugated to the surface. Finally, the Bovine BSA PBS solution was added to block the remaining active sites and to improve the selectivity of the biosensor. As a result, PAN/ZnO_{20nm}/APTES/GA/Anti-AFB1 structure was formed.

It also was supposed to add the Protein A (Prot.A) during the functionalization process to achieve oriented Anti-AFB1 immobilization, however, this step does not lead to the correct PAN/ZnO_{20nm}/APTES/GA/Prot.A/Anti-AFB1 assembly. The possible reason for the incorrect assembly can be associated with the weak binding affinity of Prot.A to anti-AFB1 antibodies [294].

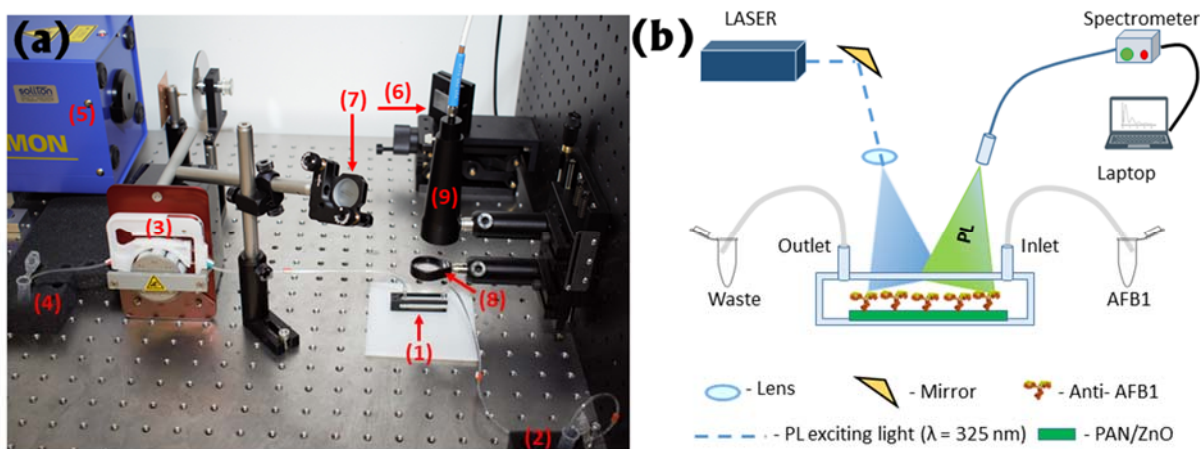


Figure 7.1. Photography of the experimental set-up, where (1) - microfluidic cell with tubes; (2) - AFB1 sample; (3) - peristaltic pump; (4) - AFB1 waste; (5) - laser; (6), (7) and (8) - system of mirrors and lens, (9) - light collector (a). Scheme of the experimental set-up for the PL – based AFB1 detection on PAN/ZnO_{20nm}/APTES/GA/Anti-AFB1 structure (b).

Analytical characterization of the biosensor based on PAN/ZnO_{20nm}/APTES/GA/Anti-AFB1 structures was performed in a microfluidic cell (Fig. 7.1.a,b) with the analyte flow rate about 37 ml/min. The cell was equipped with an inlet and outlet for analyte infusion. PL was excited with He-Cd ($\lambda = 325$ nm) and collected by optical fiber spectrometer using multimode optical fibers

equipped with semispherical lenses. An output laser power was around 1-2 mW. Before measurements, 600 microliters of buffer solution were pumped through the cell by using a peristaltic pump. The PL spectra of the sample were collected every 10 s. The sample was stored in a buffer solution until the PL signal reached equilibrium. Then, 600 microliters of various AFB1 concentrations were subsequently infused to the cell via pumping.

7.3. Results and discussion

7.3.1. Structural and optical properties

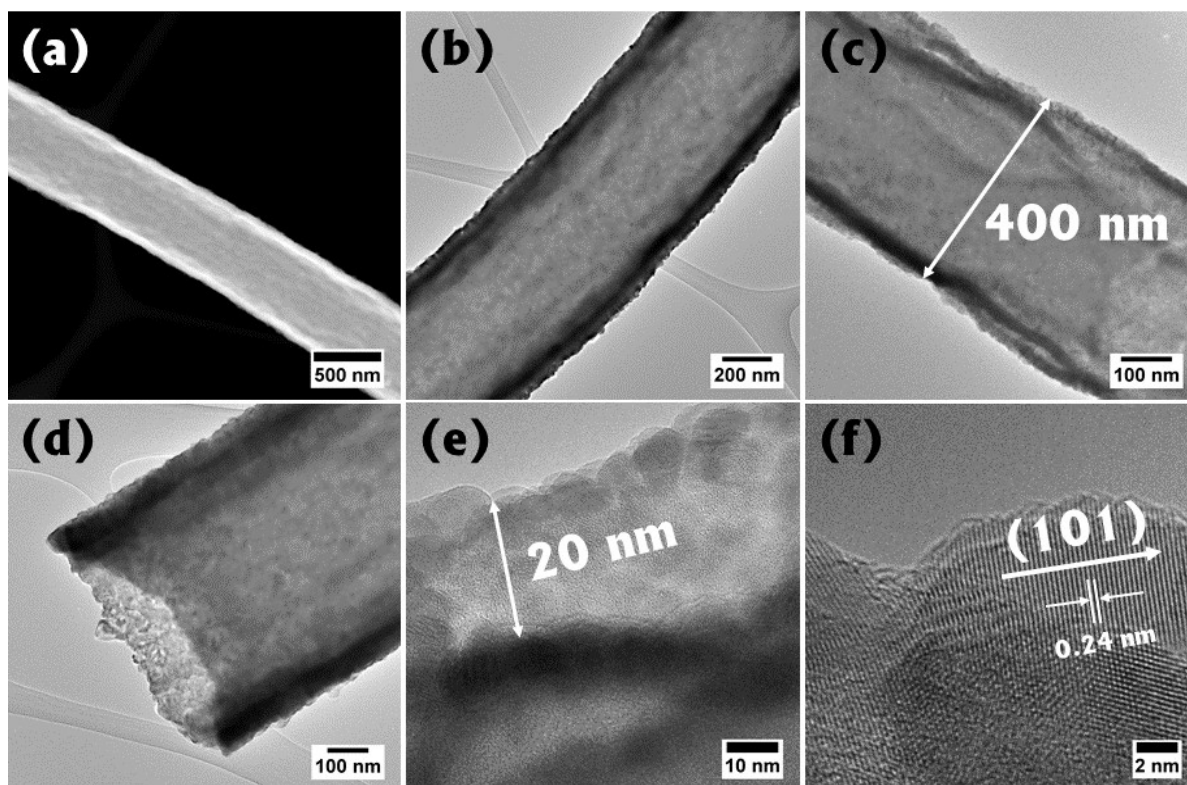


Figure 7.3. TEM images of PAN/ZnO nanofibers: ZnO layer 20 nm (c, e, f); ZnO layer 50 nm (a, b, d).

In order to investigate the structure, surface morphology and optical properties of fabricated PAN/ZnO nanofibers with different ZnO thicknesses, SEM, TEM, XRD, EDX, and PL analysis were performed. Figure 7.2 shows SEM images of PAN/ZnO nanocomposites with different numbers of ALD cycles (25 to 250) corresponding to different layer thicknesses. It was confirmed that applying both techniques one was able to produce PAN/ZnO nanofibers with tuned structural parameters and optical properties [155]. Figures 7.2 (a-c) indicate the solid “spaghetti-like” morphology with an average fiber diameter of 500 nm. Figures 7.2 (d-f) show the crystalline

structure of ZnO layers with the visually evaluated crystallites with the size around 15-30 nm. Moreover, Figure 7.2d indicates the core-shell structure with a clear border between the core (PAN polymer) and the shell (ZnO crystalline layer).

In order to confirm the ZnO conformal layer TEM experiments were conducted. Figure 7.3 shows the TEM images of PAN/ZnO nanofibers: PAN/ZnO_{50nm} (Fig. 7.3 (a,b,d)) and PAN/ZnO_{20 nm} (Fig. 7.3 (c,e,f)). The TEM image (Fig. 7.3a) shows a uniform fiber with the conformal ZnO layer. TEM images (Fig. 7.3 (a-c)) show the single fibers with an approximate diameter of 400-500 nm. Figures 7.3(d-f) shows the crystalline structure of the ZnO layer over PAN fiber with an average crystallites size of about 10-15 nm. Besides, Figure 7.3f represents (101) lattice plane with the interplanar distance of 0.24 nm suggest the stabilization of the wurtzite phase of ZnO. High-resolution TEM proves the polycrystalline nature of produced ALD ZnO layers for all samples.

To confirm the crystalline phase of the obtained PAN/ZnO nanofibers, XRD analysis has been also performed (Fig. 7.4a). The peaks at $2\theta = 31.74^\circ$ (001), $2\theta = 34.42^\circ$ (002), $2\theta = 36.22^\circ$ (101), and $2\theta = 47.53^\circ$ (102) confirm ZnO wurtzite structure [154]. The XRD peak at $2\theta = 17^\circ$ directly corresponds to PAN fiber [154]. It is clearly seen that the crystallinity of the PAN/ZnO_{5nm} structure is weak and the ZnO coverage which is attributed to the small amount of material, the miss orientation of the fibers towards the bragg-brentano condition and the polycrystallinity of the films.[295]. With the growth of the ZnO layer from 10 to 50 nm, the crystallinity of the structure is increasing, which allows to estimate the average size of ZnO nanocrystallites the Debye–Scherrer’s equation [296]

$$D = \frac{0,9 \cdot \lambda}{\beta \cdot \cos(\theta)}, \quad (1)$$

where β , θ , and λ are full width of half maximum, diffraction angle, and x-ray wavelength ($\lambda = 0.154$ nm), respectively. The calculated average size of ZnO nanocrystallites was about 9 ± 2 nm for all samples what in agreement with the TEM measurements.

Furthermore, EDX mapping of a single PAN/ZnO nanofiber (Fig. 7.4b) indicate the oxygen and zinc content and distribution on the ZnO shell, while the carbon content attributed the PAN fiber, remains at the fiber’s core. Besides, this mapping confirms that Zn and O are homogeneously dispersed.

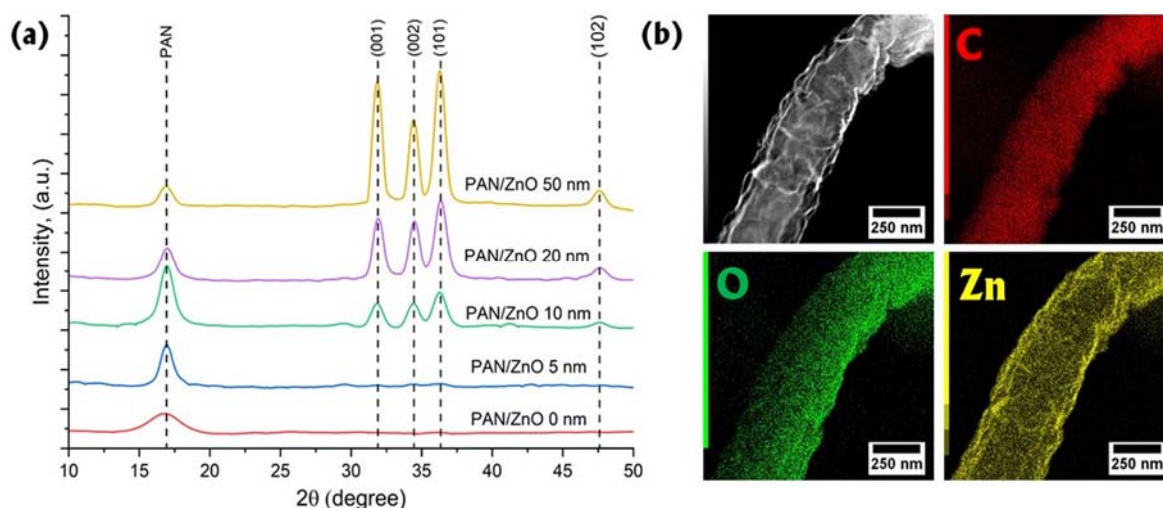


Figure 7.4. XRD spectra of the obtained PAN/ZnO nanofibers (a) and EDX mapping of the single nanofiber with ZnO layer thickness 20 nm (b).

The PL spectra of PAN/ZnO nanofibers are shown in Figure 7.5a. The narrow peak in the ultraviolet (UV) region (375 ± 5 nm) corresponds to the near band emission (NBE) [152,154]. This band can also be interpreted by the emission (3.34 eV) of free excitons (FE) in the bandgap of ZnO nanocrystallites [210]. The broad peak in the visible range around 565 nm corresponds to the deep defect levels (DLE) such as zinc vacancies (Zn_i^{++}), single (V_o^+) and double (V_o^{++}) ionized oxygen vacancies, neutral oxygen vacancies (V_o), and oxygen interstitials (O_i) [297]. The deconvolution of DLE emission (Fig. 7.5b) reveals three general types of defects involved in the green-blue PL process: V_o^+ (2.45 eV), V_o^{++} (2.23 eV), O_i (2 eV) (inset Fig. 7.5b) [152,298]. The peak around 785 nm attributes to the residual PL emission of PAN nanofibers. The decrease of PL in the visible region upon increasing the thickness of the ZnO layer can be explained by the improvement of the crystallinity of semiconductor and thus, the reduction of defect concentration [299]. However, the low UV emission and high DLE to NBE ratio indicate the high defects concentration within the ZnO structure [152,210].

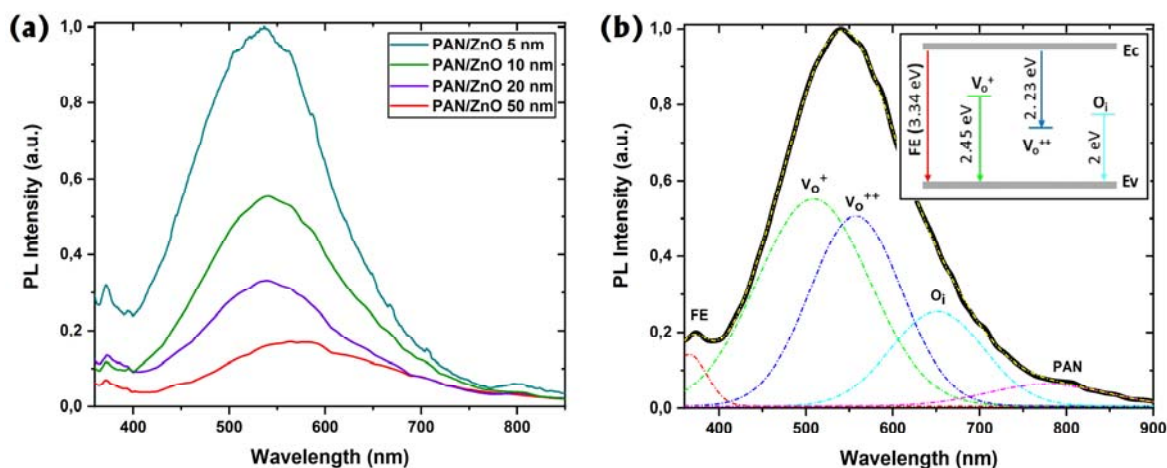


Figure 7.5. PL spectra of PAN/ZnO nanofibers with different thicknesses of ZnO layer (a) and PL deconvolution with Gaussian function; inset - possible optical transitions and their energies in ZnO nanostructures, where free excitons (FE), single ionized oxygen vacancies (V_o^+), double ionized oxygen vacancies (V_o^{++}), and oxygen interstitials (O_i) (b).

Taking into account the findings from PL analysis, and to achieve a stable, reliable, and repeatable results for the developed PL biosensing platform, it was decided to use PAN/ZnO nanofibers with an oxide layer of 20 nm that is capable of providing the conformal coverage over the PAN, relatively high PL emission and the stable biorecognition layer.

7.3.2. Biofunctionalization of PAN/ZnO

It is important for biosensors to detect selectively the target molecules while the remaining molecules must not affect the sensor's response. In order to achieve the selective adsorption of AFB1 to the PAN/ZnO surface, the bioselective (biorecognition) layer containing Anti-AFB1 was formed along the step-by-step biofunctionalization process (Fig. 7.6a). The blank PAN/ZnO_{20nm} nanofibers during the silanization (APTES treatment) process and GA activation were prepared for conjugation with the Anti-AFB1. The detailed biofunctionalization protocol was as follows: i) to achieve the thin APTES layer which acts as a coupling agent between the PAN/ZnO_{20nm} and Anti-AFB1, nanofibers were treated by 10 μ l of 2% APTES solution in Ethanol (99.9%) at room temperature (RT) for 10 min. Then the sample was gently washed with Ethanol (99.9%) with the following drying on a hot plate at 85 °C for 1 hour. ii) At the next step, PAN/ZnO_{20nm}/APTES samples were immersed in a 1% GA water solution (at RT for 1 h) to activate APTES modified surface. Subsequently, the PAN/ZnO/APTES/GA was rinsed with DI water to avoid non-specific adsorption of the Anti-AFB1. iii) The GA-activated surface was then reacted

with 10 μl of 50 $\mu\text{g}/\text{ml}$ Anti-AFB1 solution in PBS buffer (pH 7.4) at RT for 30 min to form a bioselective layer of anti-AFB1. Then, PAN/ZnO/APTES/GA/Anti-AFB1 was rinsed with PBS to wash out non – conjugated antibodies. iv) 10 μl of 5 $\mu\text{g}/\text{ml}$ of BSA was added to block the remaining active sites that enable adsorb proteins. v) As a result, PAN/ZnO_{20nm}/APTES/GA/Anti-AFB1 was formed.

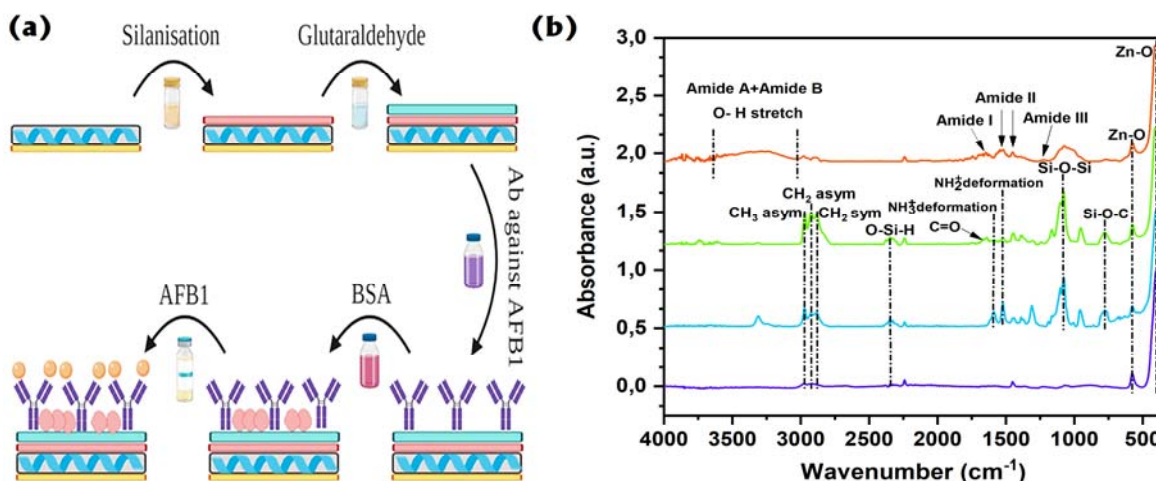


Figure 7.6. Step by step biofunctionalization process (a) and FTIR spectra of the following biofunctionalization stages: dark blue – bulk PAN/ZnO_{20nm} sample; bright blue line – PAN/ZnO_{20nm}/APTES; green – PAN/ZnO_{20nm}/APTES/GA; red line – PAN/ZnO_{20nm}/APTES/GA/Anti-AFB1 (b).

To confirm the biofunctionalization of PAN/ZnO_{20nm} nanofibers by APTES, GA, and Anti-AFB1 a series of FTIR measurements were performed (Fig. 7.6b). The peak at 480 cm^{-1} is attributed to an electronic transition to deep surface states that originated from defects (oxygen vacancies) in the ZnO layer [300]. The significant changes have appeared in the FTIR spectrum when the silanization process is done. Peaks from the Si-O-C (777 cm^{-1}), Si-O-Si (1078 cm^{-1}), NH₂ (1529 cm^{-1}), NH₃ (1596 cm^{-1}), O-Si-H (2341 cm^{-1}), and, CH₂ (2878-2931 cm^{-1}) and CH₃ (2977 cm^{-1}) groups indicate the formation of APTES layer. The GA-activation of APTES modified nanofibers results in appearing of peaks at 1635-1690 cm^{-1} which can be attributed to the C=O or/and C=C stretching of GA molecule [301]. Afterward, Anti-AFB1 were added to form layer selective to AFB1 molecules. The aldehyde groups on the surface react with amino groups of antibodies and proteins for covalent immobilization by an amide bond formation. The peaks in the range of 1226 - 1666 cm^{-1} can be associated with the amide I (1642-1660 cm^{-1}), amide II (1450-1535 cm^{-1}) and amide III (1226-1233 cm^{-1}) bonds. Additionally, one can assume that peaks in the range of

3005-3730 cm^{-1} correspond to the amide A and amide B bonds, on the other hand, such a broad peak can appear due to the O-H stretching.

7.3.3. Aflatoxin B1 PL detection

Quantitative analysis of the interactions between PAN/ZnO_{20nm}/APTES/GA/Anti-AFB1 structure and AFB1 molecules was performed in the concentration range of 0.1-100 ng/ml (target AFB1). To simplify the calculation of the main biosensors parameters (LOD, sensitivity range, etc.), PL signals of PAN/ZnO_{20nm} nanocomposite were normalized as follows:

$$I_{Cn} = \frac{I_c}{I_{Cmax}}, \quad (7.2)$$

where I_{Cn} is the normalized PL signal for each concentration as shown in the Figure 7.7, I_c is the non-normalized PL signal for each AFB1 concentration, and I_{Cmax} – maximum PL signal ($C_{\text{AFB1}} = 118.1 \text{ ng/ml}$).

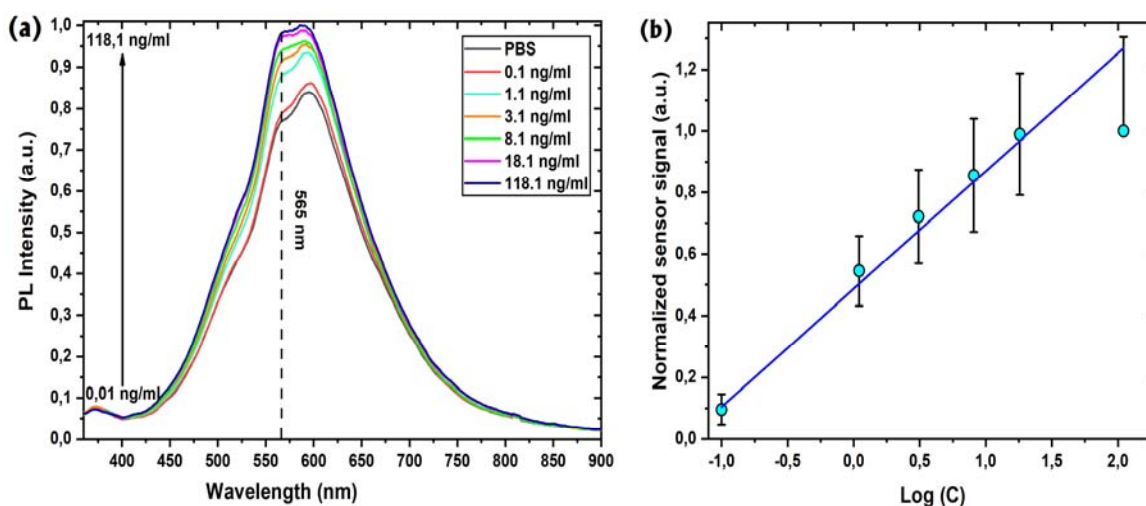


Figure 7.7. Photoluminescence spectra of PAN/ZnO_{20nm}/APTES/GA/Anti-AFB1 biosensor after incubation in different AFB1 concentrations (from bottom to top) containing samples after the reaching of steady state conditions (a); the response curve, measured at PL peak position ($\lambda = 565 \text{ nm}$) (b).

Figure 7.7a shows that the PL signal increases while the AFB1 molecules bind to the PAN/ZnO_{20nm}/APTES/GA/Anti-AFB1 surface. One may observe the 25 % increasing of the PL intensity for the concentration of AFB1 around 100 ng/ml. The saturation of the analytical PL signal is observed in the range of 20-100 ng/ml what imposes an upper limit for the AFB1 detection (Fig. 7.7a). The saturation can be explained considering that the great majority of antibodies (anti-AFB1) are bonded

to the AFB1 molecules. Besides, no significant changes in the PL were identified for control samples. Figure 7.7b shows the sensor signal (response curve) of PAN/ZnO_{20nm}/APTES/GA/Anti-AFB1 structure *vs* the concentration of AFB1. The linear fitting (dark blue line) of the experimental data (bright blue spots) can be expressed by the formula:

$$I_{PL565,2} = 0.489 - 0.385 \cdot \text{Log}(C), \quad (7.3)$$

where C is the AFB1 concentration.

Considering the equation (7.3), the LOD was calculated using the formula:

$$LOD = 3.3 \cdot \sqrt{n} \cdot \sigma/b, \quad (7.4)$$

where σ is the standard deviation of the negative control at small concentrations, n – number of tests, b is the slope of the curve, extracted from equation (7.3). The calculated value of LOD was around 39 ± 1 pg/ml, which is significantly lower than the acceptable levels of AFB1 in human foods and beverages (European Commission, No 401/2006). The calculated LOD value for PAN/ZnO PL-based biosensor is comparable with results obtained elsewhere [279,302,303] or even lower than that reported by Alshannaq *et al.* and Moon *et al.* [304,305]. This result shows that the studied nanostructures and the detection approach could be further applied for the development of efficient immunosensors and novel biosensors with other types of biorecognition agents (e.g. enzymes, DNA). A comparison of typical optical (label-free) biosensors for AFB1 detection is presented in the Table 7.1, in which the LOD of current immunosensor is at a low level, with the sensitivity range similar to the others.

Table 7.1. Representative results of recent label-free optical biosensors for AFB1 detection

Biosensor performance	Transducer	Sensitivity range	LOD	Reference
Polarized optical microscopy	Liquid crystal	0.1 – 1ng/ml	0.1 ng/ml	[306]
Fluorescence	g-C ₃ N ₄ + Fe ₃ O ₄	0.01– 0.5 ng/ml	0.002 ng/ml	[307]
Fluorescence	TPE-Z + GO	-	0.25 ng/ml	[308]
Fluorescence	MIP-membrane	14– 500 ng/ml	14 ng/ml	[309]
Plasmonic ELISA	AuNRs	0.0031– 0,15 ng/ml	0.0125 ng/ml	[310]
Localized SPR	AuNPs	1–10 ng/ml	0.36 ng/ml	[311]
Colorimetric	G-quadruplex signal reporter	1 pM-100 nM	1pM	[312]
Electro-chemiluminescence	Printed bipolar electrode	0.1– 100 ng/ml	0.033 ng/ml	[313]
Photoluminescence	PAN/ZnO	0.1-20 ng/ml	0.039 ng/ml	This work

7.3.4. The mechanism of PL biosensing

To gain further insights regarding the mechanisms of PL detection, we decided to develop a model that could explain the PL changes in semiconductors during the adsorption of molecules. According to the theory of PL in semiconductors, the changes of PL signal can be associated with the bandgap modification (e.g. band bending) under additional external forces that could be caused by the adsorption of the proteins which will affect the surface band bending. Those forces mostly initiate the surface potential ψ_s changes resulting in expanding or constriction of the space charge region (SCR) and/or energy band bending. The existence of a surface potential barrier that needs to be overcome by the photogenerated carriers and the value of SCR strongly affects the recombination processes, and as a consequence, the PL in semiconductors.

Being in liquids/electrolytes, semiconductor experience a significant influence of ions and the surface potential ψ_s depends on the total charge of all ions at the defined distance from the surface (Debye length) [91]. Besides, if the liquid contains macromolecules, such as proteins (antibodies, antigens, etc.), they will induce an additional effect on φ_D . It means that the PL signal is defined by the ψ_s , which is determined by the total electrostatic potential of both ions in the liquid and protein charges near the semiconductor surface.

There are two hypotheses of the electrostatic influence of protein charges which penetrate the diffuse layer (Helmholtz layer) to the semiconductor interface [314]. The first hypothesis is based on the Debye model, which defines the thickness of diffuse-charged layers by the distance (Debye length) where the electrostatic field has dropped to $1/e$ of its initial value. However, the Debye length in a physiological salt solution is limited to be around 0.8 nm [314]. It means only that the charge density changes comparable to the value of a Debye length can be detected. As we deal with proteins, such as antibodies and antigens, with an average size ($> 10\text{ nm}$) much bigger than the Debye length, one may conclude that their charges will be “not seen” for the detection platform [314].

The second hypothesis can be described by the so-called Donnan model [315]. This model enables to consider the influence of charge density changes caused by antibodies and antigens at the distances comparable to the Debye length. The main idea of this model based on the assumption that there are two phases (s and m) at the interface semiconductor/electrolyte, in which ions can freely diffuse to the surface until the electrostatic equilibrium state is achieved. Phases m and s represent the protein layer on the semiconductor surface and the volume of the electrolyte, respectively. The total electrostatic potential of the surface φ_D caused by ions and proteins in the Helmholtz layer (phase m) can be described by the equation [316]:

$$\varphi_D = \frac{RT}{F} \ln \left(\frac{C_{p+} + \sqrt{4C_s^2 + C_{p+}^2}}{2C_s} \right), \quad (7.5)$$

where R , T , F are the universal gas constant, temperature, and Faraday constant respectively, while C_{p+} and C_s are the concentration of protein-fixed positive charges and the ion concentrations in phase m [314]. As seen from the equation (7.5), the Donnan potential (potential arises between two phases) mostly depends

on the ion equilibrium concentrations in phase m. It worth to mention that there is a smooth transition between the φ_D and the surface potential (ψ_s) of semiconductor [317], which means that the changes of φ_D caused by ions transfer between m and s phases will influence on the surface potential $\psi_s(\varphi_D)$. Taking into account that the value of SCR is proportional to the square root of ψ_s , it becomes obvious that the changes of φ_D will affect the SCR as well [318].

One may consider two different cases: (i) the surface potential of $\psi_{s1}(\varphi_{D1})$ for the surface functionalized by antibodies, and (ii) the surface potential of $\psi_{s2}(\varphi_{D2})$ for the surface with antibody-antigen complexes. While the n-type semiconductor (e.g. ZnO) possesses the positive ψ_s (bending up), the binding of the positively-charged proteins (e.g. AFB1) induces a downward band-bending and decreasing of ψ_s ($\psi_{s1}(\varphi_{D1}) > \psi_{s2}(\varphi_{D2})$) due to the ion concentrations change in the phase m [319]. Such antibody-antigen interaction will promote decreasing of the semiconductor ψ_s and the value of SCR. This will promote an increase of charge carrier concentration and, as a consequence, it will enhance the radiative recombination from the bulk defect states.

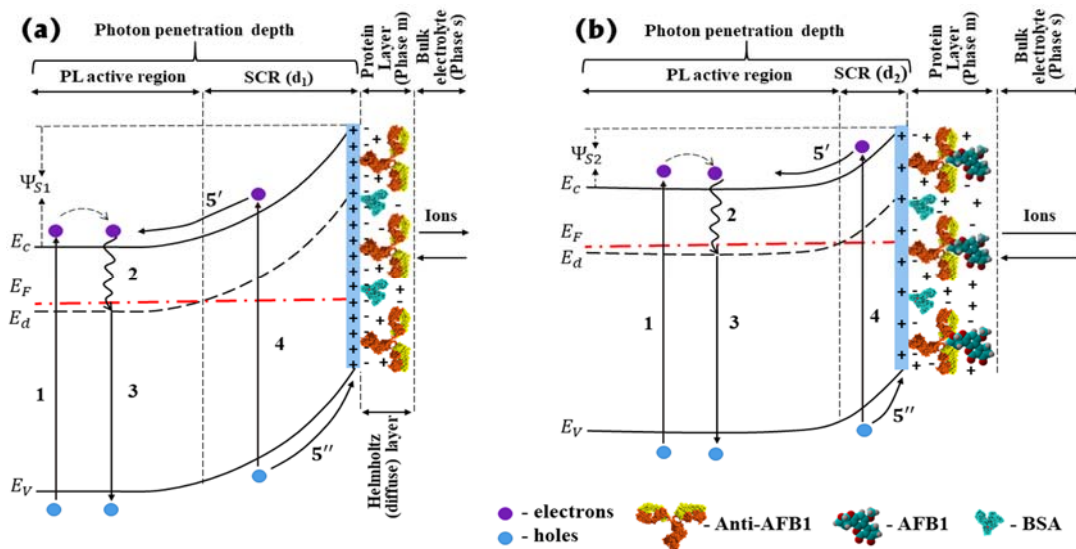


Figure 7.8. Sketch of the energy band diagram of the ZnO nanolayer with two types of surface modifications: PAN/ZnO_{20nm}/APTES/GA/Anti-AFB1/BSA (a) and PAN/ZnO_{20nm}/APTES/GA/Anti-AFB1/BSA&AFB1 (b). The transition 1 is the excitation of the electron-hole pair under UV light irradiation, 2 – non-radiative transition of the electron to the defect level, 3 is the radiative transition, which is the PL in the visible region, 4 – non-radiative transition in the space charge region (SCR), 5' indicates the electron migration from the surface to the volume of ZnO, 5'' indicates the hole migration from volume to the ZnO interface.

Based on this analysis, one may present the mechanism of PL changes in PAN/ZnO nanostructures after the adsorption of AFB1 molecules. Taking into account that we deal with the n-type semiconductor and positively charged AFB1 molecules [320], the bandgap diagrams of PAN/ZnO_{20nm}/APTES/GA/Anti-AFB1 in PBS solution before and after the adsorption of AFB1 molecules are shown in Figures 7.8a and 7.8b, respectively. Let us assume that only one type of defects (see Fig. 7.8, E_d level) in ZnO defines the radiative recombination and the PL intensity. However, the radiative recombination of photogenerated holes and electrons will take place only when the defect level energy lies below the Fermi level (E_F) of ZnO. This condition will only be met for the bulk region called here the PL active region (Fig. 7.8). It is clearly seen that the width of the PL active region is modulated by the value of SCR and the ψ_s , which values strongly depend on the concentration of adsorbed AFB1 molecules and the ion concentrations in the Helmholtz layer.

Figure 7.8a shows the upward band bending with the surface potential $\psi_{s1}(\varphi_{D1})$ and the SCR (d_1), for PAN/ZnO_{20nm}/APTES/GA/Anti-AFB1. The PL intensity is determined by radiative transitions 1→2→3 (Fig. 7.8). The expanding of SCR (increasing of ψ_s) will subsequently lead to the constriction of the PL active region and it will decrease the probability of radiative transitions 1→2→3. On the other hand, the reducing of SCR will have an opposite effect and, as a result, increasing PL intensity. After positively charged AFB1 molecules interact with antibodies (Anti-AFB1), it should downward the band bending (Fig. 7.8b). This downward band bending is associated with the lower value of ZnO surface potential $\psi_{s2}(\varphi_{D2})$ and it promotes constriction of the SCR to the value d_2 . Thus, the probability of radiative transitions 1→2→3 in the PL active region increases, while the probability of non-radiative transitions (transition 4) and the charge carriers separation (transition 5'-5'') becomes lower. This condition promotes increasing of PL intensity for PAN/ZnO_{20nm}/APTES/GA/Anti-AFB1/BSA&AFB1 nanostructures after the adsorption of positively charged AFB1 molecules on the surface.

7.3.5. Kinetic and thermodynamic aspects

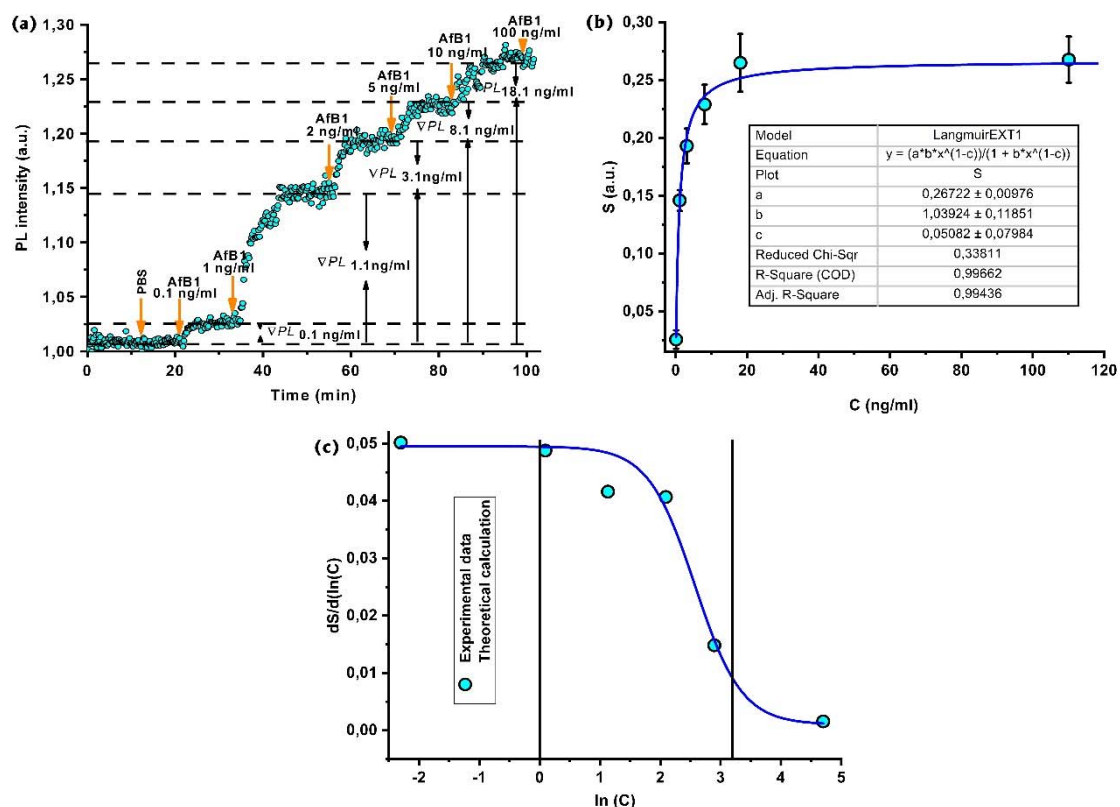


Figure 7.9. Dependence of PL peak maximum (at $\lambda = 565$ nm) vs AFB1 concentration (a); the isotherm of analyte (AFB1) interaction with PAN/ZnO_{20nm}/APTES/GA/Anti-AFB1 structure (b); and calculated sensitivity of PAN/ZnO_{20nm}/APTES/GA/Anti-AFB1 structure towards AFB1 (c).

Kinetic and thermodynamic analysis may provide important information on biomolecular interactions between antibody and antigen. Moreover, kinetic analysis offers insights concerning the relationships between structure and biochemical activities. The basis of kinetic and thermodynamic analysis is adsorption isotherm interpretation, which allows to calculate some important biosensor parameters, such as adsorption affinity constant, Gibbs free energy change, and power coefficient. Figure 7.9a presents the time-resolved PL intensity changes of the PAN/ZnO_{20nm}/APTES/GA/Anti-AFB1 sample vs different AFB1 concentrations. The immunosensor response time to the different AFB1 concentrations was in the range of 15–20 min. The dashed lines indicate the steady-state conditions for each concentration. The total AFB1 concentration interacted with the PAN/ZnO_{20nm}/APTES/GA/Anti-AFB1 surface was calculated as the sum of all infused concentrations during the test. Biosensor responses vs various AFB1 concentrations were calculated using the formula [279]:

$$S(C) = I_{eq}(C) - 1, \quad (7.6)$$

where I_{eq} and C are the normalized PL signal value of the PAN/ZnO_{20nm}/APTES/GA/Anti-AFB1 sample in steady state conditions and the value of AFB1 concentration, respectively.

Adsorption isotherm indicates a pseudo-first-order interaction between AFB1 and PAN/ZnO_{20nm}/APTES/GA/Anti-AFB1 structure as shown in Figure 7.9b. This type of interaction can be described by the first order kinetic equation (Langmuir equation) obtained from the fitting (dark blue curve) [321]:

$$\frac{dN}{dt} = k_a \cdot C \cdot (N_s - N) - k_d \cdot N, \quad (7.7)$$

where N , k_a , k_d , N_s and C are a number of adsorbed molecules, an association constant, a dissociation constant, a number of adsorption sites and the concentration, respectively.

In this particular case, the number of adsorbed molecules has maximum value, while the sensitivity is highest. It means that those parameters are proportional $N_s \sim S_{max}$, and N is proportional to the biosensor sensitivity ($N \sim S$, where $S < S_{max}$).

It should be noted, that after adding of AFB1 into the microfluidic cell, the PL intensity increases until its saturation, which indicates the steady-state conditions between PAN/ZnO_{20nm}/APTES/GA/Anti-AFB1 and AFB1. Thus, the rate of AFB1 adsorption is equal to zero ($\frac{dN}{dt} = 0$), and the equation (7.7) can be rewritten as follows:

$$k_a \cdot C \cdot (S_{max} - S) - k_d \cdot S = 0. \quad (7.8)$$

After some additional calculations, the Langmuir equation (7.8) is transformed to the equation (7.9), while fitting parameters are taken from the equation (7.10) (inset, Fig. 7.9b):

$$\frac{S}{S_{max}} = \frac{K_A \cdot C}{1 + K_A \cdot C}, \quad (7.9)$$

$$\frac{y}{a} = \frac{b \cdot x^n}{1 + b \cdot x^n}, \quad (7.10)$$

where $b = K_A = \frac{k_a}{k_d}$, is the affinity constant, $x = C -$ concentration, $n = 1 - c$ is the power coefficient (c -fitting parameter from the inset table of Fig. 7.9b), y, a are S and S_{max} respectively.

The affinity dissociation constant $K_D = 0.96 \pm 0.11 \text{ ng/ml}$ was calculated as the reversed value of K_A and allows one to estimate the change in Gibbs free energy (ΔG) of PAN/ZnO_{20nm}/APTES/GA/Anti-AFB1 & AFB1 complex formation:

$$\Delta G = RT \cdot \ln K_D^0, \quad (7.11)$$

where R and T are the universal gas constant and the absolute temperature, respectively. The value $K_D^0 = K_D/C$, in this case, C is the standard reference concentration of 1 M.

The obtained value of the change in Gibbs free energy $\Delta G = -44.6 \pm 1.4 \text{ kJ/mol}$ indicates the thermodynamically favorable reaction of the chemical adsorption [264] for the PAN/ZnO_{20nm}/APTES/GA/Anti-AFB1&AFB1 complex formation [322]. One can conclude that a strong electrostatic chemical bonding occurs between the PAN/ZnO_{20nm}/APTES/GA/Anti-AFB1 and AFB1 molecules. The calculated ΔG is in good agreement with the value obtained in our previous research [279] and higher than recently reported for the AFB1 physisorbed onto the detection platform [323].

The calculated power coefficient $n = 0.95 \pm 0.01$ indicates a favorable sorption process ($n < 1$) of the analyte onto the PAN/ZnO_{20nm}/APTES/GA/Anti-AFB1 structure [324] and the fast diffusion of AFB1 molecules to the developed nanofibers structure [281]. Besides, such value of the power coefficient ($0.5 < n < 1$) can be additionally explained by the partially negative cooperative adsorption [325]. The negative cooperative adsorption indicates the decreasing of affinity while the molecule covalently binds with the binding site. Taking into account that the structure of antibodies assumed to be bivalent [326], because of V regions of the two heavy and light chains, it offers two identical antigen-binding sites [327]. Therefore, it can be supposed that binding affinity (capability) of Anti-AFB1 toward AFB1 becomes lower after the first Anti-AFB1&AFB1 binding and tends to the zero value after the second Anti-AFB1&AFB1 binding.

Finally, the sensitivity of PAN/ZnO_{20nm}/APTES/GA/Anti-AFB1 was calculated as the derivative of the sensor signal response *S* to the natural logarithm of AFB1 concentration *C* (Fig. 7.9c). Analysis of the sensitivity indicates, that the PAN/ZnO_{20nm}/APTES/GA/Anti-AFB1 biosensor shows the sensitivity towards AFB1 molecules in the range of 0.1-20 ng/ml. However, the upper limit can achieve higher values than 20 ng/ml of AFB1 concentration, if more Anti-AFB1 would be immobilized on the PAN/ZnO_{20nm}/APTES/GA structure.

All analytical parameters and kinetic constants of the PAN/ZnO_{20nm}/APTES/GA/Anti-AFB1&AFB1 complex are presented in Table 7.2.

Table 7.2. Calculated parameters of real – time AFB1 detection and adsorption.

LOD, pg/ml	S, ng/ml	n	K_D, ng/ml	K_D, M	ΔG, kJ/mol
39 ± 1	0.1–20	0.95 ± 0.01	0.96 ± 0.11	29.5·10 ⁻¹⁰ ± 2.2·10 ⁻¹¹	-44.6 ± 1.2

7.3.6. Microscopy visualization

In the final stage of the research, the two-photon PL microscopy was used to visualize immunosensor response during PAN/ZnO_{20nm}/APTES/GA/Anti-AFB1&AFB1 complex formation. Figures 7.10 (a,b) demonstrate the PL emission from PAN/ZnO_{20nm} and PAN/ZnO_{20nm}/APTES/GA/Anti-AFB1, respectively. It is clearly seen the more intense PL emission for the sample with immobilized antibodies that proves the mechanism provided in section 7.3.4. This means that after immobilization of Anti-AFB1 to the surface of the PAN/ZnO_{20nm} sample, the downward band-bending and decreasing of ψ_s lead to increasing of PL intensity. Besides, the uniform PL emission from PAN/ZnO_{20nm}/APTES/GA/Anti-AFB1 nanofibers proves the conformal functionalization of the ZnO surface. Then, the probe of AFB1 with a concentration of 10 ng/ml was injected into the cell with the PAN/ZnO_{20nm}/APTES/GA/Anti-AFB1 and the control sample. The PL images/frames have been recorded every 5 min until signal saturation. Figure 7.10c shows the time-dependent average intensity of PL for the PAN/ZnO_{20nm}/APTES/GA/Anti-AFB1&AFB1. It is seen that the PL intensity progressively increases over time. The PL images were analyzed using ImageJ software. The inset image indicates the change in average PL intensity during the APTES/GA/Anti-AFB1&AFB1 complex formation. The average PL intensity was

about (~26%), and has a good agreement with the value (~25%) from PL-based real-time measurement for AFB1 10 ng/ml concentration (Fig. 7.9b). A control experiment was also conducted on the PAN/ZnO_{20nm} sample. No significant non-specific adsorption of AFB1 was observed. The results confirm that the produced immunosensor provides a sensing capability with a high signal-to-noise ratio and diminished non-specific adsorption.

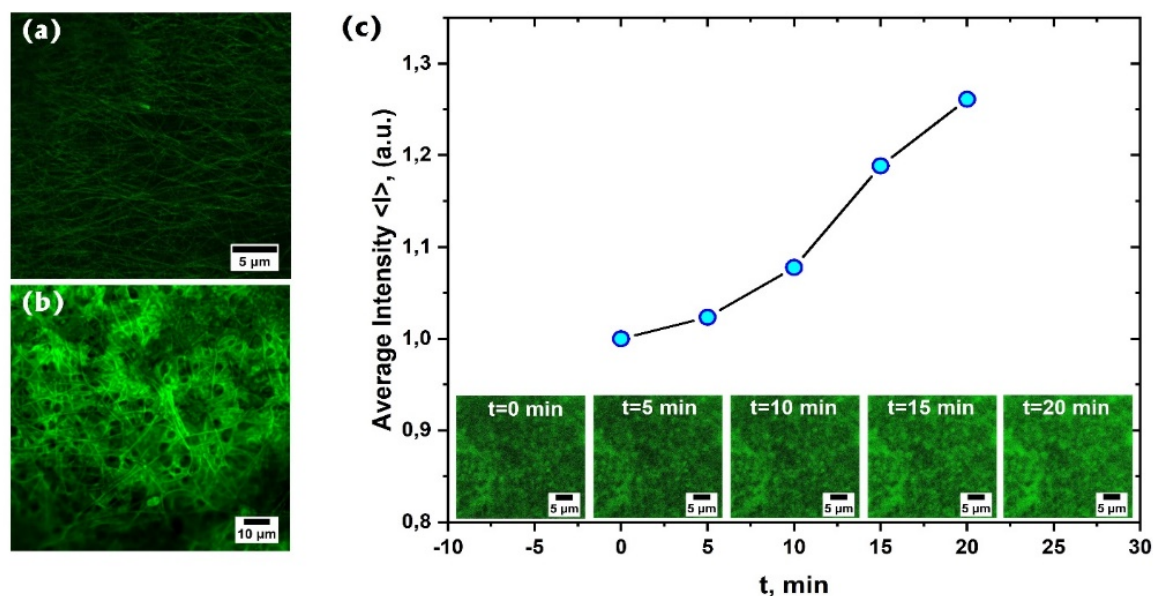


Figure 7.10. The images obtained via fluorescent confocal microscopy: (a) bulk PAN/ZnO_{20nm} nanofibers (b) and PAN/ZnO_{20nm}/APTES/GA/Anti-AFB1 structures. (c) the time-resolved PL intensity of PAN/ZnO_{20nm}/APTES/GA/Anti-AFB1, concentration of AFB1 - 10 ng/ml.

7.4. Conclusions

In conclusion, PAN/ZnO nanofibers prepared by electrospinning and ALD was successfully examined as a PL-based platform for AFB1 detection. The intensity of the PL emission of PAN/ZnO_{20nm} modified by APTES/GA/Anti-AFB1 is seen to be dependent on the AFB1 concentration, evidencing an increase of PL with increasing concentration of the analyte. PAN/ZnO_{20nm}/APTES/GA/Anti-AFB1 samples were integrated into the microfluidic cell, which showed high sensitivity towards AFB1 molecules in the range of 0.1-20 ng/ml, and the LOD was evaluated as 39 pg/ml. The immunosensor response time to the different AFB1 concentrations was in the range of 15-20 min. The calculated values of kinetic constants and thermodynamic parameters indicate favorable AFB1 adsorption to the PAN/ZnO_{20nm}/APTES/GA/Anti-AFB1 immunosensor as well as high electrochemical interaction between immunosensor and AFB1 due to the Anti-

AFB1&AFB1 complex formation. The results obtained by the two-photon PL microscopy confirm that the developed immunosensor is capable to detect AFB1 with a high signal-to-noise ratio and diminished non-specific adsorption. Besides, the model of semiconductor – analyte interaction and its effect on PL emission was proposed and analyzed. The obtained results indicate the suitability of our materials and detection approach to be employed in the fabrication of biosensing devices for probing other relevant analytes.

Publication IV

The content of this chapter has been already published in [Biosensors and Bioelectronics Journal](#)

Biosensors and Bioelectronics, Volume 207, 2022, 114141, ISSN 0956-5663,

doi.org/10.1016/j.bios.2022.114141.

Authors: **Valerii Myndrul**, Emerson Coy, Nataliya Babayevska, Veronika Zahorodna, Vitalii Balitskiy, Ivan Baginskiy, Oleksiy Gogotsi, Mikhael Bechelany, Maria Teresa Giardi, Igor Iatsunskyi

8. MXene nanoflakes decorating ZnO tetrapods for enhanced performance of skin-attachable stretchable enzymatic electrochemical glucose sensor

8.1. Introduction

With the increased demand for real-time monitoring of health-related small molecular weight biomarkers, the portable medical device industry has grown rapidly over the past decade [328]. These devices have an advantage over conventional medical detection tools since they are user-friendly and require non-invasive biological fluids such as sweat, saliva, or tears [329]. With remote patient monitoring capabilities and non-invasiveness, portable medical devices are good candidates for painless harvesting of physiologically relevant data in real-time mode. For example, skin-attached, stretchable portable devices can meet the requirements of painless and continuous glucose monitoring in diabetic patients, eliminating the daily inconvenience of finger-prickling. While real-time glucose monitoring can minimize the risk of serious complications caused by diabetes, and also can provide insights into body glucose dynamics, especially after mealtimes, during physical activity and at rest.

Although many approaches to non-invasive glucose monitoring are currently proposed, portable and wearable devices are still poorly implemented on a large industrial scale, despite their growth potential and advantages [330]. Such a slow implementation is mainly due to the unclear correlation between sweat and blood glucose levels [330,331]. Nevertheless, this drawback does not negate the fact that sweat glucose still can qualitatively indicate hypo- or hyperglycemia and the

necessity for self-care intervention to control and stabilize blood glucose levels. Besides, the skin-attachable sweat glucose sensor performance can be improved by developing novel and effective transducers. In this case, significant attention should be given to the materials and composites with enhanced catalytic activity towards glucose oxidation and superior electrical conductivity, particularly in complex matrices, i.e. blood or sweat [141].

Among all known semiconductors, the nanoscale zinc oxide (ZnO) is considered to be one of the most suitable for biomedical applications. A variety of morphologies, the enhanced surface to volume ratio, high isoelectric point (IEP ~ 9.5), high electron transport capacity, and biocompatibility are just a few of its many superior physical-chemical properties [88,156,332]. Today, ZnO still meets scientists' expectations and is increasingly used in a variety of detection techniques, such as optical [333], electronic [334], SPR [335], SERS [336], and piezoelectric (bio)sensors [337]. Among ZnO nanostructures, ZnO tetrapods (ZnO TPs) occupy an important position on biosensing development because of their higher active surface area provided by the large pods and highly porous 3D interconnected networks, which provide more sites for analyte adsorption and, as a consequence, better sensitivity to small molecular weight compounds detection [132,338]. It was recently reported that the high catalytic activity of ZnO TPs towards the sulfonamide antibacterial degradation, which was 2-3 times higher when compared with ZnO nanoparticles or nanoflowers [339]. The enhanced surface to volume ratio and high catalytic activity were the reasons for the higher sensitivity of TP ZnO to L-lactic acid than that of ZnO nanorods with similar analytical performance [338,340]. However, the high electrical resistivity of ZnO TPs is a significant drawback for electrochemical sensing applications. Yet, there is still a possibility to improve the electrochemical sensor performance by integrating ZnO TPs with high conductive 2D nanomaterials [341].

Although the history of 2D materials is short and has not even crossed the 20-year mark (since the synthesis of graphene in 2004) [342], they have emerged in a wide variety of scientific areas. 2D materials have become popular due to the enhanced optoelectronic properties that differ from those of conventional bulk materials [343]. Until now, particular attention has been paid to the high catalytic activity of those atomically thin structures driven by enhanced surface area and carrier transport. In this context, 2D materials are used to enhance the water splitting and CO₂ reduction performances [344]. while high stability and biocompatibility make

them attractive for medical and biological applications [345]. For example, biosensors based on 2D sheets of graphene, MoS₂, and MXene (transition metal carbides, e.g. Ti₃C₂T_x) [346] demonstrate enhanced sensitivity towards proteins, bacteria, H₂O₂, and glucose detection.[347] However, the low electrical conductivity of MoS₂, high hydrophobicity of both graphene and MoS₂, and laborious functionalization can complicate the biosensing performance.[348] In contrast, MXene has advantages over graphene and MoS₂ since it possesses outstanding metal-like conductivity and hydrophilic surface with termination groups (–OH, =O and –F), facilitating the functionalization process. Composites based on MXene and ZnO exhibit unique properties that enable application in various applications, including solar cells [349], water splitting [350], electromagnetic wave absorption [143], photocatalytic performance [145], light-emitting diodes [351], and sensing [352]. Moreover, due to the enhanced catalytic activity of ZnO/MXene composites [353], it may be an ideal candidate for biosensor applications, especially for electrochemical glucose detection.

In this report, catalytically active composites of ZnO TPs/MXene were prepared and deposited on a stretchable electrode as an electroactive transducer layer for the qualitative analysis of glucose in Phosphate-buffered saline (PBS), artificial and human sweat. To the best of our knowledge, this is the first proposed protocol for decorating ZnO nanostructures with MXene nanoflakes and not vice versa. The structural, chemical, electrochemical and optical properties of produced composites were analyzed. ZnO TPs/MXene/GOx nanocomposites exhibited enhanced catalytic activity towards glucose oxidation in PBS and artificial sweat compared to the pristine ZnO TPs and MXene. The higher catalytic activity of ZnO TPs/MXene resulted in a better sensitivity and a lower limit of detection (LOD) for glucose in PBS and artificial sweat. Moreover, the low applied negative potential of -0.24 V allowed to avoid the impact of the interference species that could contribute to the response of the ZnO TPs/MXene/GOx-based electrode. The ZnO TPs/MXene stretching experiments have shown the high mechanical stability (up to 30% of strain) of developed electrodes. We also performed *in vivo* measurements of glucose in sweat, and we demonstrated the good correlation of obtained data with one collected by a conventional amperometric blood glucometer.

8.2. Experimental section

8.2.1. Materials

(3-Aminopropyl)triethoxysilane (APTES, purity $\geq 98\%$) glucose oxidase (GOx) (N^o G7141), D-(+)-Glucose (N^o 8270), Nafion 117 ($\sim 5\%$) containing solution (N^o 70160), Glutaraldehyde (GA, 50 wt. % in H₂O), Sodium hydroxide (NaOH, grade $\geq 98\%$), Zn powder (N^o 324930, purity of 99,9%), ascorbic acid (AA) (N^o PHR1008), urea (purity $\geq 99\%$), uric acid (UA, purity $\geq 99\%$, crystalline) dopamine (N^o H8502), sodium chloride (NaCl, grade $\geq 99\%$), potassium chloride (KCl) (N^o P3911), glycine (purity $\geq 99\%$), Ammonium hydroxide solution (NH₄OH) (N^o 221228), were purchased from Sigma Aldrich. PBS, pH 7.4 was used as the diluent for glucose oxidase and glucose dissolution. Polyethylene terephthalate (PET) was provided by Policrom Screens S.P.A. (Carvico, BG, Italy). Silver reference electrodes and contacts on all produced electrodes were printed using LOCTITE® ECI 1010 E&C (Henkel); working and reference electrodes were printed using LOCTITE® EDAG 407C E&C (Henkel). Lithium fluoride (LiF, 98.5% grade) powder and hydrochloric acid (HCl, 37 wt. %) were purchased from Alfa Aesar.

8.2.2. Instruments

Morphologies of the ZnO TPs, MXene and ZnO TPs/MXene were investigated by scanning electron microscopy (SEM) (JEOL, JSM7001F) with a dispersive energy X-ray (EDX) analyzer and transmission electron microscopy (TEM) (JEOL ARM 200F) high-resolution transmission electron microscope (200 kV) with an EDX analyzer. The structural state of samples was analyzed by means of X-ray diffraction (XRD) (PANalytical, X'pert3pro MPD diffractometer) working with a Cu lamp ($\lambda = 1.5418 \text{ \AA}$). X-ray photoelectron spectroscopy (XPS) measurements were carried out by ESCALAB 250 spectrometer (Thermo Fisher) using Al K α monochromatic excitation source (1486.6 eV). Raman spectrum was measured by means of a Renishaw micro-Raman spectrometer with a confocal microscope. The samples' optical properties (absorbance, photoluminescence) have been studied with Ocean Optics spectrophotometer QE65pro. Electrochemical measurement and glucose detection, including cycling voltammetry and chronoamperometry regimes, were performed using potentiostats ER466 and GAMRY 620. The sonication of the MXene sheets to divide them into MXene nanoflakes was performed by Sonifier ultrasonic processor (SFX 20:0.55).

8.2.3. Preparation of ZnO TPs

ZnO tetrapods (ZnO TPs) were obtained by the simple catalyst-free oxidative-metal-vapour-transport method. The method was based on thermal evaporation of Zn powder at 1000°C for 1h in the air in a ceramic crucible [354]. After the reaction, the white powder of ZnO was deposited, which confirmed the oxidation of zinc metal powder.

8.2.4. Preparation of MXene

Ti₃C₂T_x MXene was prepared by etching Ti₃AlC₂ (MAX-phase) ternary carbide using MILD method in a solution of lithium fluoride (LiF) in hydrochloric (HCl) acid [355]. Etching mixture was prepared from 40 ml of 12 M HCl (37%), 10 ml of DI-water and then 3.2 g of LiF are dissolved in this solution. The mixture was placed in a plastic container with a volume of 50 ml. Then 2 g of Ti₃AlC₂ powder with particle sizes of less than 40 µm is gradually added into etching solution under continuous stirring for 24 hours at 25°C. Then MXene slurry was rinsed with DI-water via repetitive centrifugation. As-prepared MXene slurry is further processed to obtain a colloidal solution of separated MXene flakes using mild delamination procedure assisted by intercalation of Li⁺ ion between Ti₃C₂ sheets with following the separation of MXene into colloidal solution in water [355]. We used the following protocol for the delamination: 2 g of lithium chloride (LiCl) were added to 40 ml of DI-water in a 50 ml plastic container. Etched MXene slurry is added to the prepared solution. The process is performed at 35 °C for 24 hours under stirring. After that, MXene slurry is rinsed via repetitive cycles of centrifuging. Purity of MXene is confirmed by XRD analysis. After synthesis MXene sediment is stored at -18°C.

8.2.5. Fabrication of skin-attachable, stretchable electrodes

The skin-attachable electrodes made of Silver/Silver-NaCl/Carbon in PTU (125 µm thickness) were produced by a conventional screen printing method, property of Eastprint-USA (<http://www.eastprint.com/electrodes-biosensors.html>) under design property of Biosensor srl (<https://www.biosensor-srl.eu/>).

8.2.6. Preparation of ZnO/MXene based electrodes

The ready-to-use MXene sheets were then placed in a PBS solution and sonicated (for 20 minutes at 70% ultrasonic processor power) to crush into MXene nanoflakes for use in the ZnO TPs decorating process. Once ready, MXene nanoflakes were then

mixed with ZnO TPs in proportion 1:2 (1 mg/ml MXene and 2 mg/ml ZnO TPs in DI water) to prepare a combined ZnO TPs/MXene structure. The sample was then investigated on SEM in order to confirm the coverage of ZnO TPs by MXene nanoflakes, and the result showed the inhomogeneity of the coverage (SI. Fig. S8.1). In order to improve the uniformity, ZnO TPs were treated with 2% ATPES solution (in anhydrous EtOH 99.6%) to achieve functional groups on their surfaces. This process was followed by 3-times rinsing of ZnO TPs (2 times in EtOH and 1 time in PBS) to eliminate APTES remains. The functionalized ZnO TPs were then mixed again with MXene in 1:2 (1 mg/ml MXene and 2 mg/ml ZnO TPs in DI water) to prepare a combined ZnO TPs/MXene structure. The process of mixing was performed under sonicating conditions (for 2 hours at RT). After the sonication, the sample was rinsed in DI water and centrifuged 3 times to remove unbound MXene nanoflakes and remove excess water.

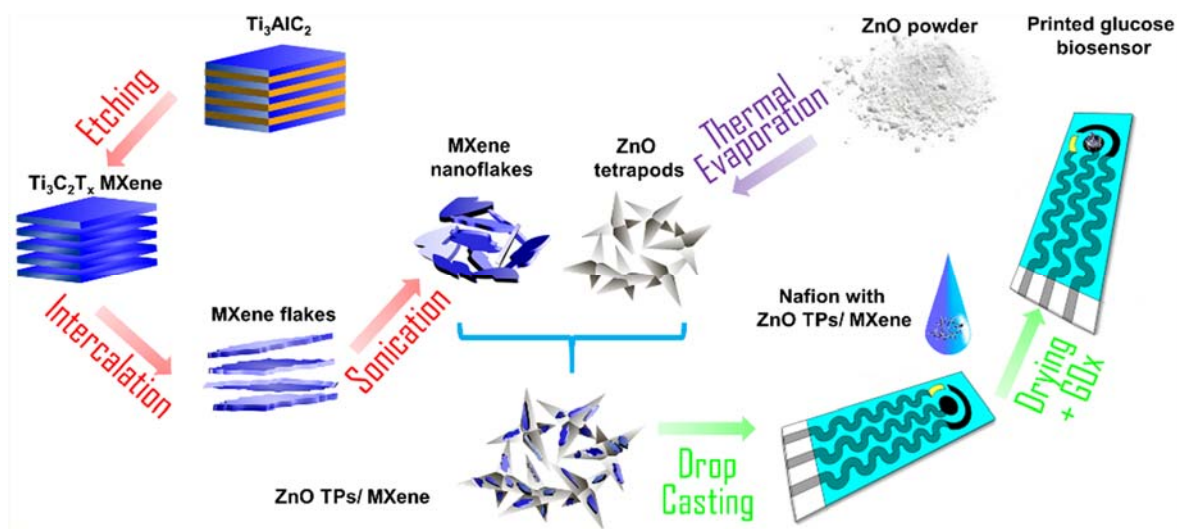


Figure 8.1. Sketch-diagram representing processes of ZnO TPs preparation, MXene nanoflakes preparation and fabrication of skin-attached ZnO TPs/MXene/GOx-based electrode.

The prepared ZnO TPs/MXene sample was mixed with Nafion (1 ml of 2% EtOH solution, neutralized to pH = 7, by use of 0.1 M NaOH). The droplet (8 μ L) of this mixture was placed on the working electrode of the stretchable sensor and dried for 1 h at 65 $^{\circ}$ C. Once cooled, the sensor's working electrode was then cross-linked by GA (30 min, RT) and GOx was added (8 μ L of 20 mg/ml in PBS, for 12 hours at 4 $^{\circ}$ C) to achieve a selective layer toward glucose. After that, the skin-attachable and stretchable sensor were coated by the additional layer of Nafion polymer (5 μ L of 2 % solution in EtOH neutralized to pH = 7) and stored for 1 day at 4 $^{\circ}$ C before use. The sketch diagram (Fig. 8.1) depicts MXene nanoflakes and ZnO TPs fabrication

stages, the deposition of ZnO TPs/MXene composite on the skin-attachable, stretchable electrode and selective layer formation using GOx and Nafion.

For the comparative analysis of the electrochemical and structural properties and the glucose detection parameters, three types of electrodes were prepared and titled as ZnO TPs/GOx-based electrode, MXene/GOx-based electrode, and ZnO TPs/MXene/GOx-based electrode. The stability of all prepared electrodes was tested in different pH.

8.2.7. Electrochemical glucose detection in PBS and artificial sweat

The fabricated electrodes were initially tested in PBS (pH 7.4) with a change of glucose concentration in the experimental cell. The electrochemical properties of ZnO TPs/GOx-, MXene/GOx-, and ZnO TPs/MXene/GOx-based electrodes were studied using CV measurements at a scan rate of 40 mV/s.

Chronoamperometry was performed to determine glucose using ZnO TPs-based electrode with an applied potential of -0.32 V (*vs* Ag), MXene/GOx-based electrode with applied a potential of -0.21 V, and for the ZnO TPs/MXene-based electrode the applied potential was equal to -0.24 V. Chronoamperometry measurements for the ZnO TPs/MXene/GOx-based electrode were carried out in artificial sweat (pH 6.5) at the same applied potential (-0.24 V) as for PBS. Artificial sweat was prepared according to the protocol EN1811:2012 and consisted of NaCl (0.5%), KCl (0.1%), and urea (0.1%), while the pH was adjusted to 6.5 by use of NH_4OH [356]. The selectivity of ZnO TPS/MXene-based electrode to glucose in artificial sweat was evaluated by means of chronoamperometry with the sequential addition of 0.1 mM AA, 0.5 mM urea, 50 μM UA, 0.05 mM dopamine, 10 mM NaCl, 10 mM KCl, and 0.1 mM glycine.

All experiments were repeated at least three times and all parameters (LODs, sensitivities, electron transfer rates, etc.) were calculated as means \pm standard error.

8.2.8. On-body sweat analysis

On-body sweat analysis was performed in two healthy subjects of 25-30 years of age. The electrode was tightly attached to the wet skin during real-time glucose monitoring. The contacts were connected to a potentiostat, and the data was displayed on a laptop screen. Chronoamperometry measurements were carried out at the same applied potential (-0.24 V) as for artificial sweat. The volunteer was

asked to take sweets and do exercises on a command. Additional invasive glucose measurements (8 discrete points) were taken by using a commercially available glucometer (VGM01, VivaCheck Ino).

8.2.9. Electrode stretching tests

Stretchability was tested using a custom made device to stretch the electrode. The discrete values of the applied strain varied from 0 to 35%. The response was measured by a potentiostat operating in amperometric mode. The 3-electrode system was sandwiched between slides to ensure a constant analyte value during experiments. Various glucose concentrations (0.1 mM, 0.2 mM, 0.5 mM, 0.7 mM, and 1 mM) were tested on the electrodes with 0%, 15%, and 30% of elongation to evaluate the stability of the electrodes under various strains.

8.3. Results and discussion

8.3.1. Material selection

As mentioned in the “Introduction” section, ZnO is a widely used material in sensor and biosensor technologies, and such popularity is due to its high stability, biocompatibility, and enhanced surface to volume ratio, especially when considering hierarchical structures. Since the stability of the transducer and its biocompatibility are the most important parameters during the electrochemical biosensor performance, ZnO was considered as the most suitable material to be used in our experiments. ZnO in the shape of tetrapods (ZnO TPs) has the highest active surface when compared with the other ZnO morphologies, and therefore, the use of ZnO TPs can enhance the efficiency of detection performance [132,338]. The choice of MXene nanoflakes for ZnO decoration was based on the assumption that MXene would facilitate the charge transfer rate between the electrolyte and ZnO, as it was reported for the ZnO nanorods and MXene sheets [139]. The enhanced charge transfer rate usually results in a better catalytic activity of the transducer towards glucose oxidation [141].

8.3.2. Characterization of ZnO TPs/MXene nanocomposite

MXene $\text{Ti}_3\text{C}_2\text{T}_x$ flakes and then nanoflakes were successfully synthesized from a titanium aluminum carbide (Ti_3AlC_2) MAX phase using a method described in the Experimental section. Figure 8.2a, b show SEM images of as-synthesized and nanoflakes of MXene ($\text{Ti}_3\text{C}_2\text{T}_x$), respectively. The lateral size of the delaminated

MXene flakes is approximately 7-8 μm , whereas the nanoflakes have a leaf-shaped morphology with an average diameter around 100 nm, indicating the use of a high-power ultrasonic treatment may induce structural changes. Figure 8.2c indicates that as-synthesized ZnO TPs are well faceted and consist of four "legs" connected to a central nucleus with an average length of $8 \pm 2 \mu\text{m}$ and a diameter of $400 \pm 150 \text{ nm}$ (SI, Fig. S8.2). ZnO TPs have hexagonal morphology, which suggests a single crystalline structure with preferred growth direction along the c-axis of the hexagonal unit cell. The zeta-potential values for ZnO TPs and MXene nanoflakes were $35 \pm 8 \text{ mV}$ and $-27 \pm 1 \text{ mV}$, respectively, which provides a strong electrostatic interaction between those two components. Despite this, it was necessary to carry out an additional chemical treatment (APTES treatment, see Experimental section) to obtain a conformal layer of MXene nanoflakes over ZnO TPs (Fig. 8.2d). Otherwise, an uneven distribution of MXene nanoflakes on the ZnO surface was observed (SI, Fig. S8.1).

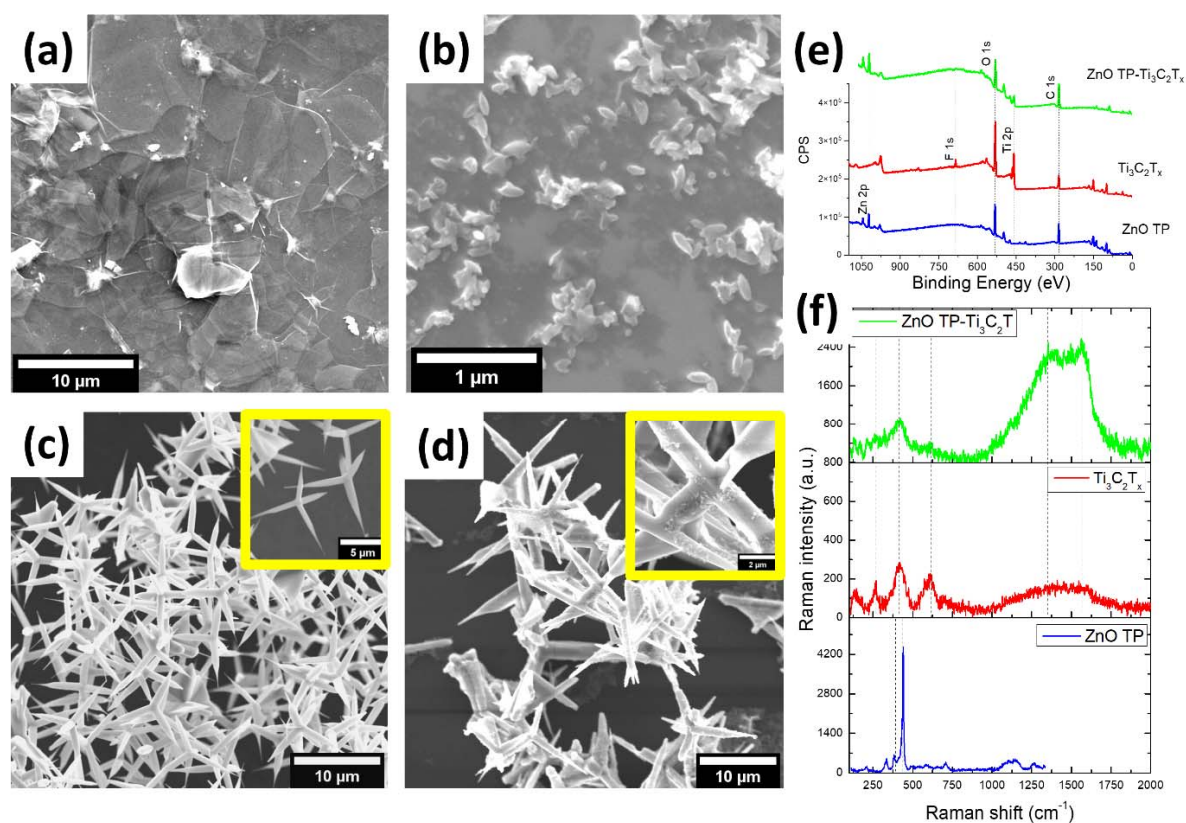


Figure 8.2. SEM images of MXene (a), MXene nanoflakes (b), ZnO TPs (c) and ZnO/MXene deposited on the Si substrate (d); survey XPS spectra (e) and Raman spectra (f) of produced samples (ZnO TPs, MXene nanoflakes and ZnO/MXene).

To analyze the chemical composition and electronic states of produced nanocomposites, XPS analysis and Raman spectroscopy were applied. The survey

spectra for ZnO TPs, MXene nanoflakes and ZnO/MXene nanocomposites are displayed in Fig. 1e. The spectrum of the ZnO TPs sample displays the signals of Zn, O and C. The XPS analysis of core level Zn 2p spectra (the difference Zn 2p_{3/2} - Zn 2p_{1/2} = 23.1 eV) indicated the wurzite phase of ZnO (SI, Fig. S8.3) [155]. Four main elements (oxygen (O), titanium (Ti), carbon (C) and fluorine (F)) were presented in the MXene samples confirming the formation of Ti₃C₂T_x with functional surface groups of -OH and -F. After the formation of ZnO/MXene nanocomposite the peak relating to the F element vanished, indicating the formation of the interface between ZnO and MXene-Ti₃C₂. The detailed XPS analysis of the fabricated ZnO/MXene nanocomposite is provided below and in the supporting information.

Figure 8.2f shows the Raman spectra of produced ZnO/MXene nanocomposites and pristine components. As-synthesized ZnO TPs exhibits Raman peaks at 440, 390, and 338 cm⁻¹ corresponding to E₂(high), E₁(TO), A₁(TO) modes of ZnO wurzite phase crystal, respectively [357]. The Raman spectrum of pristine Ti₃C₂T_x nanoflakes consists of a minimum of five vibrational modes: 125, 255, 425, 608, and 1520 cm⁻¹. Recently, it was shown that a Raman spectrum of Ti₃C₂T_x consists of many peaks in the 100-800 cm⁻¹ range, and it can be distinguished into several spectrum regions [358]. According to Sarycheva *et al.* [358], one may conclude that the Raman mode at 125 cm⁻¹ is attributed to the resonant plasmonic peak. Two Raman modes at 255 and 425 cm⁻¹ are associated with out-plane (A_{1g}) and in-plane (E_g) vibrations of C, Ti atoms and surface groups (-OH, -F). The peak at 608 cm⁻¹ indicates the carbon vibration (E_g, A_{1g}). The broad Raman peak at 1520 cm⁻¹ is attributed to the D and G bands of amorphous and graphitic carbon. Peaks relating to anatase and rutile phases (140, 512 cm⁻¹ and 393, 587 cm⁻¹) were not observed, indicating the presence only -OH group on the surface of MXene nanoflakes. As for ZnO/MXene nanocomposites, one can observe the changes of the Raman spectrum. Apart from graphitic carbon bands, there are four weak peaks at 133, 170, 213, and 414 cm⁻¹. It is clearly seen that the resonance peak shifted to higher wavenumbers. On the other hand, Raman modes associated with in-plane vibrations of functional groups shifted to the red region. These shifts of both modes and the high-intense D band can be explained by an increased concentration of defects that are formed during the production of ZnO/MXene nanocomposites [358].

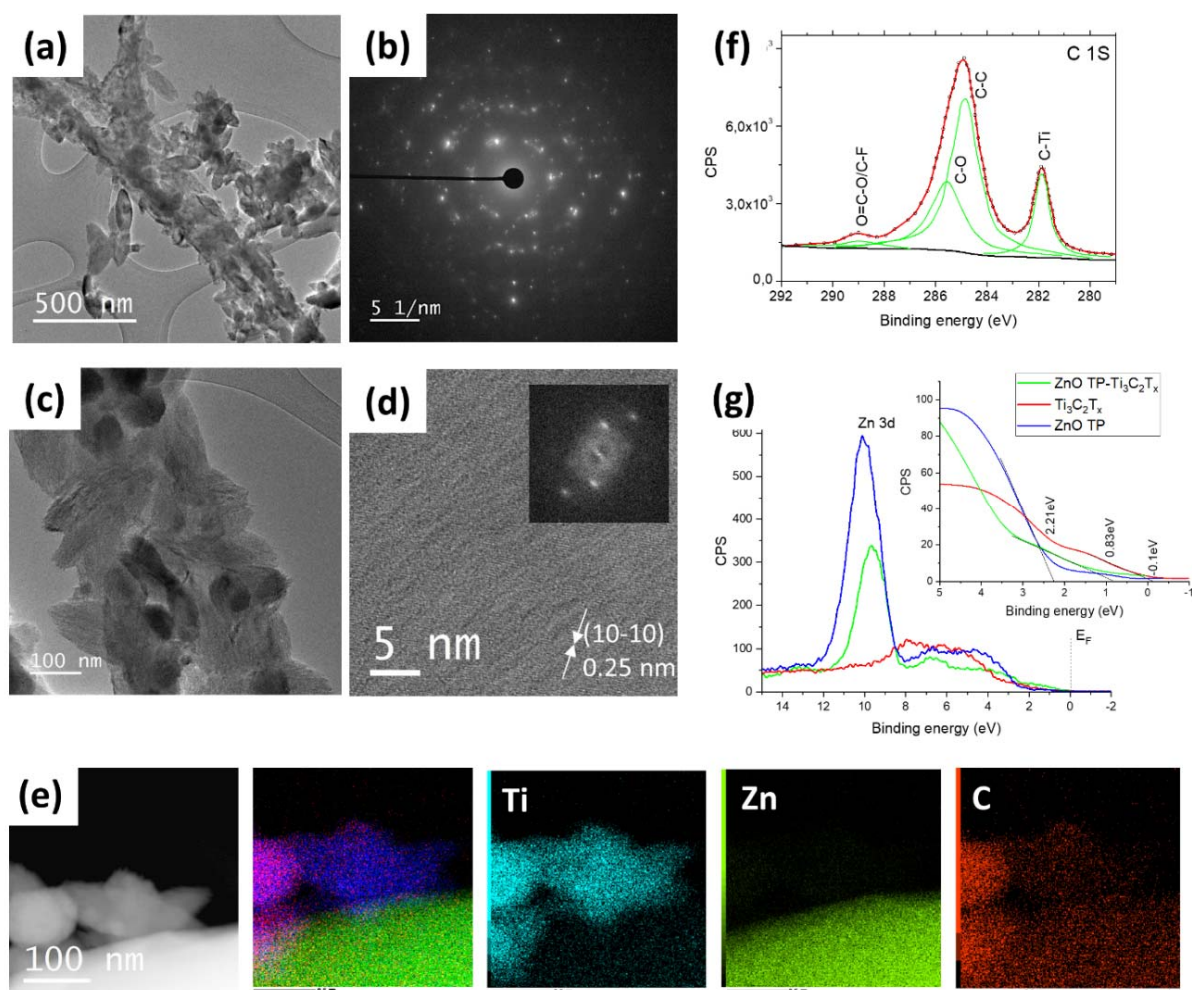


Figure 8.3. TEM and SAED images of ZnO/MXene nanocomposites (a-d); EDX element map scanning images of the interface between ZnO and MXene nanoflakes (e); the carbon core-level XPS spectrum of ZnO/MXene nanocomposites (f); Valence-band XPS spectra of ZnO TPs, MXene nanoflakes and ZnO/MXene nanocomposites (g).

The detailed structural and chemical properties of ZnO/MXene nanocomposites were analyzed using TEM and XPS (including Valence Band XPS). Figure 8.3a demonstrates the separate "leg" of ZnO TPs covered by MXene Ti₃C₂T_x nanoflakes. The uniform distribution of nanoflakes is clearly seen over the whole surface of ZnO (Fig. 8.3c, SI, Fig. S8.4). The corresponding selected area electron diffraction (SAED) pattern demonstrates the polycrystalline nature of ZnO/MXene nanocomposites (Fig. 8.3b). Figure 8.3d shows the high-resolution TEM image of the separate MXene nanoflakes. The lattice parameter of the Ti₃C₂T_x corresponding to (10 $\bar{1}$ 0) planes is measured to be about 0.255 nm. EDX elemental mapping images for the interface of ZnO-Ti₃C₂T_x are shown in Figure 8.3e. The uniform distribution of zinc, titanium, and carbon confirms the formation of the interface between the ZnO surface and Ti₃C₂T_x MXene nanoflakes.

The high-resolution XPS spectra of C 1s and other elements for ZnO/MXene nanocomposites were analyzed (Fig. 8.3f; SI, Fig. S8.5). The core level C 1s peak was fitted with four main components at 281.9, 284.8, 285.6, and 289.0 eV, which were attributed to C–Ti, C–C, C–O and C=O–O/C–F, respectively [359]. The O 1s deconvoluted spectrum (SI, Fig. S8.5) shows three main components at 529.7, 531.5, and 532.9 eV corresponding to O²⁻, –OH surface groups and absorbed water, respectively [359]. Recently, it was shown that Ti–O bonds are the most stable among the terminated groups of Ti₃C₂T_x MXene [360]. One may conclude that most terminated groups after the formation of ZnO/MXene nanocomposites are Ti–OH bonds, which was also confirmed by the high-resolution XPS Ti 2p peak (SI, Fig. S8.5).

One may suggest, both chemical and physical interactions between ZnO surface and MXene may lead to changes in the energy bands of obtained nanocomposites. To study this, the valence band (VB) XPS analysis was used, which can provide valuable information about the modification of the ZnO/MXene electronic structure. Figure 8.3g demonstrates the VB spectra for ZnO TP, Ti₃C₂T_x nanoflakes and ZnO/MXene nanocomposites. Typically, the VB spectrum determines the density of states (DOS) below the Fermi level. In the case of ZnO TPs samples, it consists of two components/bands at about 10 eV and 5 eV corresponding to Zn 3d and O 2p orbitals, respectively [155]. The broad VB XPS peak at 8–3 eV for pristine Ti₃C₂T_x MXene may be associated with the C 2s – Ti 3d hybridization region and the terminated groups on the surface [361]. The VB maximum (VBM) for those samples was evaluated using the standard method as previously described [362]. The VBM values were estimated to be 2.2 eV below and 0.1 eV above the Fermi level (E_F) for ZnO TPs and MXene, respectively. A high DOS above E_F is correlated to the low resistivity of Ti₃C₂T_x MXene. After the formation of ZnO/MXene nanocomposite, one may observe the shift to the lower energies of Zn 3d peak, confirming the chemical interaction of MXene nanoflakes with a ZnO surface. In addition, the estimated value of VBM for the ZnO/MXene nanocomposite becomes significantly lower (0.83 eV) in comparison to as-prepared ZnO TPs. It may be suggested the decreasing of the overall resistivity which must provide the enhanced electrocatalytic efficiency. Besides, according to the "d-band center theory", the modification of VBM can optimize the catalytic ability for the produced nanocomposites [363].

8.3.3. Electrochemical properties of the fabricated electrodes

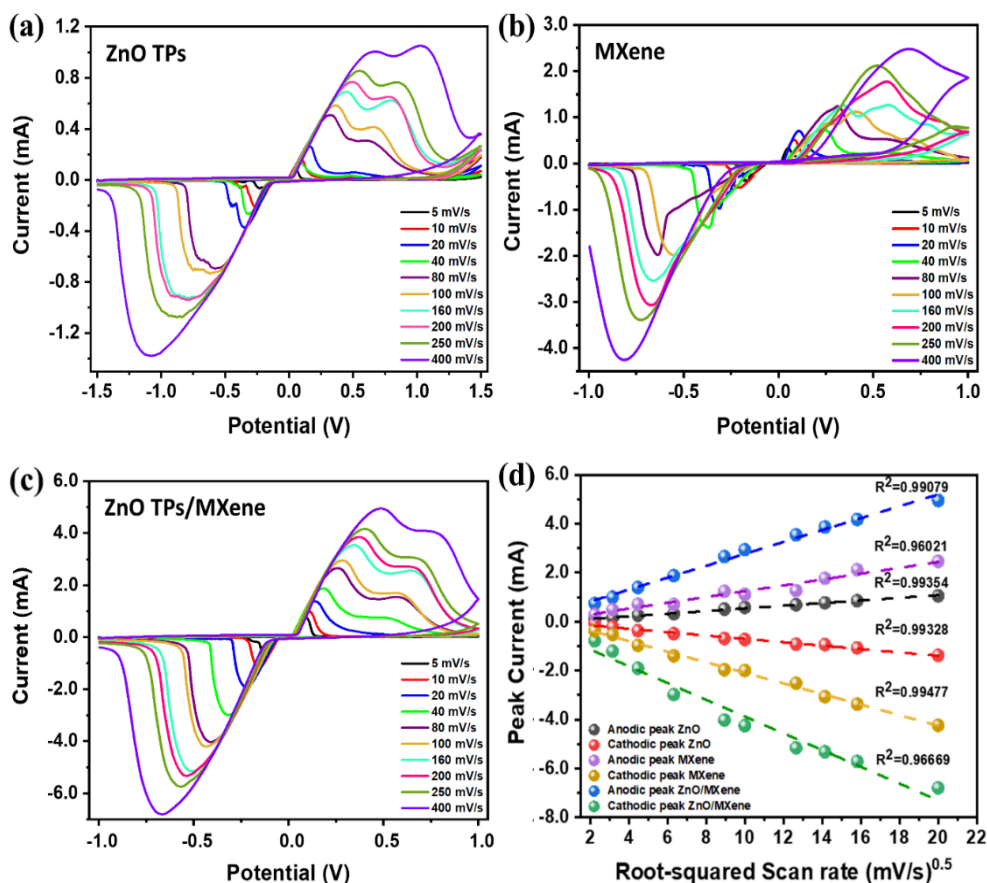


Figure 8.4. CV curves of ZnO TPs/GOx-based electrode (a), MXene/GOx-based electrode (b), ZnO TPs/MXene/GOx-based electrode (c) scanned in 0.3 mM of glucose in PBS (pH = 7.4) at different scan rates from 5 to 400 mV/s. The calibration plots of the anodic and cathodic peak currents vs the root-squared scan rate (for ZnO/GOx-, MXene/GOx-, and ZnO/MXene/GOx-based electrodes) (d).

In order to study the electrochemical behavior of prepared skin-attachable electrodes based on ZnO TPs/GOx, MXene/GOx, and ZnO TPs/MXene/GOx, the CV curves were recorded at different scan rates, and obtained plots are shown in Figure 8.4. The CV of ZnO TPs/GOx-based electrode (Fig. 8.4a) indicates that the peak current increases as the scan rate rises, pointing to the quasi-reversible redox reaction [364]. The quasi-reversibility was also observed for electrodes based on MXene/GOx (Fig. 8.4b) and ZnO TPs/MXene/GOx (Fig. 8.4c). Figure 8.4d shows that the peak current vs. the square root of scan rate is linear (R^2 varies from 0.96021 to 0.99477) for all samples, which indicates a typical diffusion-controlled electrochemical behavior [365]. In addition, the electron transfer rates between ZnO TPs-, MXene-, and ZnO TPs/MXene-based electrodes and immobilized GOx were calculated according to the Laviron formulation using the following equations [366]:

$$E_{p,c} = E^{o'} - \frac{2.3RT}{\alpha nF} \log \left[\frac{\alpha nFv}{RTk_s} \right], \quad (8.1)$$

$$E_{p,a} = E^{o'} - \frac{2.3RT}{(1-\alpha)nF} \log \left[\frac{(1-\alpha)nFv}{RTk_s} \right], \quad (8.2)$$

where $E_{p,a}$ is the potential of the anodic peak, $E_{p,c}$ is the potential of the cathodic peak, $E^{o'}$ is the standard surface potential calculated by averaging the anodic and cathodic potentials at slow scan rates, v is the scan rate, α is the electron-transfer coefficient, k_s is the electron-exchange rate constant, R is the ideal gas constant, T is the absolute temperature (K), F is the Faraday constant, and n is the number of electrons transferred. Electron transfer parameters (α , and k_s) were determined by plotting E_p vs. the log of the scan rate (Laviron plots) [367]. Using the slopes of linear portions of the Laviron curves (not shown here) for the ZnO TPs/GOx-, MXene/GOx-, and ZnO TP/MXene/GOx-based electrodes, the electron transfer constants were calculated as 0.46 ± 0.09 , 0.67 ± 0.11 , and 0.4 ± 0.04 , respectively, while the electron-exchange rate constants were determined equal to 0.48 ± 0.03 s⁻¹, 0.36 ± 0.08 s⁻¹, 1.01 ± 0.11 s⁻¹, respectively. The analysis of the obtained k_s values shows that ZnO TP decorating by MXene facilitate the transfer of electrons between the GOx and the electrode. Generally, the higher value of electron-exchange rate indicates the lower resistivity of the electrode modifier. The electrochemical impedance spectroscopy (EIS) confirmed the lower resistivity of ZnO TP/MXene in comparison to the pure ZnO TP electrode (Fig. 8.5).

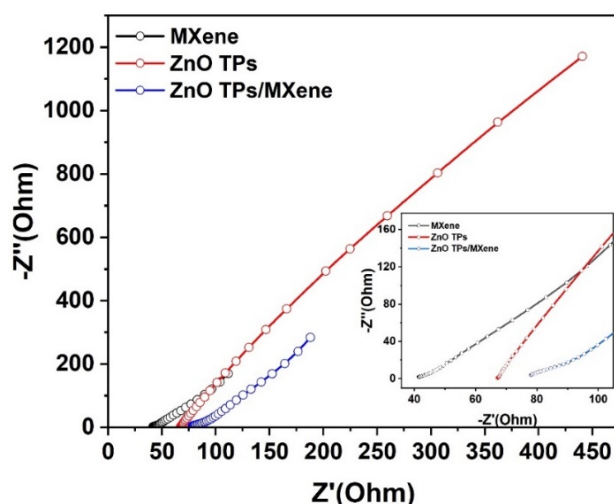


Figure 8.5. EIS spectra. Nyquist plots of MXene, ZnO TPs and ZnO TPs/MXene.

The above results comply well with the recently reported results for Ti₃C₂/ZnO composites, where the interaction between ZnO and Ti₃C₂ (MXene) facilitates

electron transport [368]. Authors also have shown that the rate capacity, in turn, was directly related to the enhanced surface to volume ratio of $\text{Ti}_3\text{C}_2/\text{ZnO}$ and an increase in the number of three-dimensional channels for the fast electron transport and the fast ion diffusion [368]. Moreover, another 2D conductive material, like graphene, was already used to decorate ZnO nanomaterials, which led to a 3-fold increase in catalytic activity due to an increase in the electron transfer rate by 3-4 times as compared to a bare ZnO-based electrode [369]. Thus, on the basis of the foregoing, it was suggested that an increase (2-3 times) in the electron exchange rate for the ZnO TPs/GOx –based electrode may lead to its better catalytic activity towards glucose oxidation.

8.3.4. CV-based sensor performance

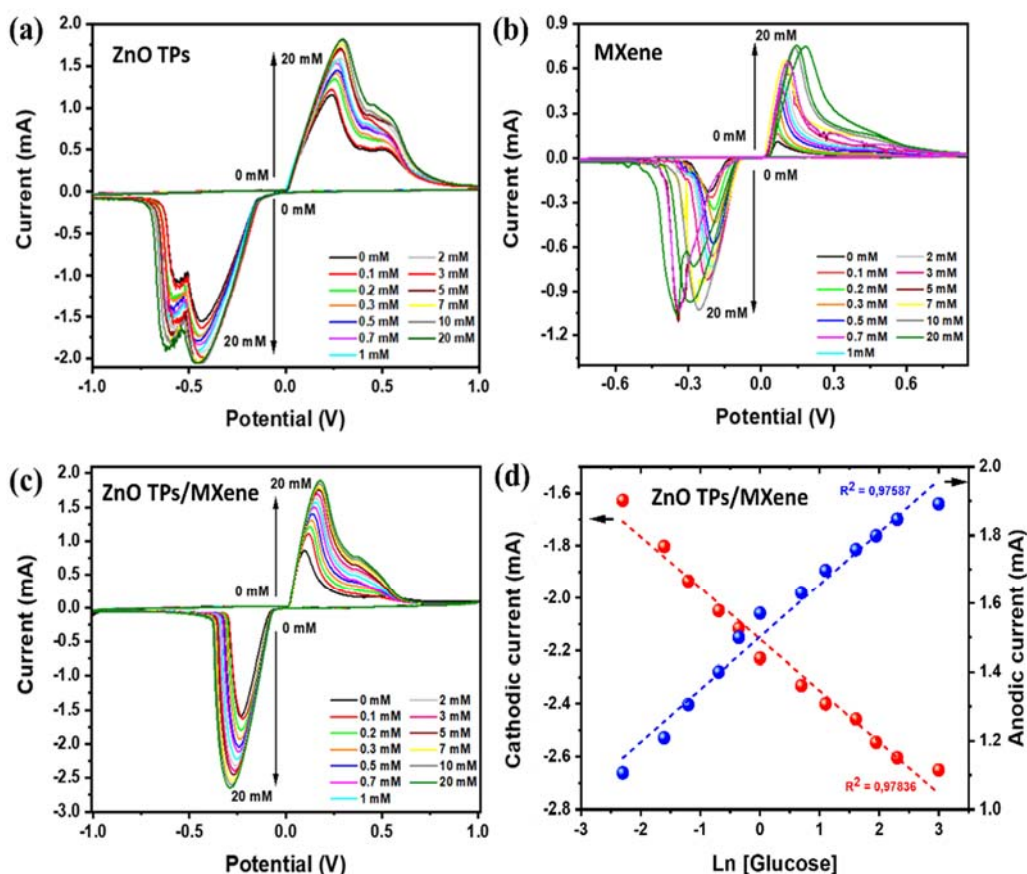
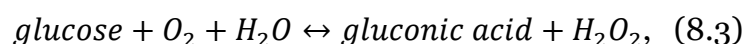
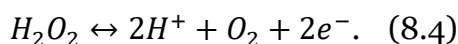


Figure 8.6. Sensor performance. CV of ZnO TPs/GOx-based electrode (a), MXene/GOx-based electrode (b), ZnO TPs/MXene/GOx-based electrode (c) on skin-attachable electrode in various concentrations of glucose in PBS (pH = 7.4). Show the calibration curves of both the anodic and cathodic peak currents vs glucose concentrations (for ZnO TPs/MXene/GOx-based electrode at scan rate 40mV/s) (d).

CV-based measurements were performed to test the catalytic oxidation of glucose on GOx produced electrodes. For this purpose, various glucose concentrations were sequentially added to the electrochemical cell containing PBS with ZnO TPs/GOx-, MXene/GOx-, and ZnO TPs/MXene/GOx-based electrodes (one type of electrode per experiment). CV curves were measured in PBS solution under stirring conditions to achieve a homogeneous glucose distribution in the electrochemical cell. Depending on the electrode, the range of the recorded potential varied from -1 V to 1 V for ZnO TPs/GOx- and ZnO TPs/MXene/GOx-based electrodes (Fig. 8.6a, b), and -0.6 to 0.6 V for MXene/GOx-based electrodes (Fig. 8.6c), and the scanning rate was chosen equal to 40 mV/s. Figure 8.6d demonstrates the peak current *vs* the natural logarithm of the glucose concentrations (sensitivity: 0.54 ± 0.09 mA mM⁻¹ cm⁻², measured in the CV mode for ZnO TPs/MXene/GOx-based electrode within the physiological range of blood glucose (0 to 20 mM). The sensitivities for ZnO TPs/GOx-, and MXene/GOx-based electrodes were calculated as 0.45 ± 0.06 mA mM⁻¹ cm⁻², and 0.43 ± 0.07 mA mM⁻¹ cm⁻² indicating the lower glucose sensitivity in comparison to ZnO TPs/MXene/GOx-based electrode. It is seen that the cathodic and anodic currents gradually increase with the glucose concentration, indicating the glucose electrocatalytic oxidation behavior for ZnO TPs/GOx-, MXene/GOx-, and ZnO TPs/MXene/GOx-based electrodes. The typical reactions occurring at the working electrode can be described as following [370]:



while, the reaction occurring at the counter electrode can be expressed by the following equation [370]:



Thus, the detection of glucose can be carried out in both the CV mode and the linear sweep voltammetry (LSV) mode [365], measuring signals corresponding to hydrogen peroxide oxidation or dissolved oxygen reduction (free oxygen is consumed during the oxidation of glucose to gluconic acid by GOx in the surroundings of the working electrode). The latter approach is based on the decrease of the cathodic current (oxygen reduction reaction – ORR) upon the addition of glucose. The operation in the cathodic regime (negative potentials) allows one to eliminate the effect of interference species. Besides, it is clearly seen the shift of the reduction potential of the ZnO TPs/MXene/GOx-based electrode to the lower values

(-0.21 V) in comparison to the ZnO TPs/GOx- based electrode. According to this, one may conclude that MXene enhances the catalytic activity of produced nanocomposites.

8.3.5. Chronoamperometry-based sensor performance in PBS (pH = 7.4)

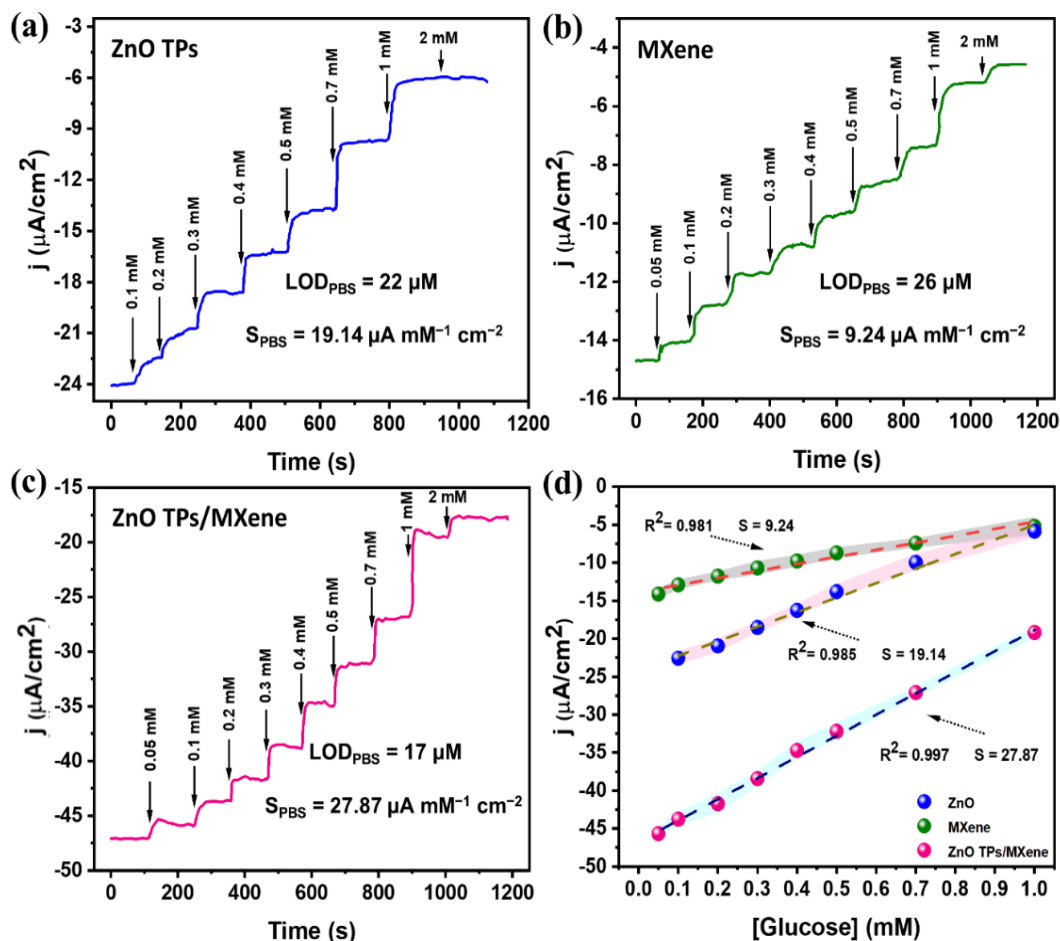


Figure 8.7. Chronoamperometry measurements in PBS with different concentrations of glucose for ZnO TPs/GOx-based electrode at applied potential -0.32 V (a), MXene/GOx-based electrode at applied potential -0.24 V (b), ZnO TPs/MXene/GOx-based electrode at applied potential -0.21 V (c). Calibration curves for the ZnO TPs-, MXene-, and ZnO TPs/MXene/GOx-based electrodes (d).

After a comprehensive analysis of the structural, optical properties, and the electrochemical behavior of the fabricated ZnO TPs/GOx-, MXene/GOx-, and ZnO TP/MXene/GOx-based electrodes, all the necessary parameters were determined for the subsequent chronoamperometric detection of glucose. Figures 8.7 (a-c) represents chronoamperometry curves during the sequential addition of glucose to PBS solution for the ZnO TPs/GOx-, MXene/GOx-, and ZnO TP/MXene/GOx-based electrodes, respectively. One may observe the well-known stairs-like behavior of the

current response vs. the concentration of glucose biosensors [329,371]. Working potentials for glucose detection varied depending on the electrode. Figure 8.7d shows the linear calibration curves obtained from the stair-like chronoamperometry curves that show current densities *vs* the glucose concentrations. The sensitivities of the ZnO TPs/GOx-, MXene/GOx-, and ZnO TP/MXene/GOx-based electrodes towards the glucose were determined from the slopes of the calibration curves and were estimated to be $19.14 \pm 1.4 \mu\text{A mM}^{-1} \text{cm}^{-2}$, $9.24 \pm 1.2 \mu\text{A mM}^{-1} \text{cm}^{-2}$, and $27.87 \pm 2.8 \mu\text{A mM}^{-1} \text{cm}^{-2}$, respectively. The LODs were calculated using eq. (5) [333].

$$LOD = 3.3 \cdot \sqrt{n} \cdot \sigma/b, \quad (8.5)$$

where σ is the standard deviations of the negative control at small concentrations, n – number of tests, b is the slope of the curve, depicted in Figure 8.7d.

The values of LODs were estimated to be $22 \pm 1.3 \mu\text{M}$, $26 \pm 1.8 \mu\text{M}$ and $17 \pm 1.7 \mu\text{M}$ for ZnO TPs/GOx-, MXene/GOx-, and ZnO TP/MXene/GOx-based electrodes, respectively. One can assume that the higher sensitivity and the lower LOD of ZnO TP/MXene/GOx-based electrode can be attributed to its enhanced electron transfer rate if compared to ZnO TPs/GOx- and MXene/GOx-based electrodes. Recent references show that the sensitivity of the prepared ZnO TPs/MXene/GOx-based electrode is competitive with the reported sensitivities of skin-attachable or screen-printed glucose electrodes (Table 8.1).

The mechanism behind these types of amperometric glucose sensors is based on the change in the concentration of free oxygen surrounding the working electrode. The reduction current depends on the activity of the electrode towards the oxygen reduction reaction since a higher oxygen concentration provides a high reduction current, and contrary. In this particular case, the oxygen concentration is governed by the oxidation of the glucose at the hydroxyl (flavin adenine dinucleotide (FAD)) group of GOx, which occurs with free oxygen consumption [372]:



The GOx catalyzes the oxidation of glucose to D-glucono-1.5-lactone with the consumption of O_2 and reduction of FAD to FADH_2 . Since FADH_2 in an aqueous solution tends to be oxidized, it gives the protons to reduce water molecules to H_2O_2 . Depending on the applied potential, either the anodic current for measuring the rate

of H₂O₂ oxidation or the current promoted by the O₂ reduction in the cathodic area can be used [373].

Table 8.1. Comparison of sensitivities to glucose for different skin-attached or screen-printed electrodes.

Sample name	Electrolyte	Sensitivity, $\mu\text{A mM}^{-1} \text{cm}^{-2}$	LOD, μM	Reference
Au/rGO/PtNPs	Artificial sweat	29.10	200	[374]
GOx/Pt graphite	PBS	0.69	10	[375]
v-Au NW film	PBS	23.72	10	[376]
CoWO ₄ /CNT	PBS	10.89	1.3	[377]
SnO ₂ and CNT on PET	PBS	7.8	-	[378]
ZnO-NW E μ PAD	PBS	2.88	94.7	[379]
PET based gold	PBS	22.05	2.7	[380]
ZnO TP/MXene	PBS	27.87	17	This work
ZnO TP/MXene	Artificial sweat	29.88	21	This work
ZnO TPs	PBS	19.14	22	This work
MXene	PBS	9.24	26	This work

8.3.6. Chronoamperometry-based sensor performance in artificial sweat (pH = 6.5)

The sensor was initially intended to be used for qualitative analysis of sweat glucose. Therefore, it was important to test the produced electrode under sweat-like conditions. For this purpose, ZnO TP/MXene/GOx- based electrode was chosen as the most efficient one. All experiments were performed in artificial sweat with pH ~6.5 (detailed information in the experimental section). The amperometric detection showed a similar stairs-like response of current density to glucose

concentrations (Fig. 8.8a). The linear detection range (LDR) (in artificial sweat) of the glucose sensor lies between 0.05 and 0.7 mM. The sensitivity to glucose was extracted from the slope of the calibration curve and was about $29.88 \pm 2.4 \mu\text{A mM}^{-1} \text{cm}^{-2}$ (Fig. 8.8b). The value of LOD was calculated to be $21 \pm 1.1 \mu\text{M}$.

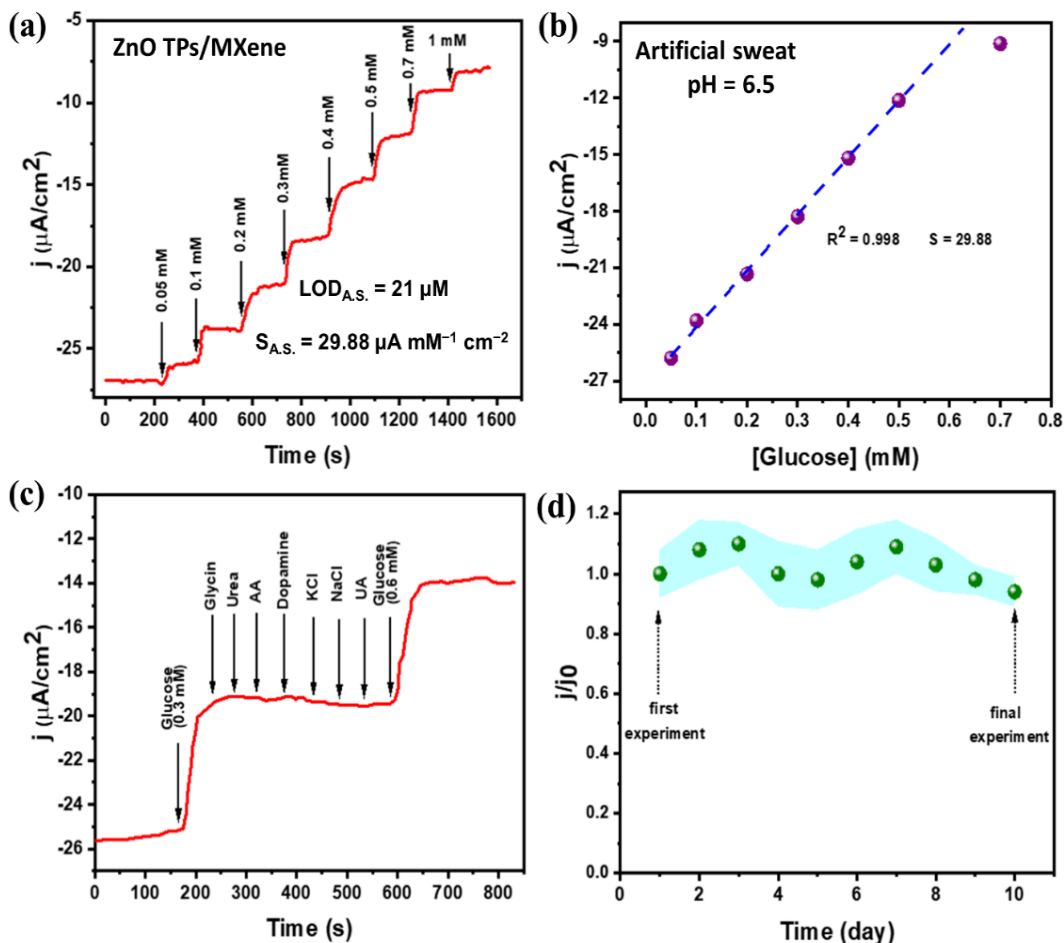


Figure 8.8. Chronoamperometry measurements for ZnO TPs/MXene/GOx-based electrode in artificial sweat containing different concentrations of glucose (applied potential -0.24 V) (a). Calibration curve indicating a linear relationship between the current density of ZnO TPs/MXene/GOx-based electrode and glucose concentration (b). Selective glucose detection by use of ZnO TPs/MXene/GOx-based electrode (c). Long-term stability and multiple use of the ZnO TPs/MXene/GOx-based electrode (d).

One of the main characteristics of the sensor is its selectivity with respect to various interfering agents contained in the analyte of interest. Figure 8.8c shows the selectivity tests of ZnO TPs/MXene/GOx-based electrode to detect 0.3 mM and 0.6 mM of glucose under the interference of different agents such as 0.1 mM AA, 0.5 mM urea, 50 μM UA, 0.05 mM dopamine, 10 mM NaCl, 10 mM KCl, and 0.1 mM glycine. As can be observed, ZnO TPs/MXene/GOx-based electrode provides highly selective glucose detection because of the specific interaction of the glucose and GOx

treated ZnO TPs/MXene composites. Moreover, the high selectivity may also be explained by the low applied potential (-0.24 V) insufficient to oxidize interfering agents (such as AA, UA, etc.) [372].

Figure 8.8d represents the long-term stability of the ZnO TPs/MXene/GOx- based electrode for glucose detection during 10 days of the experiments. After each experiment (one per day) the electrode was rinsed in PBS and deionized water, and then stored in a refrigerator at 4°C ready to be reused for further tests. The maximum deviation of the current density was about 10%, which barely affects the sensitivity of the ZnO TPs/MXene/GOx- based electrode up to 10 days. Besides, the reproducibility of produced ZnO TPs/MXene/GOx- based electrodes was studied. Twelve sets of samples/electrodes were produced using the same protocol. The deviation of sensor performance parameters was about of 10% (SI, Fig. S8.6).

8.3.7. Sensors performance under different applied strains

Considering skin-attachable sensor performance, studying its stability under various mechanical stresses is important. This research analyzed the sensor's performance of ZnO TPs/MXene/GOx-based electrodes under different applied strains ranging from 0% to 35%. This value of strains range is enough for flexible sensors to enable its application as a skin-attachable device. Figure 8.9a shows the experimental setup for analysis of the stretch abilities of produced sensors. The working, auxiliary, and counter electrodes were sandwiched between slides to prevent the spread out of the analyte and to maintain a constant analyte volume during the experiment. The inset of Figure 8.9b shows the relative change of the sensor response, where j and j_0 current densities before and after applied strains, respectively. It can be seen that the ZnO TPs/MXene/GOx electrode demonstrates a stable response (95% – 100%) up to 30% elongation, while significant instability occurs at 35% elongation. It might be explained by the fact that the deformation of the ZnO TPs/MXene matrix leads to a decrease in the number of electron path-ways and, consequently, to the current reduction. The glucose detection under application of strains up to 30% (Fig. 8.9b) showed nearly identical calibration curves (current densities *vs* glucose concentrations) with similar slopes, indicating similar sensitivities and LODs. It may be noted, that the developed ZnO TPs/MXene/GOx-based sensors demonstrate the better or comparable with other stretchable sensors

based on CoWO_4/CNT [377], and v-Au NW-electrodes, where the 30% elongation caused a significant current reduction (~ 5 times) [376].

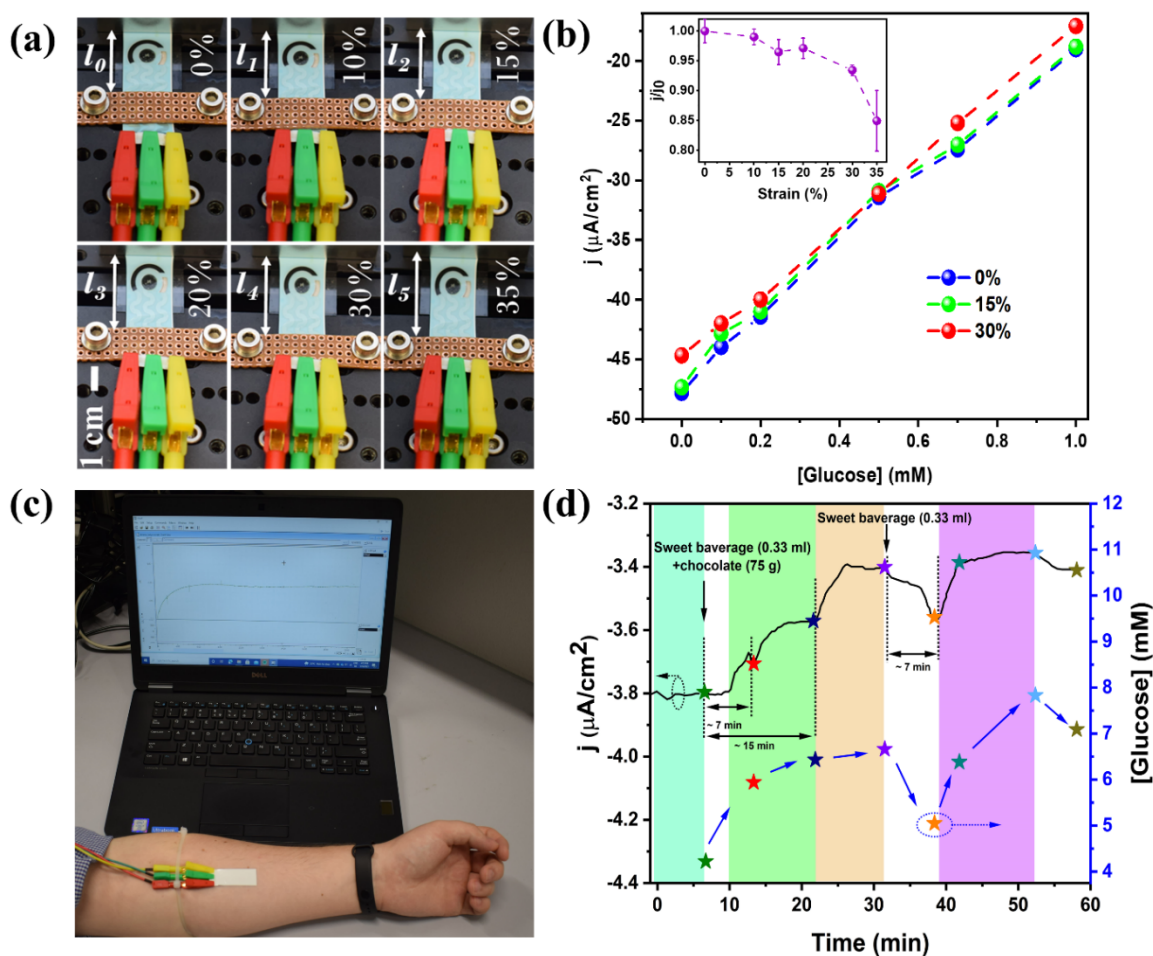


Figure 8.9. Digital photographs of the stretchable ZnO TPs/MXene/GOx-based electrode at various strains (0% - 35%) (a). Performance of the glucose sensor (in artificial sweat) at various applied strains (the insert graph represents the change of ZnO TPs/MXene/GOx electrode current density vs applied strains) (b). Digital photograph of skin-attachable sensor performance for sweat glucose qualitative analysis (c). Graph representing the current density changes of the ZnO TPs/MXene/GOx-based sensor under the sweets consumption (d).

8.3.8. Qualitative glucose monitoring using stretchable ZnO TPs/MXene/GOx electrode

In the final stage of the research, the developed glucose sensor based on ZnO TPs/MXene/GOx nanocomposites were applied for human sweat analysis. The sensing skin-attachable pathway is depicted in Figure 8.9c. The change in current density was recorded in real-time, during sweets consumption and exercising after the signal stabilization (blue area, Fig. 8.9d). The sweets were followed by exercises (squats) to stimulate sweating, which is associated with higher post-meal blood

glucose levels [92]. It is considered that sugar from beverages is absorbed in the intestine within 10-15 minutes [381], which corresponds to the decrease in current density and its saturation within 15 minutes (the light green area in Fig. 8.9d).

Such a behavior of the current density correlates well with the experiments in PBS and artificial sweat, thereby pointing to the increment of the glucose content (post-meal glucose) in a naturally produced sweat. The second decrease in current density (light orange area) may be due to the sugar from the chocolate as it takes longer time (15-30 min) to reach the bloodstream [382]. After the two-stage decline (up to 31th min), the current density increased (31-38 min), indicating a drop in the sweat glucose. This decrease in post-meal sweat sugar may be related to muscle glucose uptake during exercise [383]. Then, the second dose of sweet beverage was consumed (at 32 min) to increase the glucose level. It is seen that the current density decreased again, thereby confirming the similar behavior of the skin-attachable sensor after the glucose level increased. In parallel with the qualitative glucose monitoring in sweat, the conventional approach for glucose levels detection has been performed by using a commercially available blood glucometer. It is obvious that the sweat glucose real-time monitoring and discrete measurements by means of glucometer had similar trends as shown in Figure 8.9d. Moreover, the real-time measurement of the current density of the amperometric glucose sensor correlates well with the other sensors for post-meal glucose monitoring [329,384,385]. In addition, qualitative glucose monitoring was performed in a second volunteer, and the results demonstrated the similar trend (SI, Fig. S8.7).

8.4. Conclusions

In this study, ZnO TPs/MXene-based electrodes were fabricated and used for on-body qualitative glucose monitoring in sweat. The synthesis of ZnO TPs/MXene was performed in accordance with the three-step manufacturing process, including the synthesis of MXene and ZnO, with the following decoration of ZnO TPs with MXene nanoflakes. The fabricated sensors exhibited high sensitivity of $27.87 \mu\text{A mM}^{-1} \text{cm}^{-2}$ and $29.88 \mu\text{A mM}^{-1} \text{cm}^{-2}$ for tests in PBS and artificial sweat, respectively. Moreover, none of the interfering agents affected the sensor response, which indicates the high selectivity of the produced ZnO TPs/MXene/GOx-based electrodes. The long-term stability of the sensor was studied during a 10-days experiment, and the result showed that the sensor response remains stable within this period. The ZnO

TPs/MXene/GOx-based electrode demonstrated mechanical stability of up to 30% elongation, with an insignificant change of the detection parameters. The real-time monitoring of post-meal glucose levels in sweat had the same trend as when measured with a conventional blood glucometer under similar conditions. The developed skin-attachable and stretchable electrodes based on ZnO TPs/MXene nanocomposites demonstrate a prospective approach towards non-invasive, continuous glucose monitoring in sweat for healthcare applications.

Supporting information

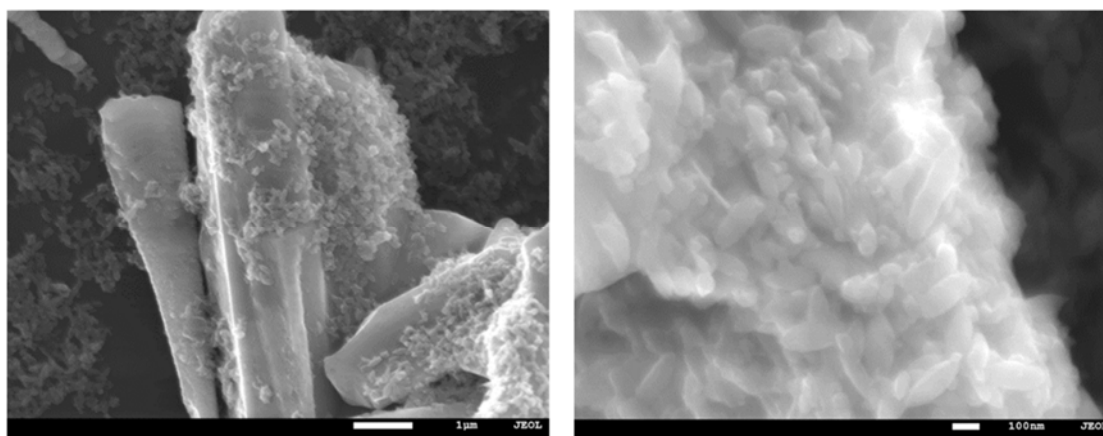


Figure S8.1. SEM images of an uneven distribution of MXene nanoflakes on the surface of ZnO TPs.

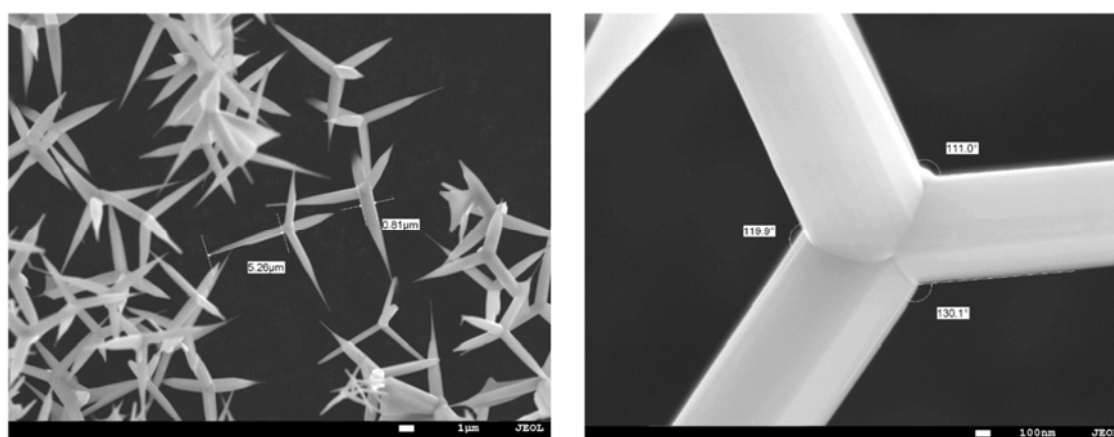


Figure S8.2. SEM images of pristine ZnO TPs.

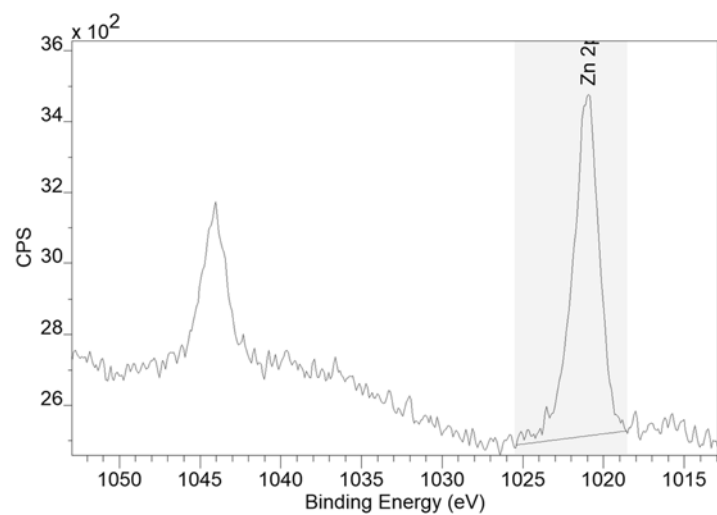


Figure S8.3. The core-shell XPS spectra of ZnO TPs sample.

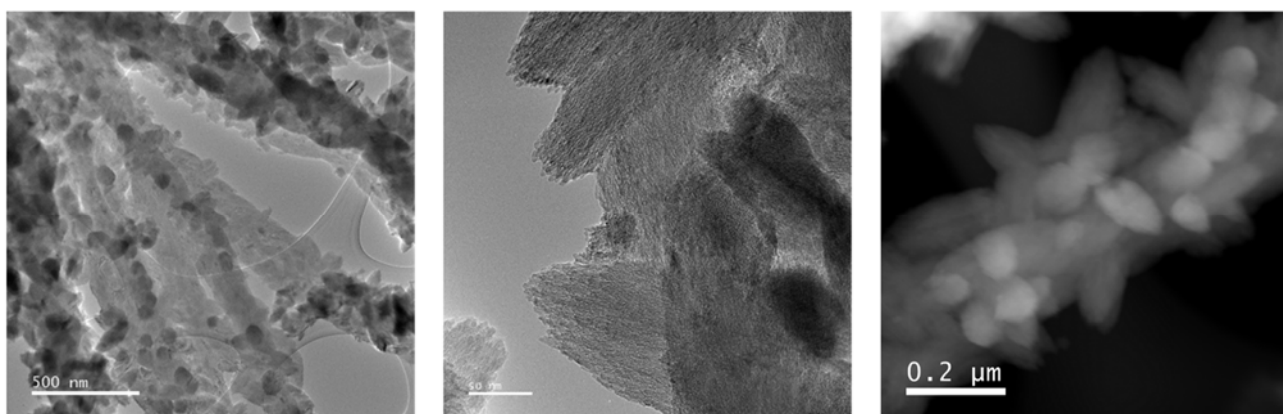
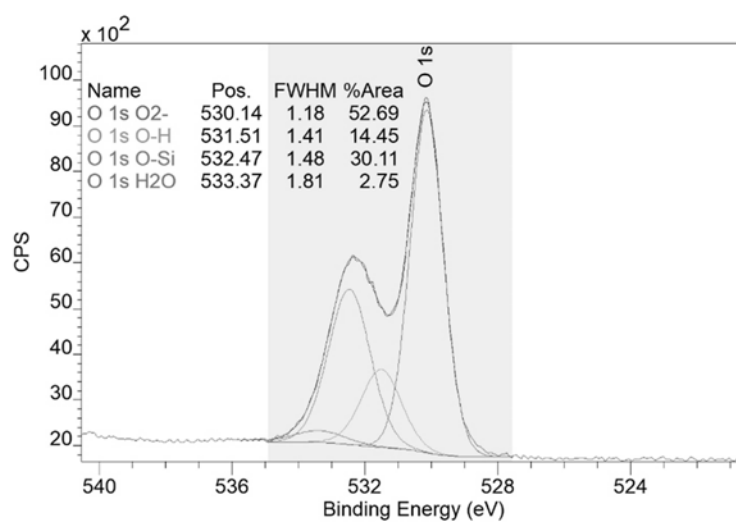


Figure S8.4. TEM image of MXene nanoflakes distribution on the surface of ZnO TPs.



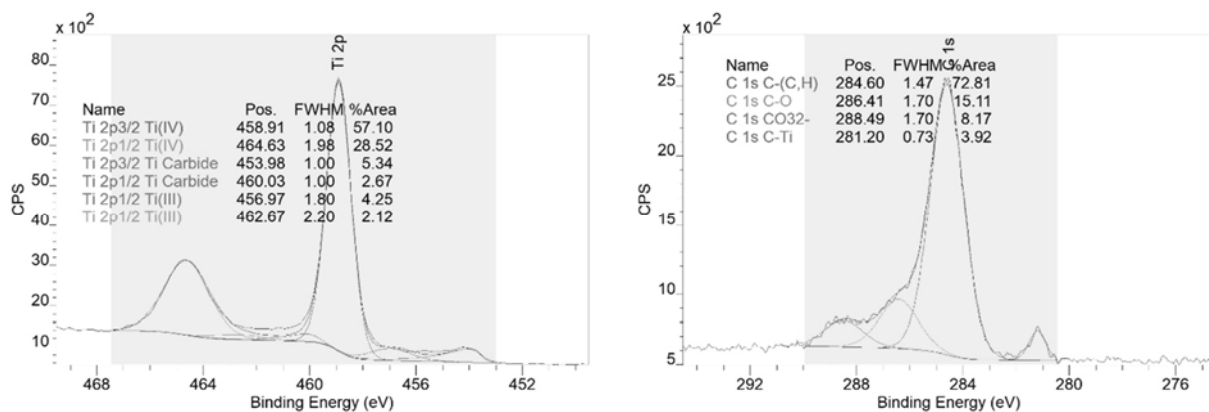


Figure S8.5. XPS analysis of ZnO TPs/MXene nanocomposites.

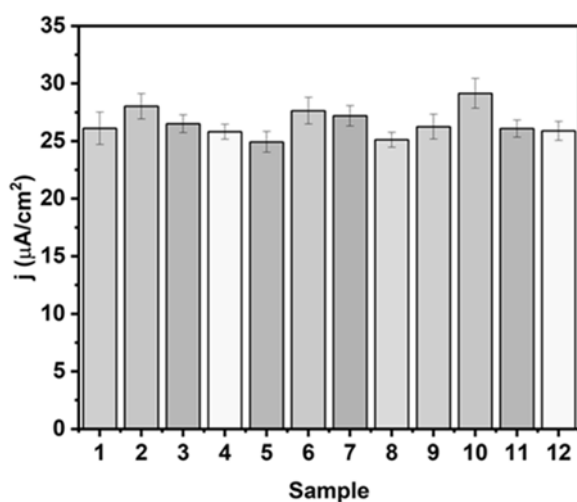


Figure S8.6. Bench to bench reproducibility of ZnO TPs/MXene electrode (measured in artificial sweat).

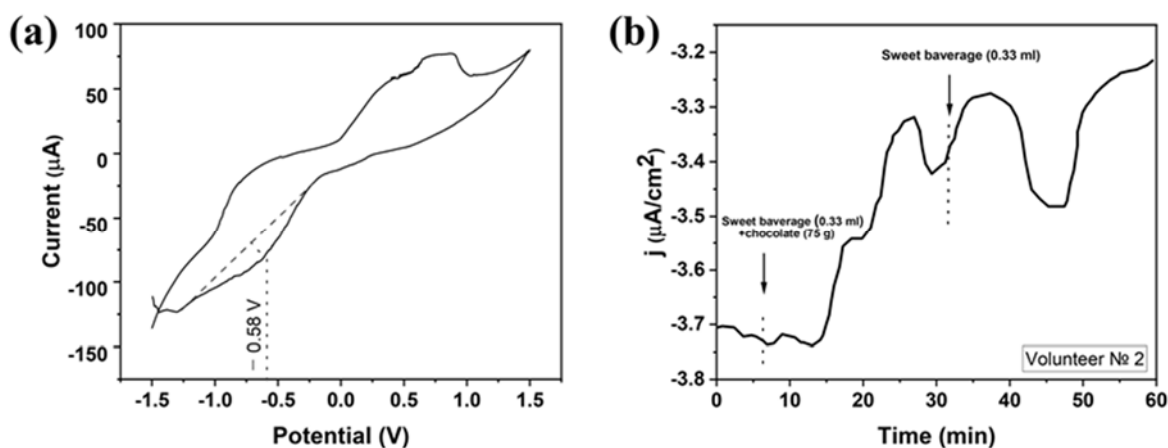


Figure S8.7. CV curve recorded before the chronoamperometry measurements in order to estimate the potential of the reduction peak (a). Graph representing the current density changes of the ZnO TPs/MXene/GOx-based sensor under the sweets consumption in a healthy 25-year-old subject (b).

References

1. Teymourian, H.; Barfidokht, A.; Wang, J. Electrochemical glucose sensors in diabetes management: an updated review (2010–2020). *Chem. Soc. Rev.* **2020**, *49*, 7671–7709, doi:10.1039/DoCS00304B.
2. Rahmani, A.R.; Leili, M.; Azarian, G.; Poormohammadi, A. Sampling and detection of corona viruses in air: A mini review. *Sci. Total Environ.* **2020**, *740*, 140207, doi:10.1016/j.scitotenv.2020.140207.
3. Zamir, D.; Galsurker, O.; Alkan, N.; Eltzov, E. Detection of quiescent fungi in harvested fruit using CMOS biosensor: A proof of concept study. *Talanta* **2020**, *217*, 120994, doi:10.1016/j.talanta.2020.120994.
4. Roointan, A.; Ahmad Mir, T.; Ibrahim Wani, S.; Mati-ur-Rehman; Hussain, K.K.; Ahmed, B.; Abraham, S.; Savardashtaki, A.; Gandomani, G.; Gandomani, M.; et al. Early detection of lung cancer biomarkers through biosensor technology: A review. *J. Pharm. Biomed. Anal.* **2019**, *164*, 93–103, doi:10.1016/j.jpba.2018.10.017.
5. Naresh, V.; Lee, N. A Review on Biosensors and Recent Development of Nanostructured Materials-Enabled Biosensors. *Sensors* **2021**, *21*, 1109, doi:10.3390/s21041109.
6. Tran, V. Van; Tran, N.H.T.; Hwang, H.S.; Chang, M. Development strategies of conducting polymer-based electrochemical biosensors for virus biomarkers: Potential for rapid COVID-19 detection. *Biosens. Bioelectron.* **2021**, *182*, 113192, doi:10.1016/j.bios.2021.113192.
7. Pundir, C.S.; Lata, S.; Narwal, V. Biosensors for determination of D and L-amino acids: A review. *Biosens. Bioelectron.* **2018**, *117*, 373–384, doi:10.1016/j.bios.2018.06.033.
8. Sabu, C.; Henna, T.K.; Raphey, V.R.; Nivitha, K.P.; Pramod, K. Advanced biosensors for glucose and insulin. *Biosens. Bioelectron.* **2019**, *141*, 111201, doi:10.1016/j.bios.2019.03.034.
9. Tian, B.; Ma, J.; Zardán Gómez de la Torre, T.; Bálint, Á.; Donolato, M.; Hansen, M.F.; Svedlindh, P.; Strömberg, M. Rapid Newcastle Disease Virus Detection Based on Loop-Mediated Isothermal Amplification and Optomagnetic Readout. *ACS Sensors* **2016**, *1*, 1228–1234, doi:10.1021/acssensors.6b00379.
10. Castle, L.M.; Schuh, D.A.; Reynolds, E.E.; Furst, A.L. Electrochemical Sensors to Detect Bacterial Foodborne Pathogens. *ACS Sensors* **2021**, *6*, 1717–1730, doi:10.1021/acssensors.1c00481.
11. Denisov, I.; Lukyanenko, K.; Yakimov, A.; Kukhtevich, I.; Esimbekova, E.; Belobrov, P. Disposable luciferase-based microfluidic chip for rapid assay of water pollution. *Luminescence* **2018**, *33*, 1054–1061, doi:10.1002/bio.3508.

12. Jayan, H.; Pu, H.; Sun, D.-W. Recent development in rapid detection techniques for microorganism activities in food matrices using bio-recognition: A review. *Trends Food Sci. Technol.* **2020**, *95*, 233–246, doi:10.1016/j.tifs.2019.11.007.
13. Felix, F.S.; Angnes, L. Electrochemical immunosensors – A powerful tool for analytical applications. *Biosens. Bioelectron.* **2018**, *102*, 470–478, doi:10.1016/j.bios.2017.11.029.
14. Gizeli, E.; Lowe, C.R. Immunosensors. *Curr. Opin. Biotechnol.* **1996**, *7*, 66–71, doi:10.1016/S0958-1669(96)80097-8.
15. Peltomaa, R.; Glahn-Martínez, B.; Benito-Peña, E.; Moreno-Bondi, M. Optical Biosensors for Label-Free Detection of Small Molecules. *Sensors* **2018**, *18*, 4126, doi:10.3390/s18124126.
16. Wang, X.; Cohen, L.; Wang, J.; Walt, D.R. Competitive Immunoassays for the Detection of Small Molecules Using Single Molecule Arrays. *J. Am. Chem. Soc.* **2018**, *140*, 18132–18139, doi:10.1021/jacs.8b11185.
17. Bange, A.; Halsall, H.B.; Heineman, W.R. Microfluidic immunosensor systems. *Biosens. Bioelectron.* **2005**, *20*, 2488–2503, doi:10.1016/j.bios.2004.10.016.
18. Shen, J.; Li, Y.; Gu, H.; Xia, F.; Zuo, X. Recent Development of Sandwich Assay Based on the Nanobiotechnologies for Proteins, Nucleic Acids, Small Molecules, and Ions. *Chem. Rev.* **2014**, *114*, 7631–7677, doi:10.1021/cr300248x.
19. Sakamoto, S.; Putalun, W.; Vimolmangkang, S.; Phoolcharoen, W.; Shoyama, Y.; Tanaka, H.; Morimoto, S. Enzyme-linked immunosorbent assay for the quantitative/qualitative analysis of plant secondary metabolites. *J. Nat. Med.* **2018**, *72*, 32–42, doi:10.1007/s11418-017-1144-z.
20. Karunakaran, C.; Pandiaraj, M.; Santharaman, P. Immunosensors. In *Biosensors and Bioelectronics*; Elsevier, **2015**; pp. 205–245 ISBN 9780128031018.
21. Ricci, F.; Adornetto, G.; Palleschi, G. A review of experimental aspects of electrochemical immunosensors. *Electrochim. Acta* **2012**, *84*, 74–83, doi:10.1016/j.electacta.2012.06.033.
22. Wen, W.; Yan, X.; Zhu, C.; Du, D.; Lin, Y. Recent Advances in Electrochemical Immunosensors. *Anal. Chem.* **2017**, *89*, 138–156, doi:10.1021/acs.analchem.6b04281.
23. Magliulo, M.; De Tullio, D.; Vikholm-Lundin, I.; Albers, W.M.; Munter, T.; Manoli, K.; Palazzo, G.; Torsi, L. Label-free C-reactive protein electronic detection with an electrolyte-gated organic field-effect transistor-based immunosensor. *Anal. Bioanal. Chem.* **2016**, *408*, 3943–3952, doi:10.1007/s00216-016-9502-3.

24. Mulla, M.Y.; Torsi, L.; Manoli, K. Electronic biosensors based on EGFETs. In *Methods in Enzymology*; **2020**; pp. 403–433 ISBN 9780128211571.
25. Wang, D.; Noël, V.; Piro, B. Electrolytic Gated Organic Field-Effect Transistors for Application in Biosensors—A Review. *Electronics* **2016**, *5*, 9, doi:10.3390/electronics5010009.
26. Nikolka, M.; Simatos, D.; Foudeh, A.; Pfattner, R.; McCulloch, I.; Bao, Z. Low-Voltage, Dual-Gate Organic Transistors with High Sensitivity and Stability toward Electrostatic Biosensing. *ACS Appl. Mater. Interfaces* **2020**, *12*, 40581–40589, doi:10.1021/acsami.0c10201.
27. Wang, J.; Ye, D.; Meng, Q.; Di, C.; Zhu, D. Advances in Organic Transistor Based Biosensors. *Adv. Mater. Technol.* **2020**, *5*, 2000218, doi:10.1002/admt.202000218.
28. Mayeen, A.; Kalarikkal, N. Development of ceramic-controlled piezoelectric devices for biomedical applications. In *Fundamental Biomaterials: Ceramics*; Elsevier, **2018**; pp. 47–62 ISBN 9780081022047.
29. Lim, S.A.; Ahmed, M.U. Chapter 1. Introduction to Immunosensors. In *RSC Detection Science*; **2019**; pp. 1–20 ISBN 9781788011020.
30. Fu, Y.Q.; Luo, J.K.; Nguyen, N.T.; Walton, A.J.; Flewitt, A.J.; Zu, X.; Li, Y.; McHale, G.; Matthews, A.; Iborra, E.; et al. Advances in piezoelectric thin films for acoustic biosensors, acoustofluidics and lab-on-chip applications. *Prog. Mater. Sci.* **2017**, *89*, 31–91, doi:10.1016/j.pmatsci.2017.04.006.
31. Li, S.; Wan, Y.; Su, Y.; Fan, C.; Bhethanabotla, V.R. Gold nanoparticle-based low limit of detection Love wave biosensor for carcinoembryonic antigens. *Biosens. Bioelectron.* **2017**, doi:10.1016/j.bios.2017.04.012.
32. Yakovleva, M.; Bhand, S.; Danielsson, B. The enzyme thermistor—a realistic biosensor concept. A critical review. *Anal. Chim. Acta* **2013**, *766*, 1–12, doi:10.1016/j.aca.2012.12.004.
33. Ramanathan, K.; Danielsson, B. Principles and applications of thermal biosensors. *Biosens. Bioelectron.* **2001**, *16*, 417–423, doi:10.1016/S0956-5663(01)00124-5.
34. Qie, Z.; Ning, B.; Liu, M.; Bai, J.; Peng, Y.; Song, N.; Lv, Z.; Wang, Y.; Sun, S.; Su, X.; et al. Fast detection of atrazine in corn using thermometric biosensors. *Analyst* **2013**, *138*, 5151, doi:10.1039/C3AN00490B.
35. Tereshchenko, A.; Bechelany, M.; Viter, R.; Khranovskyy, V.; Smyntyna, V.; Starodub, N.; Yakimova, R. Optical biosensors based on ZnO nanostructures: advantages and perspectives. A review. *Sensors Actuators B Chem.* **2016**, *229*, 664–677, doi:10.1016/j.snb.2016.01.099.

36. Chen, C.; Wang, J. Optical biosensors: an exhaustive and comprehensive review. *Analyst* **2020**, *145*, 1605–1628, doi:10.1039/C9AN01998G.
37. Kozma, P.; Kehl, F.; Ehrentreich-Förster, E.; Stamm, C.; Bier, F.F. Integrated planar optical waveguide interferometer biosensors: A comparative review. *Biosens. Bioelectron.* **2014**, *58*, 287–307, doi:10.1016/j.bios.2014.02.049.
38. Souto, D.E.P.; Volpe, J.; Gonçalves, C. de C.; Ramos, C.H.I.; Kubota, L.T. A brief review on the strategy of developing SPR-based biosensors for application to the diagnosis of neglected tropical diseases. *Talanta* **2019**, *205*, 120122, doi:10.1016/j.talanta.2019.120122.
39. Vahed, H.; Nadri, C. Sensitivity enhancement of SPR optical biosensor based on Graphene–MoS₂ structure with nanocomposite layer. *Opt. Mater. (Amst)*. **2019**, *88*, 161–166, doi:10.1016/j.optmat.2018.11.034.
40. Meyer, S.A.; Auguié, B.; Le Ru, E.C.; Etchegoin, P.G. Combined SPR and SERS Microscopy in the Kretschmann Configuration. *J. Phys. Chem. A* **2012**, *116*, 1000–1007, doi:10.1021/jp2107507.
41. Damborský, P.; Švitel, J.; Katrlík, J. Optical biosensors. *Essays Biochem.* **2016**, *60*, 91–100, doi:10.1042/EBC20150010.
42. Hutter, E.; Fendler, J.H. Exploitation of Localized Surface Plasmon Resonance. *Adv. Mater.* **2004**, *16*, 1685–1706, doi:10.1002/adma.200400271.
43. Sepúlveda, B.; Angelomé, P.C.; Lechuga, L.M.; Liz-Marzán, L.M. LSPR-based nanobiosensors. *Nano Today* **2009**, *4*, 244–251, doi:10.1016/j.nantod.2009.04.001.
44. Fong, K.E.; Yung, L.-Y.L. Localized surface plasmon resonance: a unique property of plasmonic nanoparticles for nucleic acid detection. *Nanoscale* **2013**, *5*, 12043, doi:10.1039/c3nr02257a.
45. Zong, C.; Premasiri, R.; Lin, H.; Huang, Y.; Zhang, C.; Yang, C.; Ren, B.; Ziegler, L.D.; Cheng, J.-X. Plasmon-enhanced Stimulated Raman Scattering Microscopy with Single-molecule Detection Sensitivity. *Nat. Commun.* **2019**, *10*, 5318, doi:10.1038/s41467-019-13230-1.
46. Alvarez-Puebla, R.A.; Liz-Marzán, L.M. SERS detection of small inorganic molecules and ions. *Angew. Chem. Int. Ed. Engl.* **2012**, *51*, 11214–23, doi:10.1002/anie.201204438.
47. Yuan, Y.; Panwar, N.; Yap, S.H.K.; Wu, Q.; Zeng, S.; Xu, J.; Tjin, S.C.; Song, J.; Qu, J.; Yong, K.-T. SERS-based ultrasensitive sensing platform: An insight into design and practical applications. *Coord. Chem. Rev.* **2017**, *337*, 1–33, doi:10.1016/j.ccr.2017.02.006.

48. Ding, S.-Y.; You, E.-M.; Tian, Z.-Q.; Moskovits, M. Electromagnetic theories of surface-enhanced Raman spectroscopy. *Chem. Soc. Rev.* **2017**, *46*, 4042–4076, doi:10.1039/C7CS00238F.
49. Kneipp, K. Chemical Contribution to SERS Enhancement: An Experimental Study on a Series of Polymethine Dyes on Silver Nanoaggregates. *J. Phys. Chem. C* **2016**, doi:10.1021/acs.jpcc.6b03785.
50. Langer, J.; Jimenez de Aberasturi, D.; Aizpurua, J.; Alvarez-Puebla, R.A.; Augu  , B.; Baumberg, J.J.; Bazan, G.C.; Bell, S.E.J.; Boisen, A.; Brolo, A.G.; et al. Present and Future of Surface-Enhanced Raman Scattering. *ACS Nano* **2020**, *14*, 28–117, doi:10.1021/acsnano.9b04224.
51. Yamamoto, Y.S.; Ozaki, Y.; Itoh, T. Recent progress and frontiers in the electromagnetic mechanism of surface-enhanced Raman scattering. *J. Photochem. Photobiol. C Photochem. Rev.* **2014**, *21*, 81–104, doi:10.1016/j.jphotochemrev.2014.10.001.
52. Mao, P.; Liu, C.; Favraud, G.; Chen, Q.; Han, M.; Fratolocchi, A.; Zhang, S. Broadband single molecule SERS detection designed by warped optical spaces. *Nat. Commun.* **2018**, *9*, 5428, doi:10.1038/s41467-018-07869-5.
53. Laing, S.; Gracie, K.; Faulds, K. Multiplex in vitro detection using SERS. *Chem. Soc. Rev.* **2016**, *45*, 1901–1918, doi:10.1039/C5CS00644A.
54. Radziuk, D.; Moehwald, H. Prospects for plasmonic hot spots in single molecule SERS towards the chemical imaging of live cells. *Phys. Chem. Chem. Phys.* **2015**, *17*, 21072–21093, doi:10.1039/C4CP04946B.
55. Wang, Z.; Zong, S.; Wu, L.; Zhu, D.; Cui, Y. SERS-Activated Platforms for Immunoassay: Probes, Encoding Methods, and Applications. *Chem. Rev.* **2017**, *117*, 7910–7963, doi:10.1021/acs.chemrev.7b00027.
56. Yap, L.W.; Chen, H.; Gao, Y.; Petkovic, K.; Liang, Y.; Si, K.J.; Wang, H.; Tang, Z.; Zhu, Y.; Cheng, W. Bifunctional plasmonic-magnetic particles for an enhanced microfluidic SERS immunoassay. *Nanoscale* **2017**, *9*, 7822–7829, doi:10.1039/C7NR01511A.
57. Pu, H.; Xiao, W.; Sun, D.-W. SERS-microfluidic systems: A potential platform for rapid analysis of food contaminants. *Trends Food Sci. Technol.* **2017**, *70*, 114–126, doi:10.1016/j.tifs.2017.10.001.
58. Li, X.; Zhang, Y.; Xue, B.; Kong, X.; Liu, X.; Tu, L.; Chang, Y.; Zhang, H. A SERS nano-tag-based fiber-optic strategy for in situ immunoassay in unprocessed whole blood. *Biosens. Bioelectron.* **2017**, *92*, 517–522, doi:10.1016/j.bios.2016.10.070.
59. Russo, L.; S  nchez-Purr  , M.; Rodr  guez-Quijada, C.; Leonardo, B.M.; Puentes, V.; Hamad-Schifferli, K. Detection of resistance protein A (MxA) in paper-

based immunoassays with surface enhanced Raman spectroscopy with AuAg nanoshells. *Nanoscale* **2019**, *11*, 10819–10827, doi:10.1039/C9NR02397F.

60. Riquelme, B.D.; Valverde, J.R.; Rasia, R.J. Kinetic study of antibody adhesion on a silicon wafer by laser reflectometry. *Opt. Lasers Eng.* **2003**, *39*, 589–598, doi:10.1016/S0143-8166(02)00048-9.

61. Kumeria, T.; Kurkuri, M.D.; Diener, K.R.; Parkinson, L.; Losic, D. Label-free reflectometric interference microchip biosensor based on nanoporous alumina for detection of circulating tumour cells. *Biosens. Bioelectron.* **2012**, doi:10.1016/j.bios.2012.02.038.

62. Alvarez, S.D.; Li, C.-P.; Chiang, C.E.; Schuller, I.K.; Sailor, M.J. A Label-Free Porous Alumina Interferometric Immunosensor. *ACS Nano* **2009**, *3*, 3301–3307, doi:10.1021/nn900825q.

63. Pacholski, C.; Yu, C.; Miskelly, G.M.; Godin, D.; Sailor, M.J. Reflective interferometric Fourier Transform Spectroscopy: A self-compensating label-free immunosensor using double-layers of porous SiO₂. *J. Am. Chem. Soc.* **2006**, doi:10.1021/ja056702b.

64. Psarouli, A.; Salapatias, A.; Botsialas, A.; Petrou, P.S.; Raptis, I.; Makarona, E.; Jobst, G.; Tukkiniemi, K.; Sopanen, M.; Stoffer, R.; et al. Monolithically integrated broad-band Mach-Zehnder interferometers for highly sensitive label-free detection of biomolecules through dual polarization optics. *Sci. Rep.* **2015**, *5*, 17600, doi:10.1038/srep17600.

65. Kussrow, A.; Enders, C.S.; Bornhop, D.J. Interferometric Methods for Label-Free Molecular Interaction Studies. *Anal. Chem.* **2012**, *84*, 779–792, doi:10.1021/ac202812h.

66. Ymeti, A.; Subramaniam, V.; Beumer, T.A.; Kanger, J.S. An ultrasensitive Young interferometer handheld sensor for rapid virus detection. *Expert Rev. Med. Devices* **2007**, *4*, 447–454, doi:10.1586/17434440.4.4.447.

67. Chen, L.H.; Chan, C.C.; Ni, K.; Hu, P.B.; Li, T.; Wong, W.C.; Balamurali, P.; Menon, R.; Shailender, M.; Neu, B.; et al. Label-free fiber-optic interferometric immunosensors based on waist-enlarged fusion taper. *Sensors Actuators B Chem.* **2013**, *178*, 176–184, doi:10.1016/j.snb.2012.12.071.

68. Schneider, B.; Dickinson, E.; Vach, M.; Hoijer, J.; Howard, L. Highly sensitive optical chip immunoassays in human serum. *Biosens. Bioelectron.* **2000**, *15*, 13–22, doi:10.1016/S0956-5663(00)00056-7.

69. Ragavan, K.V.; Neethirajan, S. Nanoparticles as Biosensors for Food Quality and Safety Assessment. In *Nanomaterials for Food Applications*; Elsevier, **2019**; pp. 147–202 ISBN 9780128141311.

70. Wu, J.; Fu, Z.; Yan, F.; Ju, H. Biomedical and clinical applications of immunoassays and immunosensors for tumor markers. *TrAC - Trends Anal. Chem.* **2007**, doi:10.1016/j.trac.2007.05.007.
71. Abhijith, K.S.; Ragavan, K. V.; Thakur, M.S. Gold nanoparticles enhanced chemiluminescence – a novel approach for sensitive determination of aflatoxin-B₁. *Anal. Methods* **2013**, *5*, 4838, doi:10.1039/c3ay40694f.
72. Sabouri, S.; Ghourchian, H.; Shourian, M.; Boutorabi, M. A gold nanoparticle-based immunosensor for the chemiluminescence detection of the hepatitis B surface antigen. *Anal. Methods* **2014**, *6*, 5059–5066, doi:10.1039/C4AY00461B.
73. Chen, L.; Zhang, Z.; Zhang, P.; Zhang, X.; Fu, A. An ultra-sensitive chemiluminescence immunosensor of carcinoembryonic antigen using HRP-functionalized mesoporous silica nanoparticles as labels. *Sensors Actuators, B Chem.* **2011**, doi:10.1016/j.snb.2011.01.007.
74. Zheng, Y.; Chen, H.; Liu, X.; Jiang, J.; Luo, Y.; Shen, G.; Yu, R. An ultrasensitive chemiluminescence immunosensor for PSA based on the enzyme encapsulated liposome. *Talanta* **2008**, *77*, 809–814, doi:10.1016/j.talanta.2008.07.038.
75. Marquette, C.A.; Blum, L.J. Electro-chemiluminescent biosensing. *Anal. Bioanal. Chem.* **2008**, *390*, 155–168, doi:10.1007/s00216-007-1631-2.
76. Habtamu, H.B.; Sentic, M.; Silvestrini, M.; De Leo, L.; Not, T.; Arbault, S.; Manojlovic, D.; Sojic, N.; Ugo, P. A Sensitive Electrochemiluminescence Immunosensor for Celiac Disease Diagnosis Based on Nanoelectrode Ensembles. *Anal. Chem.* **2015**, doi:10.1021/acs.analchem.5b02801.
77. Berezin, M.Y.; Achilefu, S. Fluorescence Lifetime Measurements and Biological Imaging. *Chem. Rev.* **2010**, *110*, 2641–2684, doi:10.1021/cr900343z.
78. Fu, L.; Qian, Y.; Zhou, J.; Zheng, L.; Wang, Y. Fluorescence-based quantitative platform for ultrasensitive food allergen detection: From immunoassays to DNA sensors. *Compr. Rev. Food Sci. Food Saf.* **2020**, doi:10.1111/1541-4337.12641.
79. Iwanaga, M. All-Dielectric Metasurface Fluorescence Biosensors for High-Sensitivity Antibody/Antigen Detection. *ACS Nano* **2020**, doi:10.1021/acsnano.0c07722.
80. Zhao, Q.; Wu, Q.; Ma, P.; Xu, L.; Zhang, F.; Li, D.; Liu, X.; Xu, S.; Sun, Y.; Song, D.; et al. Selective and sensitive fluorescence detection method for pig IgG based on competitive immunosensing strategy and magnetic bioseparation. *Talanta* **2019**, doi:10.1016/j.talanta.2018.11.041.

81. Wei, Q.; Lee, M.; Yu, X.; Lee, E.K.; Seong, G.H.; Choo, J.; Cho, Y.W. Development of an open sandwich fluoroimmunoassay based on fluorescence resonance energy transfer. *Anal. Biochem.* **2006**, *358*, 31–37, doi:10.1016/j.ab.2006.08.019.
82. Zhang, Y.; Liao, Z.; Liu, Y.; Wan, Y.; Chang, J.; Wang, H. Flow cytometric immunoassay for aflatoxin B1 using magnetic microspheres encoded with upconverting fluorescent nanocrystals. *Microchim. Acta* **2017**, doi:10.1007/s00604-017-2116-4.
83. Müller, S.M.; Galliardt, H.; Schneider, J.; Barisas, B.G.; Seidel, T. Quantification of Förster resonance energy transfer by monitoring sensitized emission in living plant cells. *Front. Plant Sci.* **2013**, *4*, doi:10.3389/fpls.2013.00413.
84. Clegg, R.M. Fluorescence resonance energy transfer. *Curr. Opin. Biotechnol.* **1995**, *6*, 103–110, doi:10.1016/0958-1669(95)80016-6.
85. Chou, K.; Dennis, A. Förster Resonance Energy Transfer between Quantum Dot Donors and Quantum Dot Acceptors. *Sensors* **2015**, *15*, 13288–13325, doi:10.3390/s150613288.
86. Lichlyter, D.J.; Grant, S.A.; Soykan, O. Development of a novel FRET immunosensor technique. *Biosens. Bioelectron.* **2003**, *19*, 219–226, doi:10.1016/S0956-5663(03)00215-X.
87. Deng, F.; Li, Y.; Hossain, M.J.; Kendig, M.D.; Arnold, R.; Goldys, E.M.; Morris, M.J.; Liu, G. Polymer brush based fluorescent immunosensor for direct monitoring of interleukin-1 β in rat blood. *Analyst* **2019**, *144*, 5682–5690, doi:10.1039/C9AN01300H.
88. Tereshchenko, A.; Bechelany, M.; Viter, R.; Khranovskyy, V.; Smyntyna, V.; Starodub, N.; Yakimova, R. Optical biosensors based on ZnO nanostructures: advantages and perspectives. A review. *Sensors Actuators B Chem.* **2016**, *229*, 664–677, doi:10.1016/j.snb.2016.01.099.
89. Viter, R.; Tereshchenko, A.; Smyntyna, V.; Ogorodniichuk, J.; Starodub, N.; Yakimova, R.; Khranovskyy, V.; Ramanavicius, A. Toward development of optical biosensors based on photoluminescence of TiO₂ nanoparticles for the detection of Salmonella. *Sensors Actuators B Chem.* **2017**, *252*, 95–102, doi:10.1016/j.snb.2017.05.139.
90. Politi, J.; Rea, I.; Dardano, P.; De Stefano, L.; Gioffrè, M. Versatile synthesis of ZnO nanowires for quantitative optical sensing of molecular biorecognition. *Sensors Actuators B Chem.* **2015**, *220*, 705–711, doi:10.1016/j.snb.2015.05.135.
91. Tereshchenko, A.; Smyntyna, V.; Ramanavicius, A. Interaction mechanism between TiO₂ nanostructures and bovine leukemia virus proteins in

photoluminescence-based immunosensors. *RSC Adv.* **2018**, *8*, 37740–37748, doi:10.1039/C8RA07347C.

92. Lee, H.; Hong, Y.J.; Baik, S.; Hyeon, T.; Kim, D. Enzyme-Based Glucose Sensor: From Invasive to Wearable Device. *Adv. Healthc. Mater.* **2018**, *7*, 1701150, doi:10.1002/adhm.201701150.

93. Zafar, H.; Channa, A.; Jeoti, V.; Stojanović, G.M. Comprehensive Review on Wearable Sweat-Glucose Sensors for Continuous Glucose Monitoring. *Sensors* **2022**, *22*, 1–35, doi:10.3390/s22020638.

94. Akhil, S.; Akash, S.; Pasha, A.; Kulkarni, B.; Jalalah, M.; Alsaiani, M.; Harraz, F.A.; Balakrishna, R.G. Review on perovskite silicon tandem solar cells: Status and prospects 2T, 3T and 4T for real world conditions. *Mater. Des.* **2021**, *211*, 110138, doi:10.1016/j.matdes.2021.110138.

95. Uhler, A. Electrolytic Shaping of Germanium and Silicon. *Bell Syst. Tech. J.* **1956**, *35*, 333–347, doi:10.1002/j.1538-7305.1956.tb02385.x.

96. Cullis, A.G.; Canham, L.T. Visible light emission due to quantum size effects in highly porous crystalline silicon. *Nature* **1991**, *353*, 335–338, doi:10.1038/353335a0.

97. Kolasinski, K.W. Metal-Assisted Catalytic Etching (MACE) for Nanofabrication of Semiconductor Powders. *Micromachines* **2021**, *12*, 776, doi:10.3390/mi12070776.

98. Adachi, S. Porous Silicon Formation by Photoetching. In *Handbook of Porous Silicon*; Springer International Publishing: Cham, **2018**; Vol. 1–2, pp. 79–87 ISBN 9783319713816.

99. Hines, M.A.; Faggin, M.F.; Gupta, A.; Aldinger, B.S.; Bao, K. Self-Propagating Reaction Produces Near-Ideal Functionalization of Si(100) and Flat Surfaces. *J. Phys. Chem. C* **2012**, *116*, 18920–18929, doi:10.1021/jp306477x.

100. Williams, M.O.; Hiller, D.; Bergfeldt, T.; Zacharias, M. How the Oxidation Stability of Metal Catalysts Defines the Metal-Assisted Chemical Etching of Silicon. *J. Phys. Chem. C* **2017**, *121*, 9296–9299, doi:10.1021/acs.jpcc.6b12362.

101. Huo, C.; Wang, J.; Fu, H.; Li, X.; Yang, Y.; Wang, H.; Mateen, A.; Farid, G.; Peng, K.-Q. Metal-Assisted Chemical Etching of Silicon in Oxidizing HF Solutions: Origin, Mechanism, Development, and Black Silicon Solar Cell Application. *Adv. Funct. Mater.* **2020**, *30*, 2005744, doi:10.1002/adfm.202005744.

102. Iatsunskiy, I.; Nowaczyk, G.; Jurga, S.; Fedorenko, V.; Pavlenko, M.; Smyntyna, V. One and two-phonon Raman scattering from nanostructured silicon. *Optik (Stuttg.)*. **2015**, *126*, 1650–1655, doi:10.1016/j.ijleo.2015.05.088.

103. Chartier, C.; Bastide, S.; Lévy-Clément, C. Metal-assisted chemical etching of silicon in HF–H₂O₂. *Electrochim. Acta* **2008**, *53*, 5509–5516, doi:10.1016/j.electacta.2008.03.009.
104. Huang, Z.; Geyer, N.; Werner, P.; de Boor, J.; Gösele, U. Metal-Assisted Chemical Etching of Silicon: A Review. *Adv. Mater.* **2011**, *23*, 285–308, doi:10.1002/adma.201001784.
105. Sahu, B.B.; Yin, Y.; Han, J.G.; Shiratani, M. Low temperature synthesis of silicon quantum dots with plasma chemistry control in dual frequency non-thermal plasmas. *Phys. Chem. Chem. Phys.* **2016**, *18*, 15697–15710, doi:10.1039/C6CP01856D.
106. Nanosilicon. In *Fundamentals and Applications of Nano Silicon in Plasmonics and Fullerenes*; Elsevier, **2018**; pp. 205–285 ISBN 9780323480574.
107. Trwoga, P.F.; Kenyon, A.J.; Pitt, C.W. Modeling the contribution of quantum confinement to luminescence from silicon nanoclusters. *J. Appl. Phys.* **1998**, *83*, 3789–3794, doi:10.1063/1.366608.
108. Barbagioanni, E.G.; Lockwood, D.J.; Simpson, P.J.; Goncharova, L. V Quantum confinement in Si and Ge nanostructures: Theory and experiment. *Appl. Phys. Rev.* **2014**, *1*, 011302, doi:10.1063/1.4835095.
109. Canham, L. Introductory lecture: origins and applications of efficient visible photoluminescence from silicon-based nanostructures. *Faraday Discuss.* **2020**, *222*, 10–81, doi:10.1039/D0FD00018C.
110. Delerue, C.; Allan, G.; Lannoo, M. Theoretical aspects of the luminescence of porous silicon. *Phys. Rev. B* **1993**, *48*, 11024–11036, doi:10.1103/PhysRevB.48.11024.
111. Prokes, S.M.; Glembocki, O.J. Role of interfacial oxide-related defects in the red-light emission in porous silicon. *Phys. Rev. B* **1994**, *49*, 2238–2241, doi:10.1103/PhysRevB.49.2238.
112. Kayahan, E. Porous silicon based CO₂ sensors with high sensitivity. *Optik (Stuttg)*. **2018**, *164*, 271–276, doi:10.1016/j.ijleo.2018.03.024.
113. Jenie, S.N.A.; Plush, S.E.; Voelcker, N.H. Singlet Oxygen Detection on a Nanostructured Porous Silicon Thin Film via Photonic Luminescence Enhancements. *Langmuir* **2017**, *33*, 8606–8613, doi:10.1021/acs.langmuir.7b00522.
114. Georgobiani, V.A.; Gonchar, K.A.; Zvereva, E.A.; Osminkina, L.A. Porous Silicon Nanowire Arrays for Reversible Optical Gas Sensing. *Phys. status solidi* **2018**, *215*, 1700565, doi:10.1002/pssa.201700565.

115. Nayef, U.M.; Khudhair, I.M. Study of porous silicon humidity sensor vapors by photoluminescence quenching for organic solvents. *Optik (Stuttg)*. **2017**, *135*, 169–173, doi:10.1016/j.ijleo.2017.01.060.
116. Ghosh, R.; Das, R.; Giri, P.K. Label-free glucose detection over a wide dynamic range by mesoporous Si nanowires based on anomalous photoluminescence enhancement. *Sensors Actuators B Chem*. **2018**, *260*, 693–704, doi:10.1016/j.snb.2018.01.099.
117. Irrera, A.; Leonardi, A.A.; Di Franco, C.; Lo Faro, M.J.; Palazzo, G.; D'Andrea, C.; Manoli, K.; Franzò, G.; Musumeci, P.; Fazio, B.; et al. New Generation of Ultrasensitive Label-Free Optical Si Nanowire-Based Biosensors. *ACS Photonics* **2018**, *5*, 471–479, doi:10.1021/acsp Photonics.7b00983.
118. Sailor, M.J.; Wu, E.C. Photoluminescence-Based Sensing With Porous Silicon Films, Microparticles, and Nanoparticles. *Adv. Funct. Mater*. **2009**, *19*, 3195–3208, doi:10.1002/adfm.200900535.
119. Mariani, S.; Paghi, A.; La Mattina, A.A.; Debrassi, A.; Dähne, L.; Barillaro, G. Decoration of Porous Silicon with Gold Nanoparticles via Layer-by-Layer Nanoassembly for Interferometric and Hybrid Photonic/Plasmonic (Bio)sensing. *ACS Appl. Mater. Interfaces* **2019**, *11*, 43731–43740, doi:10.1021/acsa mi.9b15737.
120. Wu, R.; Jin, Q.; Storey, C.; Collins, J.; Gomard, G.; Lemmer, U.; Canham, L.; Kling, R.; Kaplan, A. Gold nanoplasmonic particles in tunable porous silicon 3D scaffolds for ultra-low concentration detection by SERS. *Nanoscale Horiz*. **2021**, *6*, 781–790, doi:10.1039/D1NH00228G.
121. Balderas-Valadez, R.F.; Schürmann, R.; Pacholski, C. One Spot—Two Sensors: Porous Silicon Interferometers in Combination With Gold Nanostructures Showing Localized Surface Plasmon Resonance. *Front. Chem*. **2019**, *7*, doi:10.3389/fchem.2019.00593.
122. Khalil, I.; Chou, C.-M.; Tsai, K.-L.; Hsu, S.; Yehye, W.A.; Hsiao, V.K.S. Gold Nanofilm-Coated Porous Silicon as Surface-Enhanced Raman Scattering Substrate. *Appl. Sci*. **2019**, *9*, 4806, doi:10.3390/app9224806.
123. Rashed, M.A.; Harraz, F.A.; Faisal, M.; El-Toni, A.M.; Alsaiari, M.; Al-Assiri, M.S. Gold nanoparticles plated porous silicon nanopowder for nonenzymatic voltammetric detection of hydrogen peroxide. *Anal. Biochem*. **2021**, *615*, 114065, doi:10.1016/j.ab.2020.114065.
124. Hui Wang; Zhenghua An; Qijun Ren; Hengliang Wang; Zhanghai Chen; Xuechu Shen Localized-surface-plasmon enhanced luminescence from porous silicon by gold nanoparticles. In Proceedings of the 2010 3rd International Nanoelectronics Conference (INEC); IEEE, **2010**; pp. 787–788.
125. de la Mora, M.B.; Bornacelli, J.; Nava, R.; Zanella, R.; Reyes-Esqueda, J.A. Porous silicon photoluminescence modification by colloidal gold nanoparticles:

Plasmonic, surface and porosity roles. *J. Lumin.* **2014**, *146*, 247–255, doi:10.1016/j.jlumin.2013.09.053.

126. Tang, H.; Liu, C.; He, H. Surface plasmon enhanced photoluminescence from porous silicon nanowires decorated with gold nanoparticles. *RSC Adv.* **2016**, *6*, 59395–59399, doi:10.1039/C6RA06019F.

127. Pavelka, O.; Dyakov, S.; Veselý, J.; Fučíková, A.; Sugimoto, H.; Fujii, M.; Valenta, J. Optimizing plasmon enhanced luminescence in silicon nanocrystals by gold nanorods. *Nanoscale* **2021**, *13*, 5045–5057, doi:10.1039/D1NR00058F.

128. Novara, C.; Chiadò, A.; Paccotti, N.; Catuogno, S.; Esposito, C.L.; Condorelli, G.; De Franciscis, V.; Geobaldo, F.; Rivolo, P.; Giorgis, F. SERS-active metal-dielectric nanostructures integrated in microfluidic devices for label-free quantitative detection of miRNA. *Faraday Discuss.* **2017**, *205*, 271–289, doi:10.1039/C7FD00140A.

129. Erhart, P.; Juslin, N.; Goy, O.; Nordlund, K.; Müller, R.; Albe, K. Analytic bond-order potential for atomistic simulations of zinc oxide. *J. Phys. Condens. Matter* **2006**, *18*, 6585–6605, doi:10.1088/0953-8984/18/29/003.

130. Sulciute, A.; Nishimura, K.; Gilshtein, E.; Cesano, F.; Viscardi, G.; Nasibulin, A.G.; Ohno, Y.; Rackauskas, S. ZnO Nanostructures Application in Electrochemistry: Influence of Morphology. *J. Phys. Chem. C* **2021**, *125*, 1472–1482, doi:10.1021/acs.jpcc.0c08459.

131. Beitollahi, H.; Tajik, S.; Garkani Nejad, F.; Safaei, M. Recent advances in ZnO nanostructure-based electrochemical sensors and biosensors. *J. Mater. Chem. B* **2020**, *8*, 5826–5844, doi:10.1039/D0TB00569J.

132. Mishra, Y.K.; Adelung, R. ZnO tetrapod materials for functional applications. *Mater. Today* **2018**, *21*, 631–651, doi:10.1016/j.mattod.2017.11.003.

133. Zhou, X.; Peng, R.; Ren, C.; Sun, L.; Hu, J.; Guo, T.; Zhang, Y.; Lin, Z. Fabrication and field emission properties of ZnO/Al₂O₃ nanocomposite tetrapods. *J. Alloys Compd.* **2017**, *695*, 1863–1869, doi:10.1016/j.jallcom.2016.11.020.

134. Yan, L.; Uddin, A.; Wang, H. ZnO Tetrapods: Synthesis and Applications in Solar Cells. *Nanomater. Nanotechnol.* **2015**, *5*, 19, doi:10.5772/60939.

135. Hoo, X.F.; Abdul Razak, K.; Ridhuan, N.S.; Mohamad Nor, N.; Zakaria, N.D. Electrochemical glucose biosensor based on ZnO nanorods modified with gold nanoparticles. *J. Mater. Sci. Mater. Electron.* **2019**, *30*, 7460–7470, doi:10.1007/s10854-019-01059-9.

136. Zhang, Z.; Yuan, Y.; Fang, Y.; Liang, L.; Ding, H.; Jin, L. Preparation of photocatalytic nano-ZnO/TiO₂ film and application for determination of chemical oxygen demand. *Talanta* **2007**, *73*, 523–528, doi:10.1016/j.talanta.2007.04.011.

137. Mao, Q.; Jing, W.; Zhou, F.; Liu, S.; Gao, W.; Wei, Z.; Jiang, Z. Depositing reduced graphene oxide on ZnO nanorods to improve the performance of enzymatic glucose sensors. *Mater. Sci. Semicond. Process.* **2021**, *121*, 105391, doi:10.1016/j.mssp.2020.105391.
138. Murugan, N.; Kumar, T.H.V.; Devi, N.R.; Sundramoorthy, A.K. A flower-structured MoS₂ -decorated f-MWCNTs/ZnO hybrid nanocomposite-modified sensor for the selective electrochemical detection of vitamin C. *New J. Chem.* **2019**, *43*, 15105–15114, doi:10.1039/C9NJ02993A.
139. Liu, X.; Chen, C. Mxene enhanced the photocatalytic activity of ZnO nanorods under visible light. *Mater. Lett.* **2020**, *261*, 127127, doi:10.1016/j.matlet.2019.127127.
140. Zhou, F.; Jing, W.; Liu, S.; Mao, Q.; Xu, Y.; Han, F.; Wei, Z.; Jiang, Z. Electrodeposition of gold nanoparticles on ZnO nanorods for improved performance of enzymatic glucose sensors. *Mater. Sci. Semicond. Process.* **2020**, *105*, 104708, doi:10.1016/j.mssp.2019.104708.
141. Zhou, F.; Jing, W.; Xu, Y.; Chen, Z.; Jiang, Z.; Wei, Z. Performance enhancement of ZnO nanorod-based enzymatic glucose sensor via reduced graphene oxide deposition and UV irradiation. *Sensors Actuators B Chem.* **2019**, *284*, 377–385, doi:10.1016/j.snb.2018.12.141.
142. Srivastava, A.; Verma, A.; Prajapati, Y.K. Effect of 2D, TMD, perovskite, and 2D transition metal carbide/nitride materials on performance parameters of SPR biosensor. In *Handbook of Nanomaterials for Sensing Applications*; Hussain, C.M., Kailasa, S.K., Eds.; Elsevier, **2021**; pp. 57–90 ISBN 9780128207833.
143. Qian, Y.; Wei, H.; Dong, J.; Du, Y.; Fang, X.; Zheng, W.; Sun, Y.; Jiang, Z. Fabrication of urchin-like ZnO-MXene nanocomposites for high-performance electromagnetic absorption. *Ceram. Int.* **2017**, *43*, 10757–10762, doi:10.1016/j.ceramint.2017.05.082.
144. Wang, J.; Yang, Y.; Xia, Y. Mesoporous MXene/ZnO nanorod hybrids of high surface area for UV-activated NO₂ gas sensing in ppb-level. *Sensors Actuators B Chem.* **2022**, *353*, 131087, doi:10.1016/j.snb.2021.131087.
145. Khadidja, M.F.; Fan, J.; Li, S.; Li, S.; Cui, K.; Wu, J.; Zeng, W.; Wei, H.; Jin, H.-G.; Naik, N.; et al. Hierarchical ZnO/MXene composites and their photocatalytic performances. *Colloids Surfaces A Physicochem. Eng. Asp.* **2021**, *628*, 127230, doi:10.1016/j.colsurfa.2021.127230.
146. Zhang, Z.-Y.; Xiong, H.-M. Photoluminescent ZnO Nanoparticles and Their Biological Applications. *Materials (Basel)*. **2015**, *8*, 3101–3127, doi:10.3390/ma8063101.

147. Galdámez-Martinez, A.; Santana, G.; Güell, F.; Martínez-Alanis, P.R.; Dutt, A. Photoluminescence of ZnO Nanowires: A Review. *Nanomater.* **2020**, *10*, 857, doi:10.3390/nano10050857.
148. Alvi, N.H.; ul Hasan, K.; Nur, O.; Willander, M. The origin of the red emission in n-ZnO nanotubes/p-GaN white light emitting diodes. *Nanoscale Res. Lett.* **2011**, *6*, 130, doi:10.1186/1556-276X-6-130.
149. Beh, H.; Hiller, D.; Salava, J.; Trojáněk, F.; Zacharias, M.; Malý, P.; Valenta, J. Photoluminescence dynamics and quantum yield of intrinsically conductive ZnO from atomic layer deposition. *J. Lumin.* **2018**, *201*, 85–89, doi:10.1016/j.jlumin.2018.04.044.
150. Tereshchenko, A.; Fedorenko, V.; Smyntyna, V.; Konup, I.; Konup, A.; Eriksson, M.; Yakimova, R.; Ramanavicius, A.; Balme, S.; Bechelany, M. ZnO films formed by atomic layer deposition as an optical biosensor platform for the detection of Grapevine virus A-type proteins. *Biosens. Bioelectron.* **2017**, *92*, 763–769, doi:10.1016/j.bios.2016.09.071.
151. Abou Chaaya, A.; Viter, R.; Bechelany, M.; Alute, Z.; Erts, D.; Zalesskaya, A.; Kovalevskis, K.; Rouessac, V.; Smyntyna, V.; Miele, P. Evolution of microstructure and related optical properties of ZnO grown by atomic layer deposition. *Beilstein J. Nanotechnol.* **2013**, *4*, 690–698, doi:10.3762/bjnano.4.78.
152. Damberga, D.; Viter, R.; Fedorenko, V.; Iatsunskyi, I.; Coy, E.; Graniel, O.; Balme, S.; Miele, P.; Bechelany, M. Photoluminescence Study of Defects in ZnO-Coated Polyacrylonitrile Nanofibers. *J. Phys. Chem. C* **2020**, *124*, 9434–9441, doi:10.1021/acs.jpcc.0c00326.
153. Kayaci, F.; Vempati, S.; Ozgit-Akgun, C.; Donmez, I.; Biyikli, N.; Uyar, T. Transformation of polymer-ZnO core–shell nanofibers into ZnO hollow nanofibers: Intrinsic defect reorganization in ZnO and its influence on the photocatalysis. *Appl. Catal. B Environ.* **2015**, *176–177*, 646–653, doi:10.1016/j.apcatb.2015.04.036.
154. Viter, R.; Chaaya, A.A.; Iatsunskyi, I.; Nowaczyk, G.; Kovalevskis, K.; Erts, D.; Miele, P.; Smyntyna, V.; Bechelany, M. Tuning of ZnO 1D nanostructures by atomic layer deposition and electrospinning for optical gas sensor applications. *Nanotechnology* **2015**, *26*, 105501, doi:10.1088/0957-4484/26/10/105501.
155. Iatsunskyi, I.; Vasylenko, A.; Viter, R.; Kempinski, M.; Nowaczyk, G.; Jurga, S.; Bechelany, M. Tailoring of the electronic properties of ZnO-polyacrylonitrile nanofibers: Experiment and theory. *Appl. Surf. Sci.* **2017**, *411*, 494–501, doi:10.1016/j.apsusc.2017.03.111.
156. Myndrul, V.; Vysloužilová, L.; Klápšťová, A.; Coy, E.; Jancelewicz, M.; Iatsunskyi, I. Formation and Photoluminescence Properties of ZnO Nanoparticles on Electrospun Nanofibers Produced by Atomic Layer Deposition. *Coatings* **2020**, *10*, 1199, doi:10.3390/coatings10121199.

157. Xue, J.; Wu, T.; Dai, Y.; Xia, Y. Electrospinning and Electrospun Nanofibers: Methods, Materials, and Applications. *Chem. Rev.* **2019**, *119*, 5298–5415, doi:10.1021/acs.chemrev.8b00593.
158. Suzuki, A.; Arino, K. Polypropylene nanofiber sheets prepared by CO₂ laser supersonic multi-drawing. *Eur. Polym. J.* **2012**, *48*, 1169–1176, doi:10.1016/j.eurpolymj.2012.04.003.
159. Tao, S.L.; Desai, T.A. Aligned Arrays of Biodegradable Poly(ϵ -caprolactone) Nanowires and Nanofibers by Template Synthesis. *Nano Lett.* **2007**, *7*, 1463–1468, doi:10.1021/nl0700346.
160. Ichimori, T.; Mizuma, K.; Uchida, T.; Yamazaki, S.; Kimura, K. Morphological diversity and nanofiber networks of poly(p -oxybenzoyl) generated by phase separation during copolymerization. *J. Appl. Polym. Sci.* **2013**, *128*, 1282–1290, doi:10.1002/app.38554.
161. Ura, D.P.; Rosell-Llompart, J.; Zaszczynska, A.; Vasilyev, G.; Gradys, A.; Szewczyk, P.K.; Knapczyk-Korczak, J.; Avrahami, R.; Šišková, A.O.; Arinstein, A.; et al. The Role of Electrical Polarity in Electrospinning and on the Mechanical and Structural Properties of As-Spun Fibers. *Materials (Basel)*. **2020**, *13*, 4169, doi:10.3390/ma13184169.
162. Haider, A.; Haider, S.; Kang, I.-K. A comprehensive review summarizing the effect of electrospinning parameters and potential applications of nanofibers in biomedical and biotechnology. *Arab. J. Chem.* **2018**, *11*, 1165–1188, doi:10.1016/j.arabjc.2015.11.015.
163. Ahmed, F.E.; Lalia, B.S.; Hashaikeh, R. A review on electrospinning for membrane fabrication: Challenges and applications. *Desalination* **2015**, *356*, 15–30, doi:10.1016/j.desal.2014.09.033.
164. Mailley, D.; Hébraud, A.; Schlatter, G. A Review on the Impact of Humidity during Electrospinning: From the Nanofiber Structure Engineering to the Applications. *Macromol. Mater. Eng.* **2021**, *306*, doi:10.1002/mame.202100115.
165. Zhao, K.; Kang, S.-X.; Yang, Y.-Y.; Yu, D.-G. Electrospun Functional Nanofiber Membrane for Antibiotic Removal in Water: Review. *Polymers (Basel)*. **2021**, *13*, 226, doi:10.3390/polym13020226.
166. Pascariu, P.; Homocianu, M. ZnO-based ceramic nanofibers: Preparation, properties and applications. *Ceram. Int.* **2019**, *45*, 11158–11173, doi:https://doi.org/10.1016/j.ceramint.2019.03.113.
167. Di Mauro, A.; Cantarella, M.; Nicotra, G.; Privitera, V.; Impellizzeri, G. Low temperature atomic layer deposition of ZnO: Applications in photocatalysis. *Appl. Catal. B Environ.* **2016**, *196*, 68–76, doi:10.1016/j.apcatb.2016.05.015.

168. Graniel, O.; Weber, M.; Balme, S.; Miele, P.; Bechelany, M. Atomic layer deposition for biosensing applications. *Biosens. Bioelectron.* **2018**, *122*, 147–159, doi:10.1016/j.bios.2018.09.038.
169. Cremers, V.; Puurunen, R.L.; Dendooven, J. Conformality in atomic layer deposition: Current status overview of analysis and modelling. *Appl. Phys. Rev.* **2019**, *6*, 021302, doi:10.1063/1.5060967.
170. Maydannik, P.; Lahtinen, K.; Kääriäinen, T.; Cameron, D.C. Continuous atomic layer deposition process development. *TAPPI Eur. PLACE Conf.* **2011**, *1*, 446.
171. Rodrigues, J.; Pereira, S.O.; Santos, N.F.; Rodrigues, C.; Costa, F.M.; Monteiro, T. Insights on luminescence quenching of ZnO tetrapods in the detection of hCG. *Appl. Surf. Sci.* **2020**, *527*, 146813, doi:10.1016/j.apsusc.2020.146813.
172. Brás, M.; Zanoni, J.; Falcão, B.P.; Leitão, J.P.; Costa, F.M.; Monteiro, T.; Pereira, S.O.; Rodrigues, J. Label-Free Nanoscale ZnO Tetrapod-Based Transducers for Tetracycline Detection. *ACS Appl. Nano Mater.* **2022**, *5*, 1232–1243, doi:10.1021/acsanm.1c03838.
173. Rodrigues, J.; Pereira, S.O.; Zanoni, J.; Rodrigues, C.; Brás, M.; Costa, F.M.; Monteiro, T. ZnO Transducers for Photoluminescence-Based Biosensors: A Review. *Chemosensors* **2022**, *10*, 39, doi:10.3390/chemosensors10020039.
174. Khodaei, D.; Javanmardi, F.; Khaneghah, A.M. The global overview of the occurrence of mycotoxins in cereals: a three-year survey. *Curr. Opin. Food Sci.* **2021**, *39*, 36–42, doi:10.1016/j.cofs.2020.12.012.
175. Tola, M.; Kebede, B. Occurrence, importance and control of mycotoxins: A review. *Cogent Food Agric.* **2016**, *2*, doi:10.1080/23311932.2016.1191103.
176. Luo, S.; Du, H.; Kebede, H.; Liu, Y.; Xing, F. Contamination status of major mycotoxins in agricultural product and food stuff in Europe. *Food Control* **2021**, *127*, 108120, doi:10.1016/j.foodcont.2021.108120.
177. Nazhand, A.; Durazzo, A.; Lucarini, M.; Souto, E.B.; Santini, A. Characteristics, Occurrence, Detection and Detoxification of Aflatoxins in Foods and Feeds. *Foods* **2020**, *9*, 644, doi:10.3390/foods9050644.
178. Eskola, M.; Kos, G.; Elliott, C.T.; Hajšlová, J.; Mayar, S.; Krska, R. Worldwide contamination of food-crops with mycotoxins: Validity of the widely cited ‘FAO estimate’ of 25%. *Crit. Rev. Food Sci. Nutr.* **2020**, *60*, 2773–2789, doi:10.1080/10408398.2019.1658570.
179. Tao, Y.; Xie, S.; Xu, F.; Liu, A.; Wang, Y.; Chen, D.; Pan, Y.; Huang, L.; Peng, D.; Wang, X.; et al. Ochratoxin A: Toxicity, oxidative stress and metabolism. *Food Chem. Toxicol.* **2018**, *112*, 320–331, doi:10.1016/j.fct.2018.01.002.

180. Li, H.; Mao, X.; Liu, K.; Sun, J.; Li, B.; Malyar, R.M.; Liu, D.; Pan, C.; Gan, F.; Liu, Y.; et al. Ochratoxin A induces nephrotoxicity in vitro and in vivo via pyroptosis. *Arch. Toxicol.* **2021**, *95*, 1489–1502, doi:10.1007/s00204-021-02993-6.
181. Nyein, H.Y.Y.; Bariya, M.; Kivimäki, L.; Uusitalo, S.; Liaw, T.S.; Jansson, E.; Ahn, C.H.; Hangasky, J.A.; Zhao, J.; Lin, Y.; et al. Regional and correlative sweat analysis using high-throughput microfluidic sensing patches toward decoding sweat. *Sci. Adv.* **2019**, *5*, doi:10.1126/sciadv.aaw9906.
182. Lee, H.; Choi, T.K.; Lee, Y.B.; Cho, H.R.; Ghaffari, R.; Wang, L.; Choi, H.J.; Chung, T.D.; Lu, N.; Hyeon, T.; et al. A graphene-based electrochemical device with thermoresponsive microneedles for diabetes monitoring and therapy. *Nat. Nanotechnol.* **2016**, *11*, 566–572, doi:10.1038/nnano.2016.38.
183. Malir, F.; Ostry, V.; Pfohl-Leszkowicz, A.; Malir, J.; Toman, J. Ochratoxin A: 50 years of research. *Toxins (Basel)*. **2016**, *8*, 12–15, doi:10.3390/toxins8070191.
184. Liang, R.; Shen, X.L.; Zhang, B.; Li, Y.; Xu, W.; Zhao, C.; Luo, Y.; Huang, K. Apoptosis Signal-regulating Kinase 1 promotes Ochratoxin A-induced renal cytotoxicity. *Sci. Rep.* **2015**, *5*, 8078, doi:10.1038/srep08078.
185. O’Callaghan, J.; Caddick, M.X.; Dobson, A.D.W. A polyketide synthase gene required for ochratoxin A biosynthesis in *Aspergillus ochraceus*. *Microbiology* **2003**, *149*, 3485–3491, doi:10.1099/mic.0.26619-0.
186. Heussner, A.H.; Bingle, L.E.H. Comparative ochratoxin toxicity: A review of the available data. *Toxins (Basel)*. **2015**, *7*, 4253–4282, doi:10.3390/toxins7104253.
187. Lippolis, V.; Ferrara, M.; Cervellieri, S.; Damascelli, A.; Epifani, F.; Pascale, M.; Perrone, G. Rapid prediction of ochratoxin A-producing strains of *Penicillium* on dry-cured meat by MOS-based electronic nose. *Int. J. Food Microbiol.* **2016**, *218*, 71–77, doi:10.1016/j.ijfoodmicro.2015.11.011.
188. Bittner, A.; Cramer, B.; Humpf, H.U. Matrix binding of ochratoxin a during roasting. *J. Agric. Food Chem.* **2013**, *61*, 12737–12743, doi:10.1021/jf403984x.
189. Jo, E.J.; Mun, H.; Kim, S.J.; Shim, W.B.; Kim, M.G. Detection of ochratoxin A (OTA) in coffee using chemiluminescence resonance energy transfer (CRET) aptasensor. *Food Chem.* **2016**, *194*, 1102–1107, doi:10.1016/j.foodchem.2015.07.152.
190. Mishra, R.K.; Hayat, A.; Catanante, G.; Istamboulie, G.; Marty, J.L. Sensitive quantitation of Ochratoxin A in cocoa beans using differential pulse voltammetry based aptasensor. *Food Chem.* **2016**, *192*, 799–804, doi:10.1016/j.foodchem.2015.07.080.

191. Afsah-Hejri, L.; Jinap, S.; Hajeb, P.; Radu, S.; Shakibazadeh, S. A review on mycotoxins in food and feed: Malaysia case study. *Compr. Rev. Food Sci. Food Saf.* **2013**, *12*, 629–651, doi:10.1111/1541-4337.12029.
192. Liu, R.; Huang, Y.; Ma, Y.; Jia, S.; Gao, M.; Li, J.; Zhang, H.; Xu, D.; Wu, M.; Chen, Y.; et al. Design and synthesis of target-responsive aptamer-cross-linked hydrogel for visual quantitative detection of ochratoxin A. *ACS Appl. Mater. Interfaces* **2015**, *7*, 6982–6990, doi:10.1021/acsami.5b01120.
193. Quintela, S.; Villarán, M.C.; López de Armentia, I.; Elejalde, E. Ochratoxin A removal in wine: A review. *Food Control* **2013**, *30*, 439–445, doi:10.1016/j.foodcont.2012.08.014.
194. Covarelli, L.; Beccari, G.; Marini, A.; Tosi, L. A review on the occurrence and control of ochratoxigenic fungal species and ochratoxin A in dehydrated grapes, non-fortified dessert wines and dried vine fruit in the Mediterranean area. *Food Control* **2012**, *26*, 347–356, doi:10.1016/j.foodcont.2012.01.044.
195. Dohnal, V.; Dvořák, V.; Malř, F.; Ostrý, V.; Roubal, T. A comparison of ELISA and HPLC methods for determination of ochratoxin A in human blood serum in the Czech Republic. *Food Chem. Toxicol.* **2013**, *62*, 427–431, doi:10.1016/j.fct.2013.09.010.
196. Entwisle, A.C.; Williams, A.C.; Mann, P.J.; Slack, P.T.; Gilbert, J.; Burdaspal, P.; Eklund, E.; Gardikis, J.; Hald, B.; Herry, M.P.; et al. Liquid chromatographic method with immunoaffinity column cleanup for determination of ochratoxin A in barley: Collaborative study. *J. AOAC Int.* **2000**, *83*, 1377–1386.
197. Soleas, G.J.; Yan, J.; Goldberg, D.M. Assay of ochratoxin A in wine and beer by high-pressure liquid chromatography photodiode array and gas chromatography mass selective detection. *J. Agric. Food Chem.* **2001**, *49*, 2733–2740, doi:10.1021/jf0100651.
198. Barna-Vetro, I.; Solti, L.; Teren, J.; Gyongyosi, A.; Szabo, E.; Wolfling, A. Sensitive ELISA Test for Determination of Ochratoxin A. *J. Agric. Food Chem.* **1996**, *44*, 4071–4074, doi:10.1021/jf960442n.
199. Bougrini, M.; Baraket, A.; Jamshaid, T.; Aissari, A. El; Bausells, J.; Zabala, M.; Bari, N. El; Bouchikhi, B.; Jaffrezic-Renault, N.; Abdelhamid, E.; et al. Development of a novel capacitance electrochemical biosensor based on silicon nitride for ochratoxin A detection. *Sensors Actuators, B Chem.* **2016**, *234*, 446–452, doi:10.1016/j.snb.2016.03.166.
200. Wang, C.; Dong, X.; Liu, Q.; Wang, K. Label-free colorimetric aptasensor for sensitive detection of ochratoxin A utilizing hybridization chain reaction. *Anal. Chim. Acta* **2015**, *860*, 83–88, doi:10.1016/j.aca.2014.12.031.
201. McKeague, M.; Velu, R.; Hill, K.; Bardóczy, V.; Mészáros, T.; DeRosa, M.C. Selection and characterization of a novel DNA aptamer for label-free fluorescence

biosensing of ochratoxin A. *Toxins (Basel)*. **2014**, *6*, 2435–2452, doi:10.3390/toxins6082435.

202. Wang, R.; Xiang, Y.; Zhou, X.; Liu, L. hua; Shi, H. A reusable aptamer-based evanescent wave all-fiber biosensor for highly sensitive detection of Ochratoxin A. *Biosens. Bioelectron.* **2015**, *66*, 11–18, doi:10.1016/j.bios.2014.10.079.

203. Liu, L. hua; Zhou, X. hong; Shi, H. chang Portable optical aptasensor for rapid detection of mycotoxin with a reversible ligand-grafted biosensing surface. *Biosens. Bioelectron.* **2015**, *72*, 300–305, doi:10.1016/j.bios.2015.05.033.

204. Bianco, M.; Sonato, A.; De Girolamo, A.; Pascale, M.; Romanato, F.; Rinaldi, R.; Arima, V. An aptamer-based SPR-polarization platform for high sensitive OTA detection. *Sensors Actuators, B Chem.* **2017**, *241*, 314–320, doi:10.1016/j.snb.2016.10.056.

205. Lu, Z.; Chen, X.; Hu, W. A fluorescence aptasensor based on semiconductor quantum dots and MoS₂ nanosheets for ochratoxin A detection. *Sensors Actuators, B Chem.* **2017**, *246*, 61–67, doi:10.1016/j.snb.2017.02.062.

206. Bueno, D.; Muñoz, R.; Marty, J.L. Fluorescence analyzer based on smartphone camera and wireless for detection of Ochratoxin A. *Sensors Actuators, B Chem.* **2016**, *232*, 462–468, doi:10.1016/j.snb.2016.03.140.

207. Tereshchenko, A.; Bechelany, M.; Viter, R.; Khranovskyy, V.; Smyntyna, V.; Starodub, N.; Yakimova, R. Optical biosensors based on ZnO nanostructures: Advantages and perspectives. A review. *Sensors Actuators, B Chem.* **2016**.

208. Viter, R.; Jekabsons, K.; Kalnina, Z.; Poletaev, N.; Hsu, S.H.; Riekstina, U. Bioanalytical system for detection of cancer cells with photoluminescent ZnO nanorods. *Nanotechnology* **2016**, *27*, 465101, doi:10.1088/0957-4484/27/46/465101.

209. Jenie, S.N.A.; Plush, S.E.; Voelcker, N.H. Recent Advances on Luminescent Enhancement-Based Porous Silicon Biosensors. *Pharm. Res.* **2016**, *33*, 2314–2336, doi:10.1007/s11095-016-1889-1.

210. Viter, R.; Khranovskyy, V.; Starodub, N.; Ogorodniichuk, Y.; Gevelyuk, S.; Gertnere, Z.; Poletaev, N.; Yakimova, R.; Erts, D.; Smyntyna, V.; et al. Application of Room Temperature Photoluminescence From ZnO Nanorods for Salmonella Detection. *IEEE Sens. J.* **2014**, *14*, 2028–2034, doi:10.1109/JSEN.2014.2309277.

211. Syshchuk, O.; Skryshevsky, V.A.; Soldatkin, O.O.; Soldatkin, A.P. Enzyme biosensor systems based on porous silicon photoluminescence for detection of glucose, urea and heavy metals. *Biosens. Bioelectron.* **2015**, *66*, 89–94, doi:10.1016/j.bios.2014.10.075.

212. Viter, R.; Smyntyna, V.; Starodub, N.; Tereshchenko, A.; Kusevitch, A.; Doychoa, I.; Geveluk, S.; Slishik, N.; Buk, J.; Duchoslav, J.; et al. Novel immune TiO₂

photoluminescence biosensors for leucosis detection. *Procedia Eng.* **2012**, *47*, 338–341, doi:10.1016/j.proeng.2012.09.152.

213. Viter, R.; Tereshchenko, A.; Smyntyna, V.; Ogorodniichuk, J.; Starodub, N.; Yakimova, R.; Khranovskyy, V. Toward development of optical biosensors based on photoluminescence of TiO₂ nanoparticles for the detection of Salmonella. *Sensors Actuators B Chem. Chem.* **2017**, *252*, 95–102, doi:10.1016/j.snb.2017.05.139.

214. Viter, R.; Savchuk, M.; Iatsunskiy, I.; Pietralik, Z.; Starodub, N.; Shpyrka, N.; Ramanaviciene, A.; Ramanavicius, A. Analytical, thermodynamical and kinetic characteristics of photoluminescence immunosensor for the determination of Ochratoxin A. *Biosens. Bioelectron.* **2018**, *99*, 237–243, doi:10.1016/j.bios.2017.07.056.

215. Myndrul, V.; Viter, R.; Savchuk, M.; Koval, M.; Starodub, N.; Silamikelis, V.; Smyntyna, V.; Ramanavicius, A.; Iatsunskiy, I. Gold coated porous silicon nanocomposite as a substrate for photoluminescence-based immunosensor suitable for the determination of Aflatoxin B₁. *Talanta* **2017**, *175*, 297–304, doi:10.1016/j.talanta.2017.07.054.

216. Dhanekar, S.; Jain, S. Porous silicon biosensor: Current status. *Biosens. Bioelectron.* **2013**, *41*, 54–64, doi:10.1016/j.bios.2012.09.045.

217. Urmann, K.; Walter, J.G.; Scheper, T.; Segal, E. Label-free optical biosensors based on aptamer-functionalized porous silicon scaffolds. *Anal. Chem.* **2015**, *87*, 1999–2006, doi:10.1021/ac504487g.

218. Tong, W.Y.; Sweetman, M.J.; Marzouk, E.R.; Fraser, C.; Kuchel, T.; Voelcker, N.H. Towards a subcutaneous optical biosensor based on thermally hydrocarbonised porous silicon. *Biomaterials* **2016**, *74*, 217–230, doi:10.1016/j.biomaterials.2015.09.045.

219. Roychaudhuri, C. A review on porous silicon based electrochemical biosensors: Beyond surface area enhancement factor. *Sensors Actuators, B Chem.* **2015**, *210*, 310–323, doi:10.1016/j.snb.2014.12.089.

220. Mathew, F.P.; Alocilja, E.C. Porous silicon-based biosensor for pathogen detection. *Biosens. Bioelectron.* **2005**, *20*, 1656–1661, doi:10.1016/j.bios.2004.08.006.

221. Rossi, A.M.; Wang, L.; Reipa, V.; Murphy, T.E. Porous silicon biosensor for detection of viruses. *Biosens. Bioelectron.* **2007**, *23*, 741–745, doi:10.1016/j.bios.2007.06.004.

222. Benito-Peña, E.; Valdés, M.G.; Glahn-Martínez, B.; Moreno-Bondi, M.C. Fluorescence based fiber optic and planar waveguide biosensors. A review. *Anal. Chim. Acta* **2016**, *943*, 17–40, doi:10.1016/j.aca.2016.08.049.

223. Iatsunskiy, I.; Jancelewicz, M.; Nowaczyk, G.; Kempinski, M.; Peplińska, B.; Jarek, M.; Załęski, K.; Jurga, S.; Smyntyna, V. Atomic layer deposition TiO₂ coated porous silicon surface: Structural characterization and morphological features. *Thin Solid Films* **2015**, *589*, 303–308, doi:10.1016/j.tsf.2015.05.056.
224. Iatsunskiy, I.; Pavlenko, M.; Viter, R.; Jancelewicz, M.; Nowaczyk, G.; Baleviciute, I.; Załęski, K.; Jurga, S.; Ramanavicius, A.; Smyntyna, V. Tailoring the structural, optical, and photoluminescence properties of porous silicon/TiO₂ nanostructures. *J. Phys. Chem. C* **2015**, *119*, 7164–7171, doi:10.1021/acs.jpcc.5b01670.
225. Buttard, D.; Dolino, G.; Bellet, D.; Baumbach, T.; Rieutord, F. X-ray reflectivity investigation of thin p-type porous silicon layers. *Solid State Commun.* **1998**, *109*, 1–5, doi:10.1016/S0038-1098(98)00531-6.
226. Bellet, D.; Dolino, G. X-ray diffraction studies of porous silicon Daniel. *Thin Solid Films* **1996**, *276*, 1–6, doi:10.1016/0040-6090(95)08035-X.
227. Iatsunskiy, I.; Nowaczyk, G.; Jurga, S.; Fedorenko, V.; Pavlenko, M.; Smyntyna, V. One and two-phonon Raman scattering from nanostructured silicon. *Optik (Stuttg)*. **2015**, *126*, 1650–1655, doi:10.1016/j.ijleo.2015.05.088.
228. O. Bisi, S. Ossicini and L. Pavesi; Bisi, O.; Ossicini, S.; Pavesi, L. Porous silicon: a quantum sponge structure for silicon based optoelectronics. *Surf. Sci. Rep.* **2000**, *38*, 1–126, doi:10.1016/S0167-5729(99)00012-6.
229. Salman, K.A.; Omar, K.; Hassan, Z. The effect of etching time of porous silicon on solar cell performance. *Superlattices Microstruct.* **2011**, *50*, 647–658, doi:10.1016/j.spmi.2011.09.006.
230. Liu, Y.; Yu, J.; Wang, Y.; Liu, Z.; Lu, Z. An ultrasensitive aptasensor for detection of Ochratoxin A based on shielding effect-induced inhibition of fluorescence resonance energy transfer. *Sensors Actuators, B Chem.* **2016**, *222*, 797–803, doi:10.1016/j.snb.2015.09.007.
231. Zhu, Z.; Feng, M.; Zuo, L.; Zhu, Z.; Wang, F.; Chen, L.; Li, J.; Shan, G.; Luo, S.Z. An aptamer based surface plasmon resonance biosensor for the detection of ochratoxin A in wine and peanut oil. *Biosens. Bioelectron.* **2015**, *65*, 320–326, doi:10.1016/j.bios.2014.10.059.
232. Ratautaite, V.; Plausinaitis, D.; Baleviciute, I.; Mikoliunaite, L.; Ramanaviciene, A.; Ramanavicius, A. Characterization of caffeine-imprinted polypyrrole by a quartz crystal microbalance and electrochemical impedance spectroscopy. *Sensors Actuators, B Chem.* **2015**, *212*, 63–71, doi:10.1016/j.snb.2015.01.109.
233. Makaraviciute, A.; Ramanavicius, A.; Ramanaviciene, A. Development of a reusable protein G based SPR immunosensor for direct human growth hormone

detection in real samples. *Anal. Methods* **2015**, *7*, 9875–9884, doi:10.1039/C5AY01651G.

234. Jodra, A.; Hervás, M.; López, M.Á.; Escarpa, A. Disposable electrochemical magneto immunosensor for simultaneous simplified calibration and determination of Ochratoxin A in coffee samples. *Sensors Actuators B Chem.* **2015**, *221*, 777–783, doi:10.1016/j.snb.2015.07.007.

235. Yang, J.; Gao, P.; Liu, Y.; Li, R.; Ma, H.; Du, B.; Wei, Q. Label-free photoelectrochemical immunosensor for sensitive detection of Ochratoxin A. *Biosens. Bioelectron.* **2015**, *64*, 13–18, doi:10.1016/j.bios.2014.08.025.

236. Chvojka, T.; Vrkoslav, V.; Jelínek, I.; Jindřich, J.; Lorenc, M.; Dian, J. Mechanisms of photoluminescence sensor response of porous silicon for organic species in gas and liquid phases. *Sensors Actuators, B Chem.* **2004**, *100*, 246–249, doi:10.1016/j.snb.2003.12.040.

237. Harper, J.; Sailor, M.J. Photoluminescence Quenching and the Photochemical Oxidation of Porous Silicon by Molecular Oxygen. *Langmuir* **1997**, *13*, 4652–4658, doi:10.1021/la960535z.

238. Dhanekar, S.; Islam, S.S.; Islam, T.; Harsh Highly sensitive porous silicon sensor: Detection of organic vapours using photoluminescence quenching technique. *Int. J. Smart Sens. Intell. Syst.* **2010**, *3*, 1–13.

239. Yu, J. Current understanding on aflatoxin biosynthesis and future perspective in reducing aflatoxin contamination. *Toxins (Basel)*. **2012**, *4*, 1024–1057.

240. Das, N.; Basu, J.; RoyChaudhuri, C. Graphene coated nanoporous silicon immunosensor for food toxin detection. *Int. J. Adv. Eng. Sci. Appl. Math.* **2015**, *7*, 204–209, doi:10.1007/s12572-015-0144-z.

241. McLean, M.; Dutton, M.F. Cellular interactions and metabolism of aflatoxin: An update. *Pharmacol. Ther.* **1995**, *65*, 163–192, doi:10.1016/0163-7258(94)00054-7.

242. Reiner-Rozman, C.; Kotlowski, C.; Knoll, W. Electronic biosensing with functionalized rGO FETs. *Biosensors* **2016**, *6*, doi:10.3390/bios6020017.

243. Li, J.; Sailor, M.J. Synthesis and characterization of a stable, label-free optical biosensor from TiO₂-coated porous silicon. *Biosens. Bioelectron.* **2014**, *55*, 372–378, doi:10.1016/j.bios.2013.12.016.

244. Mares, J.W.; Fain, J.S.; Weiss, S.M. Variable conductivity of nanocomposite nickel oxide/porous silicon. *Phys. Rev. B - Condens. Matter Mater. Phys.* **2013**, *88*, 1–8, doi:10.1103/PhysRevB.88.075307.

245. Zhu, G.; Liu, J.-T.; Wang, Y.; Zhang, D.; Guo, Y.; Tasciotti, E.; Hu, Z.; Liu, X. In Situ Reductive Synthesis of Structural Supported Gold Nanorods in Porous

Silicon Particles for Multifunctional Nanovectors. *ACS Appl. Mater. Interfaces* **2016**, *8*, 11881–11891, doi:10.1021/acsami.6b03008.

246. Coluccio, M.L.; De Vitis, S.; Strumbo, G.; Candeloro, P.; Perozziello, G.; Di Fabrizio, E.; Gentile, F. Inclusion of gold nanoparticles in meso-porous silicon for the SERS analysis of cell adhesion on nano-structured surfaces. *Microelectron. Eng.* **2016**, *158*, 102–106, doi:10.1016/j.mee.2016.03.045.

247. Zhao, Y.; Wang, L.; Min, J.; Shi, W. Effect of Au film and absorption groups on minority carrier life of porous silicon. *Curr. Appl. Phys.* **2010**, *10*, 871–873, doi:10.1016/j.cap.2009.10.010.

248. Sánchez De La Morena, S.; Recio-Sánchez, G.; Torres-Costa, V.; Martín-Palma, R.J. Hybrid gold/porous silicon thin films for plasmonic solar cells. *Scr. Mater.* **2014**, *74*, 33–37, doi:10.1016/j.scriptamat.2013.06.015.

249. Sainato, M.; Strambini, L.M.; Rella, S.; Mazzotta, E.; Barillaro, G. Sub-Parts Per Million NO₂ Chemi-Transistor Sensors Based on Composite Porous Silicon/Gold Nanostructures Prepared by Metal-Assisted Etching. *ACS Appl. Mater. Interfaces* **2015**, *7*, 7136–7145, doi:10.1021/am5089633.

250. Zhang, H.; Jia, Z.; Lv, X. Surface layer reflective index changes of Au nanoparticle functionalized porous silicon microcavity for DNA detection. *Curr. Appl. Phys.* **2014**, *15*, 870–876, doi:10.1016/j.cap.2015.03.023.

251. Li, X.; Tan, J.; Yu, J.; Feng, J.; Pan, A.; Zheng, S.; Wu, J. Use of a porous silicon-gold plasmonic nanostructure to enhance serum peptide signals in MALDI-TOF analysis. *Anal. Chim. Acta* **2014**, *849*, 27–35, doi:10.1016/j.aca.2014.08.028.

252. Thakur, M.; Isaacson, M.; Sinsabaugh, S.L.; Wong, M.S.; Biswal, S.L. Gold-coated porous silicon films as anodes for lithium ion batteries. *J. Power Sources* **2012**, *205*, 426–432, doi:10.1016/j.jpowsour.2012.01.058.

253. Dridi, H.; Moadhen, A.; Haji, L. Comparative SERS study carried out on unsilanized and silanized oxidized porous silicon surface coated by small gold nanoparticles. *J. Porous Mater.* **2014**, *22*, 239–245, doi:10.1007/s10934-014-9890-8.

254. Amran, T.S.T.; Hashim, M.R.; Al-Obaidi, N.K.A.; Yazid, H.; Adnan, R. Optical absorption and photoluminescence studies of gold nanoparticles deposited on porous silicon. *Nanoscale Res. Lett.* **2013**, *8*, 35, doi:10.1186/1556-276X-8-35.

255. Sakamoto, S.; Philippe, L.; Bechelany, M.; Michler, J.; Asoh, H.; Ono, S. Ordered hexagonal array of Au nanodots on Si substrate based on colloidal crystal templating. *Nanotechnology* **2008**, *19*, 405304, doi:10.1088/0957-4484/19/40/405304.

256. Iatsunskyi, I.; Coy, E.; Viter, R.; Nowaczyk, G.; Jancelewicz, M.; Baleviciute, I.; Załęski, K.; Jurga, S. Study on Structural, Mechanical, and Optical Properties of

Al₂O₃–TiO₂ Nanolaminates Prepared by Atomic Layer Deposition. *J. Phys. Chem. C* **2015**, *119*, 20591–20599, doi:10.1021/acs.jpcc.5b06745.

257. Chourou, M.L.; Fukami, K.; Sakka, T.; Ogata, Y.H. Gold electrodeposition into porous silicon: Comparison between meso- and macroporous silicon. *Phys. Status Solidi Curr. Top. Solid State Phys.* **2011**, *8*, 1783–1786, doi:10.1002/pssc.201000094.

258. Pavlenko, M.; Coy, E.L.; Jancelewicz, M.; Zał□ski, K.; Smyntyna, V.; Jurga, S.; Iatsunskyi, I. Enhancement of optical and mechanical properties of Si nanopillars by ALD TiO₂ coating. *RSC Adv.* **2016**, doi:10.1039/c6ra21742g.

259. Rong, G.; Ryckman, J.D.; Mernaugh, R.L.; Weiss, S.M. Label-free porous silicon membrane waveguide for DNA sensing. *Appl. Phys. Lett.* **2008**, *93*, doi:10.1063/1.3005620.

260. Bisi, O.; Ossicini, S.; Pavesi, L. Porous silicon: A quantum sponge structure for silicon based optoelectronics. *Surf. Sci. Rep.* **2000**, *38*, 1–126, doi:10.1016/S0167-5729(99)00012-6.

261. Prokes, S.M. Light emission in thermally oxidized porous silicon: Evidence for oxide-related luminescence. *Appl. Phys. Lett.* **1993**, *62*, 3244–3246, doi:10.1063/1.109087.

262. Gelloz, B.; Sano, H.; Boukherroub, R.; Wayner, D.D.M.; Lockwood, D.J.; Koshida, N. Stabilization of porous silicon electroluminescence by surface passivation with controlled covalent bonds. *Appl. Phys. Lett.* **2003**, *83*, 2342–2344, doi:10.1063/1.1613812.

263. Yugender Goud, K.; Catanante, G.; Hayat, A.; M., S.; Vengatajalabathy Gobi, K.; Marty, J.L. Disposable and portable electrochemical aptasensor for label free detection of aflatoxin B1 in alcoholic beverages. *Sensors Actuators B Chem.* **2016**, *235*, 466–473, doi:10.1016/j.snb.2016.05.112.

264. Baleviciute, I.; Ratautaite, V.; Ramanaviciene, A.; Balevicius, Z.; Broeders, J.; Croux, D.; Mcdonald, M.; Vahidpour, F.; Thoelen, R.; Ceuninck, W. De; et al. Evaluation of theophylline imprinted polypyrrole film. *Synth. Met.* **2015**, *209*, 206–211, doi:10.1016/j.synthmet.2015.07.021.

265. Chauhan, R.; Singh, J.; Sachdev, T.; Basu, T.; Malhotra, B.D. Recent advances in mycotoxins detection. *Biosens. Bioelectron.* **2016**, *81*, 532–545, doi:10.1016/j.bios.2016.03.004.

266. D. J., M. Fungi and mycotoxins in grains: Implication for stored roducts research. *J. Stored Prod. Res.* **1995**, *31*, 1–16.

267. Rieswijk, L.; Claessen, S.M.H.; Bekers, O.; van Herwijnen, M.; Theunissen, D.H.J.; Jennen, D.G.J.; de Kok, T.M.C.M.; Kleinjans, J.C.S.; van Breda, S.G.J. Aflatoxin B1 induces persistent epigenomic effects in primary human hepatocytes

associated with hepatocellular carcinoma. *Toxicology* **2016**, doi:10.1016/j.tox.2016.05.002.

268. Marchese, S.; Polo, A.; Ariano, A.; Velotto, S.; Costantini, S.; Severino, L. Aflatoxin B1 and M1: Biological Properties and Their Involvement in Cancer Development. *Toxins (Basel)*. **2018**, *10*, 214, doi:10.3390/toxins10060214.

269. Adegbeye, M.J.; Reddy, P.R.K.; Chilaka, C.A.; Balogun, O.B.; Elghandour, M.M.M.Y.; Rivas-Caceres, R.R.; Salem, A.Z.M. Mycotoxin toxicity and residue in animal products: Prevalence, consumer exposure and reduction strategies – A review. *Toxicon* **2020**, doi:10.1016/j.toxicon.2020.01.007.

270. Battilani, P.; Toscano, P.; Van Der Fels-Klerx, H.J.; Moretti, A.; Camardo Leggieri, M.; Brera, C.; Rortais, A.; Goumperis, T.; Robinson, T. Aflatoxin B 1 contamination in maize in Europe increases due to climate change. *Sci. Rep.* **2016**, *6*, 1–7, doi:10.1038/srep24328.

271. Xu, Q.; Shi, W.; Lv, P.; Meng, W.; Mao, G.; Gong, C.; Chen, Y.; Wei, Y.; He, X.; Zhao, J.; et al. Critical role of caveolin-1 in aflatoxin B1-induced hepatotoxicity via the regulation of oxidation and autophagy. *Cell Death Dis.* **2020**, *11*, doi:10.1038/s41419-019-2197-6.

272. Lee, N.A.; Wang, S.; Allan, R.D.; Kennedy, I.R. A Rapid Aflatoxin B1 ELISA: Development and Validation with Reduced Matrix Effects for Peanuts, Corn, Pistachio, and Soybeans. *J. Agric. Food Chem.* **2004**, *52*, 2746–2755, doi:10.1021/jf0354038.

273. Ammida, N.H.S.; Micheli, L.; Piermarini, S.; Moscone, D.; Palleschi, G. Detection of Aflatoxin B 1 in Barley: Comparative Study of Immunosensor and HPLC. *Anal. Lett.* **2006**, *39*, 1559–1572, doi:10.1080/00032710600713248.

274. Puiu, M.; Zamfir, L.G.; Buiculescu, V.; Baracu, A.; Mitrea, C.; Bala, C. Significance testing and multivariate analysis of datasets from surface plasmon resonance and surface acoustic wave biosensors: Prediction and assay validation for surface binding of large analytes. *Sensors (Switzerland)* **2018**, *18*, 1–15, doi:10.3390/s18103541.

275. Pan, D.; Li, G.; Hu, H.; Xue, H.; Zhang, M.; Zhu, M.; Gong, X.; Zhang, Y.; Wan, Y.; Shen, Y. Direct Immunoassay for Facile and Sensitive Detection of Small Molecule Aflatoxin B1 based on Nanobody. *Chem. - A Eur. J.* **2018**, doi:10.1002/chem.201801202.

276. Myndrul, V.; Iatsunskyi, I. Nanosilicon-Based Composites for (Bio)sensing Applications: Current Status, Advantages, and Perspectives. *Materials (Basel)*. **2019**, *12*, 2880, doi:10.3390/ma12182880.

277. Han, D.; Ni, D.; Zhou, Q.; Ji, J.; Lv, Y.; Shen, Y.; Liu, S.; Zhang, Y. Harnessing Photoluminescent Properties of Carbon Nitride Nanosheets in a Hierarchical Matrix. *Adv. Funct. Mater.* **2019**, doi:10.1002/adfm.201905576.

278. Myndrul, V.; Viter, R.; Savchuk, M.; Shpyrka, N.; Erts, D.; Jevdokimovs, D.; Silamiķelis, V.; Smyntyna, V.; Ramanavicius, A.; Iatsunskiy, I. Porous silicon based photoluminescence immunosensor for rapid and highly-sensitive detection of Ochratoxin A. *Biosens. Bioelectron.* **2018**, *102*, 661–667, doi:10.1016/j.bios.2017.11.048.
279. Myndrul, V.; Viter, R.; Savchuk, M.; Koval, M.; Starodub, N.; Silamiķelis, V.; Smyntyna, V.; Ramanavicius, A.; Iatsunskiy, I. Gold coated porous silicon nanocomposite as a substrate for photoluminescence-based immunosensor suitable for the determination of Aflatoxin B1. *Talanta* **2017**, *175*, 297–304, doi:10.1016/j.talanta.2017.07.054.
280. Tereshchenko, A.; Fedorenko, V.; Smyntyna, V.; Konup, I.; Konup, A.; Eriksson, M.; Yakimova, R.; Ramanavicius, A.; Balme, S.; Bechelany, M. ZnO films formed by atomic layer deposition as an optical biosensor platform for the detection of Grapevine virus A-type proteins. *Biosens. Bioelectron.* **2017**, *92*, 763–769, doi:10.1016/j.bios.2016.09.071.
281. Viter, R.; Savchuk, M.; Iatsunskiy, I.; Pietralik, Z.; Starodub, N.; Shpyrka, N.; Ramanaviciene, A.; Ramanavicius, A. Analytical, thermodynamical and kinetic characteristics of photoluminescence immunosensor for the determination of Ochratoxin A. *Biosens. Bioelectron.* **2018**, *99*, 237–243, doi:10.1016/j.bios.2017.07.056.
282. Hariharan, S.; Karthikeyan, B. Band bending effect induced non-enzymatic highly sensitive glucose sensing in ZnO nanoparticles. *J. Lumin.* **2017**, *183*, 1–6, doi:10.1016/j.jlumin.2016.10.046.
283. Politi, J.; Rea, I.; Dardano, P.; De Stefano, L.; Gioffrè, M. Versatile synthesis of ZnO nanowires for quantitative optical sensing of molecular biorecognition. *Sensors Actuators, B Chem.* **2015**, *220*, 705–711, doi:10.1016/j.snb.2015.05.135.
284. Tamashevski, A.; Harmaza, Y.; Viter, R.; Jevdokimovs, D.; Poplausks, R.; Slobozhanina, E.; Mikoliunaite, L.; Erts, D.; Ramanaviciene, A.; Ramanavicius, A. Zinc oxide nanorod based immunosensing platform for the determination of human leukemic cells. *Talanta* **2019**, *200*, 378–386, doi:10.1016/j.talanta.2019.03.064.
285. Tereshchenko, A.; Bechelany, M.; Viter, R.; Khranovskyy, V.; Smyntyna, V.; Starodub, N.; Yakimova, R. Optical biosensors based on ZnO nanostructures: Advantages and perspectives. A review. *Sensors Actuators, B Chem.* **2016**, *229*, 664–677, doi:10.1016/j.snb.2016.01.099.
286. Zhang, Y.; Ram, M.K.; Stefanakos, E.K.; Goswami, D.Y. Synthesis, characterization, and applications of ZnO nanowires. *J. Nanomater.* **2012**, *2012*, 1–22, doi.org/10.1155/2012/624520.
287. Liu, F.; Wong, M.M.K.; Chiu, S.K.; Lin, H.; Ho, J.C.; Pang, S.W. Effects of nanoparticle size and cell type on high sensitivity cell detection using a localized

surface plasmon resonance biosensor. *Biosens. Bioelectron.* **2014**, *55*, 141–148, doi:10.1016/j.bios.2013.11.075.

288. Sang, C.H.; Chou, S.J.; Pan, F.M.; Sheu, J.T. Fluorescence enhancement and multiple protein detection in ZnO nanostructure microfluidic devices. *Biosens. Bioelectron.* **2016**, *75*, 285–292, doi:10.1016/j.bios.2015.08.050.

289. Barhoum, A.; Pal, K.; Rahier, H.; Uludag, H.; Kim, I.S.; Bechelany, M. Nanofibers as new-generation materials: From spinning and nano-spinning fabrication techniques to emerging applications. *Appl. Mater. Today* **2019**, *17*, 1–35, doi:10.1016/j.apmt.2019.06.015.

290. Nagarajan, S.; Belaid, H.; Pochat-Bohatier, C.; Teyssier, C.; Iatsunskiy, I.; Coy, E.; Balme, S.; Cornu, D.; Miele, P.; Kalkura, N.S.; et al. Design of Boron Nitride/Gelatin Electrospun Nanofibers for Bone Tissue Engineering. *ACS Appl. Mater. Interfaces* **2017**, *9*, 33695–33706, doi:10.1021/acsami.7b13199.

291. Graniel, O.; Weber, M.; Balme, S.; Miele, P.; Bechelany, M. Atomic layer deposition for biosensing applications. *Biosens. Bioelectron.* **2018**, *122*, 147–159, doi:10.1016/j.bios.2018.09.038.

292. Pavlenko, M.; Coy, E.L.; Jancelewicz, M.; Załęski, K.; Smyntyna, V.; Jurga, S.; Iatsunskiy, I. Enhancement of optical and mechanical properties of Si nanopillars by ALD TiO₂ coating. *RSC Adv.* **2016**, *6*, 97070–97076, doi:10.1039/C6RA21742G.

293. Weber, M.; Julbe, A.; Ayril, A.; Miele, P.; Bechelany, M. Atomic Layer Deposition for Membranes: Basics, Challenges, and Opportunities. *Chem. Mater.* **2018**, *30*, 7368–7390, doi:10.1021/acs.chemmater.8b02687.

294. Hober, S.; Nord, K.; Linhult, M. Protein A chromatography for antibody purification. *J. Chromatogr. B* **2007**, *848*, 40–47, doi:10.1016/j.jchromb.2006.09.030.

295. Libera, J.A.; Elam, J.W.; Pellin, M.J. Conformal ZnO coatings on high surface area silica gel using atomic layer deposition. *Thin Solid Films* **2008**, *516*, 6158–6166, doi:10.1016/j.tsf.2007.11.044.

296. Patterson, A.L. The Scherrer Formula for X-Ray Particle Size Determination. *Phys. Rev.* **1939**, *56*, 978–982, doi:10.1103/PhysRev.56.978.

297. Baitimirova, M.; Viter, R.; Andzane, J.; Van Der Lee, A.; Voiry, D.; Iatsunskiy, I.; Coy, E.; Mikoliunaite, L.; Tumenas, S.; Zaleski, K.; et al. Tuning of Structural and Optical Properties of Graphene/ZnO Nanolaminates. *J. Phys. Chem. C* **2016**, doi:10.1021/acs.jpcc.6b07221.

298. Garimella, L.B.V.S.; Dhiman, T.K.; Kumar, R.; Singh, A.K.; Solanki, P.R. One-Step Synthesized ZnO np-Based Optical Sensors for Detection of Aldicarb via a Photoinduced Electron Transfer Route. *ACS Omega* **2020**, doi:10.1021/acsomega.9b01987.

299. Moore, J.C.; Covington, L.R.; Stansell, R. Affect of film thickness on the blue photoluminescence from ZnO. *Phys. Status Solidi Appl. Mater. Sci.* **2012**, doi:10.1002/pssa.201127613.
300. Lee, J.; Choi, S.; Bae, S.J.; Yoon, S.M.; Choi, J.S.; Yoon, M. Visible light-sensitive APTES-bound ZnO nanowire toward a potent nanoinjector sensing biomolecules in a living cell. *Nanoscale* **2013**, *5*, 10275, doi:10.1039/c3nr03042c.
301. Gunda, N.S.K.; Singh, M.; Norman, L.; Kaur, K.; Mitra, S.K. Optimization and characterization of biomolecule immobilization on silicon substrates using (3-aminopropyl)triethoxysilane (APTES) and glutaraldehyde linker. *Appl. Surf. Sci.* **2014**, *305*, 522–530, doi:10.1016/j.apsusc.2014.03.130.
302. Bhardwaj, H.; Sumana, G.; Marquette, C.A. A label-free ultrasensitive microfluidic surface Plasmon resonance biosensor for Aflatoxin B1 detection using nanoparticles integrated gold chip. *Food Chem.* **2020**, *307*, 125530, doi:10.1016/j.foodchem.2019.125530.
303. Wei, M.; Zhao, F.; Xie, Y. A novel gold nanostars-based fluorescent aptasensor for aflatoxin B1 detection. *Talanta* **2020**, *209*, 120599, doi:10.1016/j.talanta.2019.120599.
304. Moon, J.; Byun, J.; Kim, H.; Lim, E.K.; Jeong, J.; Jung, J.; Kang, T. On-site detection of aflatoxin B1 in grains by a palm-sized surface plasmon resonance sensor. *Sensors (Switzerland)* **2018**, *18*, doi:10.3390/s18020598.
305. Alshannaq; Yu A Liquid Chromatographic Method for Rapid and Sensitive Analysis of Aflatoxins in Laboratory Fungal Cultures. *Toxins (Basel)*. **2020**, *12*, 93, doi:10.3390/toxins12020093.
306. An, Z.; Jang, C.H. Label-free optical detection of aflatoxin by using a liquid crystal-based immunosensor. *Microchem. J.* **2018**, doi:10.1016/j.microc.2018.07.013.
307. Xie, H.; Dong, J.; Duan, J.; Hou, J.; Ai, S.; Li, X. Magnetic nanoparticles-based immunoassay for aflatoxin B1 using porous g-C₃N₄ nanosheets as fluorescence probes. *Sensors Actuators, B Chem.* **2019**, doi:10.1016/j.snb.2018.09.089.
308. Jia, Y.; Wu, F.; Liu, P.; Zhou, G.; Yu, B.; Lou, X.; Xia, F. A label-free fluorescent aptasensor for the detection of Aflatoxin B1 in food samples using AIEgens and graphene oxide. *Talanta* **2019**, doi:10.1016/j.talanta.2019.01.078.
309. Sergeyeva, T.; Yarynka, D.; Piletska, E.; Lynn timer, R.; Zaporozhets, O.; Brovko, O.; Piletsky, S.; El'skaya, A. Fluorescent sensor systems based on nanostructured polymeric membranes for selective recognition of Aflatoxin B1. *Talanta* **2017**, doi:10.1016/j.talanta.2017.07.030.

310. Xiong, Y.; Pei, K.; Wu, Y.; Duan, H.; Lai, W.; Xiong, Y. Plasmonic ELISA based on enzyme-assisted etching of Au nanorods for the highly sensitive detection of aflatoxin B1 in corn samples. *Sensors Actuators, B Chem.* **2018**, doi:10.1016/j.snb.2018.04.027.
311. Lerdsri, J.; Chananchana, W.; Upan, J.; Sridara, T.; Jakmune, J. Label-free colorimetric aptasensor for rapid detection of aflatoxin B1 by utilizing cationic perylene probe and localized surface plasmon resonance of gold nanoparticles. *Sensors Actuators, B Chem.* **2020**, doi:10.1016/j.snb.2020.128356.
312. Wu, J.; Zeng, L.; Li, N.; Liu, C.; Chen, J. A wash-free and label-free colorimetric biosensor for naked-eye detection of aflatoxin B1 using G-quadruplex as the signal reporter. *Food Chem.* **2019**, doi:10.1016/j.foodchem.2019.125034.
313. Xiong, X.; Li, Y.; Yuan, W.; Lu, Y.; Xiong, X.; Li, Y.; Chen, X.; Liu, Y. Screen printed bipolar electrode for sensitive electrochemiluminescence detection of aflatoxin B1 in agricultural products. *Biosens. Bioelectron.* **2020**, *150*, doi:10.1016/j.bios.2019.111873.
314. Schasfoort, R.B.M.; Bergveld, P.; Kooyman, R.P.H.; Greve, J. Possibilities and limitations of direct detection of protein charges by means of an immunological field-effect transistor. *Anal. Chim. Acta* **1990**, *238*, 323–329, doi:10.1016/S0003-2670(00)80554-1.
315. Bergveld, P. A critical evaluation of direct electrical protein detection methods. *Biosens. Bioelectron.* **1991**, *6*, 55–72, doi:10.1016/0956-5663(91)85009-L.
316. Haustein, N.; Gutiérrez-Sanz, Ó.; Tarasov, A. Analytical Model to Describe the Effect of Polyethylene Glycol on Ionic Screening of Analyte Charges in Transistor-Based Immunosensing. *ACS Sensors* **2019**, doi:10.1021/acssensors.8b01515.
317. Ohshima, H.; Ohki, S. Donnan potential and surface potential of a charged membrane. *Biophys. J.* **1985**, *47*, 673–678, doi:10.1016/S0006-3495(85)83963-1.
318. Zhang, Z.; Yates, J.T. Band bending in semiconductors: Chemical and physical consequences at surfaces and interfaces. *Chem. Rev.* **2012**, *112*, 5520–5551, doi:10.1021/cr3000626.
319. Yang, W.; Butler, J.E.; Russell, J.N.; Hamers, R.J. Direct electrical detection of antigen-antibody binding on diamond and silicon substrates using electrical impedance spectroscopy. *Analyst* **2007**, *132*, 296–306, doi:10.1039/b612201a.
320. Ramales-Valderrama, R.; Vázquez-Durán, A.; Méndez-Albores, A. Biosorption of B-aflatoxins Using Biomasses Obtained from Formosa Firethorn [*Pyracantha koidzumii* (Hayata) Rehder]. *Toxins (Basel)*. **2016**, *8*, 218, doi:10.3390/toxins8070218.

321. Azizian, S.; Eris, S.; Wilson, L.D. Re-evaluation of the century-old Langmuir isotherm for modeling adsorption phenomena in solution. *Chem. Phys.* **2018**, *513*, 99–104, doi:10.1016/j.chemphys.2018.06.022.
322. Saadi, Z.; Fazaeli, R.; Vafajoo, L.; Naser, I.; Mohammadi, G. Promotion of clinoptilolite adsorption for azithromycin antibiotic by Tween 80 and Triton X-100 surface modifiers under batch and fixed-bed processes. *Chem. Eng. Commun.* **2020**, *0*, 1–21, doi:10.1080/00986445.2020.1715955.
323. Haidukowski, M.; Casamassima, E.; Cimmarusti, M.T.; Branà, M.T.; Longobardi, F.; Acquafredda, P.; Logrieco, A.; Altomare, C. Aflatoxin B1-adsorbing capability of pleurotus eryngii mycelium: Efficiency and modeling of the process. *Front. Microbiol.* **2019**, *10*, doi:10.3389/fmicb.2019.01386.
324. Lim, W.-R.; Kim, S.W.; Lee, C.-H.; Choi, E.-K.; Oh, M.H.; Seo, S.N.; Park, H.-J.; Hamm, S.-Y. Performance of composite mineral adsorbents for removing Cu, Cd, and Pb ions from polluted water. *Sci. Rep.* **2019**, *9*, 13598, doi:10.1038/s41598-019-49857-9.
325. Luo, Q.; Andrade, J.D. Cooperative Adsorption of Proteins onto Hydroxyapatite. *J. Colloid Interface Sci.* **1998**, *200*, 104–113, doi:10.1006/jcis.1997.5364.
326. Eisen, H.N.; Karush, F. Immune Tolerance and an Extracellular Regulatory Role for Bivalent Antibody. *Nature* **1964**, *202*, 677–682, doi:10.1038/202677a0.
327. Wang, W.; Singh, S.; Zeng, D.L.; King, K.; Nema, S. Antibody Structure, Instability, and Formulation. *J. Pharm. Sci.* **2007**, *96*, 1–26, doi:10.1002/jps.20727.
328. Cucciniello, M.; Petracca, F.; Ciani, O.; Tarricone, R. Development features and study characteristics of mobile health apps in the management of chronic conditions: a systematic review of randomised trials. *npj Digit. Med.* **2021**, *4*, 144, doi:10.1038/s41746-021-00517-1.
329. Chen, Y.; Lu, S.; Zhang, S.; Li, Y.; Qu, Z.; Chen, Y.; Lu, B.; Wang, X.; Feng, X. Skin-like biosensor system via electrochemical channels for noninvasive blood glucose monitoring. *Sci. Adv.* **2017**, *3*, 1–8, doi:10.1126/sciadv.1701629.
330. Lee, H.; Song, C.; Hong, Y.S.; Kim, M.S.; Cho, H.R.; Kang, T.; Shin, K.; Choi, S.H.; Hyeon, T.; Kim, D.-H. Wearable/disposable sweat-based glucose monitoring device with multistage transdermal drug delivery module. *Sci. Adv.* **2017**, *3*, e1601314, doi:10.1126/sciadv.1601314.
331. Sempionatto, J.R.; Lin, M.; Yin, L.; De la paz, E.; Pei, K.; Sonsa-ard, T.; de Loyola Silva, A.N.; Khorshed, A.A.; Zhang, F.; Tostado, N.; et al. An epidermal patch for the simultaneous monitoring of haemodynamic and metabolic biomarkers. *Nat. Biomed. Eng.* **2021**, *5*, 737–748, doi:10.1038/s41551-021-00685-1.

332. Pavlenko, M.; Myndrul, V.; Gottardi, G.; Coy, E.; Jancelewicz, M.; Iatsunskyi, I. Porous Silicon-Zinc Oxide Nanocomposites Prepared by Atomic Layer Deposition for Biophotonic Applications. *Materials (Basel)*. **2020**, *13*, 1987, doi:10.3390/ma13081987.
333. Myndrul, V.; Coy, E.; Bechelany, M.; Iatsunskyi, I. Photoluminescence label-free immunosensor for the detection of Aflatoxin B1 using polyacrylonitrile/zinc oxide nanofibers. *Mater. Sci. Eng. C* **2021**, *118*, 111401, doi:10.1016/j.msec.2020.111401.
334. Wang, S.; Zhao, J.; Tong, T.; Cheng, B.; Xiao, Y.; Lei, S. Bias-Controlled Tunable Electronic Transport with Memory Characteristics in an Individual ZnO Nanowire for Realization of a Self-Driven UV Photodetector with Two Symmetrical Electrodes. *ACS Appl. Mater. Interfaces* **2019**, *11*, 14932–14943, doi:10.1021/acsami.9b00267.
335. Kuranaga, Y.; Matsui, H.; Ikehata, A.; Shimoda, Y.; Noiri, M.; Ho, Y.-L.; Delaunay, J.-J.; Teramura, Y.; Tabata, H. Enhancing Detection Sensitivity of ZnO-Based Infrared Plasmonic Sensors Using Capped Dielectric Ga₂O₃ Layers for Real-Time Monitoring of Biological Interactions. *ACS Appl. Bio Mater.* **2020**, *3*, 6331–6342, doi:10.1021/acsabm.0c00792.
336. Zhai, Y.; Zheng, Y.; Ma, Z.; Cai, Y.; Wang, F.; Guo, X.; Wen, Y.; Yang, H. Synergistic Enhancement Effect for Boosting Raman Detection Sensitivity of Antibiotics. *ACS Sensors* **2019**, *4*, 2958–2965, doi:10.1021/acssensors.9b01436.
337. Zhao, Y.; Fu, Y.; Wang, P.; Xing, L.; Xue, X. Highly stable piezo-immunoglobulin-biosensing of a SiO₂/ZnO nanogenerator as a self-powered/active biosensor arising from the field effect influenced piezoelectric screening effect. *Nanoscale* **2015**, *7*, 1904–1911, doi:10.1039/C4NR06461E.
338. Lei, Y.; Luo, N.; Yan, X.; Zhao, Y.; Zhang, G.; Zhang, Y. A highly sensitive electrochemical biosensor based on zinc oxide nanotetrapods for l-lactic acid detection. *Nanoscale* **2012**, *4*, 3438, doi:10.1039/c2nr30334e.
339. Yi, Z.; Wang, J.; Jiang, T.; Tang, Q.; Cheng, Y. Photocatalytic degradation of sulfamethazine in aqueous solution using ZnO with different morphologies. *R. Soc. Open Sci.* **2018**, *5*, 171457, doi:10.1098/rsos.171457.
340. Zhao, Y.; Yan, X.; Kang, Z.; Fang, X.; Zheng, X.; Zhao, L.; Du, H.; Zhang, Y. Zinc oxide nanowires-based electrochemical biosensor for L-lactic acid amperometric detection. *J. Nanoparticle Res.* **2014**, *16*, 2398, doi:10.1007/s11051-014-2398-y.
341. Theerthagiri, J.; Salla, S.; Senthil, R.A.; Nithyadharseni, P.; Madankumar, A.; Arunachalam, P.; Maiyalagan, T.; Kim, H.-S. A review on ZnO nanostructured materials: energy, environmental and biological applications. *Nanotechnology* **2019**, *30*, 392001, doi:10.1088/1361-6528/ab268a.

342. Novoselov, K.S.; Geim, A.K.; Morozov, S. V.; Jiang, D.; Zhang, Y.; Dubonos, S. V.; Grigorieva, I. V.; Firsov, A.A. Electric Field Effect in Atomically Thin Carbon Films. *Science* (5696). **2004**, 306, 666–669, doi:10.1126/science.1102896.
343. Kang, M.-H.; Lee, D.; Sung, J.; Kim, J.; Kim, B.H.; Park, J. Structure and Chemistry of 2D Materials. In *Comprehensive Nanoscience and Nanotechnology*; Andrews, D.L.; Lipson, R.H.; Nann, T. (Second E., Eds.; Elsevier: Oxford, **2019**; pp. 55–90 ISBN 9780128122969.
344. Fan, F.R.; Wang, R.; Zhang, H.; Wu, W. Emerging beyond-graphene elemental 2D materials for energy and catalysis applications. *Chem. Soc. Rev.* **2021**, 50, 10983–11031, doi:10.1039/C9CS00821G.
345. Tao, W.; Kong, N.; Ji, X.; Zhang, Y.; Sharma, A.; Ouyang, J.; Qi, B.; Wang, J.; Xie, N.; Kang, C.; et al. Emerging two-dimensional monoelemental materials (Xenes) for biomedical applications. *Chem. Soc. Rev.* **2019**, 48, 2891–2912, doi:10.1039/C8CS00823J.
346. VahidMohammadi, A.; Rosen, J.; Gogotsi, Y. The world of two-dimensional carbides and nitrides (MXenes). *Science* (6547). **2021**, 372, doi:10.1126/science.abf1581.
347. Zeng, R.; Wang, W.; Chen, M.; Wan, Q.; Wang, C.; Knopp, D.; Tang, D. CRISPR-Cas12a-driven MXene-PEDOT:PSS piezoresistive wireless biosensor. *Nano Energy* **2021**, 82, 105711, doi:10.1016/j.nanoen.2020.105711.
348. Kalambate, P.K.; Gadhari, N.S.; Li, X.; Rao, Z.; Navale, S.T.; Shen, Y.; Patil, V.R.; Huang, Y. Recent advances in MXene-based electrochemical sensors and biosensors. *TrAC Trends Anal. Chem.* **2019**, 120, 115643, doi:10.1016/j.trac.2019.115643.
349. Hou, C.; Yu, H. ZnO/Ti₃C₂Tx monolayer electron transport layers with enhanced conductivity for highly efficient inverted polymer solar cells. *Chem. Eng. J.* **2021**, 407, 127192, doi:10.1016/j.cej.2020.127192.
350. Sreedhar, A.; Noh, J.-S. Interfacial engineering insights of promising monolayer 2D Ti₃C₂ MXene anchored flake-like ZnO thin films for improved PEC water splitting. *J. Electroanal. Chem.* **2021**, 883, 115044, doi:10.1016/j.jelechem.2021.115044.
351. Lu, P.; Wu, J.; Shen, X.; Gao, X.; Shi, Z.; Lu, M.; Yu, W.W.; Zhang, Y. ZnO–Ti₃C₂ MXene Electron Transport Layer for High External Quantum Efficiency Perovskite Nanocrystal Light-Emitting Diodes. *Adv. Sci.* **2020**, 7, 2001562, doi:10.1002/advs.202001562.
352. Yang, Z.; Jiang, L.; Wang, J.; Liu, F.; He, J.; Liu, A.; Lv, S.; You, R.; Yan, X.; Sun, P.; et al. Flexible resistive NO₂ gas sensor of three-dimensional crumpled MXene Ti₃C₂Tx/ZnO spheres for room temperature application. *Sensors Actuators B Chem.* **2021**, 326, 128828, doi:10.1016/j.snb.2020.128828.

353. Lv, J.; Zhang, L.; Zhu, L.; Wang, F.; Zhang, Y.; Zheng, W.; Tan, L. A fast and mild method to prepare d-Ti₃C₂T_x/ZnO composites at room temperature with excellent catalytic performance. *Appl. Surf. Sci.* **2021**, *558*, 149863, doi:<https://doi.org/10.1016/j.apsusc.2021.149863>.
354. Tawale, J.S.; Dey, K.K.; Pasricha, R.; Sood, K.N.; Srivastava, A.K. Synthesis and characterization of ZnO tetrapods for optical and antibacterial applications. *Thin Solid Films* **2010**, *519*, 1244–1247, doi:[10.1016/j.tsf.2010.08.077](https://doi.org/10.1016/j.tsf.2010.08.077).
355. Alhabeab, M.; Maleski, K.; Anasori, B.; Lelyukh, P.; Clark, L.; Sin, S.; Gogotsi, Y. Guidelines for Synthesis and Processing of Two-Dimensional Titanium Carbide (Ti₃C₂T_x MXene). *Chem. Mater.* **2017**, *29*, 7633–7644, doi:[10.1021/acs.chemmater.7b02847](https://doi.org/10.1021/acs.chemmater.7b02847).
356. Meng, L.; Turner, A.P.F.; Mak, W.C. Conducting Polymer-Reinforced Laser-Irradiated Graphene as a Heterostructured 3D Transducer for Flexible Skin Patch Biosensors. *ACS Appl. Mater. Interfaces* **2021**, *13*, 54456–54465, doi:[10.1021/acsami.1c13164](https://doi.org/10.1021/acsami.1c13164).
357. Zhang, R.; Yin, P.-G.; Wang, N.; Guo, L. Photoluminescence and Raman scattering of ZnO nanorods. *Solid State Sci.* **2009**, *11*, 865–869, doi:<https://doi.org/10.1016/j.solidstatesciences.2008.10.016>.
358. Sarycheva, A.; Gogotsi, Y. Raman Spectroscopy Analysis of the Structure and Surface Chemistry of Ti₃C₂T_x MXene. *Chem. Mater.* **2020**, *32*, 3480–3488, doi:[10.1021/acs.chemmater.0c00359](https://doi.org/10.1021/acs.chemmater.0c00359).
359. Näslund, L.-Å.; Persson, P.O.Å.; Rosen, J. X-ray Photoelectron Spectroscopy of Ti₃AlC₂, Ti₃C₂T_x, and TiC Provides Evidence for the Electrostatic Interaction between Laminated Layers in MAX-Phase Materials. *J. Phys. Chem. C* **2020**, *124*, 27732–27742, doi:[10.1021/acs.jpcc.0c07413](https://doi.org/10.1021/acs.jpcc.0c07413).
360. Liu, R.; Li, W. High-Thermal-Stability and High-Thermal-Conductivity Ti₃C₂T_x MXene/Poly(vinyl alcohol) (PVA) Composites. *ACS Omega* **2018**, *3*, 2609–2617, doi:[10.1021/acsomega.7b02001](https://doi.org/10.1021/acsomega.7b02001).
361. Magnuson, M.; Halim, J.; Näslund, L.-Å. Chemical bonding in carbide MXene nanosheets. *J. Electron Spectros. Relat. Phenomena* **2018**, *224*, 27–32, doi:<https://doi.org/10.1016/j.elspec.2017.09.006>.
362. Iatsunskyi, I.; Gottardi, G.; Micheli, V.; Canteri, R.; Coy, E.; Bechelany, M. Atomic layer deposition of palladium coated TiO₂/Si nanopillars: ToF-SIMS, AES and XPS characterization study. *Appl. Surf. Sci.* **2021**, *542*, 148603, doi:<https://doi.org/10.1016/j.apsusc.2020.148603>.
363. Hammer, B.; Nørskov, J.K. Theoretical surface science and catalysis—calculations and concepts. In *Impact of Surface Science on Catalysis*; Academic Press, **2000**; Vol. 45, pp. 71–129 ISBN 0360-0564.

364. Hu, F.; Chen, S.; Wang, C.; Yuan, R.; Chai, Y.; Xiang, Y.; Wang, C. ZnO nanoparticle and multiwalled carbon nanotubes for glucose oxidase direct electron transfer and electrocatalytic activity investigation. *J. Mol. Catal. B Enzym.* **2011**, *72*, 298–304, doi:10.1016/j.molcatb.2011.07.005.
365. Tian, K.; Alex, S.; Siegel, G.; Tiwari, A. Enzymatic glucose sensor based on Au nanoparticle and plant-like ZnO film modified electrode. *Mater. Sci. Eng. C* **2015**, *46*, 548–552, doi:10.1016/j.msec.2014.10.064.
366. Laviron, E. General expression of the linear potential sweep voltammogram in the case of diffusionless electrochemical systems. *J. Electroanal. Chem. Interfacial Electrochem.* **1979**, *101*, 19–28, doi:10.1016/S0022-0728(79)80075-3.
367. Oztekin, Y.; Ramanaviciene, A.; Yazicigil, Z.; Solak, A.O.; Ramanavicius, A. Direct electron transfer from glucose oxidase immobilized on polyphenanthroline-modified glassy carbon electrode. *Biosens. Bioelectron.* **2011**, *26*, 2541–2546, doi:10.1016/j.bios.2010.11.001.
368. Wang, F.; Cao, M.; Qin, Y.; Zhu, J.; Wang, L.; Tang, Y. ZnO nanoparticle-decorated two-dimensional titanium carbide with enhanced supercapacitive performance. *RSC Adv.* **2016**, *6*, 88934–88942, doi:10.1039/C6RA15384D.
369. Xu, T.; Zhang, L.; Cheng, H.; Zhu, Y. Significantly enhanced photocatalytic performance of ZnO via graphene hybridization and the mechanism study. *Appl. Catal. B Environ.* **2011**, *101*, 382–387, doi:10.1016/j.apcatb.2010.10.007.
370. Kim, J.Y.; Jo, S.Y.; Sun, G.J.; Katoch, A.; Choi, S.W.; Kim, S.S. Tailoring the surface area of ZnO nanorods for improved performance in glucose sensors. *Sensors Actuators, B Chem.* **2014**, *192*, 216–220, doi:10.1016/j.snb.2013.10.113.
371. He, W.; Wang, C.; Wang, H.; Jian, M.; Lu, W.; Liang, X.; Zhang, X.; Yang, F.; Zhang, Y. Integrated textile sensor patch for real-time and multiplex sweat analysis. *Sci. Adv.* **2019**, *5*, 1–8, doi:10.1126/sciadv.aax0649.
372. González-Gaitán, C.; Ruiz-Rosas, R.; Morallón, E.; Cazorla-Amorós, D. Effects of the surface chemistry and structure of carbon nanotubes on the coating of glucose oxidase and electrochemical biosensors performance. *RSC Adv.* **2017**, *7*, 26867–26878, doi:10.1039/C7RA02380D.
373. Soto, J.; Hughes, T.; Li, Y.S. Silicon-Based Glucose Oxidase Working Electrode for Glucose Sensing. *ACS Omega* **2019**, *4*, 18312–18316, doi:10.1021/acsomega.9b02384.
374. Yoon, S.; Yoon, H.; Zahed, M.A.; Park, C.; Kim, D.; Park, J.Y. Multifunctional hybrid skin patch for wearable smart healthcare applications. *Biosens. Bioelectron.* **2021**, 113685, doi:10.1016/j.bios.2021.113685.
375. Abellán-Llobregat, A.; Jeerapan, I.; Bandodkar, A.; Vidal, L.; Canals, A.; Wang, J.; Morallón, E. A stretchable and screen-printed electrochemical sensor for

glucose determination in human perspiration. *Biosens. Bioelectron.* **2017**, *91*, 885–891, doi:10.1016/j.bios.2017.01.058.

376. Zhai, Q.; Gong, S.; Wang, Y.; Lyu, Q.; Liu, Y.; Ling, Y.; Wang, J.; Simon, G.P.; Cheng, W. Enokitake Mushroom-like Standing Gold Nanowires toward Wearable Noninvasive Bimodal Glucose and Strain Sensing. *ACS Appl. Mater. Interfaces* **2019**, *11*, 9724–9729, doi:10.1021/acsami.8b19383.

377. Oh, S.Y.; Hong, S.Y.; Jeong, Y.R.; Yun, J.; Park, H.; Jin, S.W.; Lee, G.; Oh, J.H.; Lee, H.; Lee, S.-S.; et al. Skin-Attachable, Stretchable Electrochemical Sweat Sensor for Glucose and pH Detection. *ACS Appl. Mater. Interfaces* **2018**, *10*, 13729–13740, doi:10.1021/acsami.8b03342.

378. Hozumi, S.; Honda, S.; Arie, T.; Akita, S.; Takei, K. Multimodal Wearable Sensor Sheet for Health-Related Chemical and Physical Monitoring. *ACS Sensors* **2021**, *6*, 1918–1924, doi:10.1021/acssensors.1c00281.

379. Li, X.; Zhao, C.; Liu, X. A paper-based microfluidic biosensor integrating zinc oxide nanowires for electrochemical glucose detection. *Microsystems Nanoeng.* **2015**, *1*, 15014, doi:10.1038/micronano.2015.14.

380. Wang, Y.; Wang, X.; Lu, W.; Yuan, Q.; Zheng, Y.; Yao, B. A thin film polyethylene terephthalate (PET) electrochemical sensor for detection of glucose in sweat. *Talanta* **2019**, *198*, 86–92, doi:10.1016/j.talanta.2019.01.104.

381. Wolever, T.M.S. Carbohydrate and the Regulation of Blood Glucose and Metabolism. *Nutr. Rev.* **2003**, *61*, S40–S48, doi:10.1301/nr.2003.may.S40-S48.

382. Shaw, K.; Singh, J.; Sirant, L.; Neary, J.P.; Chilibeck, P.D. Effect of Dark Chocolate Supplementation on Tissue Oxygenation, Metabolism, and Performance in Trained Cyclists at Altitude. *Int. J. Sport Nutr. Exerc. Metab.* **2020**, *30*, 420–426, doi:10.1123/ijsnem.2020-0051.

383. Sylow, L.; Kleinert, M.; Richter, E.A.; Jensen, T.E. Exercise-stimulated glucose uptake — regulation and implications for glycaemic control. *Nat. Rev. Endocrinol.* **2017**, *13*, 133–148, doi:10.1038/nrendo.2016.162.

384. Bae, C.W.; Toi, P.T.; Kim, B.Y.; Lee, W. Il; Lee, H.B.; Hanif, A.; Lee, E.H.; Lee, N.-E. Fully Stretchable Capillary Microfluidics-Integrated Nanoporous Gold Electrochemical Sensor for Wearable Continuous Glucose Monitoring. *ACS Appl. Mater. Interfaces* **2019**, *11*, 14567–14575, doi:10.1021/acsami.9b00848.

385. Zaharieva, D.P.; Turksoy, K.; McGaugh, S.M.; Pooni, R.; Vienneau, T.; Ly, T.; Riddell, M.C. Lag Time Remains with Newer Real-Time Continuous Glucose Monitoring Technology During Aerobic Exercise in Adults Living with Type 1 Diabetes. *Diabetes Technol. Ther.* **2019**, *21*, 313–321, doi:10.1089/dia.2018.0364

List of other publications

[i]. I. Brytavskyi, K. Hušeková, **V. Myndrul**, M. Pavlenko, E. Coy, K. Zaleski, D. Gregušová, L. Yate, V. Smyntyna, I. Iatsunskyi, *Effect of porous silicon substrate on structural, mechanical and optical properties of MOCVD and ALD ruthenium oxide nanolayers*, **Applied Surface Science**. 471 (2019) 686–693. <https://doi.org/10.1016/j.apsusc.2018.12.022>;

IF₂₀₂₁ = 7.392

Ministerial Points₂₀₂₁ = 140 points

[ii]. **V. Myndrul**, I. Iatsunskyi, Nanosilicon-based composites for (Bio)sensing applications: *Current status, advantages, and perspectives*, **Materials (Basel)**. 12 (2019). <https://doi.org/10.3390/ma12182880>;

IF₂₀₂₁ = 3.748

Ministerial Points₂₀₂₁ = 140 points

[iii]. M. Pavlenko, **V. Myndrul**, G. Gottardi, E. Coy, M. Jancelewicz, I. Iatsunskyi, *Porous silicon-zinc oxide nanocomposites prepared by atomic layer deposition for biophotonic applications*, **Materials (Basel)**. (2020). <https://doi.org/10.3390/MA13081987>;

IF₂₀₂₁ = 3.748

Ministerial Points₂₀₂₁ = 140 points

[iv]. **V. Myndrul**, L. Vysloužilová, A. Klápšřová, E. Coy, M. Jancelewicz, I. Iatsunskyi, *Formation and Photoluminescence Properties of ZnO Nanoparticles on Electrospun Nanofibers Produced by Atomic Layer Deposition*, **Coatings**. 10 (2020) 1199. <https://doi.org/10.3390/coatings10121199>

IF₂₀₂₁ = 3.236

Ministerial Points₂₀₂₁ = 100 points

List of conference presentations

[i]. *Study on structural and optical properties of TiO₂ ALD coated silicon nanostructures* [International conference SPIE Photonics West in Brussels, Belgium, 3/4/2016 – 6/4/2016];

[ii]. *Fabrication of silicon nanopillar structures covered with zinc and titan oxides for solar energy and biosensor applications* [9th Ukrainian – Polish Conference “Electronics and information technologies in Lviv – Chynadiyevo, 28/8/2017 – 31/8/2017];

[iii]. *Optical biosensors based on nano-Si for detection of mycotoxins,* [International conference Nanotech in Poznań, Poland, 5/6/2019-8/6/2019];

[iv]. *Gold coated porous silicon nanocomposite as a biosensor platforms suitable for the Aflatoxin B1 detection* [International conference and school Ampere in Zakopane, Poland, 23/6/2019 – 29/6/2019];

[v]. *Optical biosensors based on porous silicon and gold decorated porous silicon nanomaterials suitable for the detection of mycotoxins* [Nanomaterials for biosensors and biomedical applications, Jurmala, Latvia, 2/7/2019 – 4/7/2019];

[vi]. *Synthesis and investigation of MXene/ZnO nanocomposites for biosensing applications* [International conference Nanotech in Poznań, Poland, (virtual meeting), 9/6/2021 – 11/6/2022];

[vii]. *Photoluminescent properties of ZnO nanoparticles grown on the electrospun polymer nanofibers* [International conference and school Ampere in Zakopane Poland, (virtual meeting), 21/6/2021 – 23/6/2021];

[viii]. *Fabrication of electrospun polymer nanofibers with introduced TiO₂ and WO₃ nanowires for photocatalytic and biosensing application* [International conference Nanotech in Poznań, Poland, 1/6/2022 – 5/6/2022].

Contribution statements

Poznań, 23 June 2022

Authorship statement

I declare that I am the co-author of the publications:

[1]. Myndrul, V., Viter, R., Savchuk, M., Koval, M., Starodub, N., Silamiķelis, V., Smyntyna, V., Ramanavicius, A., Iatsunskyi, I., 2017. Gold coated porous silicon nanocomposite as a substrate for photoluminescence-based immunosensor suitable for the determination of Aflatoxin B1. *Talanta* 175, 297–304. <https://doi.org/10.1016/j.talanta.2017.07.054>.

My contribution was to prepare the PSi/Au samples, data collection and analysis. I did all the biosensing experiments and prepared all the figures. I also prepared the first version of the manuscript.

[2]. Myndrul, V., Viter, R., Savchuk, M., Shpyrka, N., Erts, D., Jevdokimovs, D., Silamiķelis, V., Smyntyna, V., Ramanavicius, A., Iatsunskyi, I., 2018. Porous silicon based photoluminescence immunosensor for rapid and highly-sensitive detection of Ochratoxin A. *Biosens. Bioelectron.* 102, 661–667. <https://doi.org/10.1016/j.bios.2017.11.048>.

My contribution was to assist in the PSi sample preparation process, data collection and analysis. I did all the biosensing experiments and prepared all the figures. I also prepared the first version of the manuscript.

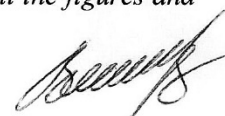
[3]. Myndrul, V., Coy, E., Bechelany, M., Iatsunskyi, I., 2021a. Photoluminescence label-free immunosensor for the detection of Aflatoxin B1 using polyacrylonitrile/zinc oxide nanofibers. *Mater. Sci. Eng. C* 118, 111401. <https://doi.org/10.1016/j.msec.2020.111401>.

I contributed to this work by conceptualizing biosensor experiments under the supervision of dr hab. Igor Iatsunskyi. I also performed all biosensing, photoluminescence and FTIR measurements. My contribution also consisted in the collection of experimental data and their analysis. I prepared all the figures and the first version of the manuscript.

[4]. Myndrul, V., Coy, E., Babayevska, N., Zahorodna, V., Balitskyi, V., Baginskiy, I., Gogotsi, O., Bechelany, M., Giardi, M.T., Iatsunskyi, I., 2022. MXene nanoflakes decorating ZnO tetrapods for enhanced performance of skin-attachable stretchable enzymatic electrochemical glucose sensor. *Biosens. Bioelectron.* 207, 114141. <https://doi.org/10.1016/j.bios.2022.114141>.

I contributed to this work by conceptualizing glucose detection experiments under the supervision of dr hab. Igor Iatsunskyi. I also performed all sensing, electrochemical and on-body glucose measurements. My contribution also included the fabrication of ZnO TPs/MXene samples, the collection of experimental data and their analysis. I prepared all the figures and the first version of the manuscript.

Best regard,



Valerii Myndrul

valmyn@amu.edu.pl

I confirm the above statement: Prof. UAM dr hab. Igor Iatsunskyi



Poznań, 15 June 2022

Co-author declaration

I declare that I am the co-author of the publications:

(1). Myndrul, V., Viter, R., Savchuk, M., Koval, M., Starodub, N., Silamiķelis, V., Smyntyna, V., Ramanavicius, A., Iatsunskiy, I., 2017. Gold coated porous silicon nanocomposite as a substrate for photoluminescence-based immunosensor suitable for the determination of Aflatoxin B1. *Talanta* 175, 297–304. <https://doi.org/10.1016/j.talanta.2017.07.054>.

My contribution was to participate in the fabrication of PSi samples, discuss the results obtained, and finalize the manuscript.

(2). Myndrul, V., Viter, R., Savchuk, M., Shpyrka, N., Ertz, D., Jevdokimovs, D., Silamiķelis, V., Smyntyna, V., Ramanavicius, A., Iatsunskiy, I., 2018. Porous silicon based photoluminescence immunosensor for rapid and highly-sensitive detection of Ochratoxin A. *Biosens. Bioelectron.* 102, 661–667. <https://doi.org/10.1016/j.bios.2017.11.048>.

I contributed by participating in the PSi samples fabrication, discussing the obtained results, and finalization of the manuscript.

(3). Myndrul, V., Coy, E., Bechelany, M., Iatsunskiy, I., 2021a. Photoluminescence label-free immunosensor for the detection of Aflatoxin B1 using polyacrylonitrile/zinc oxide nanofibers. *Mater. Sci. Eng. C* 118, 111401. <https://doi.org/10.1016/j.msec.2020.111401>.

Together with Valery Myndrul, I developed the concept of experiments with biosensors, I also carried out measurements using SEM and confocal fluorescence microscopy, and participated in the finalization of the manuscript.

(4). Myndrul, V., Coy, E., Babayevska, N., Zahorodna, V., Balitskiy, V., Baginskiy, I., Gogotsi, O., Bechelany, M., Giardi, M.T., Iatsunskiy, I., 2022. MXene nanoflakes decorating ZnO tetrapods for enhanced performance of skin-attachable stretchable enzymatic electrochemical glucose sensor. *Biosens. Bioelectron.* 207, 114141. <https://doi.org/10.1016/j.bios.2022.114141>.

I and Valerii Myndrul conceptualized glucose detection experiments. I also performed SEM Raman spectroscopy measurements, participated in finalizing the manuscript.

Best regard,



Igor Iatsunskiy
igoyat@amu.edu.pl

Dr. Michael Bechelany

Institut Européen des Membranes, IEM, UMR5635,

Univ Montpellier, ENSCM, CNRS,

34095, Montpellier, CEDEX5, France

Co-author statement

I declare that I am the co-author of the publications:

[1]. V. Myndrul, E. Coy, M. Bechelany, I. Iatsunskiy, *Photoluminescence label-free immunosensor for the detection of Aflatoxin B1 using polyacrylonitrile/zinc oxide nanofibers*, Mater. Sci. Eng. C. 118 (2021) 111401. doi:10.1016/j.msec.2020.111401.

[2]. V. Myndrul, E. Coy, N. Babayevska, V. Zahorodna, V. Balitskiy, I. Baginskiy, O. Gogotsi, M. Bechelany, M.T. Giardi, I. Iatsunskiy, *MXene nanoflakes decorating ZnO tetrapods for enhanced performance of skin-attachable stretchable enzymatic electrochemical glucose sensor*, Biosens. Bioelectron. 207 (2022) 114141. <https://doi.org/10.1016/j.bios.2022.114141>

My contribution to the publication [1] was the production of PAN/ZnO nanofibers by electrospinning and ALD methods. In [2], I contributed by performing XPS measurements of the ZnO TPs and ZnO TPs/MXene composite.

SIGNATURE



Dr. Michael Bechelany

mikhael.bechelany@umontpellier.fr

Riga, 15 December 2021

Dr. Roman Viter
University of Latvia "House of Science"
Jelgavas street 3, Rīga, LV-1004
roman.viter@lu.lv

Co-author statement

I hereby declare that I contributed to the following publications:

[1]. V. Myndrul, R. Viter, M. Savchuk, M. Koval, N. Starodub, V. Silamiķelis, V. Smyntyna, A. Ramanavicius, I. Iatsunskiy, **Gold coated porous silicon nanocomposite as a substrate for photoluminescence-based immunosensor suitable for the determination of Aflatoxin B1**, Talanta. 175 (2017) 297–304. doi:10.1016/j.talanta.2017.07.054. My contribution to this work consisted of conceptualization of Aflatoxin B1 (AFB1) detection experiments, analysis of the thermodynamic parameters of AFB1 detection, finalization of the manuscript.

[2]. V. Myndrul, R. Viter, M. Savchuk, N. Shpyrka, D. Erts, D. Jevdokimovs, V. Silamiķelis, V. Smyntyna, A. Ramanavicius, I. Iatsunskiy, **Porous silicon based photoluminescence immunosensor for rapid and highly-sensitive detection of Ochratoxin A**, Biosens. Bioelectron. 102 (2018) 661–667. doi:10.1016/j.bios.2017.11.048. I contributed to this work by conceptualizing the Ochratoxin A (OTA) detection experiments. I also participated in manuscript correction and finalization.

With best regards,

Dr. Roman Viter



Vilnius, 06 July 2022

Prof. Habil. Dr. Arūnas Ramanavičius
Department of Physical Chemistry,
Faculty of Chemistry and Geoscience, Vilnius University,
Naugarduko str. 24, 03225, Vilnius, Lithuania
E-mail: arunas.ramanavicius@chf.vu.lt

Co-author statement

I declare that I am the co-author of the following publications:

[1]. V. Myndrul, R. Viter, M. Savchuk, M. Koval, N. Starodub, V. Silamiķelis, V. Smyntyna, A. Ramanavicius, I. Iatsunskyi, *Gold coated porous silicon nanocomposite as a substrate for photoluminescence-based immunosensor suitable for the determination of Aflatoxin B1*, Talanta. 175 (2017) 297–304. doi:10.1016/j.talanta.2017.07.054.

[2]. V. Myndrul, R. Viter, M. Savchuk, N. Shpyrka, D. Erts, D. Jevdokimovs, V. Silamiķelis, V. Smyntyna, A. Ramanavicius, I. Iatsunskyi, *Porous silicon based photoluminescence immunosensor for rapid and highly-sensitive detection of Ochratoxin A*, Biosens. Bioelectron. 102 (2018) 661–667. doi:10.1016/j.bios.2017.11.048.

My contribution to work [1] consisted of the conceptualization of porous silicon/gold (PSi/Au) composite fabrication process. I also participated in the finalization process of both manuscripts [1,2].

With best regards,



Arūnas Ramanavičius

Riga, 10 December 2021

Dr. Donats Erts

Institute of Chemical Physics, University of Latvia,

Raina Blvd. 19, LV-1586 Riga, Latvia

Co-author statement

I declare that I am the co-author of the publication:

V. Myndrul, R. Viter, M. Savchuk, N. Shpyrka, D. Erts, D. Jevdokimovs, V. Silamiķelis, V. Smyntyna, A. Ramanavicius, I. Iatsunskyi, *Porous silicon based photoluminescence immunosensor for rapid and highly-sensitive detection of Ochratoxin A*, Biosens. Bioelectron. 102 (2018) 661–667. doi:10.1016/j.bios.2017.11.048.

My contribution to this work consisted of supervision during SEM imaging of porous silicon (PSi) samples and the finalization of the manuscript.

SIGNATURE


Dr. Donats Erts
donats.erts@lu.lv





Poznań, 13 June 2022

Declaration of co-authorship

I declare that I am the co-author of the publications:

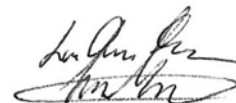
1. Myndrul, V., Coy, E., Bechelany, M., Iatsunskiy, I., 2021a. Photoluminescence label-free immunosensor for the detection of Aflatoxin B1 using polyacrylonitrile/zinc oxide nanofibers. *Mater. Sci. Eng. C* 118, 111401. <https://doi.org/10.1016/j.msec.2020.111401>.

✦ My contribution to this work was to carry out TEM and XRD measurements of PAN/ZnO composites.

2. Myndrul, V., Coy, E., Babayevska, N., Zahorodna, V., Balitskiy, V., Baginskiy, I., Gogotsi, O., Bechelany, M., Giardi, M.T., Iatsunskiy, I., 2022. MXene nanoflakes decorating ZnO tetrapods for enhanced performance of skin-attachable stretchable enzymatic electrochemical glucose sensor. *Biosens. Bioelectron.* 207, 114141. <https://doi.org/10.1016/j.bios.2022.114141>.

✦ I contributed to this publication by performing TEM and EDX measurements of ZnO TPs/MXene nanocomposites.

Best regard,



Emerson Coy

coyeme@amu.edu.pl



Poznań, 21 June 2022

Co-author declaration

I declare that I am the co-author of the publications:

1. Myndrul, V., Coy, E., Babayevska, N., Zahorodna, V., Balitskyi, V., Baginskiy, I., Gogotsi, O., Bechelany, M., Giardi, M.T., Iatsunskyi, I., 2022. MXene nanoflakes decorating ZnO tetrapods for enhanced performance of skin-attachable stretchable enzymatic electrochemical glucose sensor. *Biosens. Bioelectron.* 207, 114141. <https://doi.org/10.1016/j.bios.2022.114141>.

- I participated in ZnO tetrapods (ZnO TPs) fabrication process.

With best regards,

Nataliya Babayevska

natbab@amu.edu.pl

Riga, 12 January 2022

Daniels Jevdokimovs

Jūrmala, Spilves iela 11-3, LV-2010, Latvia

Co-author statement

I hereby declare that I am a co-author of the following publication:

V. Myndrul, R. Viter, M. Savchuk, N. Shpyrka, D. Erts, D. Jevdokimovs, V. Silamiķelis, V. Smyntyna, A. Ramanavicius, I. Iatsunskyi, **Porous silicon based photoluminescence immunosensor for rapid and highly-sensitive detection of Ochratoxin A**, Biosens. Bioelectron. 102 (2018) 661–667. doi:10.1016/j.bios.2017.11.048.

My contribution to this work consisted of scanning electron spectroscopy (SEM) imaging of porous silicon/gold (PSi/Au) nanocomposites.

Sincerely yours,



Daniels Jevdokimovs

daniel.jevdokimov@gmail.com

Maryna Koval

<http://www.marinakoval.com>

Tel.:+38 (063) 59-12-989

Co-author statement

I declare that I am the co-author of the publication:

V. Myndrul, R. Viter, M. Savchuk, M. Koval, N. Starodub, V. Silamiķelis, V. Smyntyna, A. Ramanavicius, I. Iatsunskyi, *Gold coated porous silicon nanocomposite as a substrate for photoluminescence-based immunosensor suitable for the determination of Aflatoxin B1*, *Talanta*. 175 (2017) 297–304. doi:10.1016/j.talanta.2017.07.054.

My contribution to this work consisted of assistance in the fabrication of porous silicon/gold (PSi/Au) nanocomposites.

Best regards



Maryna Koval

Kyiv, 10 December 2021

Prof. Nikolay Starodub

National University of Life and Environmental Sciences,

15, Geroyiv Oborony street, Kyiv 03041, Ukraine

Co-author statement

I declare that I am the co-author of the publication:

V. Myndrul, R. Viter, M. Savchuk, M. Koval, N. Starodub, V. Silamiķelis, V. Smyntyna, A. Ramanavicius, I. Iatsunskyi, *Gold coated porous silicon nanocomposite as a substrate for photoluminescence-based immunosensor suitable for the determination of Aflatoxin B1*, Talanta. 175 (2017) 297–304. doi:10.1016/j.talanta.2017.07.054.

My contribution to this work consisted in the provision of biological samples of Aflatoxin B1 (AFB1) and antigens against AFB1 (anti-AFB1).



SIGNATURE

Prof. Nikolay Starodub

nfstarodub@gmail.com

Dr. Maryna Savchuk

State University of Infrastructure and Technologies

9 Kyrylivska Street, 04071 Kyiv, Ukraine

Co-author statement

I declare that I am the co-author of the following publications:

[1]. V. Myndrul, R. Viter, M. Savchuk, N. Shpyrka, D. Erts, D. Jevdokimovs, V. Silamiķelis, V. Smyntyna, A. Ramanavicius, I. Iatsunskyi, *Porous silicon based photoluminescence immunosensor for rapid and highly-sensitive detection of Ochratoxin A*, Biosens. Bioelectron. 102 (2018) 661–667. doi:10.1016/j.bios.2017.11.048.

[2]. V. Myndrul, R. Viter, M. Savchuk, M. Koval, N. Starodub, V. Silamiķelis, V. Smyntyna, A. Ramanavicius, I. Iatsunskyi, *Gold coated porous silicon nanocomposite as a substrate for photoluminescence-based immunosensor suitable for the determination of Aflatoxin B1*, Talanta. 175 (2017) 297–304. doi:10.1016/j.talanta.2017.07.054.

My contribution to work [1] consisted of assistance during the detection of Ochratoxin A (OTA) on porous silicon (PSi) samples. In work [2], I assisted during the detection of Aflatoxin B1 (AfB1) on gold coated porous silicon (PSi/Au) nanocomposites.



SIGNATURE

Dr. Maryna Savchuk

taranmaruna@gmail.com

Nelya Shpyrka

National University of Life and Environmental Sciences,

15, Geroyiv Oborony street, Kyiv 03041, Ukraine

Co-author statement

I declare that I am the co-author of the publication:

V. Myndrul, R. Viter, M. Savchuk, N. Shpyrka, D. Erts, D. Jevdokimovs, V. Silamiķelis, V. Smyntyna, A. Ramanavicius, I. Iatsunskyi, *Porous silicon based photoluminescence immunosensor for rapid and highly-sensitive detection of Ochratoxin A*, Biosens. Bioelectron. 102 (2018) 661–667. doi:10.1016/j.bios.2017.11.048.

My contribution to this work consisted of assistance in the biofunctionalization process of porous silicon (PSi) samples.



SIGNATURE

Nelya Shpyrka

Nelya.Shpyrka@gmail.com

Kyiv, 25 May 2022

Vitalii Balitskyi

Materials Research Centre,

3, Krzhizhanovskogo street, Kyiv 03142, Ukraine

Co-author statement

I declare that I am the co-author of the publication:

V. Myndrul, E. Coy, N. Babayevska, V. Zahorodna, V. Balitskyi, I. Baginskiy, O. Gogotsi, M. Bechelany, M.T. Giardi, I. Iatsunskiy, *MXene nanoflakes decorating ZnO tetrapods for enhanced performance of skin-attachable stretchable enzymatic electrochemical glucose sensor*, Biosens. Bioelectron. 207 (2022) 114141. <https://doi.org/10.1016/j.bios.2022.114141>.

My contribution to this work was to synthesize 2D MXene sheets by operating of Etching Reactor for MXene synthesis from MAX-phase powder.

SIGNATURE



Vitalii Balitskyi

vitalik@mrc.org.ua



Formello, Rome, 25 May 2022

Dr. Maria Teresa Giardi

Biosensor Srl,

Via Degli Olmetti 44,

00060, Formello, Rome, Italy

Co-author statement

I declare that I am the co-author of the publication:

V. Myndrul, E. Coy, N. Babayevska, V. Zahorodna, V. Balitskyi, I. Baginskiy, O. Gogotsi, M. Bechelany, M.T. Giardi, I. Iatsunskyi, *MXene nanoflakes decorating ZnO tetrapods for enhanced performance of skin-attachable stretchable enzymatic electrochemical glucose sensor*, Biosens. Bioelectron. 207 (2022) 114141. <https://doi.org/10.1016/j.bios.2022.114141>

My contribution to this publication was the fabrication of the flexible, stretchable electrode by the screen printing method.

SIGNATURE

A handwritten signature in black ink that reads "Maria Teresa Giardi".

Dr. Maria Teresa Giardi

mt.giardi@biosensor.it

Via degli Olmetti 44 00060 Formello (Roma) – Italy Tel. e Fax +39 06 9075116
<http://www.biosensor.it> - E-mail:
info@biosensor.it

P.I. e C.F.: 07650601003 - R.E.A. 1046997

Kyiv, 25 May 2022

Ivan Baginskiy

Materials Research Centre,

3, Krzhizhanovskogo street, Kyiv 03142, Ukraine

Co-author statement

I declare that I am the co-author of the publication:

V. Myndrul, E. Coy, N. Babayevska, V. Zahorodna, V. Balitskyi, I. Baginskiy, O. Gogotsi, M. Bechelany, M.T. Giardi, I. Iatsunskyi, *MXene nanoflakes decorating ZnO tetrapods for enhanced performance of skin-attachable stretchable enzymatic electrochemical glucose sensor*, Biosens. Bioelectron. 207 (2022) 114141. <https://doi.org/10.1016/j.bios.2022.114141>.

My contribution to this work was the synthesis of the MAX-phase powder for its subsequent use in the MXene synthesis process.

SIGNATURE



Ivan Baginskiy

ibaginskiy@mrc.org.ua

Kyiv, 25 May 2022

Oleksiy Gogotsi, Materials Research Centre Director,

3, Krzhizhanovskogo street, Kyiv 03142, Ukraine

Co-author statement

I declare that I am the co-author of the publication:

V. Myndrul, E. Coy, N. Babayevska, V. Zahorodna, V. Balitskyi, I. Baginskiy, O. Gogotsi, M. Bechelany, M.T. Giardi, I. Iatsunskyi, *MXene nanoflakes decorating ZnO tetrapods for enhanced performance of skin-attachable stretchable enzymatic electrochemical glucose sensor*, Biosens. Bioelectron. 207 (2022) 114141. <https://doi.org/10.1016/j.bios.2022.114141>.

My contribution to this work was to synthesize 2D MXene sheets and exfoliate them.



Oleksiy Gogotsi

alex@mrc.org.ua

Veronika Zahorodna

Materials Research Centre,

3, Krzhizhanovskogo street, Kyiv 03142, Ukraine

Co-author statement

I declare that I am the co-author of the publication:

V. Myndrul, E. Coy, N. Babayevska, V. Zahorodna, V. Balitskyi, I. Baginskiy, O. Gogotsi, M. Bechelany, M.T. Giardi, I. Iatsunskyi, *MXene nanoflakes decorating ZnO tetrapods for enhanced performance of skin-attachable stretchable enzymatic electrochemical glucose sensor*, Biosens. Bioelectron. 207 (2022) 114141. <https://doi.org/10.1016/j.bios.2022.114141>.

I have been involved in the MXene delamination and purification processes to produce a high-quality MXene slurry.



Veronika Zahorodna

veronika@mrc.org.ua

Co-author statement

I hereby declare that I contributed to the following publications:

[1]. V. Myndrul, R. Viter, M. Savchuk, M. Koval, N. Starodub, V. Silamiķelis, V. Smyntyna, A. Ramanavicius, I. Iatsunskyi, *Gold coated porous silicon nanocomposite as a substrate for photoluminescence-based immunosensor suitable for the determination of Aflatoxin B1*, Talanta. 175 (2017) 297–304. doi:10.1016/j.talanta.2017.07.054.

[2]. V. Myndrul, R. Viter, M. Savchuk, N. Shpyrka, D. Erts, D. Jevdokimovs, V. Silamiķelis, V. Smyntyna, A. Ramanavicius, I. Iatsunskyi, *Porous silicon based photoluminescence immunosensor for rapid and highly-sensitive detection of Ochratoxin A*, Biosens. Bioelectron. 102 (2018) 661–667. doi:10.1016/j.bios.2017.11.048.

My contribution to these works [1,2] consisted of fabrication of the cell for the photoluminescence-based (PL) detection of Aflatoxin B1 on PSi/Au samples and the detection of Ochratoxin A on PSi samples, respectively.

Best regards,

Viesturs Silamiķelis
University of Latvia “House of Science”
Jelgavas street 3, Rīga, LV-1004
viesturs.silamikelis@lu.lv



Copyright and Permissions



Gold coated porous silicon nanocomposite as a substrate for photoluminescence-based immunosensor suitable for the determination of Aflatoxin B1

Author: Valerii Myndrul, Roman Viter, Maryna Savchuk, Maryna Koval, Nikolay Starodub, Viesturs Silamiķelis, Valentyn Smyntyna, Arunas Ramanavicius, Igor Iatsunskiy

Publication: Talanta

Publisher: Elsevier

Date: 1 December 2017

© 2017 Elsevier B.V. All rights reserved.

Journal Author Rights

Please note that, as the author of this Elsevier article, you retain the right to include it in a thesis or dissertation, provided it is not published commercially. Permission is not required, but please ensure that you reference the journal as the original source. For more information on this and on your other retained rights, please visit: <https://www.elsevier.com/about/our-business/policies/copyright#Author-rights>



Porous silicon based photoluminescence immunosensor for rapid and highly-sensitive detection of Ochratoxin A

Author: Valerii Myndrul, Roman Viter, Maryna Savchuk, Nelya Shpyrka, Donats Erts, Daniels Jevdokimovs, Viesturs Silamiķelis, Valentyn Smyntyna, Arunas Ramanavicius, Igor Iatsunskiy

Publication: Biosensors and Bioelectronics

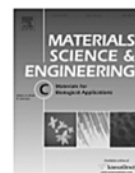
Publisher: Elsevier

Date: 15 April 2018

© 2017 Elsevier B.V. All rights reserved.

Journal Author Rights

Please note that, as the author of this Elsevier article, you retain the right to include it in a thesis or dissertation, provided it is not published commercially. Permission is not required, but please ensure that you reference the journal as the original source. For more information on this and on your other retained rights, please visit: <https://www.elsevier.com/about/our-business/policies/copyright#Author-rights>



Photoluminescence label-free immunosensor for the detection of Aflatoxin B1 using polyacrylonitrile/zinc oxide nanofibers

Author: Valerii Myndrul, Emerson Coy, Mikhael Bechelany, Igor Iatsunskiy

Publication: Materials Science and Engineering: C

Publisher: Elsevier

Date: January 2021

© 2020 Elsevier B.V. All rights reserved.

Journal Author Rights

Please note that, as the author of this Elsevier article, you retain the right to include it in a thesis or dissertation, provided it is not published commercially. Permission is not required, but please ensure that you reference the journal as the original source. For more information on this and on your other retained rights, please visit: <https://www.elsevier.com/about/our-business/policies/copyright#Author-rights>



MXene nanoflakes decorating ZnO tetrapods for enhanced performance of skin-attachable stretchable enzymatic electrochemical glucose sensor

Author: Valerii Myndrul, Emerson Coy, Nataliya Babayevska, Veronika Zahorodna, Vitalii Balitskiy, Ivan Baginskiy, Oleksiy Gogotsi, Mikhael Bechelany, Maria Teresa Giardi, Igor Iatsunskiy

Publication: Biosensors and Bioelectronics

Publisher: Elsevier

Date: Jul 1, 2022

Copyright © 2022, Elsevier

Journal Author Rights

Please note that, as the author of this Elsevier article, you retain the right to include it in a thesis or dissertation, provided it is not published commercially. Permission is not required, but please ensure that you reference the journal as the original source. For more information on this and on your other retained rights, please visit: <https://www.elsevier.com/about/our-business/policies/copyright#Author-rights>